TRANSPORTATION RESEARCH

RECORD

No. 1406

Soils, Geology, and Foundations

Construction Robotics and Automation, and Foundations Engineering

A peer-reviewed publication of the Transportation Research Board

TRANSPORTATION RESEARCH BOARD
NATIONAL RESEARCH COUNCIL

NATIONAL ACADEMY PRESS
WASHINGTON, D.C. 1993

Transportation Research Record 1406
ISSN 0361-1981
ISBN 0-309-05553-9
Price: $31.00

Subscriber Category
IIIA soils, geology, and foundations

TRB Publications Staff
Director of Reports and Editorial Services: Nancy A. Ackerman
Associate Editor/Supervisor: Luanne Crayton
Associate Editors: Naomi Kassabian, Alison G. Tobias
Assistant Editors: Susan E. G. Brown, Norman Solomon
Production Coordinator: Sharada Gilkey
Graphics Coordinator: Terri Wayne
Office Manager: Phyllis D. Barber
Senior Production Assistant: Betty L. Hawkins

Printed in the United States of America

Transportation Research Record 1406

Contents

Foreword

The seventeen papers in this volume provide information on current technological advances and traditional geotechnical investigations. The papers may be grouped into three themes. The first five papers address construction robotics and automation, and expert systems. The next four cover different aspects of geotechnical engineering. Das et al. discuss the effect of surface footings on layered foundation material. Wong et al. report on the use of deep soil mixing to construct a braced retaining wall, and Nevels describes erosion of dispersive clay used as embankment material. Budiman and Wibowo discuss the effects of the compactor footprints on the constitutive response of a clayey sand. Authors of the remaining eight papers describe testing, characteristics, and behavior of soils, subgrades, and other materials that are part of pavement systems.

Technical and Economic Feasibility of Automated Reinforcement Bar Fastening on Bridge Decks

DAVID MARTINELLI, JOHN ABRAHAM, AND TERRANCE STOBBE

The investment of public funds for construction and rehabilitation of transportation facilities continues to grow. At the same time, productivity in such projects remains stagnant, and injury rates and compensation claims are excessively high. Construction automation presents opportunities to overcome productivity, safety, and cost problems associated with transportation projects. The feasibility of automating rebar fastening is examined. Rebar fastening could be an ideal candidate for automation. Because of related occupational hazards and the repetitive and voluminous nature of the task, automated rebar fastening could yield high benefits without significant investments in technical innovation.

Because the construction industry plays a critical role in the development, rehabilitation, and maintenance of the U.S. transportation infrastructure, advancements in the construction industry can have significant positive effects on the life-cycle development and performance of transportation systems. This paper discusses and evaluates the potential for automation of rebar fastening, which is particularly prevalent in bridge deck construction and rehabilitation.

BACKGROUND

The use of robots to perform various production tasks is increasing in manufacturing industries. The American Robot Association estimated that the number of robots used in the United States exceeded 100,000 in 1990 (*1*). Many industries are realizing the impact that full automation could have on their production. Currently, several industries have complete automation. Automation also has been accompanied by a considerable research and development effort. Robotics research is being conducted at a number of universities and commercial enterprises.

Construction, the largest U.S. industry, has not been a part of this automation trend. To date, there has been limited research in construction automation and relatively few practical construction robots developed. In addition to institutional barriers, other factors inherent to construction, such as a dynamic work environment, harsh climates, heavy materials and building components, impede automation. Thus construction robots require a higher level of sophistication, reliability, and durability than those used in manufacturing.

D. R. Martinelli and J. Abraham, Department of Civil Engineering, West Virginia University, Morgantown, W.Va. 26506. T. Stobbe, Department of Industrial Engineering, West Virginia University, Morgantown, W.Va. 26506.

Construction is an ideal industry for automation because construction operations are typically repetitious and physically demanding. Specifically, the special hazards associated with high elevations, toxic and combustible materials, noise, vibrations, heavy lifting, falls, and routine exposure to weather and dirt are highly undesirable. The construction industry expends significant amounts for medical expenses and compensation claims, and automating construction operations has the potential for reducing such claims.

In addition to enhancing safety and increasing productivity, automating certain construction activities could improve the quality of the finished product. Quality includes reliability, constructability, performance, minimum life-cycle costs, and customer satisfaction. In such a competitive industry (particularly on the international scale), the enhanced quality realized from automation could be substantial.

Only a few experimental robots have been developed in Japan, the United States, and Europe. Applications of construction robot prototypes include slab finishing, pavement cutting, excavation, sand blasting, and crack filling.

PROBLEM DESCRIPTION

Efforts to introduce partial automation into rebar preparation and positioning account for only about 30 percent of the rebar placement operation. Although most of the remaining time of reinforcement bar workers (rodmen) involves fastening, no documented studies on automation of this activity have been found.

Current rebar fastening methods call for tying bars with wire. This process requires that the worker perform in a near-constant stooping position, inducing prolonged pressure on the back, particularly the lower back. It has been estimated that disorders of the lower back region account for 400,000 work-related disabling injuries annually and result in approximately 19 to 25 percent of all workers' compensation claims (*2,3*). Tying bars with wire is highly repetitive and strenuous at sites such as bridge decks, and it often leads to musculoskeletal problems (*4*). Furthermore, the rebar "mat" forms an unstable walking surface that is strenuous on the feet, thus contributing to tripping and stumbling accidents.

Because rebar fastening may be characterized as repetitive, of low productivity, and hazardous, it could be an ideal candidate for automation. The technical aspects of automated rebar fastening include the robot components, their configuration, manipulator characteristics, motors employed, method

of fastening, and choice of sensors. In studying the economic feasibility of automated rebar fastening, the quantifiable benefits and costs were assessed, and a present worth analysis was conducted.

DESCRIPTION OF REBAR FASTENING

The construction activity proposed for automation is reinforcement bar fastening on decks, floors, and other horizontal surfaces. Rebar fastening is necessary to ensure that proper orientation and spacing of rebars are preserved during the pouring of concrete to avoid jeopardizing the quality of the cast slab. To gain further knowledge of the activity, three major bridge reconstruction projects were visited, and rodmen were videotaped over nearly an entire workday. As expected, the crew spent approximately 70 percent of the day tying rebar.

The videotapes show that bar tying is a simple but rugged process. The rodman has a waist belt of tools, a pair of pliers, and a loop of tying wire. In addition to a hard hat, rodmen must wear hard-sole boots and heavy gloves to minimize the piercing of the wire to the feet and hands. The worker first moves to the local area that he intends to tie, lodges his feet on the rebar mat for stability, stoops in a double-bent position, and then ties intersections within his reach (Figure 1), which takes an average of 6 sec for an experienced worker. The worker then moves on to the next intersection to be tied.

Typically, to maximize productivity from one position, the worker reaches to tie intersections beyond a comfortable reach of the initial location. This may be one of the causes of the periodic cramping in the legs and loss of balance. After tying an average of 20 intersections, the worker straightens up to look for untied intersections, providing temporary relief to the worker's back but causing worker downtime.

At one site the workers tied bars continuously for 65 min, with the periodic pauses described, then took a 20-min water break. The workers stopped for lunch at the end of 4 hr. The rodmen had to work constantly on the rebar surface. It was observed that even those workers with years of experience tended to trip on the mat. Discussions with the workers revealed other instances in which they had tripped and fallen on mats and falls that they and other workers had taken from decks or at work sites. The videotape of the rodmen working also revealed that workers often lodged their feet in uncomfortable positions to attain stability.

Further discussions with workers revealed that they are prone to slipping on the mat during even slightly wet and icy conditions. Bridge decks are usually the hottest or coldest areas of a construction project during periods of extreme temperatures. In winter, winds are usually high and hands tend to cramp. In summer, heat reflects off the forms, adding to the heat of the rebars themselves. One worker noted during an interview, "Rebar tying is one of the most difficult and demanding tasks in construction; there is not a day that goes by without back pain, [and] it's very tough and hazardous . . . ."

TECHNICAL FEASIBILITY OF AUTOMATED REBAR FASTENING

Establishing technical feasibility of the development and implementation of automated equipment is somewhat less structured than economic feasibility because no standard measure of technical feasibility exists. Hence, the following criteria serve as the basis for technical feasibility for this discussion:

1. Does the robot development primarily consist of off-the-shelf or otherwise proven technologies?
2. Is it likely that key technical issues can be resolved within 5 years?
3. Are many of the system components adaptable to different project environments (as opposed to being site-specific configurations)?
4. Is the task somewhat standard from one project to the next?
5. Is it possible to incorporate one or more workers "into the loop," or does the task require full automation?
6. Is any part of the task at least partially mechanized or automated?

First the technical issues associated with an automated rebar fastening system based on information found in documenta-

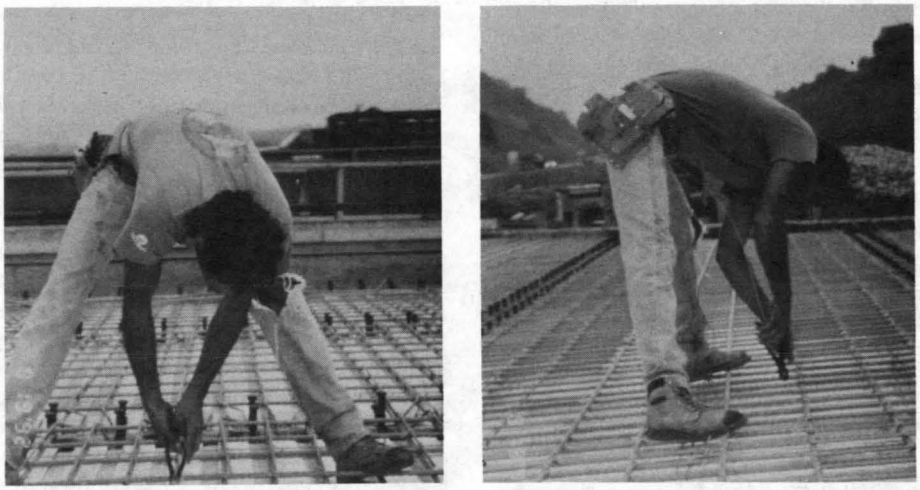

FIGURE 1 Front and side views of rebar tying.

tion of other construction or field robotic developments must be identified (*5,6*). Next, a concept and preliminary design of a rebar robot must be generated. This design should include the system configuration, definition of subsystems, technologies for subsystems, and a typical implementation scenario. A future study would address integration of subsystems, functional specifications, and machine drawings.

Mechanized Fastening

The method used by a robot end effector is one of the fundamental technical issues identified in the literature. Currently, rebars are fastened almost exclusively through tying intersections with wire. Developing a method for mechanized fastening poses one of the key technical issues. It is probably possible to mechanize and automate rebar fastening with wire, but it is likely that a mechanically simpler process exists.

In 1986 Rely Manufacturing of Ontario, Canada, marketed a mechanized rebar tier; however, the effort proved to be unsuccessful. Users cited low reliability and awkward maneuverability of the machine as the reasons for not adopting this product. The 70-lb machine had to be pushed by hand as its grooved wheel "rode" the rebar like rails. For this reason, other fastening concepts have been explored by equipment manufacturers attempting to mechanize the process.

Recently, Glim Manufacturing of Sweden developed a product that fastens rebar intersections by "clamping" them. The 14-lb Glim-Loc Gun (Figure 2) consists of a channelized hopper that carries the clamps that fasten the rebars and an end effector that performs the clamping. The gun is positioned vertically over the intersection to be clamped, and the worker exerts a downward force over the handles (Figure 2). This applied pressure forces the clamps out of the metal channel, automatically locking the two bars in position. The clamps are made of high-density polyethylene and offer high resistance to corrosion and extreme temperatures. They are molded in cartridges that have several clamps. The metal hopper, which stocks cartridges, is a channelized metal container that holds the clamps and feeds them to the end effector.

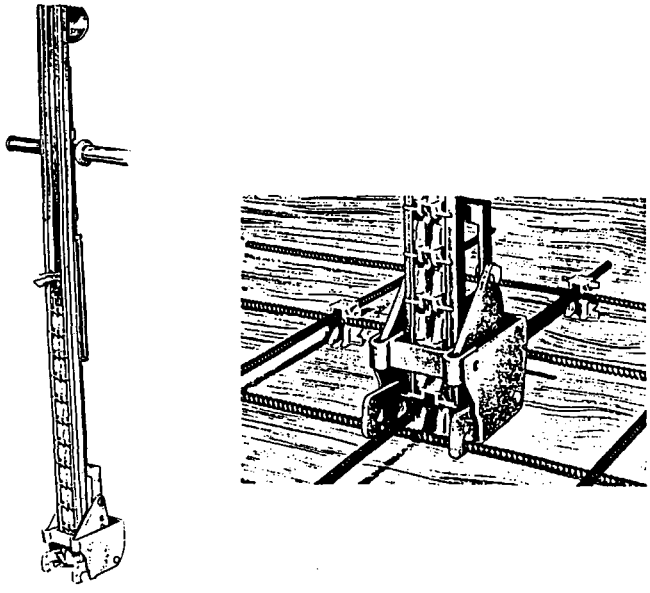

FIGURE 2 Glim Loc Gun system.

The primary shortcoming of the Glim-Loc Gun is the 40 lb of vertical force that must be applied each time a rebar junction is fastened. Workers using the gun have experienced shoulder strain from applying this amount of vertical force repeatedly. However, the concept of the Glim-Loc Gun is relatively simple from an automation standpoint. Whereas the mechanical operations of tying with wire are quite intricate, only a vertical force is required to "fire" the Glim-Loc Gun. It is this concept of mechanized fastening that is adopted for the automated fastening robot.

Conceptual Design and Operation

The system components include the robot manipulator and end effector, local sensors, global sensors, controls, suspension, locomotion, power, and human interfaces. The overall system concept for a typical bridge deck application is shown in Figure 3. Suspension and locomotion are provided through a cage structure that performs similarly to an XY table and rests on the Bidwell rails that are erected before bridge decks are poured to support the paving equipment. The cage would have wheels that allow it to advance along the rails (manually or by power) as well as a clamp switch that locks the cage on the rails while the robot is in operation. The controls and the power source are housed in a box that moves over the rebar mat on all-terrain tires.

The cage supports a gantry robot that hangs from a telescopic rod. The end effector of the robot is the Glim-Loc Gun or similar system for clamping. (Figure 4 shows the manipulator and end effector in more detail.) The two-link manipulator has 5 degrees of freedom: major-z (Link 1), minor-z (Link 2), x (telescopic mount), y (rod advance), and rotation about Link 1.

A maximum of four workers are involved. Worker 1, situated "near" the current position of the robot, monitors the progress of the clamping operation. Worker 1 periodically stocks the manipulator with clamps and also has access to a kill switch to shut down the system in an emergency. Worker 2 monitors the controls, advances the controls and power supply box, and, if necessary, shuts down the system at any time. Worker 3, in front of the cage, inspects the prefastened rebars and makes any necessary adjustments in alignment and spacing. Finally, Worker 4 is an inspector or foreman who inspects postfastened rebars.

Technical Issues

The first technical issue is that of adapting the robot to bridge deck construction sites. Construction robots usually must operate in situ and therefore cannot be designed assuming a controlled environment. Instead, they must be flexible and rugged so as to function in a variety of environments with at least partial exposure to the elements, placing additional technical constraints on development. The proposed concept allows for adjustments in dimensions so as to accommodate decks of variable widths. Further, because the task does not

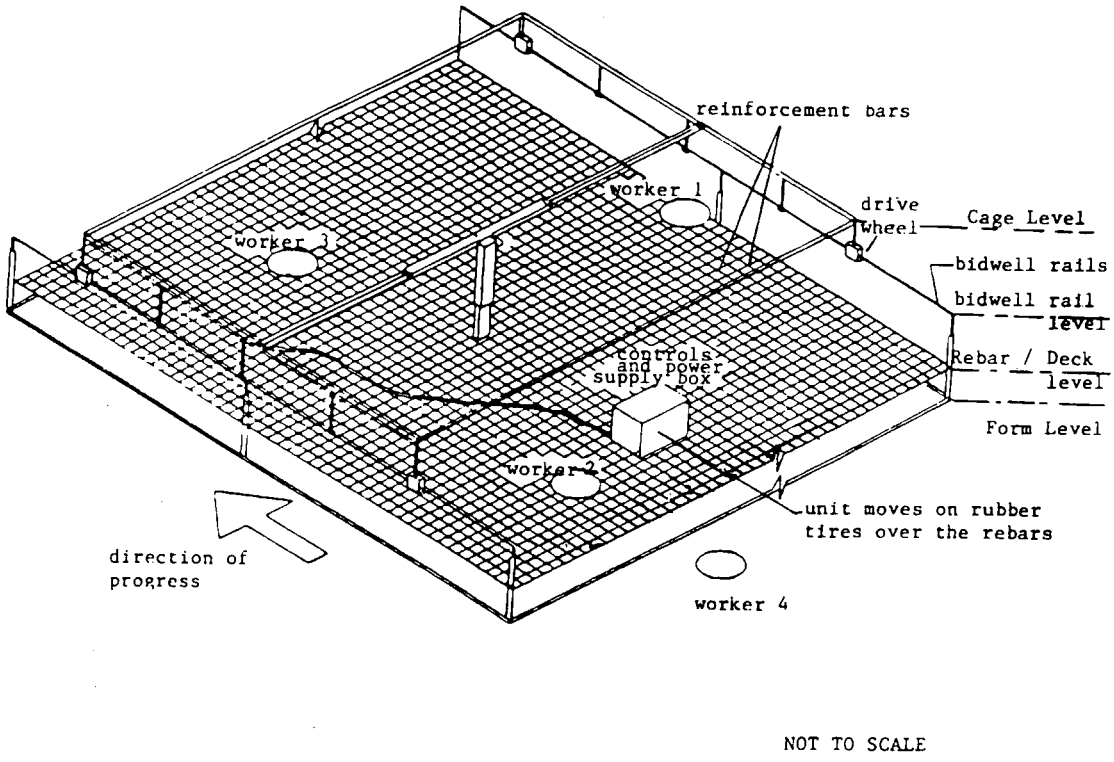

FIGURE 3 Conceptual design of rebar fastening automation system.

require using harsh materials such as solvents, concrete, sand, tars, or dust, the robot components would not be subjected to an environment as harsh as that for many other construction applications.

Construction automation must also prove safe. Although the introduction of automation eliminates many hazards, it has the potential to create new ones. For example, workers may accidentally come into contact with the robot while it is in operation. The sonar scanner on the rebar fastening robot will help to reduce occurrences of this hazard. A more detailed analysis in the laboratory or through simulation would detect other operating hazards.

Another technical issue of concern is that of mechanized fastening. While the Glim-Loc Gun or similar mechanism appears to fasten rebar effectively given an adequate vertical force, much testing and detailed adjustments are likely to be necessary, which would probably take 6 months to 1 year. Also, it may be necessary to "pull" one rebar up against the other before fastening.

A key technical issue is sensing rebar junctions so as to align the gantry link of the robot in a vertical position directly above the junctions. Characteristics of the rebar fastening problem that affect the resolution of this technical issue include the following:

1. Typically, for reinforced concrete decks, there are two layers of rebar "mats," one about 2 in. above the form and the second (laid after the first is fastened) 4 to 6 in. above the first. This presents a complication because the sensing system must differentiate between intersections of the top and bottom mats.
2. Forms for bridge decks may be either wood or metal (stay-in-place), which have different properties with respect to certain sensors. For example, infrared sensors may successfully differentiate the heat levels between rebars and wood forms but would be less successful in differentiating between rebars and metal forms.
3. Besides vertically aligning the robot with the rebar junction, it is necessary to extend the gantry to the proper distance so that the end effector is just over the rebar intersection. The implication here is that the sensing system must also be able to measure accurately its distance above the rebars.
4. The intersection of the rebars may not necessarily be perpendicular. Thus, it may be necessary to provide an added degree of freedom in the manipulator or end effector to accommodate the realm of possible orientations of the rebar.

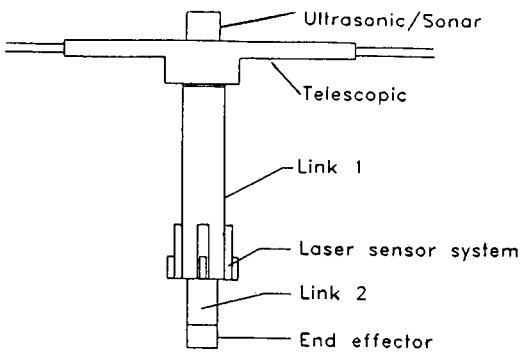

FIGURE 4 Conceptual design of robot manipulator.

A number of sensor systems may be adapted to the rebar alignment task, but some are more effective in addressing the preceding technical concerns. For example, an infrared system may produce a relatively clear image of intersecting rebar; however, it does not provide the vertical distance from the sensor to the rebar. Therefore, it is unable to differentiate between rebar junctions of the bottom and top mats.

A laser optical sensor system is recommended. The system would consist of four lasers with optical sensors mounted on Link 1 of the manipulator. Each laser would be able to send a laser beam downward and, using the reflected beam, measure the distance from the sensor mount to the first obstacle below.

A final technical issue is that of control software. Some development time must be spent writing and testing the software that will control the positioning and sensing of the manipulator and mobility (cage) systems. The software should allow for the exploitation of known information such as the design depth and spacing of the rebars. For example, if design specifications require a 6-in. spacing between rebars, the telescopic joint could advance the manipulator 5 in. and then employ the sensing system to determine the final local positioning for the next junction. The research and development time for coding and testing the software would most likely be 6 months to 1 year.

In light of the criteria stated for technical feasibility, it appears from the conceptual design and technical discussion that automated rebar fastening is technically feasible. The more difficult technical issues—namely, mechanized fastening and local sensing—could take advantage of technical components that are commercially available. Thus the task is primarily one of technical integration instead of technical innovation. Further, development time may be conservatively estimated at 3 to 5 years because the control software is likely to be straightforward. Automated rebar fastening requires no image processing or other complex control task requiring sophisticated algorithms.

The conceptual design of the rebar fastening robot is a unit that is assembled on site by workers according to the dimensions of the bridge deck; therefore, the concept could be adapted to a wide variety of project sites. The procedure of installation of the robot would be standard and repeated at every bridge site. Subsequent activities of the workers are also similar on all bridge decks. The system appears to be conceptually safe. Ultrasonic scanning is used to sense obstacles and a kill switch is activated automatically or manually by one of the operators whenever an obstruction is sensed.

ECONOMIC FEASIBILITY OF AUTOMATED REBAR FASTENING

For this study, economic feasibility was defined in an investment analysis framework. Within this framework the quantifiable benefits and costs of an automated rebar fastening concept were assessed and compared with the current practice. The benefits and costs were assessed for the period beginning with the present, extending through the research and development and through the expected life of the robot. The criteria for feasibility of automated equipment are typically to achieve a positive net present value or to break even on an investment in automation (7). This section identifies the probable benefits and costs of automated rebar fastening and provides insight to the types of data necessary for their assessment.

Ergonomic Evaluation of Rebar Fastening

Ergonomics is the science of designing and evaluating the workplace and work task such that the work performed is within the normal range of human physical capability, thus allowing the work to be performed safely (i.e., without injury or disease) and productively. Failure to design ergonomically can, and generally does, lead to a variety of acute and chronic injuries and illnesses, including low back pain and carpal tunnel syndrome.

Within the past 10 to 15 years, both the Occupational Safety and Health Administration (OSHA) and worker's compensation systems have recognized that this type of injury and illness is work-related, and the associated medical and legal costs have soared. (Typical compensation costs are $10,000 for a low back injury and $20,000 for a carpal tunnel syndrome case. OSHA routinely cites and fines employers with a high number of incidences of these injuries.) These costs must be considered in the economic evaluation of new approaches to fastening rebar.

A comprehensive ergonomic analysis can be used to assess the types of injuries likely to affect rodmen as well as their frequency and severity. Such an analysis is particularly useful when data revealing such information are difficult to obtain. This study, however, introduces only the concepts of ergonomic analysis as they apply to rebar tying. In the next phase of the study, field experimentation and laboratory analysis will be significantly extended, thus providing the basis for safety benefits associated with automation.

To begin assessing the ergonomics of the task, the videotapes taken at the bridge sites were studied in the laboratory. The results of this initial ergonomic study of rebar tying are briefly described, with the tasks' effects organized and discussed by body part.

The first body part of concern is the back; tying rebar involves at least two tasks that stress the back. The first is carrying and placing the rebar. Typically, the rebar is delivered to a temporary storage site at one end of the bridge. The tying personnel then carry bundles of the rebar material to the area where it will be used. From there, they set the individual pieces in place. The hazards of lifting are well known. The hazards of carrying are not thoroughly described. In this case, the workers may be carrying the rebar while walking across an uneven and unstable surface of rebar that has already been placed, thus subjecting the worker to a significantly increased chance of losing his balance. This in turn leads to an unexpected load on the body that could result in a "sudden movement injury."

Besides lifting and carrying, the actual tying task produces a prolonged static load on the lower back. All 10 persons observed tying rebar did so by bending at the waist with their legs straight. They reached down to the rebar (all the time standing on the uneven and unstable surface of the rebar they were tying) and tied. Depending on their relative leg and arm lengths, this typically required them to bend such that their

torso was below horizontal. In future work, the biomechanics of this posture will be evaluated in detail, but for this study, suffice it to say that the workers used this posture because it was the most energy-efficient, most stable, and fastest way of doing the work. In addition, the workers found that as they aged their knees would not tolerate the load associated with squatting and moving up and down. All of the workers also complained of chronic lower back discomfort.

The other body part of serious concern is the combination of hand, wrist, and arm. A number of injuries to and illnesses of these body parts that result from repetitive motion have been well documented. They include carpal tunnel syndrome, tendinitis, tenosynovitis, and ganglionic cysts. Such illnesses result from a combination of three factors: (a) relatively forceful exertions by the hand, wrist, or forearm; (b) postures that move these body parts out of the neutral position; and (c) a high rate of repetition. The initial study shows that tying rebar involves all three factors. In addition, discussions with the working personnel revealed that wrist and forearm pain, ganglionic cysts, and carpal tunnel syndrome are common complaints among people who tie rebar. A comparison of the three causative factors and the rebar tying task activities follows.

The most critical factor is posture. The wrist is in a neutral posture when the hand is a linear extension of the forearm. Tasks that cause the wrist to deviate from the neutral posture lead to injuries of the hand, wrist, and forearm. In rebar tying, the person holds pliers in one hand (which must be repeatedly closed and opened while tying) and uses the pliers to maneuver the wire around the crossed rebar. In the process, this hand makes 7 to 11 distinct movements per tie (some in flexion, some in ulnar deviation, and some in a combination of twisting one or both types of deviation). The other hand, which controls the other end of the wire, has five to eight distinct movements per tie, holds the wire in a pinch grip, and is sometimes in flexion or ulnar deviation. This combination of simultaneously twisting, squeezing, and deviating will, if done often enough, lead to a variety of injuries and illnesses to the hand, wrist, and forearm.

The second causal factor to consider is repetition or frequency. The initial observation indicated that people tie at a rate that ranges from 12 to 20 ties per minute depending on the individual, the type of tie, time of day, and the bridge location. A typical rodman's work pattern is to move to an area, place his feet as securely as possible, bend over, and then tie as many rebar junctions as he can reach from that spot, ranging from two to eight rebar junctions. The number of ties per minute multiplied by the number of hand and wrist motions per tie results in a hand/wrist movement rate of about 100 motions per minute—a very high frequency.

The last factor, force, was evaluated subjectively by observing the apparent forcefulness of the movements, having the study directors perform the task themselves, and observing muscle use on the videotape. The authors would estimate them as moderate (25 to 60 percent MVC), and we plan to quantitatively evaluate them in a follow-up study.

In summary, both the back and the hand/wrist are at significant risk of injury during rebar tying. For the hand/wrist in particular, all of the known risk factors are present and inherent to the task as it is currently done. Furthermore, persons performing rebar tying frequently complain of hand/wrist pain. A new method of fastening rebar that removes workers from such hazards would yield significant safety benefits.

The ergonomic problems associated with rebar tying lead to a variety of musculoskeletal injuries, including lower back pain and carpal tunnel syndrome. These in turn lead to a variety of costs, including worker's compensation (medical and lost time), administrative (paper processing, injury investigations, training replacements, and supervisory time), and lost production. Worker's compensation costs vary from state to state but may be estimated on the basis of injury cost data published by state agencies and other researchers (*8,9*). Compensable lower back injuries average $10,000/case, and upper extremity injuries such as carpal tunnel syndrome average $15,000 to $25,000/case. The administrative and lost production costs will obviously vary considerably from company to company, but they have been studied by Heinrich (*10*) and others who have concluded that they average at least 100 percent to 400 percent of the direct medical and lost time costs.

As described, the nature of rebar tying is such that most of the persons who have worked for a number of years at this activity will experience upper extremity injuries and many will experience lower back pain. Nationally, the number of compensable cumulative trauma disorders increased by a factor of 10 during the 1980s. This rapid nationwide increase in the reporting of these injuries will most likely spread to the construction industry, and it is reasonable to expect that at least 5 to 10 percent of the work force will be affected annually. Assuming that about 4,000 bridges will be rehabilitated per year nationally, this equates to an annual direct worker's compensation cost of about $300,000 to $600,000 for these injuries. An additional $300,000 to $1.2 million will be incurred for indirect costs.

In addition to these costs, one must add the costs of an OSHA citation for failing to alleviate a source of lower back or repetitive motion injuries. OSHA has, under the "general duty" clause (5a1), levied substantial fines ($100,000 to $1 million) against the red meat, automobile, and other industries for these types of injuries. Companies in these industries have been fined for failing to report injuries (injured persons sought help through other sources), as well as for the injuries themselves and the failure to abate the hazard. The fines may be as high as $7,000/occurrence (i.e., each day of exposure per worker).

Estimation of Benefits

Reduction in Related Accidents

Accidents related to rebar tying include long-term back injuries; carpal tunnel syndrome; tripping; falling; piercing of the eyes, feet, and hands; and muscle cramping. By removing the worker from a stooping position to a standing position, it is expected that most of these types of injuries may be eliminated. From the ergonomic evaluation, it is found that for the approximate 4,000 bridge reconstruction projects annually, the direct costs and the indirect costs associated with injuries to rodmen due to the task of rebar fastening is $1.1 million. This study assumes that one robot could do the job

of a crew of six workers, and an average crew takes 2 weeks to complete rebar fastening tasks on these projects. A crew normally works for 8 months a year, so one crew works on 20 bridge sites in a year, therefore about 200 crews are employed in a given year.

Hence the benefits due to eliminating or reducing human involvement for one robot, or one crew, will be at least $5,500/year ($1.1 million/200). While this assessment is not extremely high, a second phase of this study would include possible injuries not yet investigated.

Increase in Rate of Fastening

Studies have shown that the productivity of a work crew for most construction tasks depreciates significantly over the course of a work shift and in periods of extreme temperatures. Automated equipment offers significant productivity advantages in that it is not likely to be significantly affected by these factors. The robot may perform the fastening task over longer work shifts and with fewer interruptions than conventional crews. Using time estimates for each of the steps of the automated fastening process and the average tying time for workers observed in the videos (Tables 1 and 2), the productivity of robot can be compared with that of current crews. The productivity of the robot has been found to be 30 percent greater than conventional crews.

Labor Cost Savings

The average rebar crew is six workers and averages about 2 weeks to complete fastening on a bridge. The crews work schedules of either 8 hr/day, 5 days a week or 10 hr/day, 4 days a week. The 10-hr-day schedule is more commonly observed. Introduction of automation will reduce the requirement of manual labor by at least two workers per crew. The level of automation proposed is partial where a crew of four workers are necessary for supporting the robot. Hence there is a savings of labor cost of two workers by the introduction of automation. This savings is calculated to be $103,240 annually. The computation is as follows:

A robot could work 11 months a year, considering 1 month as downtime for maintenance and repairs, and is 30 percent more efficient. Hence the robot can tie rebar for 29 bridges per year (22 × 1.3).

$$\text{Labor savings} = 2 \times 10 \times 8 \times \$22.25 \times 29$$
$$= \$103{,}240/\text{year}$$

where

2 = number of workers,
10 = hours per day,
8 = days per bridge,
$22.25 = labor cost per hour assuming a 30 percent overhead, and
29 = number of bridges.

This quantity is significantly higher than the benefits derived from reduced injuries.

TABLE 1 Productivity Estimates for Automated System

Step	Execution Time (sec)
Sensing and local orientation	2.0
Clamping and fastening	1.5
Advancing from one junction to next	1.5
Global movement	1.5
Setup and dismantling	1.0
Total (average per clamp)	7.0

TABLE 2 Productivity Estimates for Conventional Rebar Tying for a Crew of Six

Step	Execution Time (sec)
Average tying time	1.0
Straightening up and resting	3.0
Moving to reachable areas	2.0
Water, lunch breaks	4.0
Total (per tie)	10.0

Estimation of Costs

System Components

The costs of system components depend on the specific configuration and technologies chosen in the equipment design. In general they involve an end effector, manipulator, mobility system, power supply, computing capability, and software. The total cost for the robot system was calculated to be $170,000. The breakdown of the costs follows.

Research and Development Costs

Research and development costs include the conceptual design, integration of subsystems, research into necessary upgrades in technology, software development, and testing. Estimation of these costs is based on projections of the necessary man-months of research personnel and the equipment necessary to conduct the research. For the purposes of this project, it is assumed that research is conducted at a university for 3 years and then transferred to industry for an additional 2 years of development. On the basis of cost per man-year, the costs at the university are assumed at $120,000/year, and in industry, $160,000/year.

Operating and Maintenance Costs

Operating and maintenance costs include setup, take down, transport, power, materials, technicians, and the like. Estimates of these costs have been derived from comparing them to an analogous system in use. The operating and maintenance costs for the robot were calculated to be $15,500/year, itemized in Tables 3 and 4.

TABLE 3 Capital Costs of Automated Rebar Fastening

Automated System Component	Estimated Cost ($)
Manipulator, including end effector	40,000
XY table, including telescopic rod	60,000
Power supply and components	20,000
Computing and controls	20,000
Controls interface	10,000
Sensors, laser and ultrasonic	20,000
Total	170,000

TABLE 4 Operating and Maintenance Costs of Automated Rebar Fastening

Automated System Component	Estimated Cost ($)
Power supply	3,500
Transfer and site installation	4,000
Software maintenance	500
Servicing	1,500
Clamps and end effector maintenance	5,000
Down time	1,000
Total	15,500

Nonquantifiable Benefits: Improved Quality

Automated equipment may perform certain tasks with a higher level of accuracy or consistency, which may lead to a higher quality of product. For rebar fastening, a mechanized process may be able to provide a stronger connection among the rebar. Hand-tied connections tend to loosen as workers continue to walk on the suspended rebar mat, thus possibly affecting the performance of the finished deck.

Present Worth Analysis

In assessing the economic feasibility of the robotic concept, a criterion of positive net present value (NPV) of investment is established. First, a cash flow consisting of the quantified benefits and costs over a planning horizon is formulated and discounted at various interest rates. Next, because assumptions were necessary in quantifying benefits and costs, a sensitivity analysis with respect to many variables is performed.

The cash flow consists of a research and development period, followed by a period of robot use until it has reached its design life. Robots are systematically purchased and replaced until the end of the specified planning horizon. For the sensitivity analysis, all base costs are increased by 10 and 20 percent and the base benefits are decreased by 10 and 20 percent. Base expenditures include $170,000 in capital, $15,000 for annual operating, and $520,000 for research and development; base revenues include annual benefits of $109,900 and a salvage value of $34,000. The design life of the system is assumed to be 6 years, and the research and development period 5 years. A planning horizon of 25 years and an annual inflation rate of 4 percent were used.

The NPV versus minimum attractive rate of return (MARR) of the corresponding cash flows are shown in Figure 5. The results indicate that over the range of reasonable interest rates, the robot system is an economically favorable investment. For example, at a MARR of 10 percent, the NPVs per crew replacement are $536,974, $393,379, and $249,784, for the base, 10 percent, and 20 percent cases, respectively. The favorable economic results stand for many other sensitivity tests conducted for the study but are not reported here.

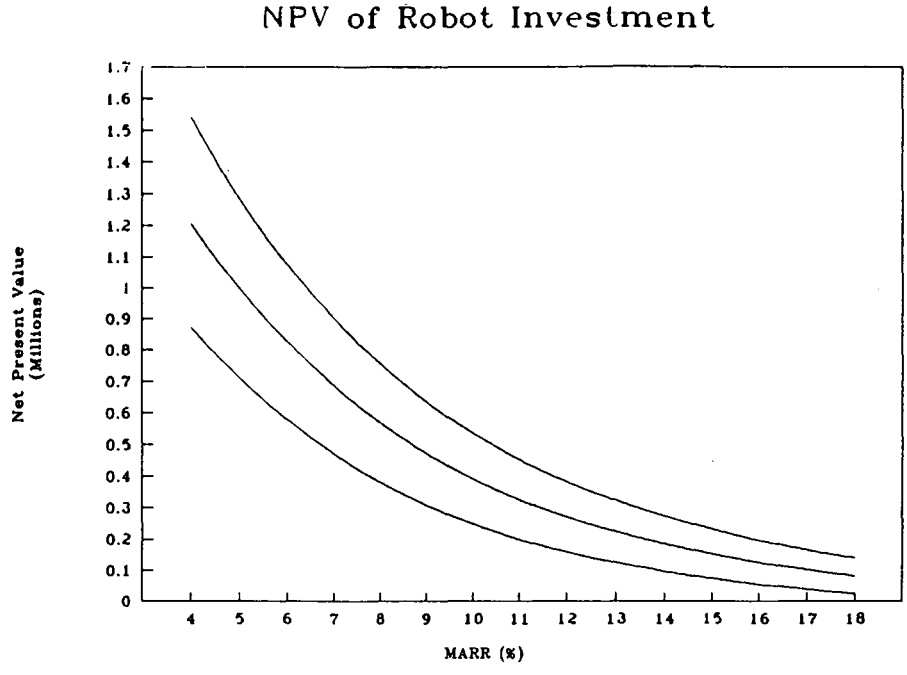

FIGURE 5 NPV versus MARR of rebar fastening automation investment.

CONCLUSIONS

Videotapes of workers in the field, discussions with workers, ergonomic analysis, and injury statistics seem to indicate that productivity and safety benefits could be increased, with relatively low financial and technical investment, through automated rebar fastening. The productivity benefits significantly exceed the safety benefits of automation of this task. For this reason, additional study of the economic feasibility should focus on increasing the precision of the relative productivities of conventional crews and a proposed robotic system.

REFERENCES

1. C. Hendrickson and T. Au. *Project Management for Construction*. Prentice-Hall, Englewood Cliffs, N.J., 1990.
2. B. Klein, R. Jensen, and L. Sanderson. Assessment of Workers Compensation Claims for Back Strains/Sprains. *Journal of Occupational Medicine*, Vol. 26, No. 6, June 1984.
3. E. J. Cremens. Productivity in Construction Industry. *Construction Review*, Nov. 1981.
4. Morse. Repetitive Motion—Musculoskeletal Problems. *Journal of Occupational Medicine*, 1979.
5. M. J. Skibneiwski and C. Hendrickson. Analysis of Robotic Surface Finishing Work on Site. *Journal of Construction Engineering and Management*, Vol. 114, No. 1, March 1988.
6. T. Kobayashi, S. Honda, Y. Tsukhara, et al. Study on a Robotic System for Pavement Cutting Work. *Proc., 5th International Symposium on Robotics in Construction*, Tokyo, Japan, 1988.
7. S. McNeil. *An Analysis of the Costs and Benefits of Automated Pavement Crack Filling*. Carnegie Mellon University, Pittsburgh, Penn., 1990.
8. H. W. Heinrich, D. Peterson, and N. Roos. *Industrial Accident Prevention*, 5th ed., McGraw Hill Inc., New York, 1985.
9. T. J. Stobbe, T. Bobick, and R. W. Plummer. Musculoskeletal Injuries in Underground Coal Mining. *Annals of the ACGIH*, Vol. 14, 1986.
10. S. Snook. Musculoskeletal Injuries in the Workplace. Presented at the American Industrial Health Conference, Boston, Mass., June 1992.

Publication of this paper sponsored by Committee on Applications of Emerging Technology.

Costs and Benefits of Automated Road Maintenance

TING-YA HSIEH AND CARL T. HAAS

Because of increasing maintenance demands and the increasing impact of maintenance operations on users, there is a tremendous need to improve maintenance technology. By improving maintenance technology, the direct costs of maintenance operations and the related user costs can be reduced. Automation technology for reducing such costs is examined. Specifically, 22 automated systems in road maintenance are identified that are used for defect surveys, traffic control, defect treatment, and other supportive activities. These systems demonstrate that automation technology is technically feasible and that it could meet the needs for technological advancements in road maintenance. The study also illustrated that automated maintenance can be economically feasible. For example, one economic analysis of crack sealing shows that it could save at least $3 million/year nationwide in operations costs. However, the corresponding potential to reduce user costs by minimizing the interference of maintenance operations with traffic is even greater. Future development of maintenance technologies should therefore focus primarily on reducing user costs as well as operations costs.

As the North American road system ages, traffic volume increases, environmental regulations proliferate, and the direct costs of maintenance grow, maintenance agencies are faced with the resulting increasing demands on maintenance activities. At the same time, road maintenance technology has remained virtually unchanged in many respects for decades. Small-scale, dispersed activities are performed under traffic conditions by generally low skilled laborers with basic equipment. Such conventional road maintenance methods may be inadequate to meet the increasing demands.

Automation technologies present opportunities to improve maintenance methods and to meet the objectives of maintenance agencies. In addition to maintaining a safe and comfortable driving environment, these objectives include reducing operating and user costs. Decreasing the operating costs of maintenance through automation will allow agencies to increase their forces and lower user costs resulting from delayed maintenance. Automated systems that can operate more quickly and in a wider range of environmental conditions will reduce lane closure time and traffic interference, again reducing the related user costs.

The benefits of automated maintenance in terms of lower user and operational costs result from the potential of automated maintenance to minimize interference with traffic, increase the flexibility and capacity of maintenance forces, improve work quality, reduce labor requirements, improve worker utilization, conform to environmental regulations, and remove workers from danger. Automated maintenance costs include development, capital acquisition, and operating costs. The economy of automated maintenance depends on the perspective taken, but in most cases the benefits outweigh the costs.

This paper examines the costs and benefits of developing and implementing automated road maintenance. After discussing the characteristics of road maintenance, the user costs of road maintenance, and the costs and benefits of automating road maintenance, the resulting economics are discussed. A recent survey of existing automation applications in road maintenance is also presented. In an attempt to illustrate broadly the magnitude and balance of the costs and the benefits of automated road maintenance, this paper is only the first stage of a more extensive and detailed quantitative research program. [For a broad introduction to road construction and maintenance automation, the reader should refer to work by Skibniewski and Hendrickson (*1*).]

CHARACTERISTICS OF ROAD MAINTENANCE ACTIVITIES

The ultimate goal of road maintenance is to provide a safe and comfortable driving environment to prevent vibrations, loss of control, and loss of traction while driving. Thus, the objectives of road maintenance activities are to restore road skid resistance and road evenness and to maintain road impermeability.

Current conventional road maintenance activities are characterized by the following:

- Small-scale operations,
- Dispersed locations,
- Work under traffic,
- Labor-intensiveness,
- Relatively low skill level of laborers,
- Off-peak work hours, and
- Affected by weather conditions.

These characteristics distinguish road maintenance from road construction and most other construction activities. They affect the design of maintenance equipment and techniques, the organization of maintenance crews, and the management of maintenance activities as well as resources. These characteristics indicate that conventional road maintenance methods may not be flexible enough to meet the changing maintenance demands and trends identified previously. As a result, road

T. Hsieh, Department of Civil Engineering, ECJ 5.412, University of Texas, Austin, Tex. 78712; current affiliation: Department of Civil Engineering, National Central University, Chung-Li, Taiwan, 32054 Republic of China. C. T. Haas, Department of Civil Engineering, ECJ 5.200, University of Texas, Austin, Tex. 78712.

users—drivers and passengers alike—inevitably, and sometimes unknowingly, spend enormous amounts of additional time and money in highway travel. These expenditures are normally described as user costs.

USER COSTS RELATED TO ROAD MAINTENANCE

User costs related to road maintenance include travel delays, vehicular operating costs (including fuel consumption), vehicular maintenance costs, and accident costs. User costs are incurred when roads need maintenance and repair and when roads are actually undergoing maintenance and repair work.

A breakdown of the user costs concerning these two categories is shown in Figure 1. As can be seen from the figure, the user costs incurred when roads are undergoing maintenance and repair work are relatively easy to measure. The computerized cost model QUEWZ (Queue and User Cost Evaluation of Work Zone) (*2,3*) can be used to estimate the repair "action" user costs. The repair "nonaction" user costs, or costs incurred when roads are in need of repair, are more complex to measure as the time lapse between a defect formation and its repair is unknown in most cases.

As well, the impact of a given defect on a specific type of vehicle is subject to different interpretations, not to mention the difference from one vehicle to another. The computerized cost model HDM-III (Highway Design and Maintenance Standards Model) (*4*) can be used to estimate the nonaction user costs. This paper uses these models to estimate the order of magnitude of the benefits that may be accrued by improving road maintenance technology.

Nonaction Costs

Higher Vehicular Operating Costs

When no immediate maintenance actions are taken after a road defect is formed, every vehicle traveling across this defect will realize a certain level of damage. Additional vehicular operating costs attributed to a single road defect are a function of the level of damage, the average maintenance costs of a specific type of vehicle, the time lapse between a defect formation and repair, and the amount of traffic traveling across the road defect. Defects may be aggregated for calculations.

Costs of Accidents to Road Users

Accident costs due to delayed maintenance are real but are difficult to estimate. The cost model used here excludes the calculation of accident costs.

Deterioration of Existing Roads

After a road defect is formed, every vehicle crossing it will cause damage to the defect. The cumulative cost of this effect is incorporated in HDM-III.

Decreased Usage of Defective Roads

As the deterioration process of the defects continues, some road users may choose other routes to substitute for the de-

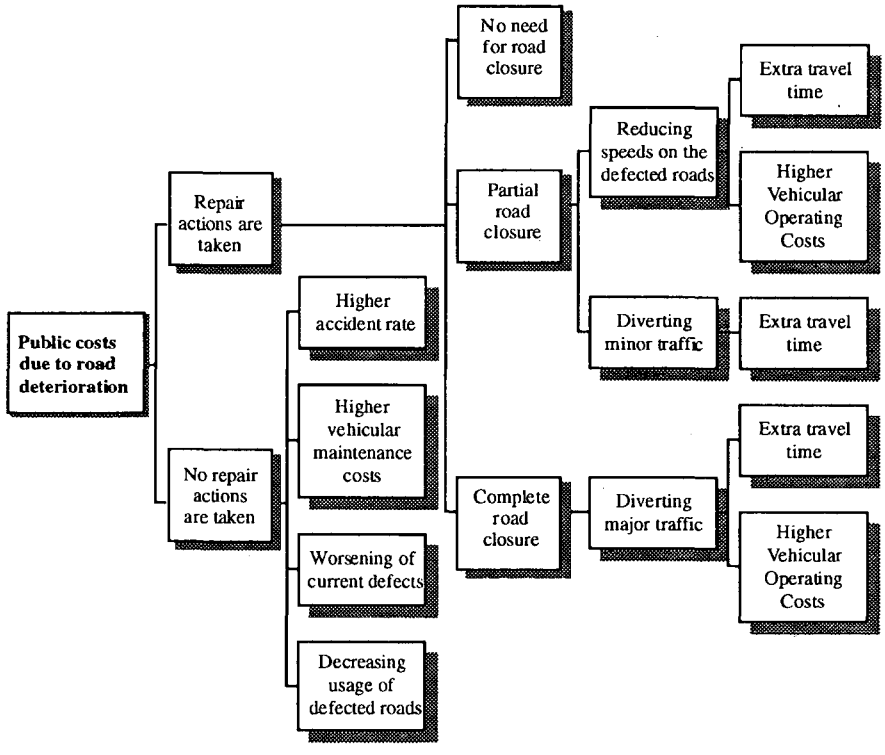

FIGURE 1 Cost breakdown structure of user costs.

teriorated one, thus imposing delay costs on themselves and adjacent route traffic.

Action Costs

Costs of Extra Travel Time

The extra travel time is due to the lower average travel speeds and the longer travel distance. When a work zone completely blocks the defective road section, highways must be provided to connect the road to other temporary or existing roads before and after that section. If highways are not provided, the traffic will be forced to travel on other routes. In both cases, the extra travel time of each vehicle is due to the longer travel distance and the potential traffic congestion. If the defective road section is partially blocked, one or both directions of the traffic may have to reduce their speeds to comply with safety requirements imposed by maintenance crews. The travel time for that particular section is increased due to the slower traffic resulting from the lower speed and the potential traffic congestion.

Additional Vehicular Operating Costs

The additional vehicular operating costs can be divided into two categories: costs due to extra travel and those due to waiting, stop-and-go cycles, and lower average speeds. The first category is a function of the extra travel distance, the average speeds, and the vehicular characteristics. The second category involves two aspects: the operating costs of speed-change cycles and the change in vehicle operating costs due to the lower average speeds. The first aspect refers to the costs of slowing down and returning to the approaching speed as a result of the presence of a work zone and the speed-change cycles in queueing. The second aspect deals with the higher operating costs when the average travel speed is lower. Simply put, when a vehicle travels at a very low speed, the fuel consumption and the vehicular maintenance needs tend to increase.

Calculation of User Costs

Calculation of Nonaction User Costs

HDM-III, issued in 1987, was developed by the World Bank to meet the needs of the highway community, particularly in developing countries, for evaluating policies, standards, and programs of road construction and maintenance. The HDM-PC Version 2.0 (*4*) calculations show that delayed maintenance can increase vehicle operating costs in the United States by tens of millions of dollars a year. Improving maintenance agencies' force capabilities by improving maintenance technology should help reduce user costs due to inaction by millions of dollars a year.

By using a hypothetical example, the magnitude of the nonaction user costs can be easily seen. This example assumes that an asphalt concrete road system is built in 1992. The vehicle operating costs of five types of vehicle (cars, pickup trucks, large cars, trucks, and articulate trucks) are calculated individually for the 1st year and the 20th year, 2011. The international roughness index (IRI) is used to represent the condition of road. An IRI value of 2.2 (good condition) is assigned to the 1st year and a value of 8.8 (poor condition) to the 20th year. A summary of vehicular operating costs of both years is given in Table 1.

The vehicular operating costs in Table 1 are calculated on the basis of 1000 vehicle-km. The daily additional nonaction user costs would be approximately $531 for a section of road identified in poor condition, measuring 1 mi (1.6 km) long, and with the following average working day traffic volumes in both directions:

- Car: 1,800,
- Pickup truck: 1,200,
- Large car: 1,200,
- Truck: 1,200, and
- Articulated truck: 300.

Consequently, the additional nonaction user costs for 200 working days in a year could be as much as $106,000 for a single mile of poor road. The potential accident costs resulting from such poor road conditions are not accounted for here.

Calculation of Action User Costs

More significant benefits from improving maintenance technology may be achieved by reducing maintenance action–related user costs. The computerized model QUEWZ was developed to estimate the additional user costs resulting from lane closures in one or both directions of travel; it is described by Memmott and Dudek (*2,3*). This program indicates that the length of work zones, the length of closure time, the number of lanes closed, and the traffic volume in both directions affect the amount of user costs extensively.

As with the nonaction user costs, the volume of the action user costs is difficult to calculate unless specific road conditions are detailed. To illustrate the magnitude of the action user costs, a road closure example is developed. In this example, a 1-mi work zone is set up in an urban freeway, and the normal capacity in each direction with two lanes is 4,000 vehicles per hour (vph). When one lane is closed from 8:00 a.m. to 4:00 p.m., the freeway capacity is reduced to 1,800

TABLE 1 Vehicular Operating Costs Based on HDM-III (In Dollars)

	Vehicular Operating Costs of 1000 Vehicle-km ($)				
Year	Car	Pickup	Truck	L. Cars	Art. Truck
1992	136.9	127.8	140.4	488.9	774.3
2011	157.4	165.0	181.5	615.6	937.1
Difference	20.5 (15%)	37.2 (29%)	41.1 (29%)	126.7 (26%)	162.8 (21%)

vph and the total additional daily user costs due to the lane closure are $17,647. It should be noted that the extra expenditures by road users accounted for in this example exclude the costs of potential accidents and the extra travel time for particular individuals.

From the previous discussion and examples, the magnitude of the impact of maintenance operations on road users is clear. For a given working day, a rough, unmaintained road or a work zone in an urban freeway can cost road users tens of thousands of dollars a day. The costs nationwide are far greater. Automated road maintenance and improved technology could decrease these user costs in many ways.

BENEFITS OF AUTOMATION IN ROAD MAINTENANCE

Automation is defined in this paper as the replacement of human labor by machinery. Depending on the level of labor replacement, different technology—including mechanical, sensing, computing, actuating, motion, and control systems—applies. Applying automation technology in road maintenance involves the following:

1. Using mechanized systems, such as XY tables and serial manipulators, to replace human labor that involves high strength or simple skills;
2. Using sensors to gather required task-related information from the environment, such as a pothole profile and a crack pattern; and
3. Training maintenance workers to operate the automated system with simple control devices.

Automation technologies have demonstrated tremendous successes in manufacturing and many other industries. In the past 10 years, the construction industry has also shown great interest in automating some of its operations. Numerous benefits could be realized by automating road maintenance.

Minimizing Work Zones and Interference of Maintenance Operations with Traffic

For most road defect treatment methods, automation would reduce the number of crew carriers, loaders, trucks, and rollers as well as the associated workers because many functions could be combined onto a fewer number of machines. Consequently, the possible interactions between maintenance operations and the traffic could be greatly reduced. Examples include the Dynapac pavement patcher (*5*) and the Thermo-Patch pothole patcher, discussed later (*6*).

In a conventional machine patching job, the equipment involved includes at least one crew carrier, a grader, a roller, and a number of dump trucks. Because the size of a pothole and the level of pothole damage vary, workers and equipment operators need a large work zone to execute the job. As the Dynapac pavement patcher has demonstrated in several field trials, the required work zone space could be reduced significantly.

Increasing Flexibility of Maintenance Forces

Automation enables crews to perform required maintenance actions at any time of day and under most weather conditions. Working at night has special appeal because the traffic volume is low. With current sensing technologies, such as that on an automated crack sealer (*7*), workers can work without lighting. Often, they do not even need to see, because a sensed image can be processed by central computing units with little human involvement. Under poor weather conditions such as rain, a pothole can be drained, covered, and treated by hot air. Once the humidity in the pothole is within the acceptable level, sensors activate the patching operation (*8,9*).

With automation technology, maintenance tasks generally involve less human labor as demonstrated by the automated crack sealer. This reduction of human labor also increases the flexibility of maintenance forces. When emergency repair is required, for example, machine operators do not have to wait for helpers and flag personnel to start the job. The smaller the crew, the shorter the delay.

Increasing Capacity of Maintenance Forces

The capacity of maintenance forces determines their responsiveness to a certain road defect once reported. Instead of extensively recruiting, training, and retraining workers and purchasing general purpose equipment such as crew carriers, loaders, and trucks, the capacity of maintenance forces can be expanded with the purchase of multipurpose automated systems. Additionally, if automated systems prove to be more economical than current methods, more capacity can be purchased with the same maintenance budget.

Improving Quality of Maintenance Operations

Better quality maintenance operations would maximize the time period between road defect treatments. However, quality is often difficult to ensure because of the nature of labor-intensive operations in which experience often plays an important role. Novice workers may not have the knowledge to deal with moisture or hot weather in patching or sealing. In planing or overlaying, the high precision of road curvature or evenness takes much skill and experience to achieve. With various types of sensors, automated systems can perform tasks with the required precision. For example, one new asphalt finisher identified in this study has precise programmable control and internal screed surface pressure and heater temperature sensors (*10*).

Shortening Operation Time

Because time of road closure has a strong impact on user costs or the action user costs, it is critical to minimize closure time through faster operations. Existing automated systems can facilitate the setup or removal of work zones and accelerate the curing process of paved materials considerably. An example of such a system is the Quick Change moveable barrier system (*11*).

Operation time for the actual defect treatments would also be reduced if manual methods were replaced by mechanized ones that use sensors and electronic control devices. Several potential applications exist in structural treatment of deteriorated roads. Traditionally, maintenance forces practice more surficial treatment methods than structural ones, even when the latter may be required. The reason often has been that structural treatment methods, such as overlays, partial reconstruction, and drainage improvement, take more time. Although no existing system has been identified so far, some existing automated road construction systems, such as automated asphalt finishers (*10*), could be modified for this purpose.

Reducing Labor Requirements

Because a single automated system can be designed to perform multiple elemental operations, such as mixing patching materials, filling potholes, and screeding patching materials, the number of equipment operators and helpers would be reduced. The amount of labor that could be saved depends heavily on the cognitive complexity of a particular maintenance task. The concept of using human cognition and decision-making capability and replacing human labor by mechanized power makes the labor reduction in many road maintenance tasks possible. In the case of the automated crack sealer, two to three workers may be replaced (*7*). A combination of portable traffic signals (*12*) and radar or laser range sensors would also negate the need for flag personnel.

Improving Worker Utilization

One of the characteristics in road maintenance is the low-skill nature of manual methods. With automated systems, workers would be more involved in operating machines and monitoring the quality of operations instead of laboring on pavement breakers, shovels, and rakers. Essentially, the new technology employs more human cognitive abilities than physical ones and can improve the image of road maintenance work.

Conforming to Environmental Regulations

Automated systems can be designed to recycle removed pavement materials, if patching or thin overlay operations are involved. Depending on the required mixture, the operator could instruct the automated system to disintegrate the removed materials, retrieve the desirable ones, and combine them with new materials. To prevent foreign materials or objects from entering the mixing system and ensure the quality of mixture, this process would involve the use of several sensors and some manipulation mechanisms.

Removing Workers from Danger or Hazards

With automated systems, many manual maintenance methods can be eliminated. Consequently, workers such as flag personnel and shovellers would not be exposed directly to traffic. Reducing even a few accidents a year in this way could result in significant savings. As well, workers could be distanced as far as possible from patching or paving materials, which often cause dermatoses and respiratory problems.

COSTS OF AUTOMATION IN ROAD MAINTENANCE

Road maintenance automation has five major cost components: (a) research and development (R&D), (b) system procurement, (c) system operation, (d) overhead, and (e) system maintenance. The R&D costs are relevant from a public economic perspective, which is discussed later. The determination of the other four costs is in many aspects similar to that for traditional maintenance methods except for new items such as maintenance of software and electronics. If automation technology is applied to road maintenance, some user training or specialty recruitment in software engineering and electronic devices repair may be required. The parameters affecting each cost component are presented in Table 2.

According to Table 2, some considerations concerning the implementation of automation technology should be high-

TABLE 2 Parameters of Cost Components

Cost Component	Parameters
1. Research and Development	• Management, Administration & Overhead • Salary and Wages • Prototype Systems • Other Permanent Equipment • Development Period
2. System Procurement	• Useful Life • Payment Plan
3. Operating	• System Setup Costs: Transportation, Setup, Dismantle • Labor Costs: Hourly Wages, Work Hours • Energy Costs: Fuel Consumption Rate, Work Hours • Material Costs: Waste Percentage, Unit Material Costs
4. Overhead	• Training • Work Force Re-organization • Safety
5. System Maintenance	• Hardware Component & Labor: Mechanical Systems, Electronic Devices • Software Labor: Updating, Debugging, Modifications

lighted. Regarding operating costs, the hourly labor wages are expected to be somewhat higher than current ones because operating the automated equipment requires higher skills. The work hours in both the labor and energy items are expected to be shorter because of the increased production. Less material is expected to be used because less material is wasted during operation. Considerable overhead costs may have to be spent on operator training and a worker safety program, and substantial leadership and managerial effort are necessary to reorganize the work force.

ECONOMICS OF AUTOMATED ROAD MAINTENANCE

To gain insight into the costs and benefits of automation and to derive a comparison between conventional and automated maintenance methods, it is critical to determine the perspective that is taken before any form of analysis is performed. Different perspectives not only affect the determination of costs and benefits but also dictate the time horizon, which is essential in the economic analysis.

From the standpoint of an equipment user, the costs of automated maintenance include the initial capital to purchase a piece of automated equipment and many other items such as labor, costs of energy, and material. The time horizon of the economic analysis is usually within 5 to 10 years. Factors that need to be considered are the potential utility rate, safety concerns during operation, workers' moral, system production rate, crew organization, system robustness, and potential system downtime. If the user is an outside contractor, he or she will also need to forecast the expected market size for a particular type of maintenance job, given the competitive edge of automation technology.

From the perspective of public economy, user benefits and the R&D costs are now also considered, with a planning horizon up to 50 years. The potential reduction of the user costs by the implementation of certain technology becomes a key factor in the economic analysis, with the costs of R&D being treated as a long-term investment to reduce the maintenance operations costs and the user costs.

Other perspectives that can be taken include those of the equipment manufacturers and large construction corporations. An equipment manufacturer will focus on the possibility of creating a larger share of the equipment market by investing in R&D. A large construction corporation is concerned with its competitive edge with respect to other maintenance contractors by investing in R&D. The authors believe that the public economy is the most appropriate perspective for the range of issues to be considered in automated road maintenance.

A formulation for the economic analysis for automated road maintenance is presented in Figures 2 and 3. The balance of these costs and benefits depends on the perspective of the analyst, the accuracy of estimates used, and the time horizon for planning. This paper attempts to make only a limited comparison of the costs and benefits, leaving open the possibility of a more extensive analysis. The following discussion, however, provides some direction of the numbers involved.

From a maintenance force's viewpoint, the benefits are the reduction of the direct costs of maintenance operations, including material, energy, labor, and accident costs. The most important area for cost reduction is in labor costs. If the hourly pay and fringe benefits for a worker are $20, the annual direct costs for employing him or her are $40,000. With automated systems, the labor requirement can be greatly reduced, and significant savings can be realized by reorganizing work crews. The decreased labor requirement introduces the potential for reducing accident costs, because the use of automated systems can eliminate manual operations and minimize the exposure of labor to traffic and hazardous materials. Other benefits to the maintenance forces are the better working conditions and enriched job content supported by the automated systems and the lower overhead due to the reduced number of workers.

From a road user's viewpoint, the benefits are the reductions of the nonaction and the action user costs. For nonaction user costs, minimizing the time lapse between defect formation and repair is essential. A previous example has shown

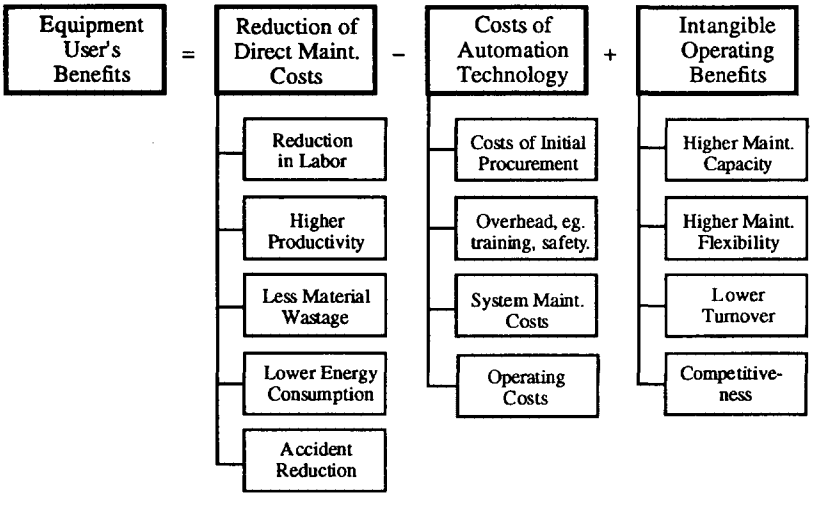

FIGURE 2 Formulation of economy analysis from equipment user's perspective: 5- to 10-year planning horizon.

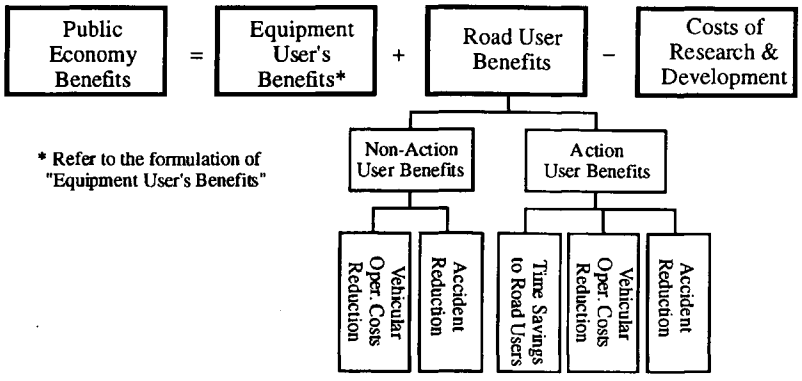

FIGURE 3 Formulation of economy analysis from public economic perspective: 5- to 10-year planning horizon.

that poor road serviceability will cost road users, given a relatively low traffic volume, $531/mi/day. If only 2,000 mi of such roads exist in 50 states, the additional costs of delayed maintenance could exceed $1 million/day, or close to $400 million/year. In this respect, the capacity of maintenance forces can be expanded by purchasing more lower-cost automated systems. With limited training, maintenance crews can repair defective roads with automated systems as soon as defects are reported. The user benefits include reducing the number of road defect–related accidents and lowering vehicular operating costs.

To road users, the potential benefits in reducing the action user costs are also high. The most significant benefit is to reduce fuel consumption by eliminating waiting, stop-and-go cycles, and lower travel speeds when passing work zones. In calculating the vehicular operating costs due to a lane closure, a previous example has shown that $17,647 worth of extra fuel may be burned in vain daily for only one lane closure, not to mention the consequences of air pollution in an urban area. If, among the largest 20 cities in all states, there are on average five such lane closures every day, the additional user costs are approximately $353 million for 200 working days in a year. Automated maintenance systems can achieve the user benefits by speeding up maintenance operations and reducing the number of lane closures required. These advancements could also limit the travel delays to other individuals in the freeway system (often very significant in urban areas) due to lane closures.

From the perspective of public investment, the costs of R&D in automating road maintenance can be paid with a combination of the operating and user benefits described earlier. As one example, the costs of R&D for an automated crack sealing system has been estimated to be in the range of $1 million to $2 million. An economic analysis of the automated crack sealing system shows potential benefits for equipment users of approximately $3 million annually nationwide (*13*). Because this system is expected to be in service for 6 years, it is clear that, even without considering user benefits, the return on the investment is still potentially high.

The next section describes current advances in road maintenance automation technology. User and operating benefits of these technologies are identified as well.

AUTOMATION APPLICATIONS IN ROAD MAINTENANCE

A survey on automated applications in road maintenance was conducted in the early stage of this research. As identified in this survey, there are three major categories of automation applications in road maintenance. The first category, which has attracted a considerable amount of research and development, is road defect surveys. The goals of automatic defect surveys are to acquire information about road surface distress quickly, objectively, accurately, and automatically. Such systems can decrease operating costs by reducing labor, and they can lower user costs of manual surveys by operating at highway speeds. Five systems are identified in this study and are given in Table 3.

A second category is traffic control. The goals of automatic traffic control are to ensure communication between maintenance crews and the traffic and to secure the safety of crews while they work under traffic conditions. Because the setup and removal of work zones will affect the total time of road closure, another goal of automatic traffic control is to accelerate the setup and removal of work zones, so that the time of road closure can be minimized. Four systems are identified in this study and are given in Table 4.

A third category is defect treatment. Most automatic systems for defect treatment focus on patching activities. The goals of such systems are to ensure the quality of maintenance operations, to reduce the labor requirement, and to improve the crews' working conditions. These systems are presented in Table 5.

In addition to these three major areas of applications, other systems have been introduced, including an asphalt finisher, an automatic snowplow, a line painting system, a multipurpose traveling vehicle, an automated litter bag retrieval system, and an automated raised marker placement system. A summary of these systems is presented in Table 6.

SUMMARY AND CONCLUSIONS

Because of increasing maintenance demands and the increasing impact of maintenance operations on users, there is a need

TABLE 3 Automation Applications in Defect Surveys (*14–22*)

System Name	Developer	Description
Automatic Pavement Distress Survey System	Komatsu Ltd. Japan	Uses laser, video and image processing techniques to measure cracking, rutting and longitudinal profile. Cracks over 1 mm wide can be measured and the survey can be performed at a speed of 60 km per hour.
PASCO ROADRECON Systems	PASCO Corporation, Japan	Makes measurements with two longitudinal profilers. Cracking, patching and other distresses can be recorded by a continuous road surface photographic recorder. The vehicle travels at speeds between 5 to 85 km per hour.
GERPHO	French Minisere Des Transports	Employs a 35-mm continuously running camera, mounted on a van with a light source that illuminates the pavement. This system takes a continuous image of the pavement surface at speeds up to 64 km per hour. Between 100 to 200 lane kms can be photographed per working night.
Automatic Road Analyzer (ARAN)	Highway Products International, Inc. of Paris, Ontario, Canada	Measures rut depth and transverse profile with ultrasonic sensors, ride/roughness quality with an accelerometer on the rear axis, takes a video picture of the road right-of-way through the windshield, takes a video picture of the pavement surface with a shuttered video camera behind the vehicle, and uses an on-board microprocessor to record distress data. Its operating speed is up to 88 km per hour.
Laser Road Surface Tester (RST)	Swedish Road and Traffic Research Institute	Measures crack depths and widths, rut depths, longitudinal profile from which roughness is computed, macrotexture cross profile and distance. The device uses eleven bumper-mounted laser range finders and an accelerometer to measure the transverse road profile and detect cracks while traveling at speeds of 30 to 88 km per hour.

to improve maintenance technology. By improving maintenance technology, the direct costs of maintenance operations and the related user costs can be reduced. This study focused on automation technology for lowering such costs. Twenty-two automated systems in road maintenance that are used for defect surveys, traffic control, defect treatment, and other supportive activities were identified. These systems demonstrate that automation technology is technically feasible and that it can meet the needs for technological advancements in road maintenance.

Some studies have illustrated that automated maintenance is economically practicable. An economic analysis of crack sealing (*13*) shows that it can save at least $3 million/year nationwide in operation costs. Although the corresponding user benefits were not investigated, they should not be overlooked or underestimated when considering adopting new technologies for road maintenance.

Significant savings can be obtained by shortening the lane closure time and minimizing the size of a work zone. It was estimated earlier that road users spend more than $300 million nationwide on extra fuel consumption alone for passing work zones every year. If, with the introduction of automated systems, the operation time and number of lane closures were reduced by 10 percent, the United States could realize fuel savings annually of $30 million or more. A near–traffic speed asphalt finisher and the Quick Change moveable barrier system show promise in this regard.

Significant user benefits could also be attained by shortening the time lapse between defect formation and repair. Clearly, increasing the capacity of maintenance forces would help do this, provided that road surveys report timely defect information. Automated systems that do reduce operations costs will allow agencies with limited budgets to expand their capacity. The resulting user benefits could approach many millions of dollars a year.

The major conclusions of this study are as follows:

1. Automation in road maintenance is technically feasible in some areas and can pay for itself.
2. Reducing the labor employment in road maintenance is a key issue in decreasing the direct costs of maintenance operations.

TABLE 4 Automation Applications in Traffic Control (*11,12,23–25*)

System Name	Developer	Description
Addco Cone	Addco Manufacturing Co. Minnesota, USA	The device attaches easily to either side of a pickup truck and can be quickly mounted and dismounted. The worker sits in the box of the truck to afford a measure of safety from on-coming traffic. The Cone Wheel also boosts productivity because the operation of placing or retrieving cones is much faster.
Quickchange Movable Barrier System	US Barrier Systems, Inc., California, USA	Consists of a 3-km chain of 636 kg hinged concrete sections and a machine to place and retrieve the barriers. The machine lifts each barrier off the surface, transports it on a large conveyor belt, and accurately repositions the barrier on its new lane location. The entire operation is 25 to 30 minutes.
Super Quartz II Portable Traffic Signals	Horizon Signal, Pennsylvania, USA	Makes it possible for highway crews to automatically control traffic flow by way of a series of microprocessor-controlled, battery-powered signals. Up to 16 traffic lights can be controlled from a single, user-programmed micro-terminal. It can continue to operate using one fully charged 12 volt battery for 72 hours.
Remote Controlled "Follower"	Minnesota Department of Transportation, USA	Consists of a large heavy truck which can be operated from a safe distance by a semi-skilled operator. The truck follows the crew slowly (approximately 8 km per hour) and the operator can control the steering and speed of forward motion. It can be fitted with signals alerting the public, as well as cushions to lessen the damage from a collision.

TABLE 5 Automation Applications in Defect Treatment (*5–9,26–29*)

System Name	Developer	Description
Dynapac Pavement Patcher	Dynapac Light Equipment, New Jersey, USA	Capable of spraying emulsion, spreading aggregate and compacting the mixture all in one pass. It can be adjusted to various widths from 0.3 to 2.1 m in 0.3 increments, and any spray pattern can be achieved including multiple parallel patches.
Thermo-Patch Pothole Patcher	Northwestern U. & UC Davis, USA	Brings several different components together and is properly sized to adequately perform the task without material waste.
"Puff" the Pothole Patcher	One Man Inc., New Mexico, USA	Can be driven to the site at highway speeds and upon arrival, a variety of traffic control warnings helps to ensure the safety of the operator and the public. All required asphalt materials are carried on the machine in heated storage containers, and space is allotted for the storage of waste materials removed during repairs.
Automatic Crack-Filling Robot	Carnegie-Mellon U. and U of Texas at Austin, USA	Integrates a video-based raster scan image with a laser range sensor that supplies information about the third dimension. The repair process is performed by an x-y table with three mounted tools: a heated air torch, a sealing wand and the infrared laser range sensor.
Robotic Crack Sealing System	California Department of Transportation and U. of California at Davis, USA	The equipment under development utilizes a machine vision system to identify the cracks while a robot manipulator prepares and seals the cracks. The automated machine will prepare and seal both longitudinal and transverse cracks.
Asphalt Paver	Barber Greene Equipment Co., USA	It features large, wide-inlet self-dumping hoppers, high capacity long-lift feeder and spreading auger systems. Fully hydrostatic drive systems provide a smooth efficient operation with a capacity to handle varying paving requirements. Automatic control systems provide fully proportional control of the material feed to match job requirements.
Hot Mix Paver	Cedarapids Equipment Co., USA	Standard features include three-point suspension, full lighting package, high alloy slat liners, power-adjustable hopper gates, dual-position swing console and the standard 8 foot Fastach screed to deliver the suspension performance needed to produce a quality mat.

3. A major emphasis of R&D for automation in road maintenance should be placed on minimizing user costs in addition to reducing the direct costs of maintenance operations.
4. As the QUEWZ model shows, to reduce the action user costs, the R&D effort should focus on shortening the required operation time and the size of work zones.
5. As the HDM-III model shows, to reduce the nonaction user costs, the R&D effort should focus on shortening the time lapse between defect formation and repair. This implies that timely information of defect surveys should be provided and that the capacity of maintenance forces needs to be expanded by the employment of automated systems.
6. The demand for road maintenance will increase rapidly over the upcoming years. Maintenance forces around this country must respond to this need by improving maintenance efficiency through automation technology.

ACKNOWLEDGMENTS

The authors would like to acknowledge the Southwest University Transportation Research Center for supporting this study as well as their colleagues at the University of Texas at Austin for their help.

TABLE 6 Automation Applications in Supportive Activities (*29–33*)

System Name	Developer	Description
Asphalt Finisher	Nippon Hodo Co., Ltd., Japan	Has a liquid crystal color display, a touch panel, voice response, etc. for ease of operation. The screed surface pressure and heater temperature can be changed freely and the range of paving materials that can be used is wider than an ordinary asphalt finisher.
Automatic Snowplow	Nichijo Manufacturing Co., Japan	Consists of the steering operation unit, the operation panel, the control unit, the hydraulic unit, the ferrite sensor unit, and the steering actuator unit. XY control, concentration control, linear motion control and pattern control in chute operations for snow throwing and driving control for steering operations are provided.
Automatic Line Painting System	Ministry of Transportation of Ontario, Canada	Increases the speed and accuracy of the operation while decreasing the demands placed on the driver. Work is being performed that will allow the lateral position of the paint guns to be automatically controlled, as well as the triggering of the guns.
Multipurpose Traveling Vehicle	Societe Nicholas of France	Is being used for mowing grass around roadway curbs. Future plans for the vehicle include sowing, ditch excavation, road marking and cleaning, surface cutting, brushwood clearing and salt dispensing.
Automatic Litter Bag Retrieval System	California Department of Transportation and U. of California at Davis, USA	Utilizing a single operator, this prototype will automatically pick up litter filled bags from the highway right of way while in motion. Future generations of this machine will have the potential to remove unbagged litter and debris.
Automated Raised Marker Placement System	California Department of Transportation and U. of California at Davis, USA	The current development will allow higher speeds of dispensing of adhesive and various types of RPMs by a single operator. One such device will place RPM s on newly paved roadways while another machine under development will replace missing RPMs on previously marked pavement with speeds up to 10 miles an hour.

REFERENCES

1. M. Skibniewski and C. Hendrickson. Automation and Robotics for Road Construction and Maintenance. *Journal of Transportation Engineering*, ASCE, Vol. 116, No. 3, 1990, pp. 261–271.
2. J. Memmott and C. Dudek. Queue and User Cost Evaluation of Work Zone (QUEWZ). *Transportation Research Record 979*. TRB, National Research Council, Washington, D.C., 1984, pp. 12–19.
3. J. Memmott and C. Dudek. *A Model to Calculate the Road User Costs at Work Zones*. Technical Report FHWA/TX-83/20+292–1. FWHA, U.S. Department of Transportation, 1982.
4. *HDM-PC Handbook*. The Highway Design and Maintenance Standard Series. World Bank, Washington, D.C., 1989.
5. R. Rollings, P. Korgemagi, and D. Lynch. An Evaluation of a High Production Integral Spray Patcher. *Public Works*, Jan. 1987, pp. 55–58.
6. C. Haas, J. Hajek, and R. Haas. Opportunities for Automation in Pavement Maintenance. *Proc., Annual Conference of Transportation Association of Canada*, Winnipeg, 1991.
7. C. Haas, C. Hendrickson, S. McNeil, and D. Bullock. A Field Prototype of a Robotic Pavement Crack Sealing System. *Proc., 9th International Symposium on Automation and Robotics in Construction*, Tokyo, Japan, 1992, pp. 313–322.
8. RQS Industries, Inc. Company Literature. Joplin, Mo., 1990.
9. *Alaskan Transportation Technology Transfer Program—Planning, Design, and Field Notes*. University of Alaska at Fairbanks, 1991.
10. F. Goto and T. Saitoh. Development of Advanced Asphalt Finisher. *Proc., 9th International Symposium on Automation and Robotics in Construction*, Tokyo, Japan, 1992, pp. 323–332.
11. C. Harris-Stewart. Work Zone Safety Arouses Concern. *Engineering News Record*, March 12, 1987, pp. 30–31.
12. Horizon Signal. Company Literature. Wayne, Penn., 1990.
13. J. Deng, A. Pearce, and S. McNeil. *Economic Analysis of Automated Pavement Crack Sealing*. Technical Report SHRP IDEA-87-ID017. Strategic Highway Research Program, National Research Council, Washington, D.C., 1992.
14. T. Fukuhara, K. Terada, and M. Nagao. Automatic Pavement-Distress-Survey System. *Journal of Transportation Engineering*, ASCE, Vol. 116, No. 3, 1990, pp. 280–286.
15. R. Hudson, G. Elkins, W. Uddin, and K. Reilley. *Improved Methods and Equipment to Conduct Pavement Distress Surveys*. Technical Report FHWA-TS-87-213. FWHA, U.S. Department of Transportation, 1987.
16. *Report on Pavement Condition Monitoring Methods and Equipment*. PASCO USA Inc., Lincoln Park, N.J., 1985.
17. *Pavement Condition Monitoring Methods and Equipment*. Final Report on GERPHO. MAP Inc., Washington, D.C., 1986.
18. M. Dewilder. GERPHO and the APL. *Proc., Roadway Evaluation Equipment Workshop*, FHWA-TS-85-210, FHWA, U.S. Department of Transportation, 1985.
19. *1 for 3, PASCO Road Survey System (PRS-System)—From Theory to Implementation*. Project and Development Division, PASCO Corporation. New York (n.d.).
20. *Automatic Road Analyzer—Mobile Data Acquisition Vehicle*. Product Bulletin, Highway Products International, Inc., 1985.
21. R. Novak. *Swedish Laser Road Surface Tester*. Technical Report FHWA-TS-85-210. FHWA, U.S. Department of Transportation, 1985.
22. *Interim Memorandum to Waheed Uddin*. Infrastructure Management Service. Sept. 1986.
23. Addco Manufacturing Co. Company Literature. St. Paul, Minn., 1990.
24. K. Smith. Work Zone Safety Devices Slated for State Trials This Year. *Strategic Highway Research Program Focus*, April 1991.
25. C. Thorpe. Outdoor Visual Navigation for Autonomous Robots. *Proc., Intelligent Autonomous Systems II Conference*, Amsterdam, The Netherlands, 1989.
26. C. Haas, C. Hendrickson, and S. McNeil. A Design for Automated Pavement Crack Sealing. *Proc., ASCE Construction Congress*, Cambridge, Mass., 1991.
27. S. Velinsky. Robotic System for Pavement Crack Sealing. Presented at the 72nd Annual Meeting of the Transportation Research Board, Washington, D.C., 1993.
28. Caterpillar Paving Products, Inc., Barber Greene Division. Company Brochure. Dekalb, Ill., 1991.
29. Cedarapids Inc. Company Brochure. Cedar Rapids, Iowa, 1990.
30. Y. Sasaki, Automation of Snowplow. *Proc., 9th International Symposium on Automation and Robotics in Construction*, Tokyo, Japan, 1992, pp. 333–340.
31. C. Coomasasary. *Pavement Markings Equipment*. Ministry of Transportation of Ontario, Canada, 1991.
32. G. Point. Two Major Innovations in Current Maintenance: The Multipurpose Vehicle and the Integrated Surface Patcher. In *Transportation Research Record 1183*, TRB, National Research Council, Washington, D.C., 1988.
33. *Advanced Highway Maintenance Technology Program Bulletin*. California Department of Transportation, Sacramento, 1992.

Publication of this paper sponsored by Committee on Applications of Emerging Technology.

Toward an Adaptive Control Model for Robotic Backhoe Excavation

XIAODONG HUANG AND LEONHARD E. BERNOLD

Research in robotic excavation has been focused mainly on path control to let a machine search and adapt trajectories automatically. Approaches to detect and handle underground obstacles such as rocks or utility lines are also critical for robotizing the operation. A newly established research facility to study robotic backhoe excavation using a real-size hydraulically powered and computer-controlled manipulator is introduced. A hierarchical planning and control model for robotic excavation is presented. The control system for this robotic backhoe is based on multiple sensors for force and position measurements and an approach for the detection and recognition of underground obstacles is discussed. Experimental data are used to analyze the force and acceleration patterns while the bucket hits an obstacle. Finally, a decision model for obstacle handling strategy derivation is introduced.

Almost all production-oriented robots today are used within the manufacturing industry. However, true robots are uncommon in the construction industry because of the unstructured and complex conditions found on a construction site. In addition, construction usually takes place in an uncontrolled environment, exposed to elements such as weather, dust, and noise. The attributes of the materials to be handled range from large, heavy, bulky, and nonhomogeneous to light, fragile, and homogeneous. In addition, although one of the traditional materials handled in construction is soil, the mechanics of excavating soil and rocks are poorly understood.

Despite the many difficulties, opportunities for applying high technology in construction are abundant. For certain applications and situations, such as construction in hazardous areas (i.e., nuclear waste disposal, space construction), robotic technology is unavoidable (*1*). However, the lack of automatic planning and control models needed for robotic operations in construction requires empirical as well as theoretical studies.

One of the high volume and repetitive operations at the construction site is the excavation of soil. Studies on the applications of robotic excavation have been undertaken by several researchers. The kinematic and dynamic control model for a robotic excavator was studied and established by Vaha (*2*). An approach for force-cognitive robotic excavation was developed by Bullock and Oppenheim (*3*). Tochizawa et al. reported about an automated excavator for excavating a trench for drainage using laser guidance (*4*) and showed that efficiency was improved 1.6 times while labor hours decreased and digging accuracy increased.

X. Huang, Department of Mechanical and Aeronautical Engineering, North Carolina State University, Raleigh, N.C. 27695. L. E. Bernold, Department of Civil Engineering, North Carolina State University, Raleigh, N.C. 27695.

PLANNING AND CONTROL HIERARCHY FOR ROBOTIC EXCAVATION

General Control Concepts

Several basic robotic control models have been developed in the past. Among them are position control (*5*), force control (*6*), hybrid control, and impedance control. Because of their relevance to robotic excavation, the last two models will be discussed briefly.

In a hybrid control model, a position and force control system tries to satisfy the task requirements by using both position and force feedback information for trajectory planning. A typical hybrid control problem is to follow a trajectory and to exert a force at contact with the environment. In free space where no external force is measurable, the position controller ensures that the end effector follows the prescribed trajectory, whereas the force controller is inactive. As soon as contact occurs between the end effector and the environment, the force sensors are able to detect contact forces which depend on the stiffness of the entire system (robot arm, end-effector, and environment) (*7*). Now, the control mode switches to force control. This type of dual control has been labeled "hybrid control" as a matter of consensus in the robotics literature.

Impedance control differs from traditional force/position control policies in that instead of controlling one state variable—position, velocity, or force—it specifies the relationship among them for trajectory planning. This type of control has many desirable attributes. Chief among them is the ability to come in contact with a hard surface without losing stability as well as to control directly the mechanical interactions with the environment (*8*). For an impedance control model, the same strategic interface can be used for both free-motion slews and manipulation requiring contact. These capabilities are critical during bucket obstacle interference because the detection and handling of any obstacle has to be automatic.

However, the above listed control models are based on a good understanding of the dynamics of the robot system and its environment. In a number of instances, however, the system to be controlled is too complex, and the basic physical relationships are not fully understood. Thus, the control model needs to be augmented with an identification technique aimed at obtaining a progressively better understanding of the dynamics of both the manipulator and its work environment (*9*). Adaptive control is generally used as a framework which is characterized by its capabilities to gather information about an unknown process and to make automatic command changes using the employed control law. Adaptive control systems

adjust their behaviors to the changing properties of the controlled processes and the sensory feedback signals (*10*).

In designing a control model for the robotic backhoe excavator, several basic characteristics of the backhoe excavation have to be considered. The end effector (e.g., a bucket) travels both in free space and in soil. The control parameters for these two distinct environments differ when only position or force control models are applied. Even within the soil environment, the characteristics of the soil may change abruptly within a short distance, not mentioning the existence of underground obstacles. Because of its capability for tasks requiring contact with external environment, the impedance control model is ideal for robotic backhoe excavation. In addition, the uniqueness of the adaptive control concept to self-adjust and compensate for the unknown system parameters makes it a well-suited overall control framework. Thus, an adaptive control framework that incorporates the impedance control model has been selected to serve as the control system for robotic backhoe excavation.

Hierarchical Model for Planning and Control

A hierarchy for planning and control has been developed shown in Figure 1. This hierarchy is composed of three major modules: master planning, path planning, and adaptive control. The master planning module is responsible for developing general plans for an entire job, such as digging a trench. Each plan is executed by initiating lower level commands.

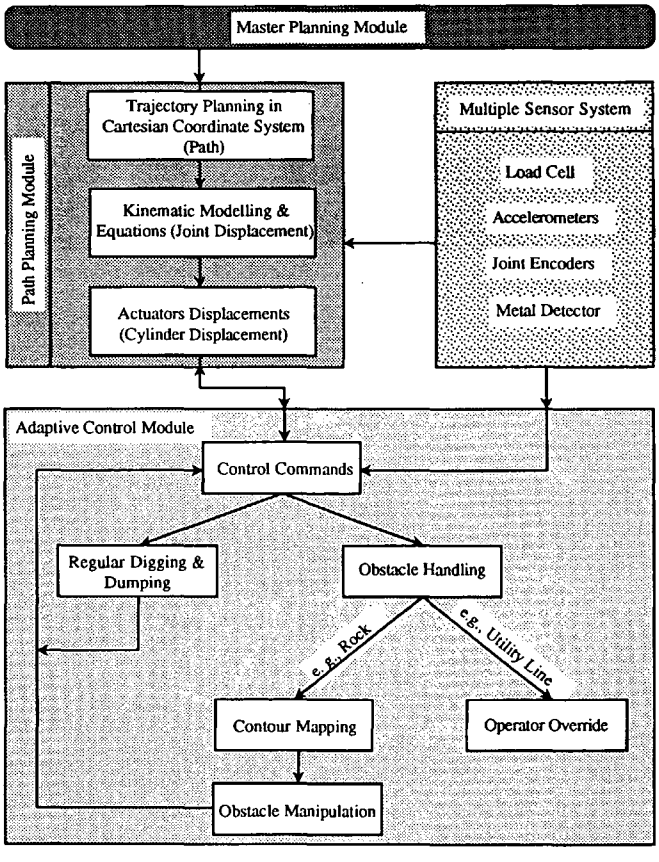

FIGURE 1 Planning and control hierarchy for robotic excavation.

The path planning module produces trajectories for the stepwise execution of the master plan. One trajectory is composed of a sequence of points defined in a fixed x-y-z Cartesian coordinate system. By defining the starting and ending position, a trajectory is developed by the computer based on the specific objective of a path (e.g., filling the bucket with soil). This trajectory is translated into manipulator joint displacements (e.g., rotational angles) using inverse kinematics. As in Figure 1, the final step in the path planning module is developing the instructions to the actuators for motion executions (e.g., linear cylinder movements) necessary to accomplish the joint displacements. Each component of the path planning module decomposes the directives until primitive instructions are obtained.

The adaptive control module shown in Figure 1 is decomposed into two main modes: regular digging and the obstacle handling. If no obstacle is encountered, the control system operates in a regular digging mode. During the excavation, the multiple sensors provide data about force, accelerations, and positions to the controller. By comparing them with the desired values (e.g., planned positions), commands are generated in real time to adapt the trajectory. If the manipulator is equipped with a metal detector search coil and a force sensor, load cell, metals (e.g., pipes) and other obstacles (e.g., rocks) could be detected. When metal is detected, it is presumed that the bucket is coming near one part of a utility line. A signal will be generated to slow down the excavation and any signal variations from the detector will be monitored. On the other hand, if no metal is detected while the force shows an abrupt and drastic change, it is presumed that the bucket has hit a rock or other nonmetallic obstacle. The control system then switches automatically to the obstacle handling mode and the path is to be adjusted around this obstacle to continue digging. For example, when hitting a rock, the impedance controller is able to modify the trajectory by moving the bucket backward and up by 0.02 m before continuing its path. If the bucket hits the same obstacle again, another adjustment to the trajectory has to be made. Thus, by recording the positions of interference, the control system will be able to derive the contour of the rock in this particular path. After a series of paths, a partial surface contour map of the rock can be obtained, which should enable the system to select an appropriate strategy to handle this removable obstacle.

EXPERIMENTAL FACILITY FOR ROBOTIC EXCAVATION

A Multipurpose Robotic Manipulator Platform (MRMP) has been built within the Construction Automation and Robotics Laboratory of North Carolina State University (see Figure 2). It is driven by one hydraulic motor for base rotation and three hydraulic actuators (cylinders), which provide a total of 4 degrees of freedom (DOF). Three kinds of sensors are used in the data collection system. One force sensor, load cell, is mounted at the rod of the third hydraulic actuator. Three accelerometers are mounted on the boom, the arm, and the end plate (connection between the bucket and arm), respec-

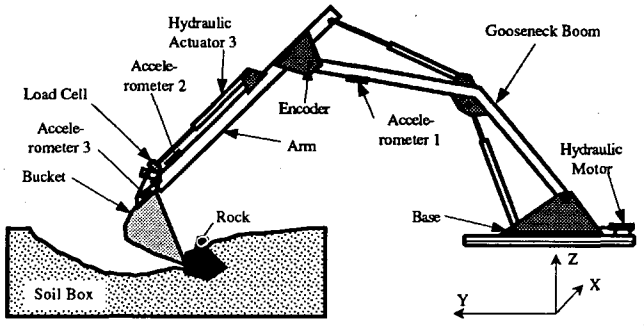

FIGURE 2 Experimental platform: robotic backhoe excavator.

tively, to detect accelerations in both the digging plane and the area perpendicular to the digging plane. One joint encoder is installed at the third joint to measure the actual joint angles. A metal detector search coil will be adopted to mount on the bottom of the arm to detect some utility lines and electric wires. By using an analog/digital board with a sampling rate over 4 KHz, the computer reads in real time the changes from the sensors. Control commands from the 386 computer are sent to the actuators through a digital/analog board. The commands act on four electrohydraulic proportional valves to open and close the valves proportionally and to change the flow directions of the oil.

IN-PROCESS OBSTACLE RECOGNITION AND HANDLING STRATEGY

Obstacles in excavation can be divided into two basic categories: removable rigid objects such as rock or lumber pieces and nonremovable objects such as utility lines. In 1989 the United Kingdom reported about 70,000 instances of damage to buried services during excavation (*11*). During excavation it becomes more critical that buried obstacles such as utility lines can be detected and distinguished from removable obstacles such as rocks to avoid accidents.

Sensor-Based Obstacle Detection and Recognition

One approach to detecting such obstacles is to include an electromagnetic detector capable of detecting metal pipes and electrical wires. By attaching such a sensor on the arm close to the actual location where the bucket will interact with a metallic obstacle, high accuracy and dependability can be achieved. Because the detector scans the area ahead of the bucket tip during actual excavation, it will send out a warning signal and stop the excavation before the bucket cuts the line. However, current technology does not effectively detect plastic pipes and other nonmetallic utility lines.

The action of digging in a uniform soil with a bucket can be compared to cutting cheese with a knife. The force caused during bucket-soil interactions increases gradually (Figure 3, before 75 samples). If a large obstacle buried in the soil is contacted, the impedance of the environment changes abruptly and significantly. The motion discontinues when the measured resistance force is larger than normally expected. Thus, the force required for digging is an excellent indication

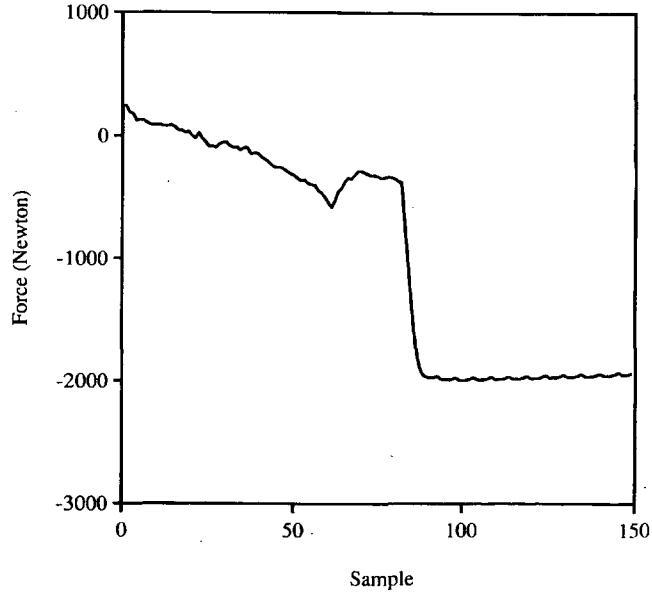

FIGURE 3 Load cell force pattern during bucket-rock impact.

of the soil conditions and the presence of a large obstacle. Figure 3 shows the output of the load cell curing a bucket-rock impact. In this figure a negative force represents compression and a positive value represents the tension mode in hydraulic actuator 3.

Figure 3 shows that after the compression force undergoes a normal increase during digging, an abrupt and drastic increase can be observed. Actually, at exactly this point, the bucket hit a buried rock in the soil box. The slope of the force curve at this point is almost vertical. As the compression force reaches -2002.5 N (-450 lb), the pressure-reducing valves in the hydraulic power system are activated. As a result, the excavation motion stops, and the impact position is recorded in the computer data base. The stable force observed after the collision indicates a horizontal line.

Before the robot can handle a removable obstacle, such as a rock, an estimate of the position, shape, and dimension of the obstacle has to be derived. This requires much more detailed information from the sensors. While two accelerometers are being used to acquire the inclinations of the boom and the arm, the third accelerometer is mounted at the end plate to detect the acceleration along the x-axis and torsional deflection in the y-axis (in Figure 2). Several experiments have been undertaken to measure and analyze the output of this accelerometer during the bucket-obstacle impact. It was hoped that the output could be used to determine at which cutting edge the bucket contacts the obstacle. From this information the control system could derive the position of the obstacle relative to the bucket. As a result, a more accurate point of interference can be identified for mapping the surface contour of the obstacle. In addition, the information about the relative position is very helpful for deciding the next digging path. Figures 4 and 5 show data sets from the experiments designed to test such a concept.

Figures 4 and 5 display two acceleration patterns from Accelerometer 3 during bucket-rock interactions. Both out-

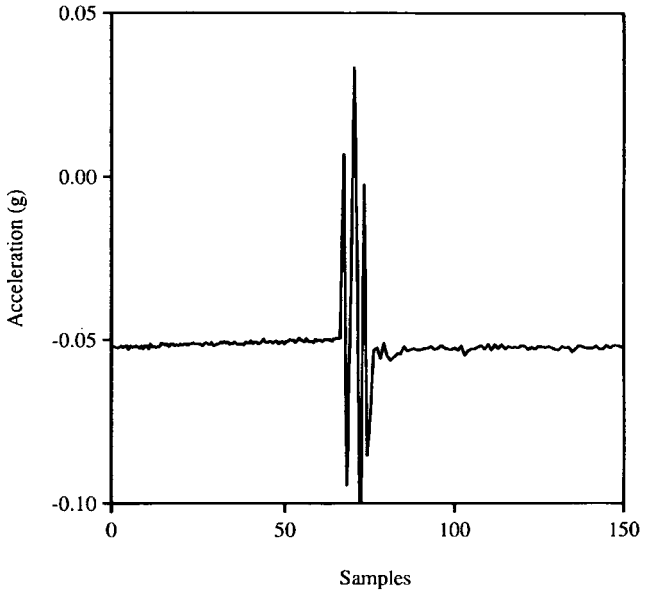

FIGURE 4 Acceleration patterns during bucket-rock impact (Accelerometer 3): bucket-rock impact at left edge.

puts start with stable accelerations (horizontal lines) between samples 0 and 75. During this period, the bucket is in a regular digging mode (also refer to Figure 3). Around the 75th sample, a positive impulse followed by high-frequency oscillations in Figure 4 and a negative impulse followed by high-frequency oscillations in Figure 5 can be observed. At these moments, the bucket collides with the buried rock in the soil box. One can notice that after the accelerations are stabilized again, the plateaus of acceleration before and after the actual impact differ. The difference is linked to the torsional deflection of the bucket during the impact. For example, when the rock is rammed by the left corner of the bucket cutting edge, a positive acceleration occurs first, followed by oscillations. The stable acceleration level before and after the impact changes from approximately -0.05 to -0.06 g ($\Delta a \approx -0.01$ g, 1 g = 9.8 m/sec^2, Figure 4).

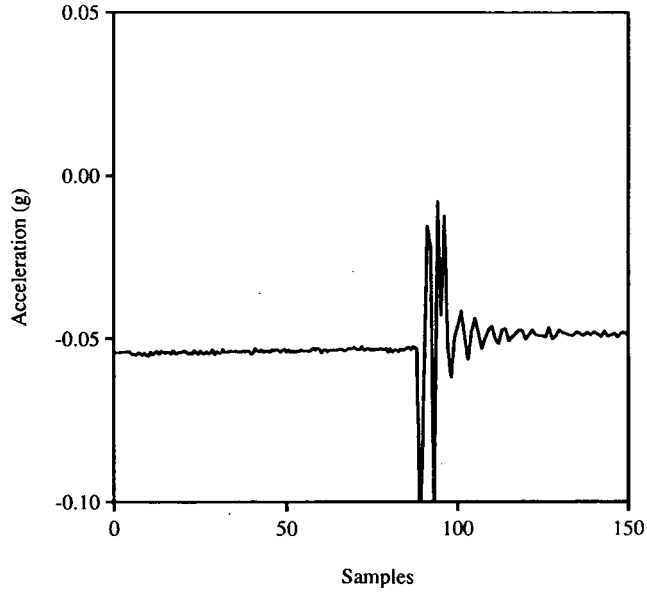

FIGURE 5 Acceleration patterns during bucket-rock impact (Accelerometer 3): bucket-rock impact at right edge.

Where the rock is hit with the right corner of the bucket cutting edge, the stable acceleration level changes from approximately -0.06 to -0.05 g ($\Delta a \approx 0.01$ g, Figure 5). The different changes in the stable acceleration outputs indicate the bucket's different directions of rotational deflection. This fact corresponds with the observed bucket rotation due to the eccentric force caused during the bucket-rock collision. And the test results indicate that the accelerations could indeed provide valuable information for adaptive, controlled obstacle handling. Both surface contour mapping and path replanning benefit from the availability of data indicating more accurately the point of interference.

Strategy Derivation for Obstacle Manipulation

A removable obstacle can be handled in a variety of ways, depending on the objective of the excavation and the characteristics of the obstacle itself. Strategies have to be developed for this purpose. Finding the "best" strategy is a decision-making process that may take advantage of a decision tree using some input conditions. These conditions include the results of obstacle recognition and contour mapping, which provide data about the dimensions of the obstacle; the excavation requirements; and mechanical system configurations. Figure 6 shows a partial decision-making tree for handling the removable obstacles.

The decision tree in Figure 6 relates conditions and goals with manipulation strategies by using artificial reasoning procedures. The goal is to find a strategy for removing a detected obstacle. Given the required conditions, the reasoning mechanism searches through this tree and derives a strategy (conclusion) to be used by the control system. If several strategies can be activated at the same time, then the one with the highest priority will be selected first. The strategy with lower priority will be chosen only if the control system fails with the removal using the higher priority scheme.

The hierarchical framework used to develop the control system allows the effective integration between different control components briefly discussed earlier in this paper. As a result, the model presented in Figure 6 is represented by only one box within the adaptive control module in Figure 2. This modularization contributes to the flexibilities of the proposed control concept.

CONCLUSION

This paper presents concepts and experimental results on the issue of adaptive control for robotic excavation. Multiple sensors, such as a load cell, and three accelerometers have been installed on a computer-controlled backhoe excavator for tests. These sensors are used not only for monitoring forces and sensing positions but also for detecting, recognizing, and handling obstacles. A hierarchical planning and control model is developed. The control system is designed to be able to detect obstacles during digging. Obstacle handling strategy can be

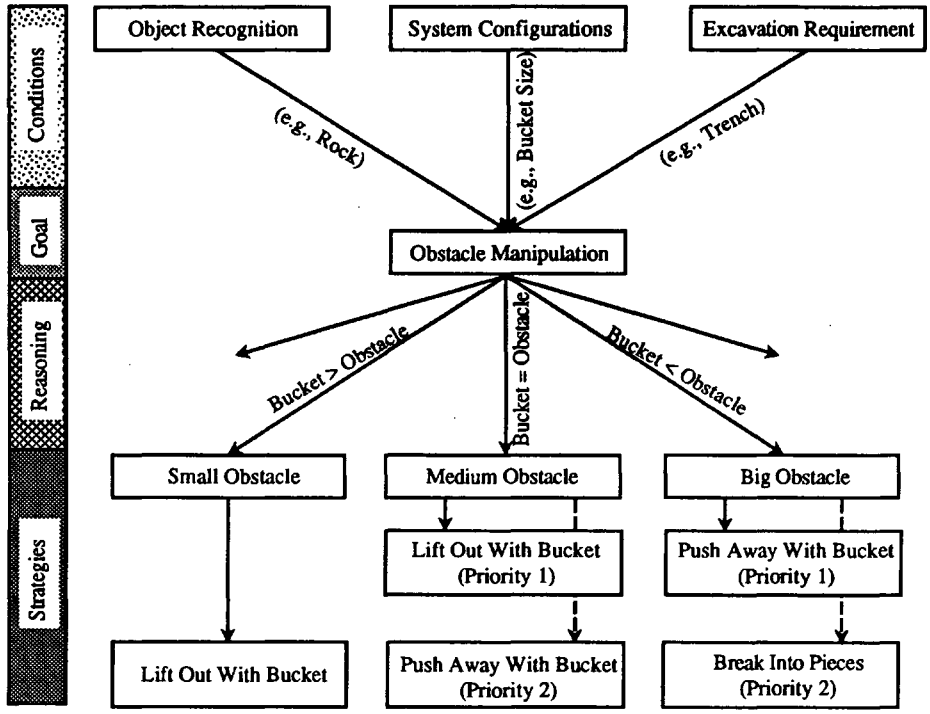

FIGURE 6 Partial decision tree for obstacle manipulation.

invoked automatically using a decision tree structure. The initial research results support the effectiveness of using multiple sensors together with the adaptive control concept for robotic excavation in unstructured environments.

ACKNOWLEDGMENTS

The College of Engineering at the North Carolina State University and the Space Studies Institute at Princeton, New Jersey, supported the research for this paper.

REFERENCES

1. R. Colbaugh and M. Jamshidi. Robot Manipulator Control for Hazardous Waste-Handling Applications. *Journal of Robotic Systems*, Vol. 9, No. 2, Sept. 1992, pp. 215–250.
2. P. Vaha. *Modelling and Control of Cognitive Excavation*. Technical Report. School of Civil Engineering, Purdue University, West Lafayette, Ind., Oct. 1990.
3. D. M. Bullock and I. J. Oppenheim. Object-Oriented Programming in Robotics Research for Excavation. *Journal of Computing in Civil Engineering*, Vol. 6, No. 3, July 1992, pp. 370–385.
4. M. Tochizawa, S. Takeda, et al. Automatic Excavator. *Proc., 8th International Symposium on Automation and Robotics in Construction*, Vol. 1, Stuttgart Killesberg, Germany, June 1991, pp. 277–284.
5. H. Asada and J.-J. E. Slotine. *Robot Analysis and Control*. John Wiley and Sons, Inc., New York, 1986, pp. 136–139.
6. Z. W. Luo and M. Ito. Control Design of Robot for Compliant Manipulation on Dynamic Environments. *Proc., of the 1991 IEEE International Conference on Robotics and Automation*, Sacramento, Calif., Vol. 1, April 1991, pp. 42–47.
7. S. Chiaverini and L. Sciavicco. Force/Position Control of Manipulator in Task Space With Dominance in Force. *Proc., Robot Control 1988 (SYROCO'88) Selected Papers from the 2nd IFAC Symposium*, Karlsruhe, Germany, Oct. 1988, pp. 137–143.
8. S. A. Schneider and R. H. Cannon, Jr. Object Impedance Control for Cooperative Manipulation: Theory and Experimental Results. *Proc., IEEE Transactions on Robotics and Automation*, Vol. 8, No. 3, June 1992, pp. 383–394.
9. S. Sastry and M. Bodson. *Adaptive Control—Stability, Convergence, and Robustness*. Prentice-Hall, Inc., Englewood Cliffs, N.J., 1989.
10. R. Isermann, K.-H. Lachmann, and D. Matko. *Adaptive Control Systems*. Prentice-Hall International (U.K.) Ltd, Great Britain, 1992.
11. D. A. Bradley, D. W. Seward, and R. H. Bracewell. Control and Operational Strategies for Automatic Excavation. *Proc., 6th International Symposium on Automation and Robotics in Construction*, Vol. 1, San Francisco, Calif. June 1989, pp. 237–244.

Publication of this paper sponsored by Committee on Applications of Emerging Technology.

Colorado's Knowledge System for Retaining Wall Selection

TERESA M. ADAMS, ROBERT K. BARRETT, AND TREVER WANG

The Bridge Branch of the Colorado Department of Transportation (CDOT) has organized a formal decision process for selecting retaining walls. The selection process facilitates implementation of new retaining wall technologies by requiring that a range of options be considered when selecting retaining wall alternatives. The CDOT retaining wall selection process falls into a general pattern of organization that can be automated using knowledge-based system technology. The computerized implementation of the decision process is described; it will reduce the time required to perform the retaining wall selection process, enforce consistency in decisions made by designers and consultants, and provide a mechanism for CDOT to encode standard designs, practices, and minimum performance criteria within the decision process.

For various reasons, some departments of transportation (DOTs) resist new retaining wall technology and avoid integrating emerging retaining wall design and construction expertise into their internal hierarchies. Instead they opt for vendor designs, alternative bids, and after-the-bid value engineering. There is an apparent need to facilitate implementation of new retaining wall technologies and to foster a paradigm change on how retaining walls are selected. For example, district offices statewide of the Colorado DOT (CDOT) were asked to review existing plans and to consider substituting the CDOT geosystem wall where other types of walls were designed. Results indicated that more than $1 million in construction costs were saved in only a few CDOT projects (*1*). Geosystem walls are projected to save Colorado from $5 million to $10 million annually. Furthermore, hundreds of millions of dollars can be saved nationwide by using new retaining wall technologies.

Many factors are involved in an office's reluctance to leave the old paradigm where retaining walls are built from concrete and steel. Many who have traditionally been responsible for wall selection and design continue to limit their expertise (*2*). The failure to develop internal expertise for retaining wall selection and design results in a major technology gap that can result in unnecessary expenditures. Under current fiscal constraints, it is imperative that DOT engineers and consultants be capable of designing not only traditional walls but also mechanically stabilized embankment (MSE) walls, modular walls, and the variety of new ground improvement techniques.

The past decade has seen enormous interest in the application of expert systems in all areas of highway design. Researchers have shown that expert systems can be applied for retaining wall selection (*3*), failure diagnosis (*4,5*), and rehabilitation design (*6–8*). In each case, the potential for retaining wall construction cost savings is apparent.

This paper describes a formal retaining wall selection process as cast into a pattern of organization that can be automated using knowledge-based system technology. System development was initiated by the Bridge Branch, CDOT. This paper provides a complete overview of the system design and implementation. This paper emphasizes the conceptual framework, including the knowledge- and symbol-level representations. The techniques for encoding and processing knowledge are described and illustrated.

OBJECTIVES

The CDOT retaining wall selection system aims to assist rather than replace a knowledgeable, experienced retaining wall design engineer. Besides significantly reducing retaining wall construction costs by improving wall selection, the system can reduce an engineer's retaining wall selection and design time by 30 percent. The objectives of the system are to

1. Enable consistency and consideration of multiple retaining wall alternatives in decisions made by designers and consultants;
2. Provide a mechanism for encoding standard designs, practices, and minimum performance criteria within the decision process; and
3. Foster a paradigm change on how retaining walls are selected and to facilitate implementation of new retaining wall technologies.

KNOWLEDGE LEVEL

Before knowledge can be organized as a symbol system and encoded in a programming language, the knowledge level must be identified. The knowledge level describes the concepts, goals, actions, behavioral laws, and knowledge components of the system (*9*). The retaining wall selection system follows a problem-solving strategy described in Section 5 of the CDOT *Bridge Design Manual* (*10*) and contains knowledge from other sources (*11–14*).

The system acts as a sieve for eliminating infeasible walls using the constraints presented in Table 1. Functional constraints are related to the purpose of the retaining structure. Spatial constraints are related to site accessibility and space

T. M. Adams, Department of Civil and Environmental Engineering, University of Wisconsin–Madison, Madison, Wis. 53706. R. K. Barrett and T. Wang, State of Colorado, Department of Transportation, Denver, Colo. 81502.

TABLE 1 Constraints That Influence Selection of Retaining Structures

Type	Constraint
Functional	Roadway (Front/Back-top)
	Grade Separation
	Landscaping
	Noise Control
	Ramp or Underpass
	Temporary Shoring of Excavation
	Stability of Steep Side Slope
	Flood Control
	Bridge Abutment
Spatial	Material and Equipment Access
	Material Storage
	Proposed Profile (Cut/Fill)
	Working Space in Front of Wall
	Traffic Maintenance
	Excavation Space Behind Wall
Behavioral	Quality of Fill Material
	Ground Water Table
	Bearing Capacity
	Differential Settlement
	Backfill Settlement
	Construction Loads
Economic	Available Skilled Labor
	Noise/Vibration Control
	Construction Time

limitations. Behavioral constraints are related to structural performance of the system. Economic considerations are related to direct and indirect construction costs. Each constraint is related to one or more wall types and directly influences the selection of retaining structures.

Starting with a set of all wall types, the process of eliminating infeasible wall types can be conceptualized as through two sieves that filter out infeasible wall types. The first sieve eliminates obviously infeasible wall types on the basis of required functions of the wall. The second sieve further reduces the number of feasible wall types according to spatial, behavioral, and economic constraints. The knowledge for elimination is both qualitative and quantitative. Five types of knowledge are used to eliminate infeasible walls.

First, unique circumstances of feasibility under certain constraints are difficult to evaluate in terms of exact data. For example, storage, workspace, and access constraints involve consideration for construction materials and equipment. In such cases, construction expertise is required to judge the sufficiency of storage or workspace and the access for a particular wall type.

Second, combinations of constraints preclude some wall types. Certain constraints, such as durability and fill quantity, work in combination with other constraints. In such situations, the relationship between interdependent constraints is inherent.

Third, the potential advantages or disadvantages of a wall type incorporate local practices and trends of construction that can result in overall economy. For example, certain wall types are a particularly good solution under some constraints and a bad solution under other constraints.

Fourth, quantitative evaluation of site-available measures can be used to determine whether wall-specific requirements are satisfied. For example, given the approximate dimension of available excavation space and the predefined approximate backspace required (in terms of percentage of wall height), then if the available space is less than required, the wall is infeasible. Also, a range of economical wall heights can be used to decide whether to eliminate a wall type that is not economical.

Fifth, qualitative evaluation of site-available measures can be used to determine whether wall-specific requirements are satisfied. Site-specific (allowable) spatial, behavior, and economic factors are logically compared with wall-specific (required) factors to eliminate infeasible wall types.

SYSTEM DESCRIPTION

Colorado's retaining wall selection system eliminates infeasible alternatives then scores and ranks feasible alternatives. The system aims to assist an experienced retaining wall design engineer with construction knowledge of 24 gravity, semigravity, nongravity, and hybrid earth retaining wall types. The architecture of the system is shown in Figure 1. The system is composed of four main modules: input, elimination, ranking, and output. A discussion of the knowledge-based techniques used for elimination and ranking follows.

Elimination

The objective of elimination is to use given constraints to reduce the set of all walls to a subset of feasible walls. The implementation is based on Bayesian decision theory, assuming that each constraint is conditionally independent. The method requires two components of knowledge: the prior probability of each wall type and the conditional likelihood ratios for each constraint. Then, on the basis of a sequence of independent constraints, the likelihood ratios are used to revise the prior estimate of the probability of each wall type.

Bayesian decision theory is used for diagnosis, identification, and selection problems and in rule-based systems (*15*). The method was established in the context of the Prospector system (*16*) for identifying ore deposits. It was also used for the diagnosis of retaining wall failures (*5*). A version of the method is described and illustrated herein for retaining wall selection. The approach differs from the plausible relations in Prospector because plausible relations are most useful for identification and diagnosis problems when both the existence and lack of evidence are needed to make a decision. For the

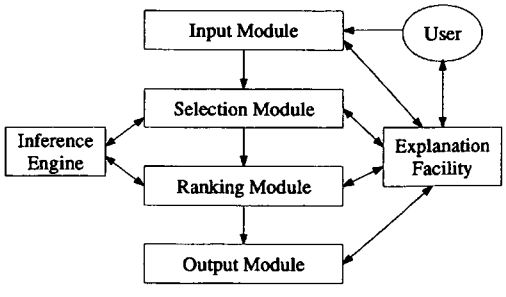

FIGURE 1 Architecture of CDOT wall selection system.

retaining wall selection problem, only existence of evidence (in the form of constraints) is needed. A secondary difference occurs because the selected paradigm of the Colorado system is to eliminate infeasible solutions rather than to search for the best solution.

The conditional probability of wall type W_k is expressed in terms of the likelihood ratio LR_k. To compute LR_k, the initial likelihood ratio LR_{k0} is updated by the appropriate conditional likelihood, CLR_j, for each constraint C_j (Equation 1). In this formulation, the subscript k denotes a particular wall type, and j denotes a particular constraint. LR_k depends on the number of constraint observations, not on the order in which they occur. CLR_{kj} and LR_{k0} are defined in Equations 2 and 3. LR implicitly defines probability such that P can be computed from Equation 4.

$$LR_k = LR_{k0} \prod (CLR_{jk}) \tag{1}$$

$$CLR_{kj} = \frac{P(C_j/W_k)}{P(C_j/\text{non}W_k)} \tag{2}$$

$$LR_{k0} = \frac{P(W_k)}{1 - P(W_k)} \tag{3}$$

$$P = \frac{LR}{(1 + LR)} \tag{4}$$

The likelihood ratio is derived from Bayes' theorem. It provides a rapid means to revise the prior estimate of probability. The advantage of using the likelihood ratios rather than Bayes' theorem is that the prior probability of each constraint $P(C_j)$ does not have to be explicitly known or updated (*17*). The conditional likelihood ratios can be determined in advance regardless of the number of constraints, and they do not depend on $P(W_k)$.

To implement the method, for each wall type k, prior probability $P(W_k)$ and a set of CLR_{kj} must be collected from experts familiar with retaining wall selection. Values of CLR can range from 0.000001 to 1,000,000. Numerical likelihood ratios are described in Table 2. The interpretation of the magnitude of CLR for supporting or refuting the feasibility of a particular wall type is related to the existence of a constraint.

$$CLR \begin{cases} > 1 & \text{degree of support} \\ = 1 & \text{indifferent} \\ < 1 & \text{degree of refutation} \end{cases}$$

TABLE 2 Verbal Description of Numerical Likelihood Ratios

Verbal Description	Likelihood Ratio
completely supports	1000000
extremely supports	10000
very supportive	100
moderately supportive	10
mildly supportive	5
weakly supportive	2
indifferent	1
weakly refutative	0.5
mildly refutative	0.2
moderately refutative	0.1
very refutative	0.01
extremely refutes	0.0001
completely refutes	0.000001

TABLE 3 Sample Prior Probabilities of Gravity Wall Types

k	Wall Type	$P(W_k)$
1	MSE	0.3
2	soil-nailed	0.05
3	modular	0.2
4	generic	0.2
5	mass-concrete-spread	0.15
6	mass-concrete-deep	0.05

To illustrate the approach, Table 3 provides prior probabilities of gravity walls, and Table 4 provides conditional likelihood ratios for the gravity walls. The reader should note that the values of $P(W_k)$ and CLR are for illustrative purposes only. (Actual values are being collected and analyzed.) If the wall functions are landscape and ramp, denoted by subscripts "ls" and "ramp," respectively, then the likelihood ratio of each gravity wall type can be computed from Equations 1 and 3.

$$LR_1 = \frac{P(W_1)}{1 - P(W_1)} CLR_{1,\text{ls}} CLR_{1,\text{ramp}} = \frac{0.3}{1 - 0.3} (1)(10) = 4.28$$

$$LR_2 = \frac{P(W_2)}{1 - P(W_2)} CLR_{2,\text{ls}} CLR_{2,\text{ramp}} = \frac{0.05}{1 - 0.05} (0.1)(0.1) = 0.00$$

$$LR_3 = \frac{P(W_3)}{1 - P(W_3)} CLR_{3,\text{ls}} CLR_{3,\text{ramp}} = \frac{0.2}{1 - 0.2} (25)(0.03) = 0.19$$

$$LR_4 = \frac{P(W_4)}{1 - P(W_4)} CLR_{4,\text{ls}} CLR_{4,\text{ramp}} = \frac{0.2}{1 - 0.2} (25)(0.05) = 0.31$$

$$LR_5 = \frac{P(W_5)}{1 - P(W_5)} CLR_{5,\text{ls}} CLR_{5,\text{ramp}} = \frac{0.15}{1 - 0.15} (1)(20) = 3.53$$

$$LR_6 = \frac{P(W_6)}{1 - P(W_6)} CLR_{6,\text{ls}} CLR_{6,\text{ramp}} = \frac{0.05}{0.05} (0.01)(20) = 0.01$$

From LR_k, the conditional probability of each wall type, given the functional constraints, can be computed from Equation 4. For this example, results indicate that Wall Types 1, 3, 4, and 5 are feasible and should be considered further.

$$P(W_1/C_{\text{ls}}, C_{\text{ramp}}) = \frac{LR_1}{1 + LR_1} = \frac{4.28}{1 + 4.28} = 0.81$$

$$P(W_2/C_{\text{ls}}, C_{\text{ramp}}) = \frac{LR_2}{1 + LR_2} = \frac{0.00}{1 + 0.00} = 0.00$$

$$P(W_3/C_{\text{ls}}, C_{\text{ramp}}) = \frac{LR_3}{1 + LR_3} = \frac{0.19}{1 + 0.19} = 0.16$$

$$P(W_4/C_{\text{ls}}, C_{\text{ramp}}) = \frac{LR_4}{1 + LR_4} = \frac{0.31}{1 + 0.31} = 0.24$$

$$P(W_5/C_{\text{ls}}, C_{\text{ramp}}) = \frac{LR_5}{1 + LR_5} = \frac{3.53}{1 + 3.53} = 0.78$$

$$P(W_6/C_{\text{ls}}, C_{\text{ramp}}) = \frac{LR_6}{1 + LR_6} = \frac{0.01}{1 + 0.01} = 0.01$$

The method just described is computationally simple and works well for constraints that can be measured as booleans.

TABLE 4 Sample Conditional Likelihood Ratios for Gravity Walls

				Construction Time			Bearing Capacity		
k	Wall Type	Landscape	Ramp	Min	Avg	Max	Min	Avg	Max
1	MSE	1	10	1	4	10	1	5	15
2	soil-nailed	0.1	0.1	0.1	0.5	1	1	1	1
3	modular	25	0.03	1	4	6	1	6	9
4	generic	25	0.05	2	4.5	6	1	6.5	12
5	mass-concrete-spread	1	20	0.1	0.4	1	0.4	0.5	1
6	mass-concrete-deep	0.01	20	0.05	0.2	1	1	8	20

If the constraint exists, then the appropriate CLR is included in Equation 1. If the constraint does not exist, then no action is necessary. Thus, with no input about the planned functions of the wall, the method returns the prior probability of each wall type. However, uncertainty about each constraint or knowledge of the user for measuring the importance or severity of each constraint is not included. Furthermore, uncertainty in the values of the conditional likelihood ratios is not included.

To include uncertainty, a severity index, S_j, is input for each constraint. The severity index, which ranges from -1 to 1, applies for all constraints and can be interpreted from Equation 5.

$$S_j = \begin{cases} 1 & \text{constraint } j \text{ is critical in the selection decision} \\ 0 & \text{constraint } j \text{ is typical} \\ -1 & \text{constraint } j \text{ does not exist} \end{cases} \tag{5}$$

Then, effective conditional likelihood, CLR', can be mapped as a piecewise linear function of severity normalized with respect to conditional likelihood. As shown in Figure 2, a separate mapping function is required when CLR supports or refutes. For $CLR \geq 1$, such that the presence of a constraint is supportive for selecting a particular wall type, the mapping function in Equation 6 should be used.

$$CLR' = \begin{cases} CLR_{max} - (CLR_{max} - CLR_{avg})(1 - S) & S \geq 0 \\ CLR_{min} + (CLR_{avg} - CLR_{min})(1 + S) & S \leq 0 \end{cases} \tag{6}$$

For $CLR \leq 1$, such that the presence of a constraint refutes selecting a particular wall type, the mapping function in Equation 7 should be used. In all cases, if $S_j = 0$, then $CLR = 1$ and has no effect on the decision.

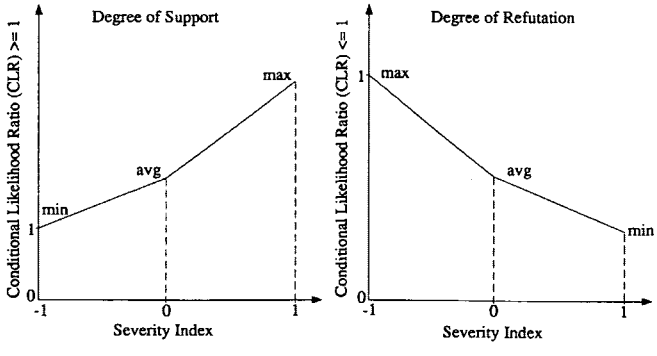

FIGURE 2 Effective conditional likelihood as piecewise linear function of severity index.

$$CLR' = \begin{cases} CLR_{min} + (CLR_{avg} - CLR_{min})(1 - S) & S \geq 0 \\ CLR_{max} - (CLR_{max} - CLR_{avg})(1 + S) & S \leq 0 \end{cases} \tag{7}$$

Then, to account for uncertainty using effective conditional likelihoods, Equation 1 could be rewritten as Equation 8.

$$LR'_k = LR_{0k} \prod (CLR'_{jk}) \tag{8}$$

To illustrate the use of the severity index, consider for construction time, $S_{time} = 0.6$, and for bearing capacity, $S_{bc} = -0.2$. CLR' values for these constraints are computed from Equations 6 or 7, depending on the range of CLR. For example, using the CLR in Table 4, the effective conditional likelihood ratios that indicate support are computed from Equation 6.

$$\begin{aligned} CLR'_{1,time} &= CLR_{max} - (CLR_{max} - CLR_{avg})(1 - S) \\ &= 10 - (10 - 4)(1 - 0.6) = 7.6 \\ CLR'_{3,time} &= CLR_{max} - (CLR_{max} - CLR_{avg})(1 - S) \\ &= 6 - (6 - 4)(1 - 0.6) = 5.2 \\ CLR'_{4,time} &= CLR_{max} - (CLR_{max} - CLR_{avg})(1 - S) \\ &= 6 - (6 - 4.5)(1 - 0.6) = 5.4 \\ CLR'_{1,bc} &= CLR_{min} + (CLR_{avg} - CLR_{min})(1 + S) \\ &= 1 + (5 - 1)(1 - 0.2) = 4.2 \\ CLR'_{3,bc} &= CLR_{min} + (CLR_{avg} - CLR_{min})(1 + S) \\ &= 1 + (6 - 1)(1 - 0.2) = 5.0 \\ CLR'_{4,bc} &= CLR_{min} + (CLR_{avg} - CLR_{min})(1 + S) \\ &= 1 + (6.5 - 1)(1 - 0.2) = 5.4 \end{aligned}$$

The refutative effective conditional likelihood ratios are computed from Equation 7.

$$\begin{aligned} CLR'_{5,time} &= CLR_{min} + (CLR_{avg} - CLR_{min})(1 - S) \\ &= 0.1 + (0.4 - 0.1)(1 - 0.6) = 0.22 \\ CLR'_{5,bc} &= CLR_{max} - (CLR_{max} - CLR_{avg})(1 + S) \\ &= 1 - (1 - 0.5)(1 - 0.2) = 0.60 \end{aligned}$$

TABLE 5 Updated Likelihood Ratio and Conditional Probability of Gravity Walls

k	Wall Type	LR	$P(W_k/C_{ls}, C_{ramp}, C_{time}, C_{bc})$
1	MSE	136.8	0.99
3	modular	4.88	0.83
4	generic	9.11	0.98
5	mass-concrete-spread	0.47	0.32

From Equation 8, CLR' for construction time and bearing capacity are used to update the likelihoods ratios found previously for wall functions of landscape and ramp. The conditional probability of each wall, given the constraints landscape, ramp, time, and bearing capacity, is provided in Table 5. For this example, Wall Types 1, 3, and 4 with high conditional probability would be considered feasible alternatives.

Ranking

After elimination, the set of feasible wall alternatives are rated according to the evaluation factors (sometimes called objectives or criteria) given in the following table:

i	*Evaluation Factor*
1	Constructability
2	Maintenance
3	Schedule
4	Aesthetics
5	Environment
6	Durability
7	Standard design
8	Cost

Using these ratings, a set of noninferior solutions is identified. A noninferior solution is one such that no other feasible solution is better on all objectives (*17*). The noninferior solutions are then scored and ranked according to the same evaluation factors given in the table.

Ranking is an application of a weighting method that transforms the multiobjective problem into a single objective problem. The weighting method starts with sets of ratings and weight values. A weight value (W_i) is assigned to each evaluation factor in the preceding table. A set of rating values (R_{ik}) is generated for each kth alternative. Each R_{ik} indicates how well wall type k satisfies evaluation factor i. A score (S_k) is computed for each kth wall type according to Equation 9.

$$S_k = \sum_{i=1}^{8} R_{ik} W_i \tag{9}$$

The alternative with the highest score is a noninferior solution. Systematic repetition of Equation 9 for different sets of weights defines most of the noninferior solutions. Thus the weights do not have to be given a meaningful interpretation.

The weights can also be interpreted as the relative values of each objective. This interpretation is valid if each unit of achievement of each ith evaluation factor is worth W_i. Then maximizing the weighted sum of the objectives maximizes the total value. In practice, one generally does not know the value of different objectives. It is also unlikely that the weights are constant over the entire range of achievement R_{ik}. At least two methods are used in practice for assigning weights to rank retaining wall alternatives; these methods are described in the CDOT *Bridge Design Manual* (*10*) and in the U.S. Department of Agriculture Forest Service Region 6 *Retaining Wall Design Guide* (*14*) used in Oregon. For both methods, the assignment of weight values is purely empirical.

According to CDOT, the range of values for R_{ik} is given by Equation 10. The summation of the weight values is defined by Equation 11. W_i represents the importance of the ith evaluation factor in the overall project decision. Each W_i is independent of any wall alternative. Another constraint (Equation 12) is that the sum of any two weights must not be greater than 70.

$$1 \leq R_{ik} \leq 5 \tag{10}$$

$$\sum_{i=1}^{8} W_i = 100 \tag{11}$$

$$W_m + W_n \leq 70 \tag{12}$$

The scores S_k are used to rank each feasible wall alternative. The alternative with the highest rank is then designated the "default wall" while the remaining feasible walls are designated "alternative walls." In special cases, such as on difficult soils or deep foundations, the default wall should be adopted for final design and detailed cost estimation. In other cases, the designer may provide full designs for the default wall and an alternative wall if the contractor wishes to bid and build one of the alternatives rather than the default.

Environment

The development tools for the system are CLIPS Version 5.1 (*18*), Microsoft Windows Version 3.1, Borland C++ Version 3.1, and Application Frameworks. A Microsoft Windows application using wall sketches, pull-down menus, sliders, and radio buttons is being prepared as the front-end and output user interfaces. The interface is being developed using Borland C++ and Application Frameworks.

CLIPS is a rule-based expert system development shell that includes an object-oriented language. CLIPS was developed by The National Aeronautics and Space Administration and is distributed through COSMIC at the University of Georgia. The system will run on an IBM-compatible microcomputer. After initial development, the system will be expanded and maintained by CDOT Bridge Branch engineers. Run-time (compiled) copies of the final system may be distributed without licensing restrictions.

CONCLUSION

The CDOT retaining wall selection system is a knowledge-based formulation of the problem-solving strategy described in the CDOT *Bridge Design Manual* (*10*). It is expected that successful implementation of the system will foster a paradigm change on how retaining walls are selected and facilitate implementation of new retaining wall technologies. The system

is being designed and coded such that individual states can customize and enhance it. It is expected that the system will benefit not only CDOT but other state DOTs as well.

ACKNOWLEDGMENTS

Funding for the conceptual design of this system was provided by CDOT. Subsequently, this material is based on work supported by an award from FHWA and the National Science Foundation, Mehmet Tumay, cognizant program director.

REFERENCES

1. R. K. Barrett. *Geofabric Wall Implementation*. Final Report. Colorado Department of Transportation, Grand Junction, Colo., Dec. 1990.
2. R. K. Barrett. Can You Build a Retaining Wall for Less Cost? *Geotechnical Fabrics Report*, Vol. 10, No. 2, March 1992, pp. 14–17.
3. M. Arockiasamy, N. Radhakrishnan, G. Sreenivasan, and S. Lee. KBES Applications to the Selection and Design of Retaining Structures. In *Geotechnical Engineering Congress* (F. G. McLean, D. A. Campbell, and D. W. Harris, eds.), ASCE, June 1991, pp. 391–402.
4. T. M. Adams, P. Christiano, and C. Hendrickson. Some Expert System Applications in Geotechnical Engineering. *Foundation Engineering: Current Principles and Practices* (F. H. Kulhawy, ed.), Vol. 2. ASCE, New York, June 1989, pp. 885–902.
5. T. M. Adams, C. Hendrickson, and P. Christiano. An Expert System Architecture for Retaining Wall Design. In *Transportation Research Record 1187*, TRB, National Research Council, Washington, D.C., 1988, pp. 9–20.
6. T. M. Adams, C. Hendrickson, and P. Christiano. Computer Aided Rehabilitation Design. *Artificial Intelligence for Engineering Design, Analysis and Manufacturing (AI EDAM)*, Vol. 5, No. 2, 1991, pp. 65–75.
7. T. M. Adams, P. Christiano, and C. Hendrickson. A Knowledge Base for Retaining Wall Rehabilitation Design. In *Design and Performance of Earth Retaining Structures* (P. C. Lambe and L. A. Hansen, eds.), ASCE, New York, 1990, pp. 125–138.
8. A. R. Ciarico, T. M. Adams, and C. Hendrickson. A Cost Estimating Module to Aid Integrated Knowledge-Based Preliminary Design. In *Computing in Civil Engineering: Computers in Engineering Practice* (T. O. Barnwell, Jr., ed.), ASCE, New York, Sept. 1989, pp. 52–59.
9. A. Newell. The Knowledge Level. *Artificial Intelligence*, Vol. 18, 1982, pp. 87–127.
10. *Bridge Design Manual*. Staff Bridge Branch, Colorado Department of Transportation, Denver, Oct. 1991.
11. R. S. Cheney. Selection of Retaining Structures: The Owner's Perspective. In *Design and Performance of Earth Retaining Structures* (P. C. Lambe and L. A. Hansen, eds.), ASCE, June 1990, pp. 52–66.
12. A. R. Schnore. Selecting Retaining Wall Type and Specifying Proprietary Retaining Walls in NYSDOT Practice. In *Design and Performance of Earth Retaining Structures* (P. C. Lambe and L. A. Hansen, eds.), ASCE, June 1990, pp. 119–124.
13. G. A. Munfakh. Innovative Earth Retaining Structures: Selection, Design and Performance. In *Design and Performance of Earth Retaining Structures* (P. C. Lambe and L. A. Hansen, eds.), ASCE, New York, June 1990, pp. 85–118.
14. D. D. Driscoll. *Retaining Wall Design Guide*. Forest Service Region 6, U.S. Department of Agriculture, Portland, Oreg., 1979.
15. R. O. Duda, P. E. Hart, and N. J. Nilsson. Subjective Bayesian Methods for Rule-Based Inference Systems. *Proc., AFIPS 1976 National Computer Conference*, 1976, pp. 1075–1082.
16. R. Duda, J. Gaschnig, and P. Hart. *Expert Systems in the Microelectronic Age*. Edinburgh University Press, Scotland, 1979, pp. 153–167.
17. R. de Neufville. *Applied Systems Analysis*. McGraw-Hill Publishing Co., New York, 1990.
18. J. C. Giarratano. *CLIPS User's Guide, Version 5.1*, Vol. 1. COSMIC, University of Georgia, Athens, Sept. 1991.

Publication of this paper sponsored by Committee on Applications of Emerging Technology.

Expert System for Drilled Shaft Construction

EMMANUEL L. ABAYA, MICHAEL W. O'NEILL, AND DEBORAH J. FISHER

Decisions on how best to install drilled shafts consist of reviewing data gathered in site investigations and estimating how they affect constructability. Decision criteria tend to be predicated on the knowledge of local conditions to which evaluators are accustomed. Neglecting to take into account the effect of any one condition, or combination of conditions, may adversely impact construction operations. A modular, computer-based system that uses several expert system programs is described. The system sorts through relevant data and proposes what methods of constructing drilled shafts can best be implemented. The system also makes suggestions about operations and develops preliminary cost estimates.

Drilled shaft construction methods are not normally forecast by detailed analysis of geotechnical data, and the final selection of construction methods and details are (and should be) left to the experience of the expert drilling contractor (*1*). This premise must be the guiding principle of constructability analyses made during the early planning and design stages of any engineering endeavor (*2*). Foundation designers need to forecast general construction methods to estimate costs and develop appropriate construction specifications. One tool that can help determine a successful, low-cost construction method uses "expert systems" that promote interaction with geotechnical experts and contractors. In an expert system, the experience of one or more experts is captured in a knowledge base that can readily be accessed and referred to in order to assist, not replace, the human decision-making process.

Emphasis has been placed on the development of "shells" or general programs to accommodate the logic in expert systems (*3*,*4*). In a literature survey, only a few expert systems on driven piling (*5*,*6*) and only a single discussion of expert system interrelationships for drilled shafts (*7*) can be found.

WHY AN EXPERT SYSTEM?

As the branch of artificial intelligence that has gained widespread acceptance in recent years (*3*), expert systems are particularly well suited for diagnostic problem-solving tasks. Both subjective and factual information are stored and "preserved" in the expert system's knowledge base. Because expert systems are supported by personal computers, they enhance productivity by providing access to information that is consistent, portable, and readily available. In addition, these programs are interactive and user-friendly, serving as an excellent tool for training novices. More specifically, an expert system for drilled shaft construction will anticipate problems by alerting users to geotechnical information that may be overlooked, inconsistent, or incomplete. Output includes constructability recommendations, appropriate inspection procedures, and relevant specifications.

E. L. Abaya, Bechtel Corporation, 3000 Post Oak Boulevard, Houston, Tex. 77252. M. W. O'Neill, Department of Civil and Environmental Engineering, University of Houston, Houston, Tex. 77204. D. J. Fisher, Department of Industrial Engineering, University of Houston, Houston, Tex. 77204.

DECISION SUPPORT MODEL FOR DRILLED SHAFTS

The decision support model contains three steps, each with a specific objective (Figure 1). The systems used in these steps have been collectively named DS^2, for Decision Support for Drilled Shafts. Each DS^2 module can be bridged to external programs, resulting in a combined effort that is not only simple and informative but also powerful. DS^2 was developed using EXSYS Professional, a commercially available, rule-based expert system shell widely used in industry today. From a survey of 37 state-of-the-art expert systems designed for civil engineering end users, EXSYS ranked as the second most popular commercial shell. The rule editor in the shell facilitates the building of heuristic rules in the if-then format. EXSYS permits both forward chaining and backward chaining search strategies to arrive at conclusions. Uncertainty is associated with each rule such that each conclusion is reached with a certain degree of confidence (*8*,*9*). Knowledge sources for DS^2 included more than 50 hr of interviews with two academicians, one consultant, seven drilled shaft contractors, three design firms, and three equipment manufacturers, among others. In addition, knowledge was obtained from videotaping more than 100 hr of job site operations in the Midwest and Southwest (*8*). DS^2 is available on request for a nominal amount, and information regarding hardware platform requirements may be obtained from the authors.

DS^2 MODULES

Virtually all drilled shaft construction practices in the United States can be placed in three categories: the dry method, the wet method, and the casing method (*2*). The first module, DS^2-GEO, recommends to the end user what construction method is most suited to a given job site. The recommendations are provided with degrees of certainty, using integers from 0 to 10. These represent the confidence with which DS^2-GEO arrives at each conclusion. Degree of certainty values represent the expert's opinion on which method has the great-

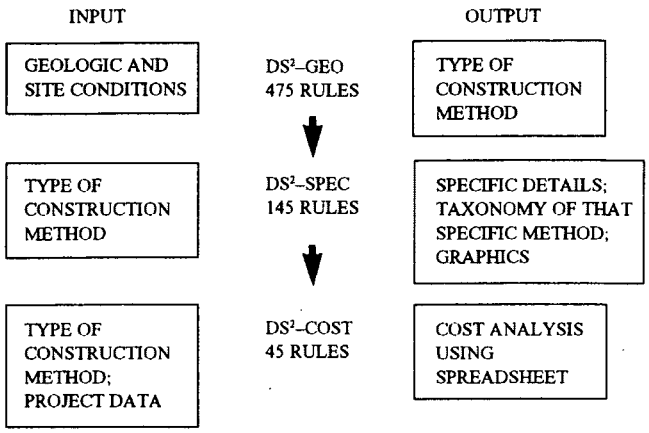

FIGURE 1 DS² decision support model (three separate models).

est likelihood of being used, rather than probability of successful implementation. A high confidence value indicates a high likelihood that the expert believes one particular method will be required, because of the unlikely success of a less expensive method. The primary bases for these recommendations are geologic and site-specific conditions, such as sand content, water table elevation, soil permeability and strength, rock joint characteristics, and job site restrictions. DS²-GEO can analyze uniform layers and geomaterial profiles with two separate primary layers (Figure 2). Graphic support is also provided to improve communication between the end user and DS²-GEO. The knowledge base can be easily modified or expanded to include additional rules developed later that will take into account more complex profiles. There are now 475 heuristic rules, each representing a possible combination of soil and site factors, that enable DS²-GEO to make recommendations. One of hundreds of possible paths in DS²-GEO is illustrated in Figure 3, in which recommendations are developed for the general construction method for a drilled shaft in a clay profile. As can be observed, the questions are posed in such a way that requires the user to either consult with a geotechnical engineer or have at hand a geotechnical report with thorough documentation of site conditions.

After using DS²-GEO, the end user can proceed to DS²-CON, which provides details and specifications that are automatically linked to the construction method in DS²-GEO. DS²-CON's knowledge base consists of information on the three operations in drilled shaft construction: excavation, setting of steel reinforcement, and concrete placement. When investigating excavation procedures, DS²-CON provides the end user with information such as specifications and tolerances for shaft dimensions, inspection procedures, type of concrete and drilling fluids that may be used, safety precautions, and maintenance of borehole quality, among others. DS²-CON also provides relevant information on the installation of steel reinforcing (i.e., precautions for using a partial- or full-length cage, auxiliary devices to support handling and installation) and concreting (i.e., mix requirements, tremie/pump operations). By providing pertinent information at each phase of the construction procedure, simple and clear guidelines can be developed for each field operation to ensure the safety of all personnel on site. There are 145 rules in DS²-CON, all of which can be easily updated or modified.

The third module, DS²-COST, estimates the total cost of the particular construction method chosen in DS²-GEO by itemizing expenditures that are associated with a specific

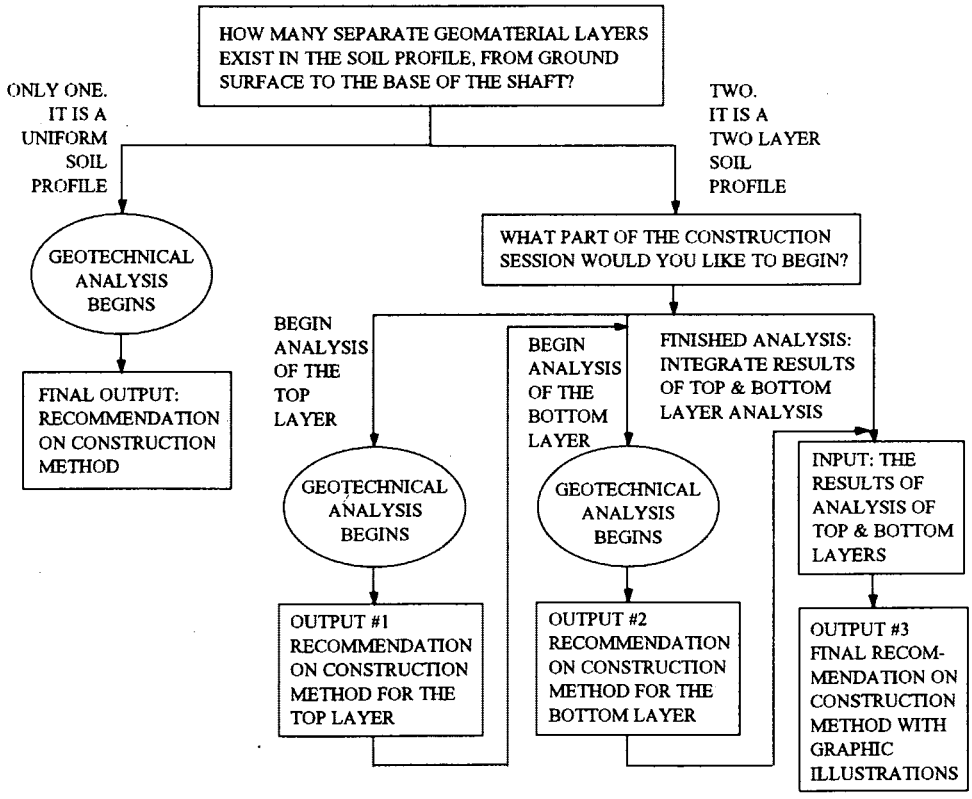

FIGURE 2 DS²-GEO module: analysis of uniform and two-layer profiles.

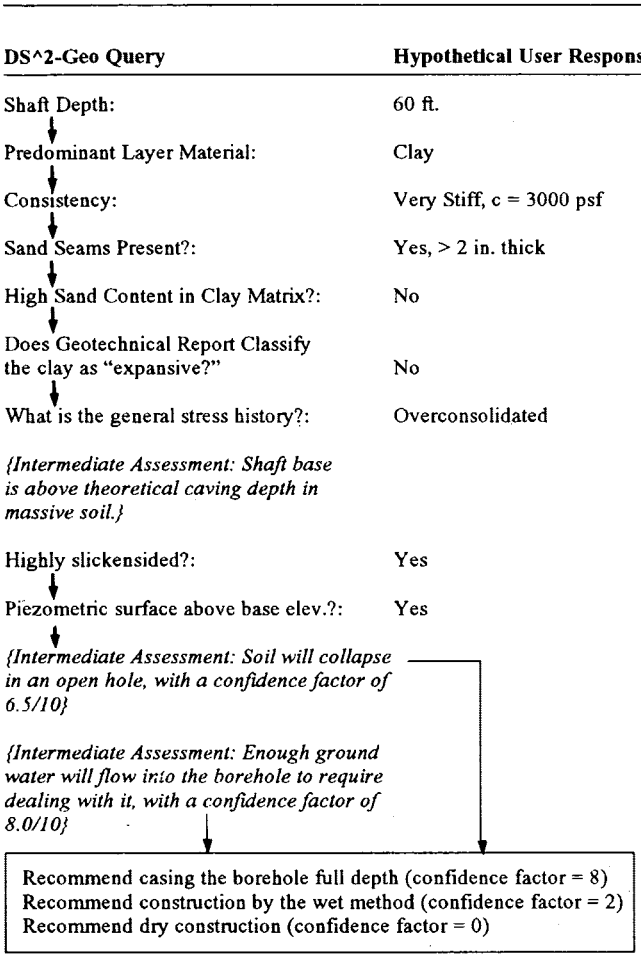

FIGURE 3 Example path for arriving at recommendations for construction method in DS²-GEO for a simple, single-soil profile.

method. Cost items are categorized into excavation costs, concreting costs, and steel placement costs. Each is further subdivided into labor wages, equipment, and miscellaneous costs. DS²-COST can interface with a spreadsheet data base containing union labor wage rates for 20 U.S. cities (*10*, p. 108) should the end user decide not to use his or her own wage rates. Unit costs for concrete and steel can be derived in the same manner. Historical cost data bases may also be accessed from this module, with comparison capabilities from presolicited criteria, such as shaft diameter, number of holes, and total linear feet. Thirty-two cases are stored in this data base.

VALIDATION AND CONCLUSIONS

An 85 percent similarity agreement was obtained for DS²-GEO recommendations and 13 published construction case studies. Further validation of 23 random cases analyzed by DS²-GEO, against recommendations provided by three consultants and four contractors resulted in a 70 percent similarity rating. Although much of the knowledge used to develop DS² was obtained in Texas and neighboring Southwestern states, the geographic locations of the 13 case studies and the areas of expertise of the three consultants represent regions throughout the United States. The various DS² modules are revolutionary not only because of the knowledge they can store and the interactive manner in which this knowledge can be retrieved, but because they provide an automated medium through which general technical consensus can be acknowledged and differences examined and reviewed. In effect, this ensures improved communication among designers, contractors, and geotechnical and field personnel.

ACKNOWLEDGMENTS

The authors thank the Texas Higher Education Coordinating Board's Advanced Technology Program for financially supporting this research. For their technical assistance, the authors thank J. D. Abrams, Jr. (J. D. Abrams, Inc.), August H. Beck III (A. H. Beck Foundation Co.), Glyen Farmer (Coastal Foundation Co.), Jene Hayes (Hayes Drilling, Inc.), J. Nakayama (Tone Boring Co., Ltd.), H. Paul Wilson (Russo Corporation), Joe G. Wilkins (Bell Bottom Foundation Co.), Lymon C. Reese, Clyde N. Baker, Jr., Jim Lewis, S. Scot Litke, and member-contractors of ADSC. The authors also thank the International Association of Foundation Drilling for providing access to construction projects around the United States. In addition, the technical support provided by Bechtel Corporation is gratefully acknowledged.

REFERENCES

1. L. C. Reese and M. W. O'Neill. *Drilled Shafts: Construction Procedures and Design Methods*. Publication FHWA-HI-88-042. FHWA, U.S. Department of Transportation, July 1988.
2. J. P. Turner, Constructability for Drilled Shafts. *Journal of Construction Engineering and Management*, ASCE, Vol. 118, No. 1, March 1992, pp. 77–93.
3. G. C. Phillip and H. K. Schultz. What's Happening With Expert Systems? *AI Expert*, Nov. 1990, pp. 57–59.
4. S. Mohan. Expert Systems Applications in Construction Management and Engineering. *Journal of Construction Engineering and Management*, ASCE, Vol. 116, No. 1, March 1990, pp. 87–89.
5. D. J. Elton and D. A. Brown. Expert System for Driven Pile Selection. *Proc., Geotechnical Congress 1991* ASCE, (F. G. McLean et al., eds.), Vol. 1, June 1991, pp. 253–263.
6. C. H. Juang and M. L. Ulshafer. Development of an Expert System for Preliminary Selection of Pile Foundation. In *Transportation Research Record 1277*, TRB, National Research Council, Washington, D.C., 1990, pp. 153–160.
7. L. C. Reese and A. Haiun. General Report: Les Techniques et Leurs Evolutions. *Proc., International Colloquium on Deep Foundations*, Presses d'École Nationale des Ponts et Chaussées, Paris, France, March 1991.
8. E. L. Abaya. *Development of an Expert System for the Construction of Drilled Shaft Foundations*. Master's thesis. Department of Civil and Environmental Engineering, University of Houston, Tex., May 1991.
9. *EXSYS Professional Advanced Expert System Development Software (User's Manual)*. EXSYS INC., Albuquerque, N.M., 1988.
10. ENR Wage Rates. *Engineering News-Record*, Aug. 30, 1990.

Publication of this paper sponsored by Committee on Foundations of Bridges and Other Structures.

Interference Effects Between Two Surface Footings on Layered Soil

BRAJA M. DAS, VIJAY K. PURI, AND BOON K. NEO

On many occasions, shallow footings are constructed too close to each other. For such conditions, the ultimate bearing capacity of the footings may be affected due to the interference of the failure surfaces in the soil below the footings. Laboratory model test results for the ultimate bearing capacity of two closely spaced surface strip footings supported by a layer of dense sand of limited thickness, underlain by a soft clay layer extending to a great depth, have been presented. The ultimate bearing capacities for a single and two closely spaced footings increase with the increase of the thickness (H) of the dense sand layer up to a maximum at $H = H_{cr}$ and remain constant thereafter. H_{cr} is the depth of the sand layer at which the failure surfaces in the soil below the footings are fully confined to the top dense sand layer. For $H < H_{cr}$, the group efficiency of the footings increases with the increase of their center-to-center spacing (S), reaching about 100 percent at $S/B \approx 4$ to 5. However, for $H > H_{cr}$, the group efficiency decreases with the increase of S/B and reaches 100 percent at $S/B \approx 4$ to 5.

The ultimate bearing capacity of shallow footings located too close to each other is different from that obtained for isolated footings primarily because, at ultimate load, the failure surfaces below the footings overlap. Das and Larbi-Cherif (*1*) conducted several laboratory model tests to determine the variation of the ultimate bearing capacity of two closely spaced strip footings located on loose angular sand extending to a great depth. The loose sand used in those tests had a relative density of about 54 percent. The experimental results of Das and Larbi-Cherif (*1*) were compared with the theory of Stuart (*2*). According to Stuart's theory, the ultimate bearing capacity of a rough strip footing closely spaced to another rough strip footing supported by a layer of sand [Figure 1 (*top*)] can be expressed as

$$q'_u = qN_q\xi_q + \frac{1}{2}\gamma_{sand}BN_\gamma\xi_\gamma \quad (1)$$

where

q'_u = ultimate bearing capacity of two closely spaced footings,
$q = \gamma D_f$,
γ_{sand} = unit weight of sand,
D_f = depth of footings (assuming both footings have same embedment depth),
B = footing width,
N_q, N_γ = Terzaghi's bearing capacity factors, and
ξ_q, ξ_γ = interference factors.

B. M. Das, Academic Affairs, Southern Illinois University, Carbondale, Ill. 62901. V. K. Puri and B. K. Neo, Department of Civil Engineering and Mechanics, Southern Illinois University, Carbondale, Ill. 62901.

The variations of the interference factors for two rough strip footings with S/B (where S is the center-to-center spacing of the footings) determined theoretically by Stuart (*2*) are shown in Figure 1 (*bottom*).

According to Terzaghi (*3*), the ultimate bearing capacity for an isolated footing supported by a sand layer can be given as

$$q_u = qN_q + \frac{1}{2}\gamma_{sand}BN_\gamma \quad (2)$$

Thus, the efficiency (η) of two closely spaced strip footings supported by a layer of sand extending to a great depth is

$$\eta = \frac{q'_u}{q_u} \quad (3)$$

For surface footing condition ($D_f = 0$):

$$\eta = \frac{q'_u}{q_u} = \xi_\gamma \quad (4)$$

where η equals efficiency with respect to ultimate bearing capacity.

In many instances footings are constructed on layered soils. Theoretical developments relating to the ultimate and allowable bearing capacities of a shallow footing on layered soil are limited (*4–6*). On some occasions the bearing capacity of shallow footings can be considerably improved by densifying a thin sand layer immediate below the footing underlain by a weak saturated clay layer extending to a great depth (Figure 2). The ultimate bearing capacity of an isolated footing constructed over a dense sand layer can be estimated by using the theory of Meyerhof and Hanna (*6*).

A review of existing literature shows that no theoretical or experimental studies are now available to determine the interference effects of two shallow footings supported by a layered soil and placed very close to each other.

This paper presents some experimental laboratory model test results for the variation of the ultimate bearing capacity of two closely spaced rough strip surface footings supported by a dense sand layer underlain by a very soft clay layer extending to a great depth (Figure 3).

ULTIMATE BEARING CAPACITY OF ISOLATED FOOTING ON LAYERED SOIL

According to Meyerhof and Hanna (*6*) and referring to the left-hand side of Figure 2, if the ratio H/B (H = thickness of

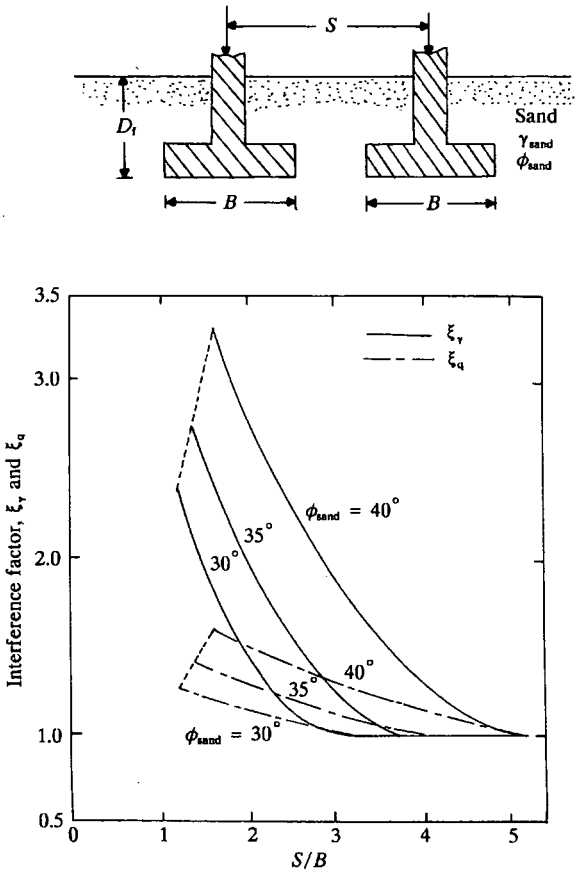

FIGURE 1 Two closely spaced rough shallow strip footings supported by sand, *top*; variation of ξ_γ and ξ_q with *S/B* for two rough shallow strip footings (*2*), *bottom*.

dense sand layer) is relatively small, then the failure surface in soil at ultimate load will extend into the soft clay layer. For a continuous isolated footing the ultimate bearing capacity q_u may be expressed as

$$q_u = c_u N_c + \gamma_{sand} H^2 \left(1 + \frac{2D_f}{H}\right) K_s \frac{\tan \phi_{sand}}{B} + \gamma_{sand} D_f \qquad (5)$$

where

c_u = undrained cohesion of lower clay layer,
N_c = bearing capacity factor (5.14 for $\phi_{clay} = 0$),
γ_{sand} = unit weight of top sand layer,
H = depth of top sand layer,
K_s = punching shear resistance coefficient, and
ϕ_{sand} = friction angle of top sand layer.

However, if the ratio H/B is large—that is, when $H/B \geq H_{cr}/B$ (H_{cr} = critical depth of the dense sand layer) as shown on the right-hand side of Figure 2, the failure surface in soil is entirely limited to the top dense sand layer. The ultimate bearing capacity q_u of a rough strip footing for this case can be expressed by Equation 2, or

$$q_u = \frac{1}{2} \gamma_{sand} B N_\gamma + \gamma_{sand} D_f N_q$$

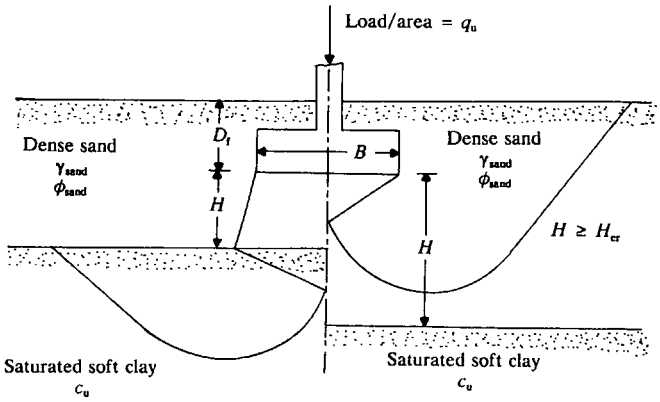

FIGURE 2 Shallow strip footing supported by dense sand layer underlain by saturated soft clay.

where N_γ and N_q are bearing capacity factors corresponding to the friction angle ϕ_{sand}.

For a given H/B, the actual ultimate bearing capacity is the lower of the two values calculated from Equations 2 and 5. The variation of K_s with the soil friction angle ϕ_{sand} is shown in Figure 4. Thus, for surface footings, the ultimate bearing capacity is

$$q_u = c_u N_c + \gamma_{sand} H^2 K_s \frac{\tan \phi_{sand}}{B} \leq \frac{1}{2} \gamma_{sand} B N_\gamma \qquad (6)$$

ULTIMATE BEARING CAPACITY OF TWO CLOSELY SPACED SURFACE STRIP FOOTINGS ON LAYERED SOIL

If two closely spaced surface strip footings are located on a dense sand layer (Figure 3) and H/B is less than H_{cr}/B, then the failure surface will be located in the dense sand and the soft clay layers with an ultimate bearing capacity equal to

$$q''_u = f(\gamma_{sand}, H, B, \phi_{sand}, c_u, S) \qquad (7)$$

For $H/B \geq H_{cr}/B$, the failure surface at ultimate load will be entirely located in the dense sand layer. For this case

$$q'_u = f(\gamma_{sand}, B, \phi_{sand}, S) \qquad (8)$$

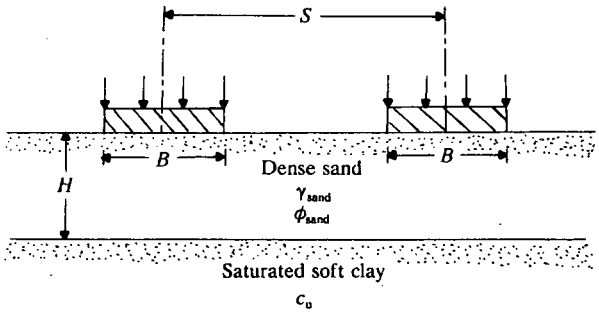

FIGURE 3 Two closely spaced rough strip surface footings on dense sand underlain by saturated soft clay.

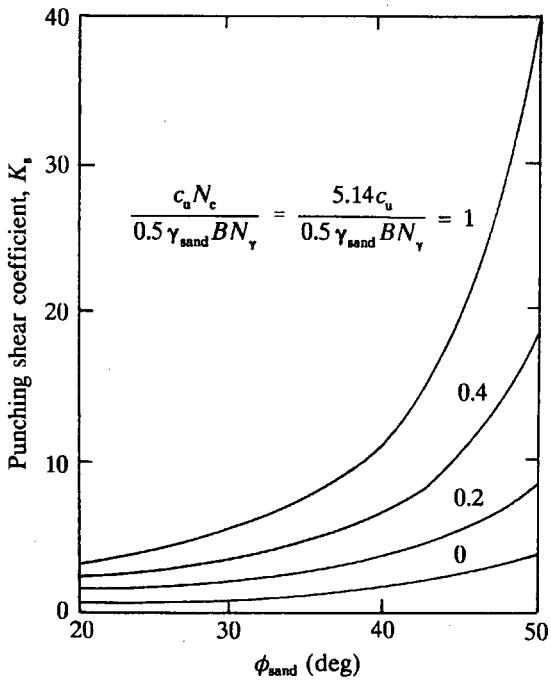

FIGURE 4 Variation of Meyerhof and Hanna's K_s with ϕ_{sand}.

The efficiency for bearing capacity of the surface footings can then be given as

$$\eta' = \frac{q_u''}{q_u} = \frac{q_u''}{c_u N_c + \gamma_{sand} H^2 K_s \left(\frac{\tan \phi_{sand}}{B}\right)}$$

$$\text{for } \frac{H}{B} < \frac{H_{cr}}{B};\ D_f = 0 \qquad (9)$$

and

$$\eta = \frac{q_u'}{q_u'} = \frac{q_u'}{\frac{1}{2}\gamma_{sand} B N_\gamma} = \xi_\gamma$$

$$\text{for } \frac{H}{B} \geq \frac{H_{cr}}{B};\ D_f = 0 \qquad (10)$$

LABORATORY MODEL TESTS

Laboratory model tests were conducted in a box measuring 1.22 × 0.305 × 0.915 m (length × width × height). The sides of the box were heavily braced with angle sections. The model footings used in this investigation were 304.8 mm long, 101.6 mm wide, and 25.4 mm thick and were made of wood. They had the same length as the inside width of the test box to ensure plane-strain conditions. The rough-base condition of the footings was achieved by cementing a thin layer of sand to their bases with epoxy glue. To minimize friction during model tests, the sides of the test box and the edges of the model footings were made as smooth as possible. Also, the edges of the model footings were coated with a thin layer of petroleum jelly. Two rectangular steel plates, 6.35 mm thick, having the same plan dimensions as the model footings, were attached to the top of the footings to load the footings.

The grain-size distribution of the sand used for this investigation is shown in Figure 5. The effective size, uniformity coefficient, and coefficient of gradation of this sand were 0.3 mm, 1.62, and 1.1, respectively. The properties of the clay soil used are as follows:

Property	*Percentage*
Passing No. 200 U.S. sieve (0.075-mm opening)	55
Liquid limit	41
Plastic limit	21

According to the unified soil classification system, it can be classified as silty clay (CL) with intermediate plasticity. The sequence of the model tests followed for this study is provided in Table 1.

In conducting tests for Series A and C, sand was placed in the test box in 25.4-mm-thick layers by means of raining from a height of 152.4 mm. For Series B the clay soil was broken into small lumps and blended with the required moisture content, which was about 39 percent, in a large mixing pan. The 39 percent moisture content was slightly below the liquid limit. This produced a soft, moist clay. However, during handling and compaction, about 1 percent moisture was lost. The moist clay was cured for about 1 week and placed in the test box in 25.4-mm-thick layers and compacted by a flat-bottomed hammer. The flat-bottomed hammer weighed 6 lb and measured 152 × 101 mm in plan. The clay was compacted in sections with 20 hammer blows per section.

For Series D and E, the procedure for clayey soil placement was the same as that for Series B. After compaction, the top of the clay layer was coated with a thin layer of petroleum jelly to prevent moisture migration into the overlying dry sand. This was followed by placing a sand layer in the same

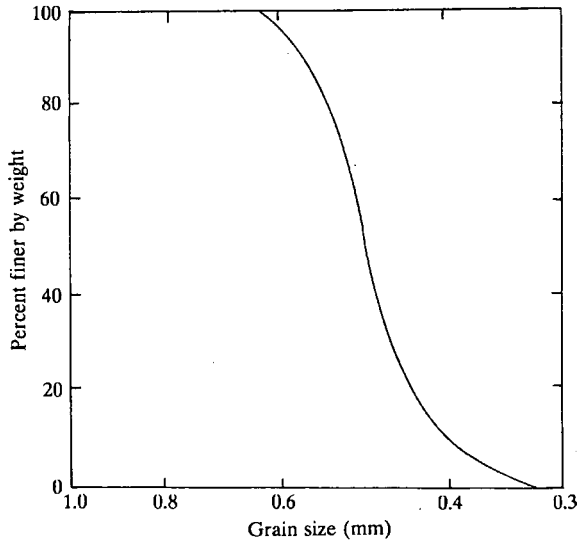

FIGURE 5 Grain-size distribution of sand used for model tests.

TABLE 1 Sequence of Model Tests

Test series	Type of soil layering	*S/B*	*H/B*
A	Sand only	∞ (single footing)	∞
B	Clay only	∞ (single footing)	0
C	Sand only	1.5, 2, 2.5, 3, 3.5, 4	∞
D	Sand over clay	∞ (single footing)	1, 1.5, 2, 2.5, 3, 4, 4.5
E	Sand over clay	1.5, 2, 3, 4	1, 1.5, 2, 2.5, 3, 4, 4.5

manner as described for Series A and C. The average values of the unit weight and the shear strength parameters of the sand and clay soil for the model test conditions were as follows:

- Sand
  - –Dry unit weight: $\gamma_{sand} = 17.29$ kN/m^3
  - –Relative density ≈ 79 percent
  - –Friction angle (from direct shear tests): $\phi_{sand} = 39.8$ degrees
- Clay
  - –Moist unit weight: $\gamma_{clay} = 18.69$ kN/m^3
  - –Moisture content ≈ 38 percent
  - –Degree of saturation ≈ 97 percent
  - –Undrained cohesion: c_u (from UU triaxial tests) = 5.51 kN/m^2

For performing the tests, the model footing was placed on the top of the soil layer. Footing loads were applied by a reaction frame and measured by a proving ring. The corresponding settlement of the footings was obtained from dial gauges placed on them.

MODEL TEST RESULTS

Series A and B

Series A and B are related to bearing capacity tests with isolated model footings on homogeneous sand and clay soil, respectively. Figure 6 shows the load per unit area q versus settlement s obtained from those tests along with the ultimate bearing capacity as defined by Vesic (*7*), according to which the ultimate bearing capacity is the peak value of q, or the magnitude of q at which the q-versus-s plot becomes practically linear and $\Delta s/\Delta q$ is maximum. For tests in sand (Series A), the magnitude of the ultimate bearing capacity q_u is 91.04 kN/m^2. For surface footings (that is, $D_f = 0$), the experimental bearing capacity factor N_γ can be calculated as $q_u/[(1/2)\gamma_{sand}B] = 103.65$. This compares reasonably well with the theoretical value of $N_\gamma \approx 108$ (*7*). For tests in clay, the experimental value of q_u is about 29 kN/m^2. Thus, the experimental value of the bearing capacity factor N_c is equal to $q_u/c_u = 5.26$, which is in good agreement with the theoretical value of $N_c = 5.14$.

Series C

Test Series C examined the interference effect of two model footings resting on homogeneous sand. The variation of the ultimate bearing capacity with *S/B* obtained from this test series is shown in Figure 7 (*top*). On the basis of the definition of bearing capacity efficiency (Equation 4), the experimental variation of η with *S/B* is shown in Figure 7 (*bottom*). For comparison purposes, the theoretical variation of $\eta = \xi_\gamma$ for surface footings as determined by Stuart (*2*) is also plotted in Figure 7 (*bottom*). As expected, although the general trend is similar, there is a wide difference in the magnitude of η for any given value of *S/B*, particularly for $S/B < 3$. Similar observations were made by Das and Larbi-Cherif (*1*). The wide difference between the theoretical and experimental values cannot be fully explained yet. However, Vesic (*8*) observed that η is a function of ϕ_{sand} and also the compressibility of sand. A better theoretical explanation needs to be developed.

Series D

Test Series D determined the ultimate bearing capacity of an isolated strip footing supported by a layer of dense sand underlain by a soft clay. The variation of q_u with *H/B* as deter-

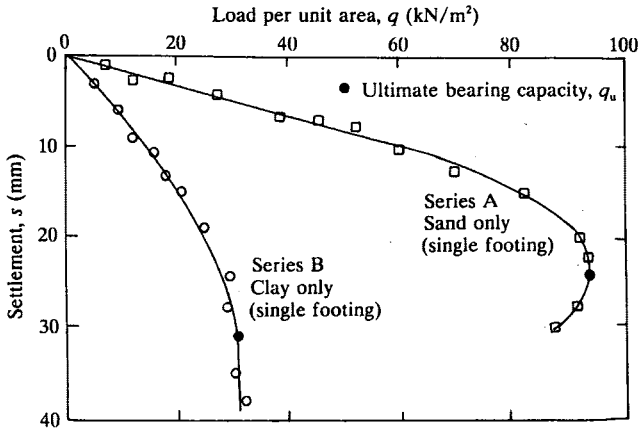

FIGURE 6 Variation of load per unit area versus settlement, Series A and B.

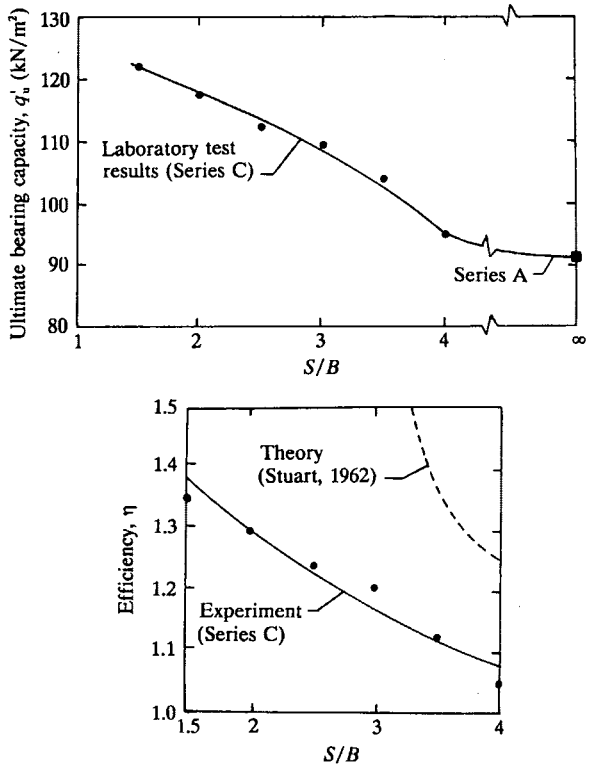

FIGURE 7 Variation of ultimate bearing capacity q'_u with *S/B*, *top*; variation of bearing capacity efficiency with *S/B*, *bottom*—Series C (sand only, two footings).

mined experimentally is shown in Figure 8. For completeness, the experimental ultimate bearing capacities determined from Test Series A (that is, $H/B = \infty$) and Test Series B (that is, $H/B = 0$) are also plotted in this figure. For surface footing conditions, the theoretical expression given by Meyerhof and Hanna (*6*) for q_u is also shown in Figure 8.

Using the experimental values of $c_u = 5.51$ kN/m² and $\gamma_{sand} = 17.29$ kN/m³ and the theoretical values of N_c (for $\phi_{clay} =$ 0 degrees) and N_γ for $\phi_{sand} = 39.8$ degrees as given by Vesic (*7*), the ratio of $c_u N_c / 0.5\gamma_{sand} N_\gamma$ can be calculated. For the calculated value of $c_u N_c / 0.5\gamma_{sand} N_\gamma$, Figure 4 provides the theoretical value of the punching shear coefficient K_s. This value of K_s was used in Equation 6 to estimate the theoretical variation of q_u with H/B as shown in Figure 8. A comparison between the experimental and theoretical curves in Figure 8 shows the following:

1. The magnitude of q_u increases with H/B up to a maximum at H_{cr}/B and remains constant thereafter.
2. The magnitude of H_{cr}/B for the present tests is about 4. This means that at $H/B \approx 4$, the failure surface at ultimate load is entirely located in the top dense sand layer.
3. Between $H/B = 1$ and $H/B = H_{cr}/B \approx 4$, the experimental values of q_u are somewhat higher than those obtained theoretically. The difference may be due to the conservative theoretical value of passive pressure distribution assumed along the failure surface in the top sand layer.

Series E

The variation of the experimental ultimate bearing capacity q''_u (and q'_u) for two closely spaced surface footings on layered soil for various H/B and S/B ratios is shown in Figure 9. From this figure it can be seen that for a given value of S/B, the variation of q''_u versus H/B is similar in nature to that shown in Figure 8, which is for the case of a single footing supported by layered soil. It is also important to note that, for each curve shown in Figure 9, the critical value of $H = H_{cr}$ is approximately equal to $4B$, which is the same as that observed for the case of a single footing (Figure 8).

By using the experimental values of q''_u and q'_u from Figure 8, the variation of the experimental bearing capacity efficiencies $\eta' = q''_u/q_u$ and $\eta = q'_u/q'_u$ for various combinations of H/B and S/B have been calculated and are shown in Figure 10. Also shown in this figure are the values of η for various S/B

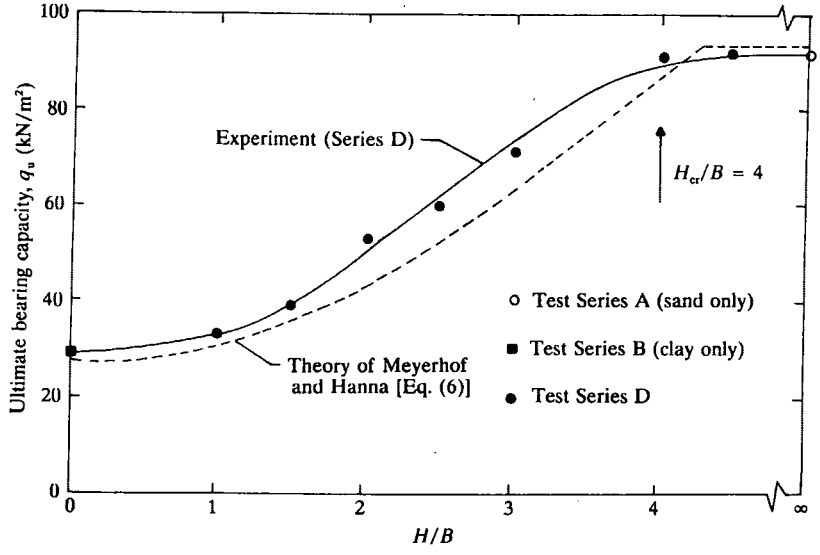

FIGURE 8 Variation of q_u with H/B, Series D (dense sand over soft clay).

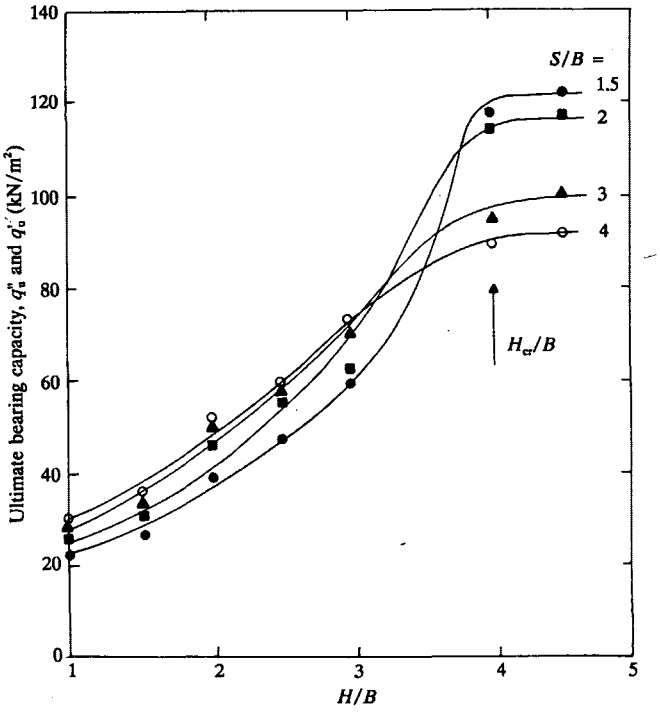

FIGURE 9 Variation of ultimate bearing capacities q_u'' and q' with H/B, Series E (sand over clay, two surface footings).

values obtained from Series C (Figure 7). From this, the following observations can be made:

1. For a given value of H/B ($<H_{cr}/B = 4$), the magnitude of η' increases with the increase of S/B and tends to reach a value of about 100 percent at $S/B \approx 4$ to 5.
2. For a given value of S/B, the bearing capacity efficiency generally decreases with the decrease of H/B (for $H/B < H_{cr}/B$).
3. When $H/B \geq H_{cr}/B$, the nature of the efficiency versus S/B plot changes. The bearing capacity efficiency decreases with the increase of S/B and reaches about 100 percent at $S/B \approx 4$ to 5. The magnitude of η for a given S/B is practically the same irrespective of the value of H/B. This implies that at $H/B \geq H_{cr}/B$, the failure surface in soil is fully located in the sand layer, and the underlying clay layer has no effect on the efficiency of the ultimate bearing capacity.

LIMITATIONS AND COMMENTS ON MODEL TEST PROCEDURE AND RESULTS

The experimental results presented in this paper, which are currently unavailable elsewhere, are instructive. However, there are several shortcomings and limitations:

1. The procedure for preparation of the clay layer in the model test box will induce an overconsolidation ratio greater than one and, thus, anisotropy. Available theoretical studies for the ultimate bearing capacity of a single footing supported by a dense sand layer underlain by a soft clay have been developed on the assumption that the sand and clay layers are isotropic with respect to the strength. Hence, some deviations between the theoretical and experimental results can be expected.

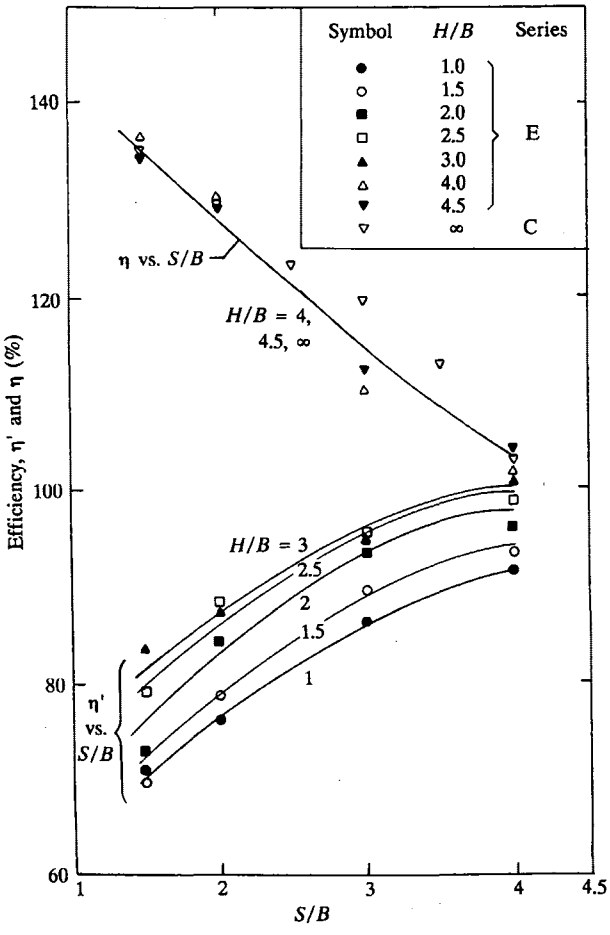

FIGURE 10 Variation of bearing capacity efficiency for various S/B and H/B values, Series C and E.

2. The present study relates to the ultimate bearing capacity of only two closely spaced footings. However, in many practical problems, closely spaced footings on both sides of a given footing can be encountered. The results of this study cannot be directly applied to those cases.
3. Questions may be raised as to the influence of the very thin layer of petroleum jelly, which was applied on the moist clay layer to avoid moisture migration to the top dense sand layer. The authors believe that the petroleum jelly would provide a potential plane of weakness only if a weaker soil layer is underlain by a stronger soil, which was not the case in this test program.
4. Results of small-scale laboratory bearing capacity tests of the type reported in this study generally suffer from scale effects. This is more pronounced in sand than in clay. DeBeer (*9*) evaluated the effect of footing size (B) on bearing capacity of single surface footings in sand. This was also reported by Vesic (*7*). According to this study, the ultimate bearing capacity decreases with the increase of $\gamma_{sand}B$ and reaches an approximate constant value at $\gamma_{sand}B \approx 0.03$ kg/cm². For this study, the value of $\gamma_{sand}B \approx 0.018$ kg/cm². Between the range of $\gamma_{sand}B = 0.018$ kg/cm² to 0.03 kg/cm², DeBeer's (*9*) study shows that the ultimate bearing capacity can decrease up to

25 percent, with an average of about 15 percent. The interference effect of two footings in this study has been expressed in terms of group efficiency, η or η'. Because $\eta = q'_u/q_u$ and $\eta' = q''_u/q_u$, and because η and η' are functions of q''_u, q'_u, and q_u, which will have scale effects, it is estimated that the magnitude of η or η' will not be affected by more than 5 to 10 percent. In analyzing bearing capacity problems, this range of variation is generally acceptable.

CONCLUSIONS

On the basis of the model test results to determine the interference effect of two closely spaced strip surface footings supported by a dense sand layer of limited thickness underlain by a very soft clay layer, the following general conclusions can be drawn:

1. The value of H_{cr}/B at which the failure surface in soil at ultimate load is located entirely in the top dense sand layer is practically the same for both an isolated footing and two closely spaced footings. For the present soil parameters, H_{cr}/B is about 4.
2. The theory proposed by Meyerhof and Hanna (*6*) for the prediction of the ultimate bearing capacity of an isolated footing on a dense sand layer of limited thickness underlain by a soft clay layer is generally in good agreement with the experimental results.
3. For any value of $H/B < H_{cr}/B$, the ultimate bearing capacity efficiency η' of two closely spaced footings increases with S/B. On the basis of the trend of the experimental results, it appears that η' will be about 100 percent at $S/B \approx 4$ to 5.
4. For $H/B \geq H_{cr}/B$, the bearing capacity efficiency decreases with S/B. The approximate value of η is the same irrespective of the H/B ratio. This is because of the fact that the failure surface in soil at ultimate load is entirely located in the sand, and the undrained shear strength of the underlying soft clay layer does not contribute to the ultimate load. For the present tests, it appears that the magnitude of η will reach a value of 100 percent at $S/B \approx 4$ to 5. Stuart (*2*) explains that η is larger than 100 percent at smaller S/B values because as S/B decreases, the soil between the two footings tends to form an inverted arch that travels down with the foundation as the load is being applied.

REFERENCES

1. B. M. Das and S. Larbi-Cherif. Bearing Capacity of Two Closely-Spaced Shallow Foundations on Sand. *Soils and Foundations*, Vol. 23, No. 1, 1983, pp. 1–7.
2. J. G. Stuart. Interference Between Foundations, with Special Reference to Surface Footings on Sand. *Geotechnique*, Vol. 12, No. 1, 1962, pp. 15–22.
3. K. Terzaghi. *Theoretical Soil Mechanics*. John Wiley, New York, 1943.
4. S. J. Button. The Bearing Capacity of Footing on a Two-Layer Cohesive Subsoil, *Proc., 3rd International Conference on Soil Mechanics and Foundation Engineering*, Zurich, Vol. 1, 1953, pp. 332–335.
5. A. S. Reddy and R. J. Srinivasan. Bearing Capacity of Footings on Layered Clay. *Journal of the Soil Mechanics and Foundations Division*, ASCE, Vol. 93, No. SM2, 1967, pp. 83–99.
6. G. G. Meyerhof and A. M. Hanna. Ultimate Bearing Capacity of Foundations Resting on Layered Soil Under Inclined Load. *Canadian Geotechnical Journal*, Vol. 15, No. 4, 1978, pp. 565–572.
7. A. S. Vesic. Analysis of Ultimate Loads on Shallow Foundations. *Journal of the Soil Mechanics and Foundations Division*, ASCE, Vol. 99, No. SM1, 1973, pp. 45–73.
8. A. S. Vesic. Bearing Capacity of Shallow Foundations. In *Foundation Engineering Handbook* (H. F. Winterkorn and H. Y. Fang, eds.), 1975, pp. 121–147.
9. E. E. DeBeer. Bearing Capacity and Settlement of Shallow Foundations on Sand. *Proc., Bearing Capacity and Settlement of Foundations*, Duke University, Durham, N.C., 1965, pp. 15–34.

Publication of this paper sponsored by Committee on Foundations of Bridges and Other Structures.

Predicted and Observed Behavior of a Deep-Soil-Mixing Braced Wall

DANIEL O. WONG, ARTHUR J. STEPHENS, CHARLES E. WILLIAMS, AND ROBERT L. RIPPLEY

Soil-mixing technique has many applications and is gaining popularity in the construction industry. An experience wherein a braced deep-soil-mixing (DSM) wall 18.3 m (60 ft) deep was used for an 11.3-m excavation 11.3 m (37 ft) deep under difficult subsurface conditions is presented. Reinforcing beams were installed inside the overlapping DSM columns, which made up a continuous retaining wall. Two levels of bracing struts at depths of 3 and 7.6 m (10 and 25 ft) were used for the complete excavation. Preconstruction prediction of the wall deflection was obtained using a beam-column computer solution, BMCOL76. Soil-structure interaction was modeled by specific nonlinear soil resistance curves. The stiffness of the composite wall was appropriately modeled on the basis of the properties of the soil-grout mixture. The measured behavior of the wall was compared with the preconstruction prediction.

Though soil-mixing technique has been widely used in many countries (*1–3*), it is a relatively new concept in the United States. The method has been applied in the industry so recently in this country that even the terminology of its many applications is a subject of debate (*4–6*). The construction application of soil mixing typically results in a series of interconnecting soil-grout mix columns referred to as "soil mixing walls," "soil-cement mixing," or "soil cement in situ walls." A special branch of this technique applied to deeper ground is called "deep soil layer mixing" or "deep soil mixing." For the particular application described herein and also because of its specific service-marked term, deep-soil-mixing wall, or DSM wall, is used throughout this paper. Applications of deep soil mixing (DSM) or shallow soil mixing (SSM) include soil stabilization, underwater soil improvement, soil remediation, foundation elements, and retaining walls. There is little documentation concerning the use of DSM or SSM techniques in soil improvement and stabilization projects (*7–9*).

This paper describes the use of a DSM wall 18.3 m (60 ft) deep as a temporary structural retaining wall for an excavation 11.3 m (37 ft) deep. DSM provided an attractive construction alternative in this case where a restricted construction area, contaminated subsoils, and shallow groundwater level limited the use of other conventional retaining structures. The predicted and observed behavior of the DSM wall are described.

D. O. Wong, McBride-Ratcliff and Associates, Inc., Houston, Tex. 77040; current affiliation: Tolunay-Wong Engineers, Inc., 1706 West Sam Houston Parkway North, Houston, Tex. 77043. A. J. Stephens, McBride-Ratcliff and Associates, Inc., Houston, Tex. 77040. C. E. Williams, Sanifill, Inc., Houston, Tex. 77008. R. L. Rippley, Morrison-Knudson Environmental Services, Denver, Colo. 80203.

37-ft EXCAVATION

The plan area of excavation was about 99.7 × 16.2 m (327 × 53 ft). The bottom of the excavation was about 11.3 m (37 ft) below existing ground surface in most of the area. The excavation area was located in a built-up area and part of the excavation boundary was only a few feet away from an adjacent facility. Intolerance of the adjacent facility to construction vibration restricted many retaining wall construction methods, such as pile driving. The situation was further complicated by another restriction minimizing the pumping of contaminated groundwater and excavation of contaminated subsoils during construction of the retention system. These environmental concerns led to a search for a retaining system that would also serve as a groundwater cutoff wall. The final decision was made that a reinforced DSM wall system should be used. The reinforced DSM system was perceived to provide a structural wall, and its construction would neither require excavation and dewatering nor produce any vibration during construction. The DSM wall system consisted of 344 DSM columns with appropriate reinforcement. Inclinometers were placed at selected locations to monitor the movement of the wall throughout the excavation process. Figure 1 presents the general project layout with inclinometer locations.

SUBSURFACE CONDITIONS

The project area is located on the upper Texas Gulf Coast and situated on Holocene alluvium (fluvial deposit) overlying the Pleistocene sediments. The generalized soil profile at the project site is shown in Figure 2. The six zones of the project area are summarized as follows:

- Zone 1 [depths of 0 to 3 m (0 to 10 ft)] consists of loose to medium-dense fine sand and silty fine sand.
- Zone 2 [depths of 3 m to 7.9 m (10 to 26 ft)] consists of very soft to firm clay with sand layers.
- Zone 3 [depths of 7.9 m to 15.2 m (26 to 50 ft)] consists of medium-dense to very dense fine sand.
- Zone 4 [depths of 15.2 m to 25.3 m (50 to 83 ft)] consists of firm to very stiff clay.
- Zone 5 [depths of 25.3 m to 34.7 m (83 to 114 ft)] consists of medium- to very dense silty fine sand and fine sand.
- Zone 6 [depths below 34.7 m (114 ft)] consists of firm to hard clay and silty clay.

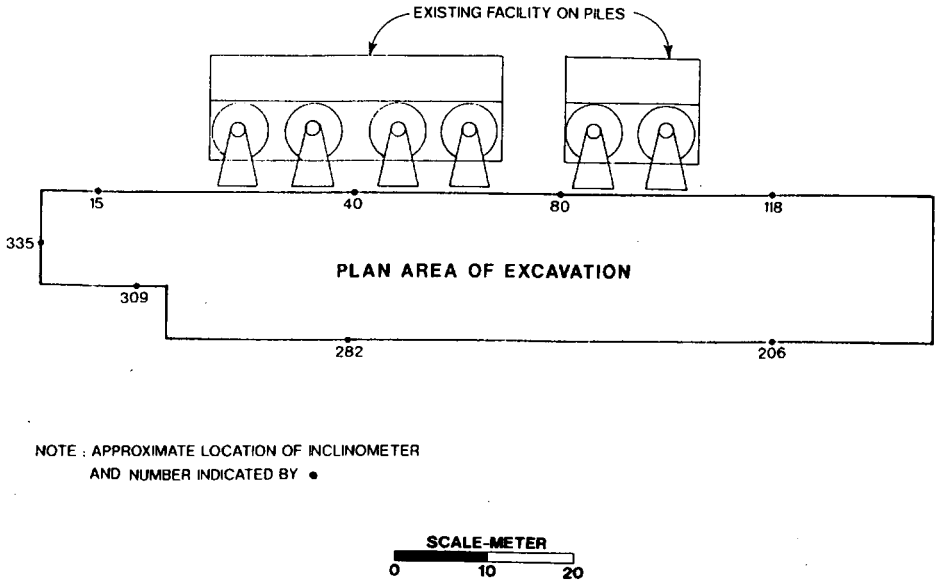

FIGURE 1 Plan area of excavation.

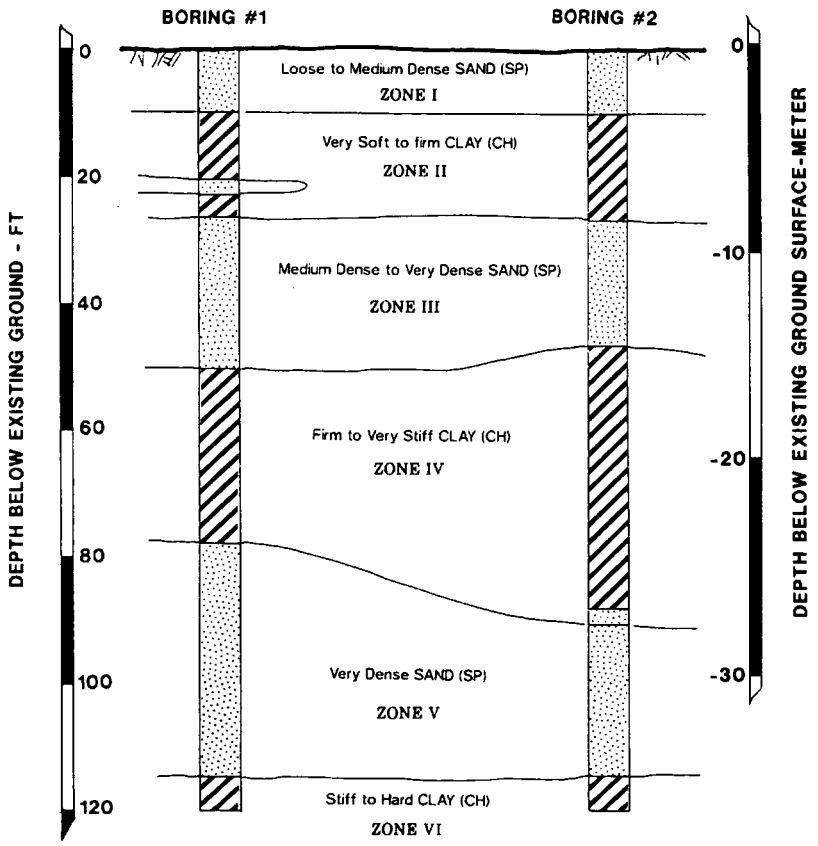

FIGURE 2 Generalized soil profile.

Figures 3 and 4 present the uncorrected standard penetration tests (SPTs) "N" profile and the undrained shear strength profile, respectively. The groundwater level was observed to be 2.4 m (8 ft) deep. The bottom of the excavation was about 11.3 m (37 ft) below ground and based within the Zone 3 cohesionless soils. Because of the high groundwater level, conventional excavation would require dewatering or a cutoff wall penetrating into the Zone 4 cohesive soils. The deep soil mixing technique provided an attractive means to construct a system serving as both a groundwater cutoff curtain and a retaining wall.

DSM WALL

The equipment used to construct the DSM wall included a specially designed soil mixing rig and a grout mixing plant. The rig used a 1335-KN (150-ton) crane with a supporting set of leads which guided four hollow-stemmed augers. A series of overlapping auger flights 914 mm (36 in.) in diameter were welded to those four augers. As the discontinuous auger flights were advanced into the ground, a cement-based grout was pumped through each hollow-stemmed auger shaft and discharged at the bottom of the auger. The soilcrete columns were produced by the rotation of the beaters along the auger stem while drilling. Once the required depth was achieved, the auger stem rotation was reversed. Mixing continued as the augers were withdrawn.

Continuity of the soilcrete columns was achieved in two ways: (a) the four augers laterally overlapped each other on each stroke drilled, up to 229 mm (9 in.), as shown in Figure 5 (*top*), and (b) each stroke drilled was vertically overlapped by one auger from the previous stroke, which created a continuous soilcrete wall, as shown in Figure 5 (*bottom*). Each DSM column in this study was designed to penetrate at least 0.6 (2 ft) into the relatively impervious cohesive soils (Zone 4), which is about 15.2 m (50 ft) below ground surface.

A wide flange (WF) 24 × 104 steel beam was inserted into each DSM column before the soilcrete was set to serve as structural reinforcement. A vibratory hammer (Model ICE 815) was used to vibrodrive the reinforcing beam below the bottom of the soilcrete column into the Zone 4 cohesive soils to tip at 18.3 m (60 ft) below ground surface. Minimum vibration was induced during driving within the deeper cohesive layer.

SOILCRETE

The soilcrete was formed by blending the grout and the soil in each DSM column. To achieve the desired strength of the soilcrete mixture, the design mix included 200 kg (450 lb) of Type I portland cement and 2 kg (4.5 lb) of M-1 Wyoming Gel injected into 0.76 m^3 (each cubic yard) of soil. The grout used in this project was prepared in a 3790 L (1,000 gal) storage tank with a specific gravity of 1.35 and a water/cement

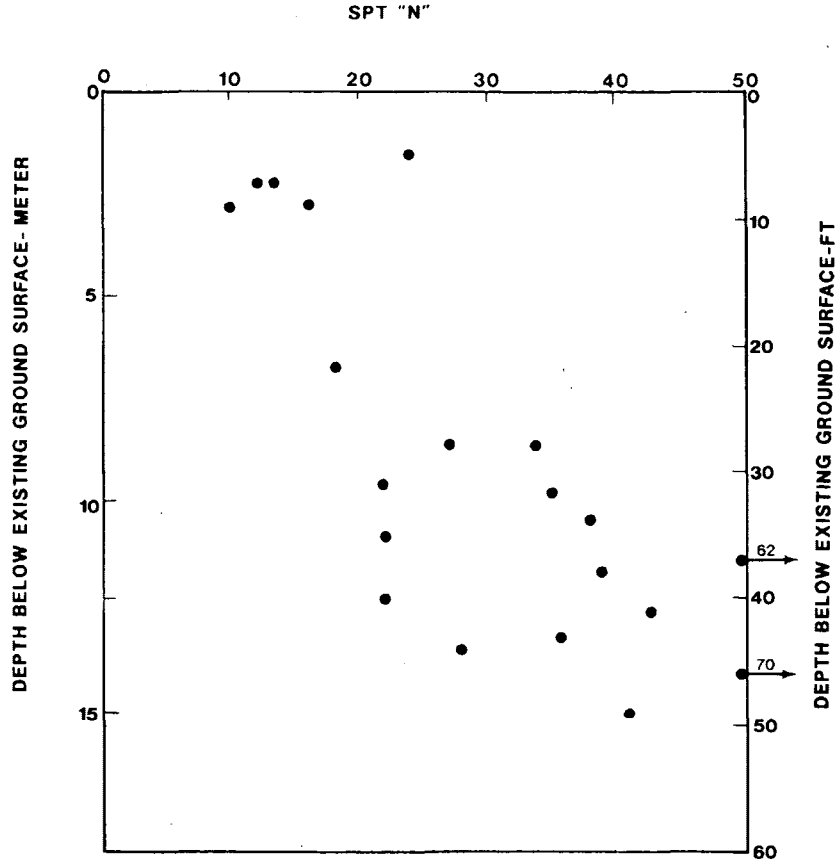

FIGURE 3 SPT "N" profile.

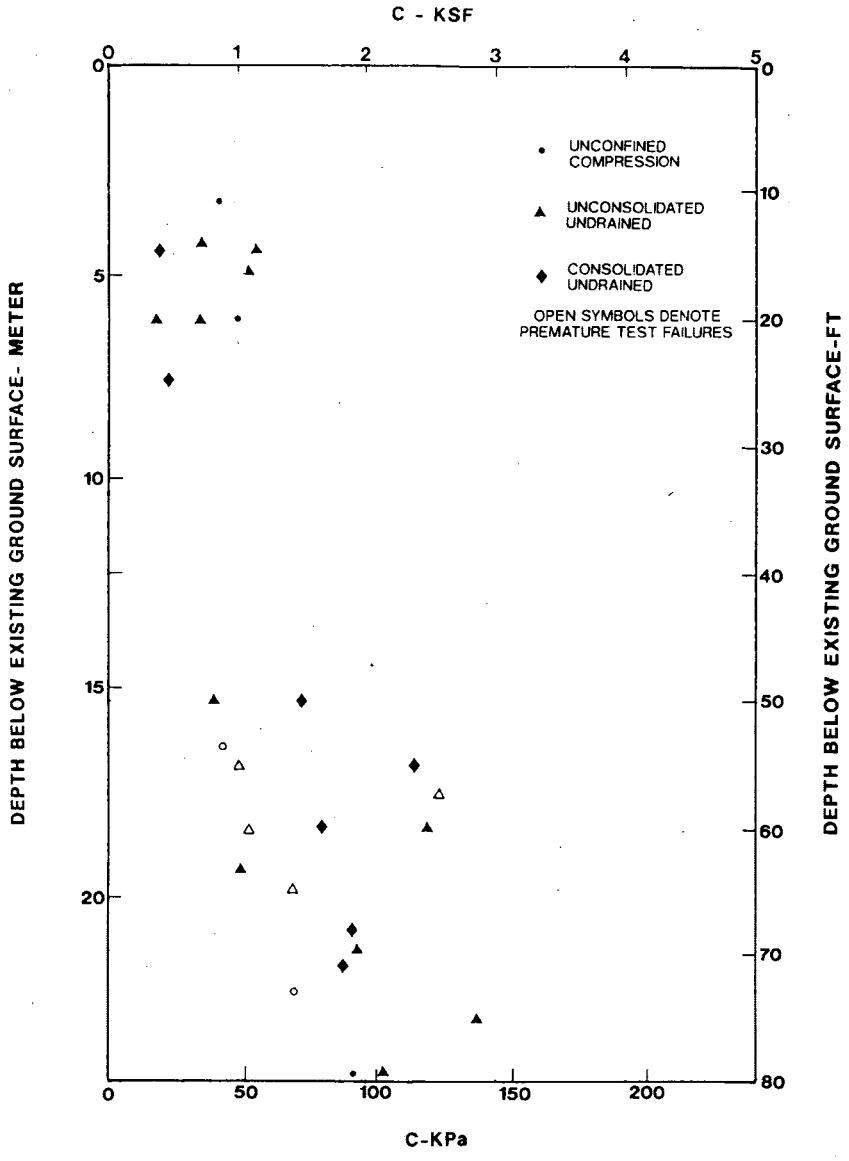

FIGURE 4 Undrained shear strength profile.

ratio of 1:2. A grout flow rate of 83 to 106 L/min (22 to 28 gal/min) was measured at the four pumps that delivered the grout to the shafts.

Many soilcrete samples were obtained throughout the construction process. Each sample was about 76 mm (3 in.) in diameter and 152 mm (6 in.) high. The samples were capped and allowed to cure at ambient temperatures of about 70°F. The samples were tested for unconfined compressive strengths and permeability in the laboratory. Table 1 summarizes the results of laboratory testing on the soilcrete samples obtained at various depths. Specific depth information was not recorded. The strength data exhibit large scatter, as evidenced by their mathematical means and their coefficients of variation. The data scatter reflects the heterogeneity of the subsoils and suggests a relatively nonuniform or nonhomogeneous mixture in the soilcrete column. The trend, however, indicates about a 100 percent increase in compressive strength between the 3- to 7-day and the 7- to 28-day curing periods. Moduli of elasticity of the soilcrete samples, based on the stress-strain relationships from the unconfined compression testing, were estimated to range from 0.1×10^6 KPa to 0.26×10^6 KPa (1.48×10^4 to 3.75×10^4 psi). The coefficients of permeability of the four soilcrete samples ranged from 1.32×10^7 to 7.10×10^7 cm/sec.

PRECONSTRUCTION PREDICTION

Because of the innovative use of the DSM columns as a retaining wall system, extensive numerical analyses were performed before the final design scheme was selected. Analyses were performed to optimize the depth of wall, the selection of reinforcing beam, and the bracing of the DSM wall. The performance of the wall was evaluated based on the predicted load-deflection characteristics using a beam-column computer solution BMCOL76 (*10*). The computer procedure used the

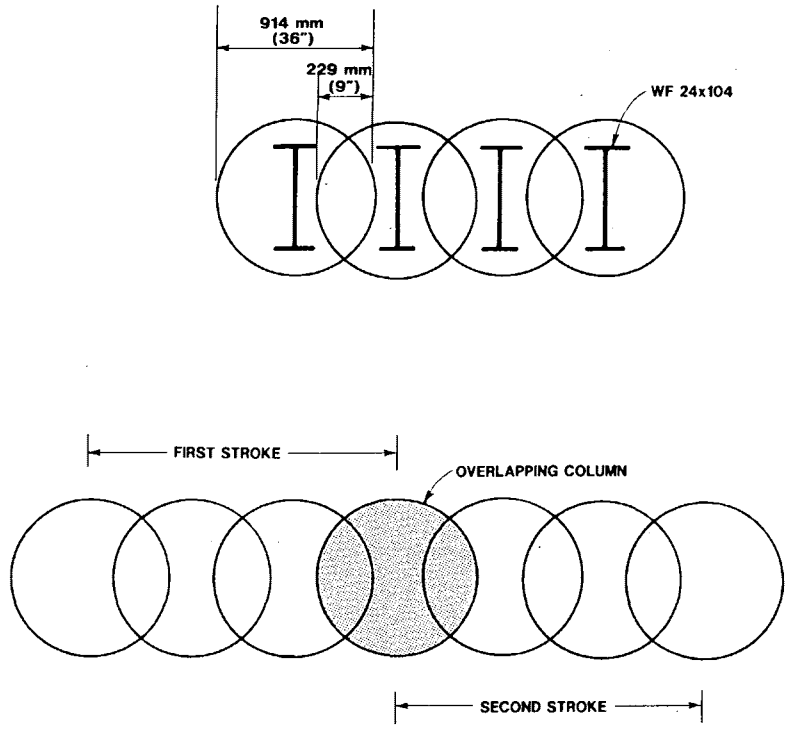

FIGURE 5 Overlapping of DSM columns: lateral overlap, *top*; vertical overlap, *bottom*.

TABLE 1 Properties of Soilcrete on Basis of Laboratory Testing

3-day strength (KPa)	7-day strength (KPa)	28-day strength (KPa)	Permeability (cm/sec)
113.0	184.0	517.4	1.32×10^{-7}
126.1	306.6	765.5	3.40×10^{-7}
136.4	311.4	834.4	3.60×10^{-7}
141.9	421.7	961.2	7.10×10^{-7}
144.0	438.2	1001.1	
149.5	498.8	1121.0	
170.9	509.2	1245.0	
171.6	531.2	1263.6	
206.7	633.9	1485.5	
209.5	672.5		
254.2	695.2		
284.6	959.1		
416.2			
427.9			
491.9			
500.2			
Mean - 246.7	Mean - 513.3	Mean - 1021.8	
Median - 189.5	Median - 504.3	Median - 1001.1	
Standard Deviation - 135.7	Standard Deviation - 208.8	Standard Deviation - 294.2	
Coefficient of Variation 55%	Coefficient of Variation 41%	Coefficient of Variation 29%	

Note: data are arranged in ascending order.
1 KPa = 0.145 psi

TABLE 2 Soil Parameters Used for Preconstruction Prediction

Range of Depth (ft)	Soil Type	Undrained Shear Strength (KPa)	Angle of Friction
0 - 8	Sand	--	29
8 - 26	Clay	23.9	--
26 - 50	Sand	--	34
50 - 60	Clay	86.1	--

Note: 1 KPa = 20.9 psf

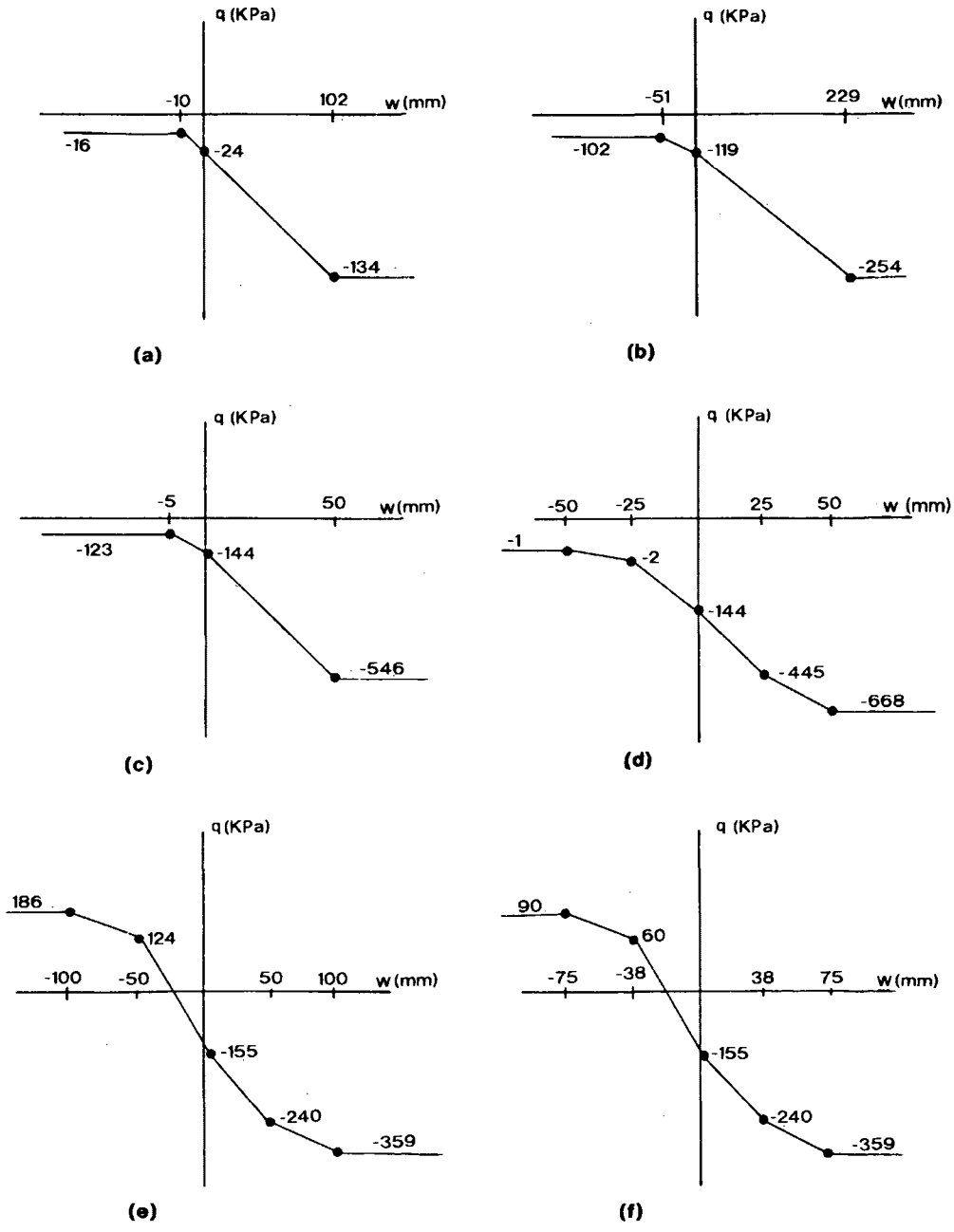

FIGURE 6 *q-w* curves for 37-ft excavation: *a*, 2.4-m depth; *b*, 7.9-m depth; *c*, 11.3-m depth; *d*, 15.2-m depth; *e*, 15.5-m depth; *f*, 18.3-m depth (negative sign denotes direction toward excavation).

concept of Hetenyi's beam on elastic foundation theory (*11*) but permitted the soil to be modeled as a nonlinear medium. Two important factors affecting the flexible wall behavior were the effects of soil-structure interaction and the wall stiffness.

The mechanism of soil-structure interaction can be modeled by entering nonlinear soil resistance relationships, termed *q-w* curves, into the computer procedure. The required *q-w* curves are typically obtained from classical wall-deflection requirements for active and passive stress states (*12,13*). Complete details of the generation of *q-w* curves at any depth along the wall are detailed by Haliburton (*14*). It is known that lateral earth pressures (both active and passive) change with time for retaining structures as strength of clay soil changes with time (*15*). Williams and Baka (*16*) have shown that mobilized active pressures, in the case of a cantilever wall system, can increase 50 percent over a 30- to 60-day period as drained shear strength of clay soil is gradually developed. Daniel and Olson (*17*) concluded that the failure of an anchored bulkhead was due to the lack of understanding of the soil behavior, particularly that the fully drained strength of cohesive soil would be less than that of the undrained strength.

The preconstruction analysis assumed the after-construction (short-term) condition because the final structural slab and concrete perimeter wall would be cast immediately after completion of excavation. The earth pressures developed for the analysis were based on short-term soil parameters (i.e., undrained shear strengths for cohesive soils). Soil parameters used to develop active and passive pressures are presented in Table 2. However, the actual lateral pressures realized during construction might be in the transition from undrained shear strength to drained shear strength as excess pore water pressures would be partially dissipated during the construction time period. Certain conservatism and judgment based on past experience were imposed in selecting the appropriate coefficients of lateral earth pressures in the preconstruction prediction process. A set of *q-w* curves used to analyze the complete excavation under the final design scheme is shown in Figure 6. The *q-w* curves were generated on the basis of the short-term soil parameters to closely model the temporary nature of the wall.

Another important parameter in the analysis was the bending stiffness of the composite wall (*EI*), where *E* is the modulus of elasticity of the wall material and *I* is the moment of inertia. On the basis of the laboratory test results of the soilcrete as described previously, the *EI* for the DSM wall without reinforcing steel was found to range from 1.88×10^6 to 4.77×10^6 N-m^2 (6.55×10^8 to 1.66×10^9 lb-in.^{2}) per 0.3 m (1 ft) width of the wall. The *EI* for the reinforcing beam was 1.19×10^8 N-m^2 (4.13×10^{10} lb-in.^{2}) per 0.3 m (1 ft) width of the wall. The *EI* of the soilcrete column was about 2 to 4 percent of the *EI* of the reinforcing beam. Thus the *EI* of the reinforcing beam was conservatively taken as the *EI* of the composite wall in this study.

The cross bracings used for the braced excavation were 16.1 m (53 ft) long, hollow steel tube sections (TS16×16). Com-

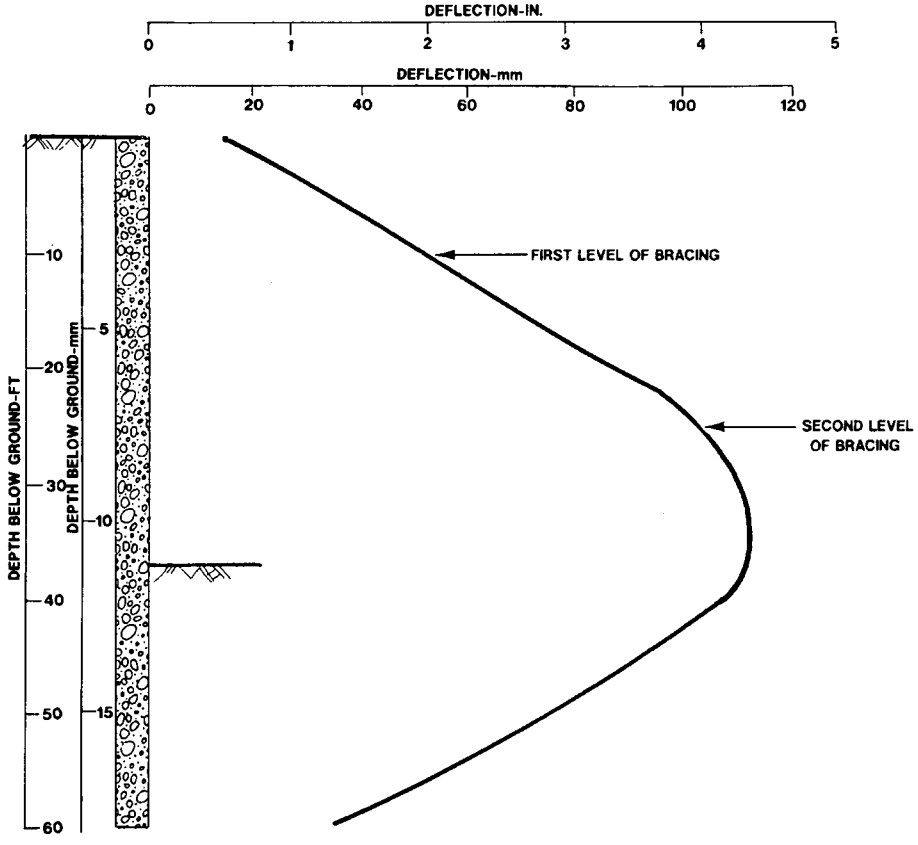

FIGURE 7 Predicted deflection profile.

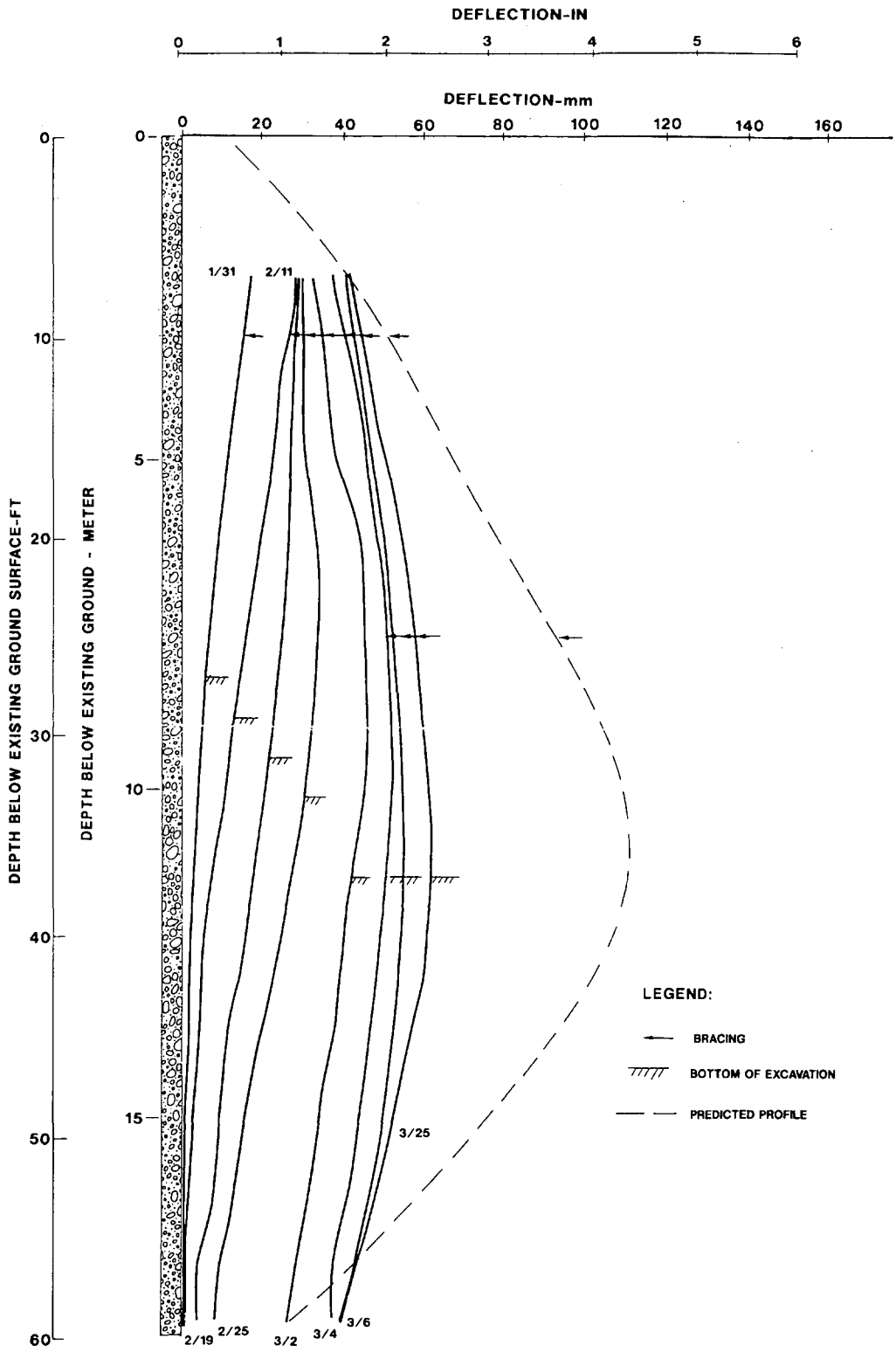

FIGURE 8 Observed and predicted deflection profiles.

plete excavation required two levels of bracing struts at respective depths of 3 m (10 ft) and 7.6 m (25 ft). The cross bracings were modeled as elastic springs. For such a long slender section of each cross bracing, the buckling load controls the ultimate axial behavior of the tube. On the basis of the critical buckling load and the allowable stress for the steel tube section, the spring constant for each cross bracing was calculated to be 1.43×10^3KN/m (8.18×10^3 lb/in.) per 0.3 m (1 ft) width of the wall.

Figure 7 presents the preconstruction prediction of the wall movement under the complete excavation condition. The wall was predicted to move laterally toward the excavation from the top to the toe, with the largest deflection occurring at the base of the excavation. The predicted deflection profile was used as a baseline for the movement criteria for the construction phase.

OBSERVED BEHAVIOR

During excavation, the DSM wall system behaved generally as expected. The DSM wall provided a complete cutoff of groundwater flow into the excavation except at one location where one DSM column had not been constructed in complete continuity and was subsequently repaired by in-place grouting. The cross-bracing loads were not measured in this study. Figure 8 shows the progressive movements of the DSM wall at various stages of construction. The deflection profiles were obtained from the Inclinometer No. 118 shown in Figure 1. Inclinometer No. 118 was selected because more data had been collected at this location. Because of construction and early termination of the monitor program, other inclinometers were not used for comparison purposes because of insufficient data. However, similar performance was observed for other inclinometers where readings could be obtained in the early stage of construction.

The preconstruction deflection prediction plotted in Figure 8 shows that the observed behavior of the DSM wall approaches toward a final profile similar to the predicted profile with the same order of magnitude in actual deflections. The predicted maximum deflections were larger than those measured; this may be due to the conservative selection of soil parameters in the active zone, which is usually done in practice. However, the measured deflection magnitudes are gradually increasing with time. This phenomenon appears to be consistent with the comments by other researchers (*16,17*) that the decrease of soil strength due to the long-term drained condition of clay soil would be gradually realized with time.

CONCLUSIONS

By analyzing and measuring the behavior of a braced DSM wall as a structural retaining wall, the following conclusions may be drawn:

1. A DSM wall successfully served as a groundwater cutoff and retaining wall at a restricted site where dewatering and driving vibration needed to be minimized.
2. Wall performance can be practically predicted before construction using beam-column analysis with appropriate nonlinear q-w curves so that baseline information can be established for subsequent monitoring activities.
3. In this particular case, the bending stiffness of the wall system was controlled by the reinforcing steel, and the behavior of the cross bracing was governed by the critical buckling load.
4. The short-term behavior of the DSM wall agreed reasonably well with the preconstruction prediction using short-term soil parameters. Progressive movement of the wall indicated that the conversion of drained shear strength from undrained shear strength of cohesive soil was gradually taking place.

REFERENCES

1. B. B. Broms and P. Boman. Lime Columns—A New Foundation Method. *Journal of the Geotechnical Engineering Division*, ASCE, Vol. 5, No. 4, 1977, pp. 539–56.
2. B. H. Jasperse and C. R. Ryan. Geotech Import: Deep Soil Mixing. *Civil Engineering*, Dec. 1987, pp. 66–68.
3. P. Hann. Taipei Untangles Its Rail Lines. *Engineering News-Record*, Feb. 1986, pp. 41–42.
4. R. Lundgren. Discussion: Deep Oil Mixing at Jackson Lake Dam. *Journal of the Geotechnical Engineering Division*, ASCE, Vol. 117, No. 12, 1991, pp. 1975–76.
5. O. Taki and W. Fillmore. Discussion: Deep Soil Mixing at Jackson Lake Dam. *Journal of the Geotechnical Engineering Division*, ASCE, Vol. 117, No. 12, 1991, pp. 1976–78.
6. C. R. Ryan and B. H. Jasperse. Discussion: Deep Soil Mixing at Jackson Lake Dam. *Journal of the Geotechnical Engineering Division*, ASCE, Vol. 117, No. 12, 1991, pp. 1978–79.
7. Weak Seabed Strata Yields Strong Support. *Engineering News-Record*, March 1983, pp. 30–31.
8. S. Sawyer. *Site Demonstration Report—In Situ Stabilization/Solidification*, Hialeah, Florida. EERU Contract 68-03-3255. Environmental Protection Agency, Cincinnati, Ohio, Nov. 1988.
9. C. R. Ryan and B. H. Jasperse. Deep Soil Mixing at Jackson Lake Dam. *Proc., Foundation Engineering Congress*, Vol. 1, June 1989, pp. 354–67.
10. H. Matlock, D. Bogard, and I. P. Lam. *BMCOL76: A Computer Program for the Analysis of Beam-Column Under Static Axial and Lateral Loading*. University of Texas, Austin; Ertec, Inc., June 1981.
11. M. Hetenyi. *Beam on Elastic Foundation*. University of Michigan Press, Ann Arbor, 1946.
12. G. B. Sowers and G. F. Sowers. *Introductory Soil Mechanics and Foundations*. MacMillan Publishing Co., Inc., New York, 1970.
13. *Engineering and Design, Retaining Walls*. EM 1110-2-2502. U.S. Army Corps of Engineers. 1975.
14. T. A. Haliburton. *Soil Structure Interaction*. Technical Publication 14. School of Civil Engineering, Oklahoma State University, 1971.
15. C. E. Williams and J. A. Focht III. Long-Term Performance of Cantilevered Retaining Walls. *Proc., Spring Texas Section Meeting*, Fort Worth, Tex., 1987.
16. C. E. Williams and J. E. Baka. Predicted and Measured Performance of Cantilevered Retention System, *Proc., Fall Texas Section Meeting*, El Paso, Tex., 1985.
17. D. E. Daniel and R. E. Olson. Failure of an Anchored Bulkhead. *Journal of the Geotechnical Engineering Division*, ASCE, Vol. 108, No. 10, 1982, pp. 1318–1327.

Publication of this paper sponsored by Committee on Foundations of Bridges and Other Structures.

Dispersive Clay Embankment Erosion: A Case History

JAMES B. NEVELS, JR.

A fine-grained soil mapped as the Cupco soil series by the U.S. Department of Agriculture's Soil Conservation Service was used as embankment material on a recent project. The project was located on US-59 in LeFlore County, near Panama, Oklahoma. The work called for embankment widening in the southbound direction. A segment of the completed embankment experienced some characteristic dispersive clay erosional patterns following a period of above-normal rainfall. Representative samples of the embankment material were taken from standard penetration tests, from thin-walled tube samplers, and by hand auger. A laboratory analysis determined the soil classification, in-place density, moisture content, and moisture-density relationships for the embankment material. To determine the dispersive characteristics, the following tests were used: pinhole, double hydrometer, soluble salts in the pore water, and crumb. Statistical analyses were conducted for the different dispersion test results. All four laboratory tests indicated a highly dispersive clay material. Correlations were observed among compaction water content and density and dispersion. The effects of the soluble salts in the pore water and clay dispersion were analyzed. It is believed that the main mechanism that triggered this embankment erosion was rainwater flowing in cracks that had resulted from earlier drying of the clay. Significant contributing factors were found in the plan design and during construction. The damaged embankment was repaired by undercutting and filling holes, gullies, and tunnels; plating with select material; and flattening the design slope.

Certain natural soils tend to disperse in the presence of relatively pure water. These soils are highly susceptible to erosion and piping. The principal difference between dispersive clays and ordinary erosion resistant clays is the nature of the cations in the pore water (*1*).

Dispersive clays contain sodium as the predominant cation in the pore water, whereas nondispersive clays contain calcium and magnesium. The presence of the dominant sodium ions increases the thickness of the diffused, double water layer surrounding the individual clay particles. This leads to a deflocculated structure in which the repulsive forces exceed the attractive forces so that the individual clay particles go into suspension in the presence of water.

Dispersive clays generally have low to very low permeability rates (*2*). As a result, the velocity of water moving through the pores is insufficient to move the soil particles, even under very high heads. However, once a crack or opening occurs, the dispersed clay particles go into suspension and are easily carried away with the water moving through the opening.

The tendency for dispersive erosion in a given soil depends on such variables as the mineralogy and chemistry of the clay. Studies have shown that soils with montmorillonite as the predominant clay mineral tend to be more dispersive than those containing kaolinite and vermiculite (*3*). Further studies have revealed that dispersive clays have at least 12 percent of their particles, computed on a dry weight basis, finer than 0.005 mm as determined by ASTM D422-63 (1990) (*2*). These clays have a plasticity index greater than 4 and tend to have a pH well on the acidic side (*4*).

The soil surveys conducted by the U.S. Department of Agriculture (USDA) Soil Conservation Service in Oklahoma provide a general indication of dispersive clays. The more recent soil surveys in Oklahoma (those published since 1975) contain significantly more engineering and chemical data and indicate the dispersive potential and location of mapped soil units more accurately. Dispersive clays are common in Oklahoma, occurring randomly within residual and alluvial soil deposits derived from shales of the Permian and Pennsylvanian geologic periods.

This paper presents a case history of the geotechnical investigation of the conditions and factors influencing severe dispersive clay erosion of a highway embankment. The project involved widening the existing two-lane section of US-59 between Panama and Poteau in LeFlore County, Oklahoma, to four lanes with a center median. To accomplish this, the existing embankment was widened as shown in Figure 1. The southbound lanes were constructed almost entirely on new fill with a 6:1 roll off slope increasing to a 2:1 side slope down to the toe. A soil type used in the embankment construction from one of the adjacent borrow pits was mapped by the USDA Soil Conservation Service as the Cupco soil series, and it was placed solely in a quarter-mile extent of the embankment, hereinafter referred to as the Cupco embankment. Cupco soils at this site consist of deep deposits of somewhat poorly drained silty clay loams that are strongly to very strongly acidic in the A-horizon ranging to neutral in the B-horizon on broad floodplains of Brazil Creek. The initial phase of the project began with the construction of the southbound embankment starting in September 1990 and ending in November 1990. The pavement surface and base courses and the vegetative mulch and sodding for embankment side slope protection were set aside from December 1990 through August 1991 until the southbound bridges were constructed. The embankment was unprotected for approximately 9 months.

Asphalt pavement construction began in late August 1991 and continued into September 1991. The pavement design called for 0.09 m (3.5 in.) asphalt concrete surface course (Type B) underlain by 0.30 m (12 in.) of a very open graded asphalt concrete base (Type G). The pavement design called for no edge drains. Shortly after the asphalt paving, the embankment slope was treated with a vegetative mulch tracked

Materials Division, Oklahoma Department of Transportation, 200 NW 21st Street, Oklahoma City, Okla. 73105.

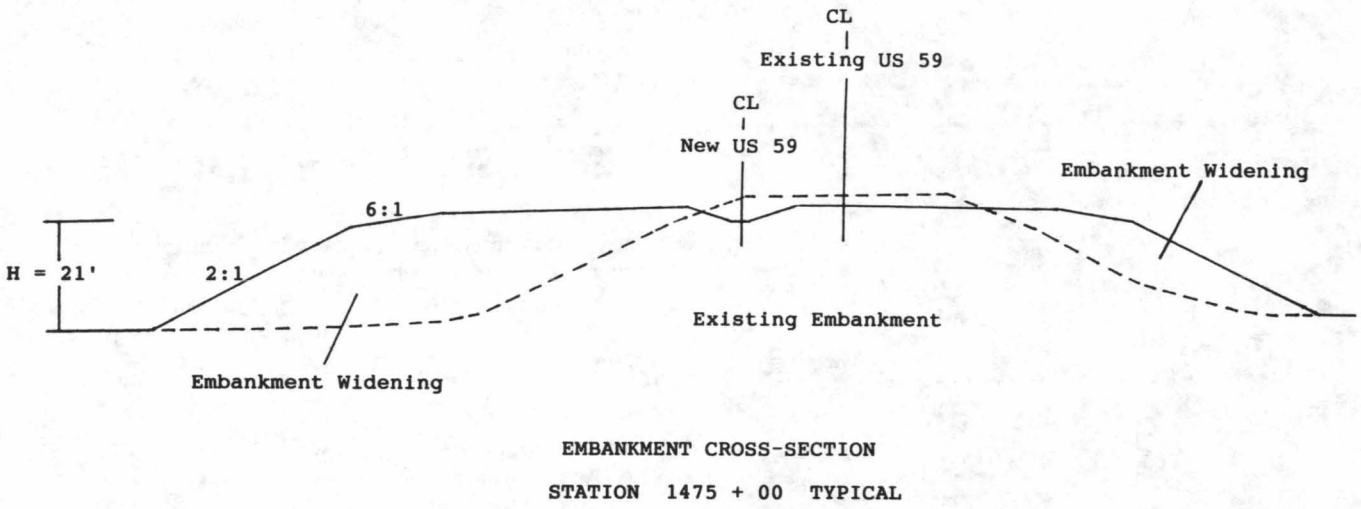

FIGURE 1 New construction for US-59, embankment cross section: Station 1475 + 00 (typical).

in by a dozer because the 2:1 side slope was too steep to use a disk. Rainfall over the 9 months before paving was near normal. However, much heavier total monthly rainfalls occurred in September, October, and November. A total of 0.31 m (12.04 in.) of heavy rain was recorded from October 24 to October 30. Within the next 2 weeks, project inspectors observed the formation of typical dispersive clay erosional features in the form of rills, gullies, tunnels, and jugs within the Cupco embankment.

SITE INVESTIGATION

A geotechnical investigation of the problem began in early November 1991. The most prominent erosional feature, an open hole on the surface, commonly called a jug, leads to an underground tunnel. The extent of the jug was surveyed. The survey identified 242 erosional holes within the extent of the 6:1 roll-out slope within the Cupco embankment that had a minimum dimension of 0.46 m (1.5 ft.). The average jug depth was 1.25 m (4.1 ft.) with a range of 0.46 to 4.48 m (1.5 to 14.7 ft). Additionally, the embankment was heavily rilled and had numerous gullies and tunnels that broke out on the 2:1 side slope. Figures 2 and 3 typify the embankment surface appearance.

Soil samples from the embankment were obtained from the standard penetration tests (SPTs), from thin-walled tube samplers, and by hand auger. Three SPT borings were continuously sampled, and adjacent to the SPT borings at five offsets, three additional borings were made in which 0.61-m (2-ft) thin-walled tube samples were taken at 0.91-m (3-ft) intervals. The appropriate sampling techniques (*5*) applied were D1586-84, D1587-83, and D1452-80, respectively. The SPT and tube samples were taken through the depth of the embankment and into the foundation soil. The length of the embankment was broken into quarters, and these borings were made at the ¼-, ½-, and ¾-point locations on the 6:1 slope. The hand auger samples were taken at random within the top 2 ft of the embankment along the 6:1 and 2:1 slopes.

A review of the 1981 USDA Soil Conservation Service soil survey for LeFlore County shows that the entire embankment and adjacent borrow pit are in a large mapped extent of the Cupco soil series. The Cupco soil series are noted in the LeFlore soil survey to have high sodium content. A pedological soil survey was made by hand auger identifying all horizons at a representative, undisturbed location between the Cupco embankment and the borrow pit. Adjacent hand auger

FIGURE 2 Formation of jugs near pavement edge.

FIGURE 3 Gullies, rills, and tunnels on 2:1 slope.

borings and exposures in the borrow pit confirmed the Cupco soil identity.

The embankment appeared to be consistent and uniform in depth, based on the soil color, and in the surface, matching the Cupco soil series.

Water was observed draining from the edge of the (Type G) asphalt concrete base at five locations. As shallow trenches were shoveled perpendicular to the pavement edge, large quantities of oily water flowed from the (Type G) base into the trenches. This process was repeated at various stations along the eroded sections of the embankment, each having the same results.

LABORATORY INVESTIGATION

The laboratory investigation consisted of two parts. The first phase documented the material type classification, moisture content, and in-place density. The second phase identified the clay as dispersive. The four currently recommended laboratory tests used to determine if clays are dispersive are as follows:

- Pinhole test,
- Chemical analysis of pore water extract,
- Double hydrometer test, and
- Crumb test.

A total of 164 samples were tested and classified according to ASTM D4318-94 and D2487-90, respectively. Seventy-six samples were taken from the thin-walled tube samplers, and the in-place densities were measured from chunk density tests according to AASHTO T233-86. Statistical data for the soil classification and in-place moisture and density are presented in Table 1. A family of curves and a line of optimums were developed from 21 Harvard miniature proctor curves for samples of the embankment material. The in-place density and moisture of the embankment material are compared to the backcalculated line of optimums in Figure 4.

To study the dispersive character of these embankment clays, all four recommended laboratory tests were conducted. The pinhole test was performed according to ASTM D4647-87 Method A on 20 embankment samples; the test results are provided in Table 2. Fifty-three samples were analyzed for soluble salts in the pore water using an ammonium acetate saturation extract by a method after Jackson (*5*, p. 85). The saturation extract was analyzed by an inductively coupled plasma apparatus, model Jarrell-ASH 2400, to determine the quantities of the four main metallic cations in the solution (calcium, magnesium, sodium, and potassium) in milliequivalents per liter (meq/L). The results and definitions for this analysis are presented in Table 3. The double hydrometer test was conducted on 89 samples. The test method applied was ASTM D4221-90 (*6*), and the test values are tabulated in Table 2. The crumb test developed by Emerson (*6*) was con-

TABLE 1 Index and In-Place Embankment Soil Property Statistical Summary

Test	Number	Mean	Standard Deviation	Range
LL	164	32	2.3	24 - 38
PI	164	13	2.2	7 - 18
Percent Passing NO. 200 Sieve	164	90.7	5.7	65.5 - 97.4
In-Place Density, Pcf	72	104.0	12.2	96.6 - 113.2
In-Place Moisture, %	72	15.5	1.8	12.5 - 20.8

163 samples classified as CL and one as CL-ML

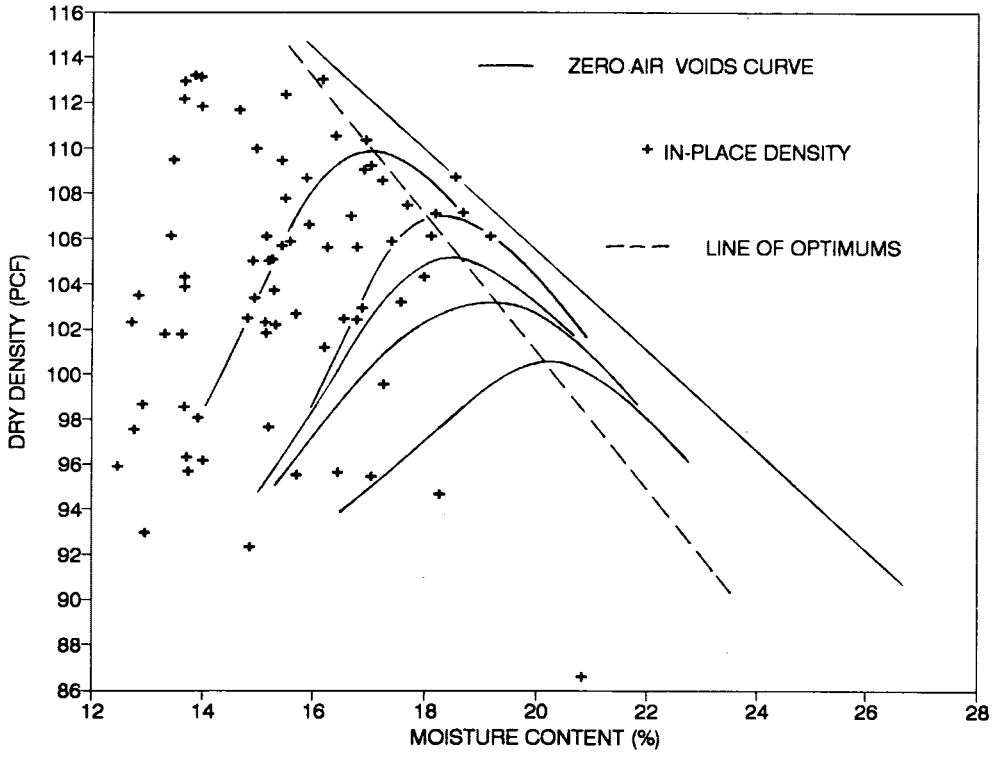

FIGURE 4 In-place densities for southbound embankment.

TABLE 2 Dispersion Test Data Statistical Summary

Test		Number	Mean	Standard Deviation	Range
Pinhole [1]					
Flow (ml/s)		20	0.92	0.30	0.51 - 1.79
Hole Diameter (mm)		20	1.90	0.20	1.50 - 2.10
Double Hydrometer					
6:1 Slope , (%)		22	81.6	20.2	57.5 - 100
Tunnel Locations , (%)		17	79.4	22.6	55.1 - 95.6
Samples with Depth , (%)		50	67.1	26.0	25.6 - 89.0
Crumb					
Rating	4	61			
	3	27			
	2	4			
	1	2			

(1) The effluent for all samples was dark. Eighteen samples were rated D2 and two samples were rated ND4.

TABLE 3 Soil Chemistry Test Data Statistical Summary

Test	Number	Mean	Standard Deviation	Range
pH	53	6.960	0.570	5.740 - 8.540
TDS[2]	53	0.652	0.429	0.129 - 2.407
CEC[1]	53	11.172	3.057	3.355 - 15.975
ESP[1]	53	19.842	6.504	3.259 - 28.768
SAR[2]	53	1.543	0.708	0.487 - 3.340
PS[2]	53	64.177	20.960	18.507 - 93.782

[2]TDS: Total Dissolved Salts = Ca + Mg + Na + K

[1]CEC: Cation Exchange Capacity

[1]ESP: Exchangeable Sodium Percentage = Na/CEC * 100%

[2]SAR: Sodium Adsorption Ratio = $Na/\sqrt{[(Ca+Mg)/2]}$

[2]PS: Percent Sodium = Na/TDS

1 - in terms of meq/100 g
2 - in terms of meq/liter

ducted on 94 samples using demineralized water. Test results are provided in Table 2.

The index, physical, and chemical properties for Cupco soil series were analyzed. The results are provided in Tables 4 and 5.

ANALYSIS AND DISCUSSION OF RESULTS

The consistency of the embankment was very uniform based on the site inspection, soil classification tests, and in-place density. Of the 164 samples tested, all were low-plasticity clays, with 163 being classified as CL and one as CL-ML (Table 1). This analysis was further confirmed by 45 SPT "N" resistance values that had a mean value of 17 and a standard deviation of 4.8.

As noted, 0.31 m (12.04 in.) of rain was recorded after the slope mulch treatment was placed on the embankment slopes. A review of precipitation records at the Poteau Water Works Station, which is located approximately 11.27 km (7 mi) south of the project, indicated that an unusually wet cycle was occurring in the area beginning in September and agreed with records kept at the site. Preceding this wet September and October were 9 months of near-average rainfall. During this period the embankment was left unprotected. As can be seen in Figure 4, the embankment soils were placed considerably dry of optimum. Compaction dry of optimum tends to increase the chances of the formation of surface cracks. There was ample time for crack development during the approximately 9-month period preceding the placement of the asphalt. It has been shown that whenever heavy rainfall and runoff can attack exposed dispersive clays, the surface drying and settlement cracks provide the avenue for dispersion to begin (*7*). This fact was observed over the 4-month investigation by noticing apparently affected embankment sections with cracks slowly degrading. Compounding the problem further the asphalt concrete (Type G) base (with no provision for drainage) was back-calculated to have a coefficient of permeability (k) of approximately 28.22μm/sec (4 in./hr). After observing the amount of water flowing from the asphalt concrete (Type G) base, there is little doubt that water from the rainfall had been

TABLE 4 Cupco Soil Index and Physical Properties

Soil Horizon	Depth (inches)	LL	PL	PI	Percent Passing No. 200 Sieve	Classification (Unified)	Maximum Dry Density (pcf)	Optimum Moisture (%)
A_1	0 - 11	48	28	20	96.1	CL	90.0	26.8
A_2	11 - 21	33	23	10	94.0	CL	102.2	21.4
B_{2t}	21 - 30	30	20	10	92.4	CL	106.3	19.4
B_{22t}	30 - 55	26	19	7	90.5	CL	106.8	18.9
B_3	55 - 83	27	19	8	94.4	CL	107.5	18.5

TABLE 5 Cupco Soil Chemistry Properties

		Cation Concentration meq/litre								
Soil Horizon	pH	Ca	Mg	Na	K	CEC[1]	ESP[1]	SAR[2]	TDS[2]	SODIUM[2]
A_1	5.5	0.157	0.106	0.115	0.001	9.404	0.978	0.317	0.3795	30.303
A_2	5.4	0.101	0.012	0.072	0.001	3.067	3.684	0.679	0.0950	75.790
B_{2t}	6.4	0.008	0.034	0.189	0.025	6.085	12.950	1.306	0.2559	73.935
B_{22t}	6.3	0.011	0.046	0.182	0.029	5.742	9.000	1.080	0.2674	68.025
B_3	6.7	0.013	0.060	0.356	0.040	6.495	18.362	1.854	0.4696	75.724

[1]CEC: Cation Exchange Capacity

[1]ESP: Exchangeable Sodium Percentage = Na/CEC * 100%

[2]SAR: Sodium Adsorption Ratio = $Na/\sqrt{[(Ca+Mg)/2]}$

[2]TDS: Total Dissolved Salts = Ca + Mg + Na + K

[2]SODIUM: Percent Sodium = Na/TDS

1 - in terms of meq/100 g
2 - in terms of meq/liter

trapped beneath the asphalt concrete surface course. Other contributing factors were as follows:

1. The 2:1 embankment slope allowed surface runoff to flow downslope faster than a flatter slope, helping to accelerate the erosion.
2. A drainage ditch was cut at the toe of the slope to allow runoff to drain to Brazil Creek. This ditch let water back up onto the slope and further accelerate the dispersive erosion during heavy rains and flooding of the creek. This event was observed twice during the investigation. On these occasions, it was noted that the erosional exit tunnels lined up slightly below the highwater marks on the 2:1 slope. The tunnels increasingly changed during the course of the rise and fall of the water in the ditch.
3. The tracking in of the slope mulch treatment by a dozer is thought to have broken up the slope surfaces, therefore providing another access for rainfall to enter into the soil. The dispersion of the embankment slopes started occurring and accelerating before the planned 0.15 m (6 in.) treatment of topsoil and sodding could be placed.

All four tests for soil dispersion showed positive results. The percentage of dispersion based on accepted criteria for the samples tested are as follows:

	Percentage
Pinhole test	100
Soluble salts in pore water	75
Double hydrometer	95
Crumb test	94

In the pinhole test, as seen from the data in Table 2, all samples are rated as dispersive. Only two samples were classified moderately dispersive (ND4) according to Method A of the test procedure. It must be pointed out that while 12 flow rates did match exactly the flow rate criteria for Method A, the test procedure does allow for some discretion. Section 5.3 states that the flow rates serve primarily as a guide to proper equipment and specimen performance. Therefore, the cloudiness of the effluent and hole diameter were considered sufficient (two out of three criteria) for Method A classification. If Method B criteria were used, then 19 samples would be classified as dispersive and 1 as slightly dispersive.

A key finding of the analysis for the soluble salts in the pore water is the high percentage of sodium, a mean exceeding 60 percent (Table 3). Generally the percentage of sodium in a saturation extract is a reliable indicator of probable dispersiveness of a soil (*8*). If the percentage of sodium versus the total amount of dissolved salts is plotted on the relationship shown in Figure 5, approximately 75 percent of the samples are dispersive. This relationship (*6*) is based on the pinhole test correlation and experience with erosion in nature. Figure 5 indicates that for these soils, dispersion is possible when the total amount of dissolved salts are less than 1.0 meq/L and the percentage of sodium is high. From these data, it would appear that for these soils the boundaries for Zones A and C of 60 and 40 percent are appropriate for separating potential dispersive clays.

The exchangeable sodium percentage (ESP) and the sodium absorption ratio (SAR) are both good indicators of the stability of clay soil structure to spontaneous dispersion in water (*8*). In this case, from data in Table 3, the ESP values are high and follow the trend seen in the percentage of sodium found. When the ESP for a soil exceeds 2 percent, it is highly susceptible to dispersion in water (*8*). There is evidence that when the ESP is between 10 and 50 percent, the sodium and calcium ions separate into distinct regions within the diffused double water layer. This phenomenon further enhances the dispersiveness of the clay soil (*8*).

A comparison with earlier Australian criteria (*6*) also indicates that when the SAR exceeds values of 1 to 2, there is the potential for a soil to be dispersive. A look at the pH for

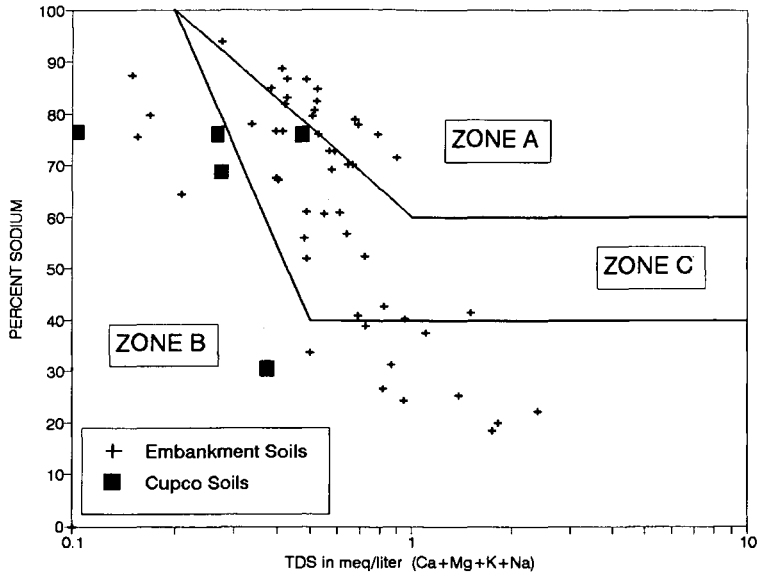

FIGURE 5 Pore water salts analysis.

these soils indicates a range from a slightly acidic to a moderately alkaline environment. As mentioned earlier, the pH in the Cupco series ranges from strongly acidic in the A-horizon to neutral in the B-horizon. The significance of the pH on dispersion is that higher pH values result in higher surface charge densities on the clay particles. Increased surface charge densities cause more concentration of ions in the diffuse double layer resulting in greater particle repulsion. However, for these soils it does not seem that the pH indicates soil dispersion.

The double hydrometer test data results are shown in Table 2 and in Figure 6. This test is good, with an 85 percent reliability for predicting dispersion when the test indicates 35 percent or more. The crumb test, likewise, proved to be a good indicator, with 29 percent showing a moderate crumb rating and 65 percent a strong crumb rating. The percentage of dispersion based on the pinhole and crumb test for the Cupco "B" horizons from the representative undisturbed location is as follows:

Horizon	*Pinhole*	*Crumb*
A1	ND1	1
A2	ND1	1
B2t	D2	4
B22t	D2	4
B3	D2	4

These results match very closely the values for the embankment material (Table 2).

RECOMMENDATIONS

At the outset of the investigation, it was suggested that the dispersive clay erosion could continue to occur underneath

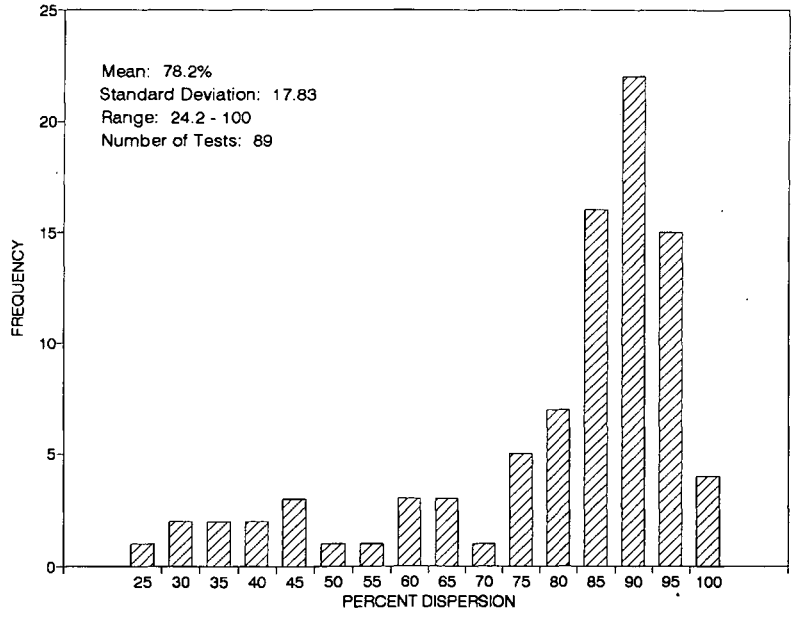

FIGURE 6 Distribution double hydrometer test results.

the newly completed asphalt pavement. However, the construction engineers pointed out that it would be unacceptable to correct this portion of the new embankment (see Figure 1) because it would require completely closing the highway at that stage of the construction. Therefore, only the following recommendations were made:

1. Stage 1 called for filling all of the known holes with a sand-cement grout. This grout was to have a sand-cement ratio ranging from 2:1 to 5:1. It was to be pumped using a conventional grout batch system while limiting the grouting pressure to 5170.5 to 6894.8 Pa (0.75 to 1.0 psi) per 0.30 m (1 ft) of overburden depth. Estimated average quantities of grout were approximately 0.25 m^3 (0.33 yd^3) per hole. Relying on grouting to fill all of the holes along and under the pavement posed a problem because it was not possible to determine the extent of hole development under the pavement.
2. Stage 2 called for lime modification of the top 0.30 m (1 ft) of the roll-off slope soil and the top lineal 3.05 m (10 ft) of the 2:1 slope. This modification would be accomplished in two phases. The top 0.15 m (6 in.) of soil would be excavated and stockpiled while the bottom 0.15 m (6 in.) would be treated in place with 5 percent hydrated lime. Upon completion of the bottom lift treatment, the bottom lift would be scarified, and the top 0.15 m (6 in.) would be returned and treated similarly. In lieu of the lime treatment of the top 0.30 m (1 ft) of the embankment, undercutting and replacing with nondispersive select material was recommended.
3. Stage 3 required filling in any holes along the 2:1 slope that were unable to be grouted. The soil used to fill these areas had to be classified as nondispersive according to double hydrometer analysis (ASTM 4221-90) and the pinhole test (ASTM 4647-87).
4. Stage 4 required flattening the existing 2:1 slope to a 4:1 slope beginning at the 6:1 roll-off slope extending to the toe of the embankment. The soil used in this stage was classified as nondispersive. This new slope construction was benched into the existing slope according to Section 202(c) of the Oklahoma Construction Specifications.
5. Stage 5 called for plating the 4:1 slope and the 6:1 slope with Bermuda grass solid slab sod.

CONCLUSIONS

The field and laboratory evidence conclusively identifies the soils used for embankment construction as high-sodium dispersive clays. Using the four tests described to identify dispersive soil is still considered appropriate practice for positive identification.

The recommendations suggested were accepted by the construction engineers responsible for the project and implemented by the project contractor. The final stage was completed in early April 1992. The side slopes of the embankment have displayed no signs of erosion, but there has been a continuing problem with depressions developing underneath the pavement where no treatment was applied. Inspection of these depressions revealed the presence of large voids under the pavement that had an average depth of 1.22 m (4 ft). This presents a significant maintenance problem as well as a liability problem if these depressions continue to appear. The project is continuing to be monitored.

At the time this study was conducted, the normal practice of the Oklahoma Department of Transportation was to allow unclassified borrow to be used as embankment material to get low contract prices. This process requires only soil classification and moisture-density tests for quality control without any preliminary screening for dispersive soils. The lesson in this case history is twofold:

1. In the reporting of preliminary soils reports, a greater effort will be made to examine the potential for dispersive soils in the highway alignment and potential borrow sources.
2. Where the use of dispersive soils appears to be unavoidable in certain areas of the state, design recommendations will be made to incorporate them in the project earthwork to negate their effect.

ACKNOWLEDGMENTS

The author would like to thank the Oklahoma Department of Transportation Materials Division for its support in this study. Special thanks is expressed to Jeff Dean and Ed Rios for participating in laboratory testing and preparing figures and tables, and to Lorraine Utley for typing.

REFERENCES

1. J. L. Sherard, L. P. Dunnigan, R. S. Decker, and E. F. Steele. Pinhole Test for Identifying Dispersive Soils. *Journal of the Geotechnical Engineering Division*, ASCE, Vol. 102, No. GT1, pp. 69–85.
2. C. H. McElroy. The Use of Chemical Additives to Control the Erosive Behavior of Dispersed Clays. In *Geotechnical Special Publication 10: Engineering Aspects of Soil Erosion, Dispersive Clay and Loess*, ASCE, pp. 1–16.
3. G. G. S. Holmgren and C. P. Flanagan. Factors Affecting Spontaneous Dispersion of Soil Materials as Evidenced by the Crumb Test. In *Special Technical Publication 623: Dispersive Clays, Related Piping, and Erosion in Geotechnical Projects*, ASTM, pp. 218–239.
4. N. L. Ryker. Encountering Dispersive Clays on Soil Conservation Service Projects in Oklahoma. In *Special Technical Publication 623: Dispersive Clays, Related Piping, and Erosion in Geotechnical Projects*, ASTM, pp. 370–389.
5. M. L. Jackson. *Soil Chemical Analysis*. Prentice-Hall, Inc., Englewood Cliffs, N.J., 1962.
6. J. L. Sherard, L. P. Dunnigan, and R. S. Decker. Identification and Nature of Dispersive Soils. *Journal of the Geotechnical Engineering Division*, ASCE, Vol. 102, No. GT4, pp. 287–301.
7. D. A. Lewis and N. O. Schmidt. Erosion of Unsaturated Clay in a Pinhole Test. In *Special Technical Publication 623: Dispersive Clays, Related Piping, and Erosion in Geotechnical Projects*, ASTM, pp. 260–273.
8. J. K. Mitchell. *Fundamentals of Soil Behavior*. John Wiley, New York, 1976, pp. 131–133, 218–221.

Publication of this paper sponsored by Committee on Transportation Earthworks.

Effects of Compactor Footprints on the Response of Subgrade Soil

JEFF BUDIMAN AND JOHANES WIBOWO

The influence of compactor footprints on the constitutive response of clayey sand subgrade soil was investigated. Three footprint types—flat base, cylindrical protrusion, and pyramid frustum protrusion—were examined using triaxial tests and pavement model tests under dynamic loading. First, each block sample was prepared using the compactor of certain footprint. The triaxial specimens were trimmed from the block sample at different orientations to represent the rotation of the principal stress direction. The results show significant variations in the responses. Samples compacted by the compactor with pyramid frustum protrusion base showed the highest lateral stiffness, followed by samples compacted with cylindrical protrusion, and finally those compacted with the smooth footprint. However, samples compacted with the flat base showed the stiffest response in the vertical direction. The subgrades of the pavement models were each compacted to the same density using compactors with different footprints. A dynamic load of 448 kPa was applied on the pavement model through a plate. Linear voltage displacement transformers and photographic techniques measured the deformation of the soil elements within the subgrade. The results show that, although the subgrade of the models were of the same density, the monitored displacements of elements within each pavement system were significantly influenced by the footprint type used during compaction. Traces of the displaced points show a significant variation of the deflection curve at the interlayer, which reflects rutting.

The performance of a flexible pavement is influenced by many factors, such as the asphalt type, asphalt content, aggregate type, gradation, density, subgrade type, compaction method, temperature, climate, magnitude and frequency of loads, and other variables. The interaction of all these factors yields a composite behavior for a particular pavement structure that can become evident in the form of distress, such as cracking, rutting, and potholes.

Approximately 70 percent of the total surface deflection of the pavement occurs within the subbase and subgrade soil. Figure 1, which illustrates the major principal stress distribution within the pavement system under the wheel load shows that the magnitude and the orientation of the major principal stresses vary from element to element within the system. The direction of the major principal stress directly under the contact area is primarily vertical and gradually rotates to other directions as the stresses are distributed away from the loaded area. The change of the in situ principal stress magnitude and direction in the pavement system is repeated as the traffic continues to flow.

J. Budiman, Department of Civil Engineering, Illinois Institute of Technology, Chicago, Ill. 60616. J. Wibowo, University of Colorado, Boulder, Colo. 80302.

Previous studies (*1–4*) indicate that both sands and clays have the weakest constitutive response in the direction perpendicular to the past major principal stress direction. As shown in Figure 1, the vertical deflection of the pavement is not only controlled by the stiffness of the material in the vertical direction, but it is also significantly affected by its stiffness moduli in other directions. Therefore, if the lateral stiffness modulus of the material could be increased during construction, the vertical deflection would be reduced.

The selection of a compactor during construction is primarily based on the effectiveness of the energy transfer to a given volume of soil to achieve a specified density. It is known, however, that a compaction roller with smooth wheels compacts the soil by a kneading mechanism, whereas the sheepsfoot roller type uses a combination of shearing and kneading mechanisms (*5*). If the soil was compacted to the same density by two rollers of different footprint types, the soil fabrics produced would also be different, directly affecting their stiffness moduli. In the current design practice, the vertical stiffness modulus of the soil has been incorporated to a certain extent; however, the lateral stiffness modulus has been either excluded as a design criterion or assumed to be equal to the stiffness in the vertical direction (isotropic).

In this investigation, three different compactor footprint types were used to study their influences on the stress-strain behavior of compacted soil. The study was conducted in a series of dynamic triaxial tests. Models of pavement segment were also tested in the laboratory to examine their performance. The three types of compactor footprints used were flat (smooth), cylindrical protrusion base, and pyramid frustum protrusion base.

TEST MATERIAL AND SPECIMEN PREPARATION

The soil for this experiment consisted of 65 percent Ottawa sand No. 30, 5 percent silica silt, and 30 percent Kaolin clay representing the subgrade material. The soil had a liquid limit of 25 percent and plastic limit of 19 percent. The compaction test performed according to AASHTO Standard T-99 revealed the optimum moisture content (OMC) of 9.75 percent and the maximum dry density of 2.03 g/cm^3. Because most design specifications for construction require 95 percent relative compaction, the specimens were compacted to that standard. For the results reported herein, the dry density of the soil was 1.93 g/cm^3, and the moisture contents were 11.5 percent and 8.25 percent. The primary reason the sand was mixed with the cohesive soil was for specimen preparation purposes.

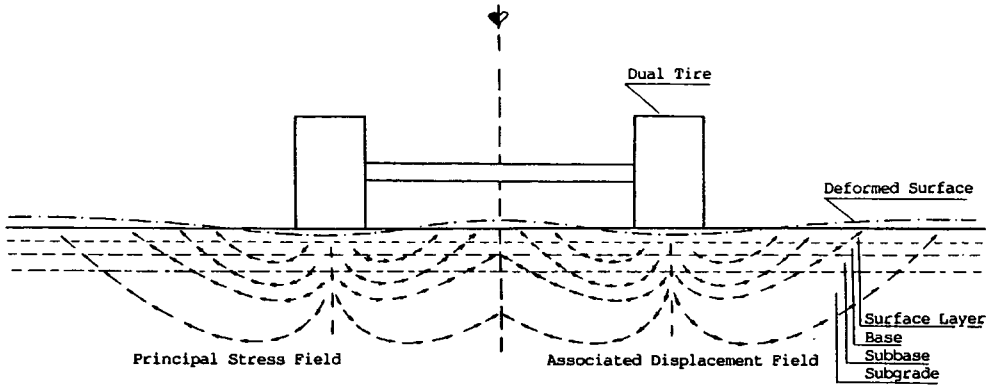

FIGURE 1 Approximate in situ principal stress field and associated displacement field.

The moisture and cohesion of the soil held the block specimen intact after compaction, enabling smaller specimens to be cut and trimmed from the large block specimen for further testing.

The soil was mixed with water to achieve the specified moisture content and then compacted in a large, stiff-walled mold of 20.32 × 30.48 × 25.4 cm to produce block samples. The block specimen was compacted in layers using the static undercompaction technique (*6*) to achieve a dry density of 1.93 g/cm^3. The compaction load was applied to the soil in the model through a rigid metal base plate in a universal loading machine, each plate representing a footprint type of the compactor. The three footprints represented were the flat smooth base, the sheepsfoot type with cylindrical protrusion, and the tampingfoot type with the pyramid frustum protrusion (Figure 2). The cylindrical protrusion was 12.7 mm in diameter and 25.4 mm high. The spacing of the protrusion was 3.5 times the diameter and was arranged in a triangular pattern. The pyramid frustum protrusion had the same height and volume as the cylindrical ones and was also arranged in the same pattern. The position of the projection on each layer was unchanged during compaction, that is, the location of each protrusion on the footprint of each succeeding layer was exactly above the previous one. The specimens for the triaxial testing were prepared from this large block sample.

Unlike the Directional Shear Cell (*1,7,8*), continuous stress rotation cannot be achieved in conventional triaxial testing. To simulate the rotation of the principal stress direction occurring within various soil elements in the subgrade, the triaxial specimens' axes were rotated. Three specimens were prepared from each block sample. Each specimen was cut and trimmed with its longitudinal axis rotated in a different orientation relative to the direction of compaction load: vertical ($\Psi = 0°$), inclined ($\Psi = 45°$), and horizontal ($\Psi = 90°$) (see Figure 3). These three specimens represented the three elements at different coordinates in the pavement system. The first specimen represented an element under the loaded area where the major principal stress direction is vertical. The second specimen represented an element where the major principal stress direction rotated to an inclined position. The third specimen represented an element where the major principal stress direction rotated to a horizontal position. The triaxial specimen was 71 mm in diameter and 152 mm high.

TRIAXIAL TEST RESULTS AND DISCUSSION

Two series of the dynamic triaxial tests were performed based on the specimen's moisture content, one test above OMC and the other below. Because the water content of the specimen was unchanged for each series of tests and the water content was insufficient to permit full saturation of the pores, there was no porewater pressure buildup during the test. The loading machine used in this experiment was the Material Testing System Closed-Loop Servo Hydraulic System Model 810.

The initial seating load was set at 34 kPa to simulate the overburden pressure. A confining pressure of 172 kPa was applied to the cell. This pressure represented approximate residual confining stress in the field. The maximum deviator stress was 275 kPa, representing the average wheel pressure within the subgrade soil. The cyclic haversine load with a frequency of 2 Hz was applied to the specimen. Because the effects of confining pressure and rate of loading in the cyclic triaxial tests have been studied by many investigators they will not be detailed here (*9–11*).

After all preliminary setting was completed, the software loaded the data and executed the test. During the test, the stress-strain data could be observed on a monitor screen or printed. Deformations during the test were recorded according to the following intervals; every cycle for the first 50 cycles, every 10th cycle for cycles 51 through 150, and every 50th cycle for cycles 151 through 10,000. The test was terminated after 10,000 cycles because the strains were relatively constant under the given load.

The results of the tests using samples with high moisture content are shown in Figures 4 through 8. Figure 4 shows the stress-strain response of samples compacted with the smooth flat base compactor. For the vertical specimen ($\Psi = 0°$), the total strain after 10,000 load cycles is about 0.56 percent, with a large percentage of the strain accumulated in the first few load cycles and little thereafter. This test result is also presented in the number of load cycles versus axial strain relationship as depicted in Figure 5. The same format is used to present other test results as well.

The maximum strain is defined here at maximum load, whereas the minimum strain is at the end of unloading; both curves show little increase in strain after the first few cycles.

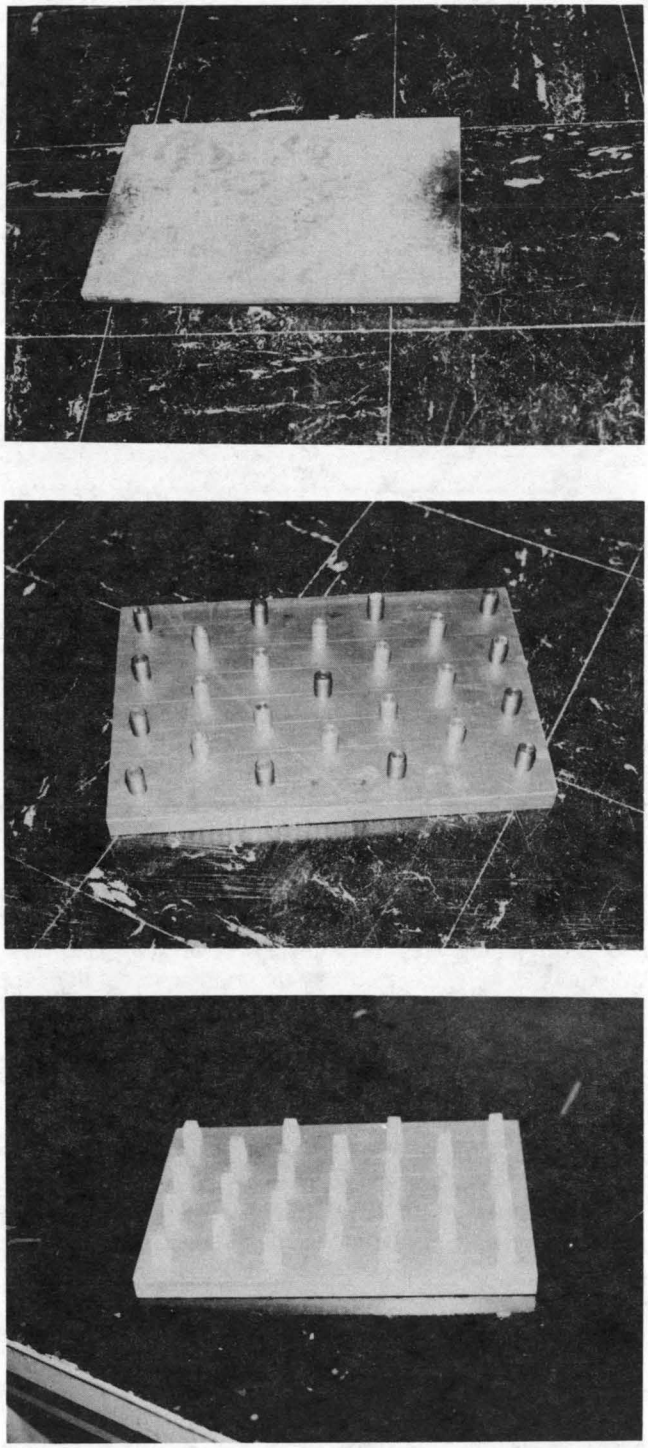

FIGURE 2 Compactor footprints: flat base (*top*), cylindrical protrusion (*middle*), pyramid frustum protrusion (*bottom*).

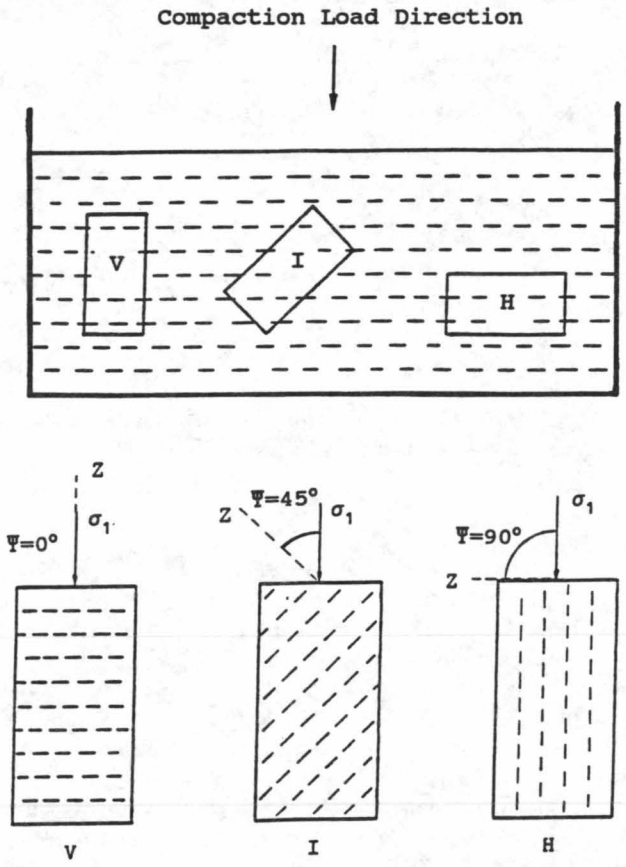

FIGURE 3 Triaxial specimens trimmed from block sample.

For the inclined specimen ($\Psi = 45°$), the response is similar to that observed in the vertical specimen; however, the magnitude of the strain is higher. For the same stress level and number of load applications, such as first cycle, the maximum strain in the vertical sample is 0.46 percent, whereas in the inclined sample the strain is 0.96 percent, or more than two magnitudes of the strain in the vertical sample. The permanent strain at the end of the test for the inclined sample is also significantly higher than the strain in the vertical sample.

The response of the horizontal sample ($\Psi = 90°$) under the same loading conditions shows a significant decrease in the stiffness modulus; here, the strain at the end of the test is 2.56 percent, or 460 percent higher than that of the vertical sample for the same loadings. In addition, unlike the response of the first and second samples, the total strain increases gradually with the number of load cycle.

The results of the tests for specimens compacted with the cylindrical protrusion compactor base are shown in Figure 6. The figure shows that the trends of the soil responses are similar to those observed in the sample compacted with the flat smooth base, that is, the largest total strain occurs in the horizontal sample followed by the inclined sample and vertical sample. Furthermore, a significant percentage of the total strain is accumulated during the earlier load cycles. However, the magnitude of the total strains for the horizontal and inclined samples are lower than the corresponding strains for specimens compacted with the flat base for the same loading condition. The total strains in the vertical samples are higher than the corresponding strains for samples compacted with the flat base.

The responses of specimens compacted with the pyramid frustum base compactor are shown in Figure 7. In general, the accumulation of the strain is similar to the previous cases, that is, the strains for the horizontal samples are always the largest compared to those of inclined and vertical samples,

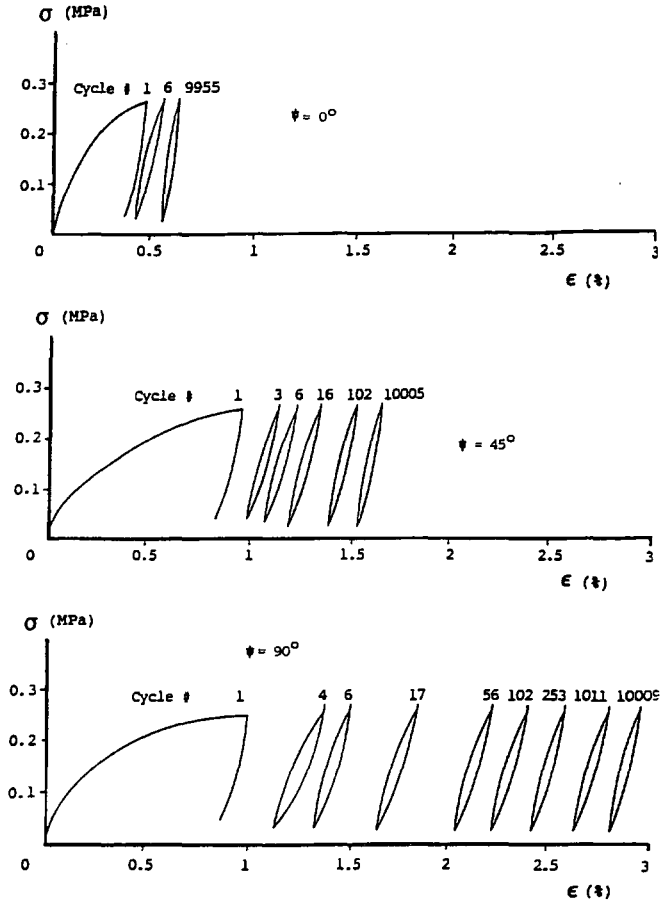

FIGURE 4 Stress-strain response of specimen compacted with flat base compactor, above OMC.

where the vertical samples produced the smallest strains. After 10,000 cycles of loading, the vertical sample produced about a 1.05 percent strain, whereas the horizontal sample produced a strain of 1.65 percent, or about 57 percent more strain than the vertical sample. The inclined sample produced a 1.45 percent strain, or about 38 percent more than the strain in vertical sample. Again, the stiffness modulus of the vertical sample is higher than that of the other two samples.

Figure 8 shows the response of the total strain with respect to the stress rotation angle relationship from all the tests above. A significant variation in strain occurred in the samples compacted with the flat base compactor, as indicated in Figure 8 by the steeper slope of the line drawn through the three points of the total strain. The slope of the curve for the samples compacted with pyramid protrusion base is the flattest among the three, showing less variation in the stiffness moduli of the material. An isotropic material would yield a perfect horizontal line. For the three vertical samples, the sample compacted with a flat base produced the lowest strain compared to those compacted with bases with cylinder or pyramid protrusions. However, for horizontal samples, the sample of flat base produced the largest strain. The strain from the three inclined samples shows the same tendency as for the horizontal samples, but to a lesser degree. The results show that samples compacted with a protruded base compactor result in less variation in the stiffness of the samples in various directions. This observation also indicates that the lateral stiffness is significantly increased and thus the degree of anisotropy is reduced. The protrusion of pyramid frustum type is more effective than that of cylinder type in increasing the horizontal stiffness of the soil. This shows the effect of the protrusion shape. It is believed that the effectiveness of the pyramid protrusion in compacting the soil is that when the soil is being compressed, the inclined walls of the pyramid

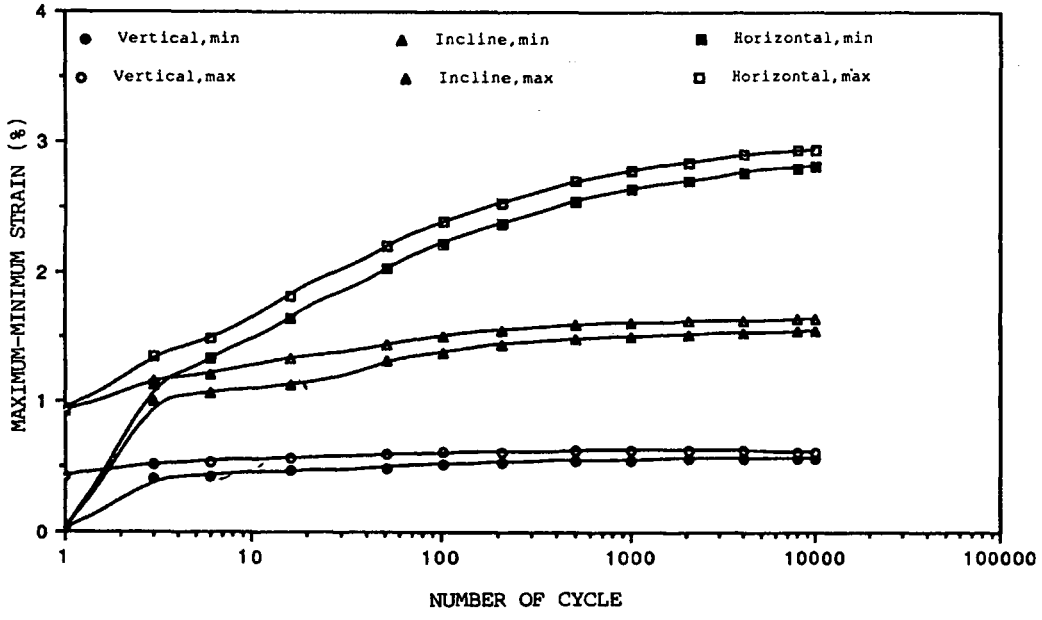

FIGURE 5 Strain versus load cycle response of specimens compacted with flat base, above OMC.

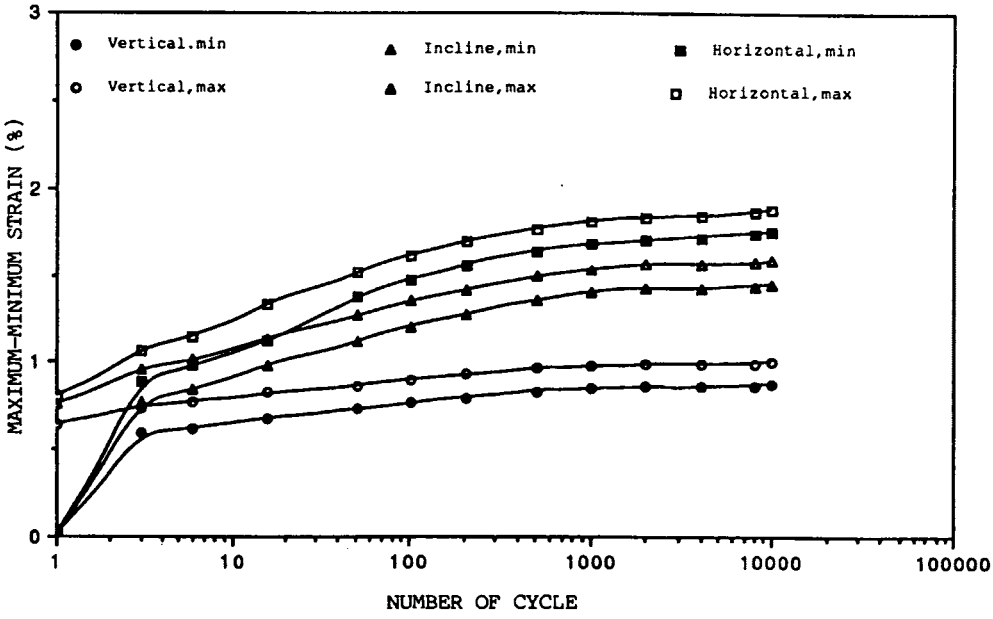

FIGURE 6 Strain versus load cycle response of specimens compacted with cylindrical protrusion base, above OMC.

also cause the soil to be displaced and thus compacted laterally as the protrusion penetrates into soil. At this stage, the lateral pressure in the soil generated by the inclined wall of the protrusion is higher than the lateral pressure generated with the soil when compacted with a flat base compactor or even with a cylinder type protrusion base.

In the second series of tests, the soil moisture content was reduced to 8.25 percent (below optimum). During compaction, significantly larger loads were required to compact this soil to achieve the same dry density than that of the soil with higher moisture content. These samples were much stiffer than the ones with higher water content. These phenomena are well known.

The response of specimens compacted by a flat footprint shows similar behavior as the ones compacted above OMC. The horizontal sample experienced the largest strain, followed by the inclined sample and the vertical sample, which experienced the smallest strain (Figure 9). The figure also shows that after 10,000 cycles of loading, the vertical sample produced about 0.32 percent strain, whereas the horizontal sam-

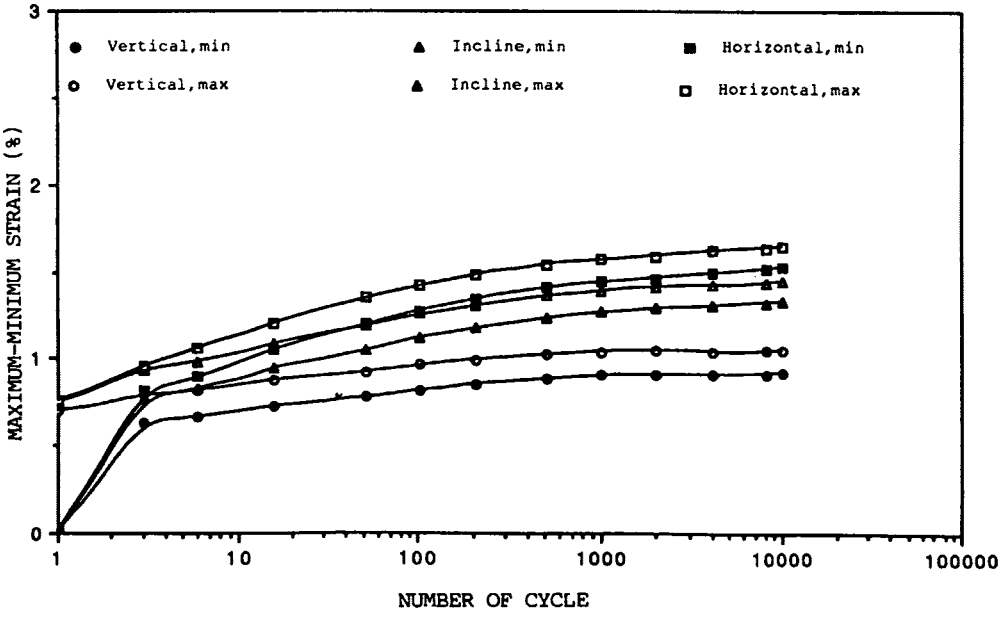

FIGURE 7 Strain versus load cycle response of specimens compacted with pyramid frustum base, above OMC.

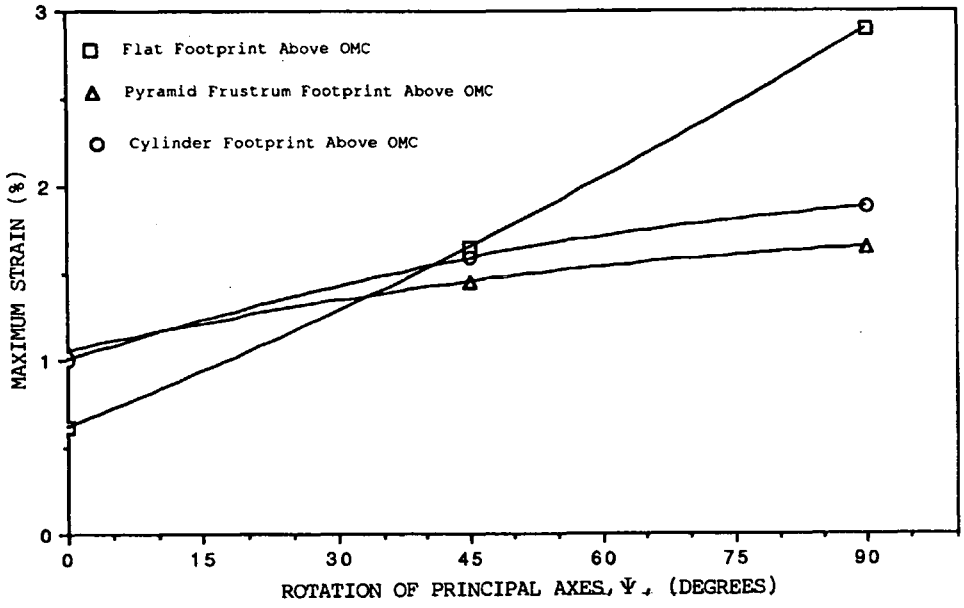

FIGURE 8 Maximum strain versus angle of principal stress direction response, above OMC.

ple produced a 0.62 percent strain, or about 94 percent higher than the strain for the vertical sample. The inclined sample produced a 0.48 percent strain, which is about 50 percent higher than the strain for vertical sample.

Figure 10 shows the results of the specimen compacted with a cylindrical protrusion footprint. The strain value of the horizontal sample is only slightly higher than that of the vertical sample. After 10,000 cycles of loading, the vertical sample produced about a 0.35 percent strain, while the horizontal sample produced a 0.37 percent strain or about 6 percent higher than the strain for vertical sample. The inclined sample produced a 0.45 percent strain, which is about 29 percent higher than the strain for the vertical sample.

Figure 11 shows the results on specimens compacted with the pyramid frustum base compactor. The trend depicted in Figure 11 is similar to that shown in Figure 10. After 10,000 cycles of loading, the vertical sample produced about a 0.34 percent strain, whereas the horizontal sample produced a strain of 0.37 percent, which is about 9 percent higher than the strain for the vertical sample. The inclined sample produced a 0.52 percent strain, which is about 53 percent higher than the strain for the vertical sample. The total strain and stress rotation

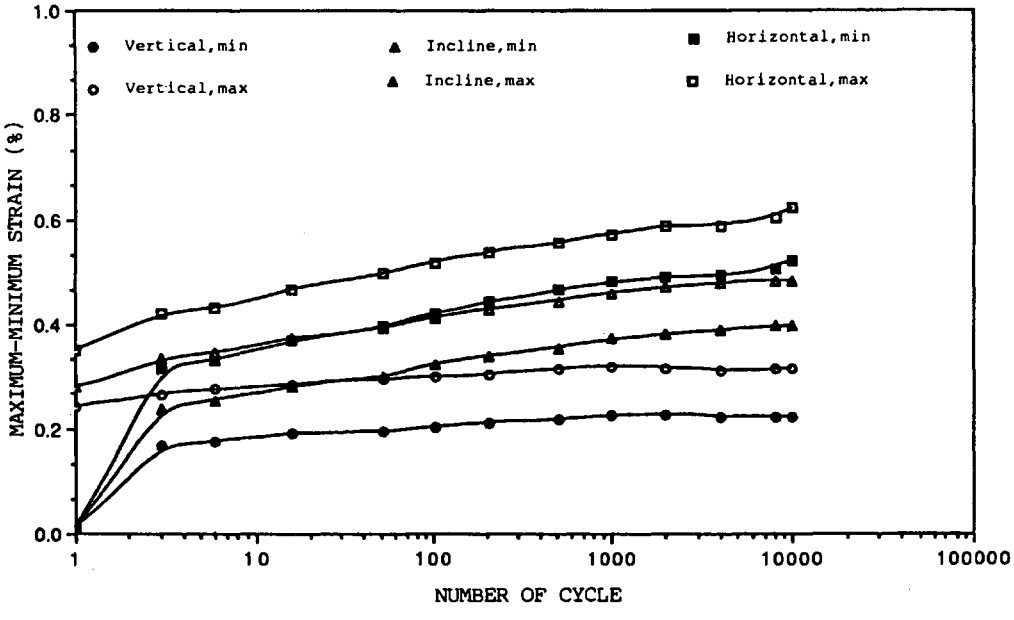

FIGURE 9 Strain versus load cycle response of specimens compacted with flat base, below OMC.

angle relationship depicted in Figure 12 shows that the protruded base resulted in stiffer samples; however, the shape of protrusion is insignificant.

As expected, the two series of tests revealed that the overall strains in the samples compacted at a lower water content are smaller than those compacted at a higher water content. Comparing the results in Figures 8 and 12 for samples of a flat base compactor, the ratio of strain in the horizontal sample to the vertical sample is about 4.7 for a sample with a high moisture content and only 1.1 for a sample with a low moisture content. Furthermore, the effects of moisture content on the anisotropy can also be observed through the difference of strain in vertical and horizontal samples. For samples compacted with a flat base, the strain difference for below OMC samples is 0.3 percent, which is significantly less than 2.3 percent, the value for the specimens with water content above OMC. Considering the difference of the strains, the degree of anisotropy of the specimens is smaller in the

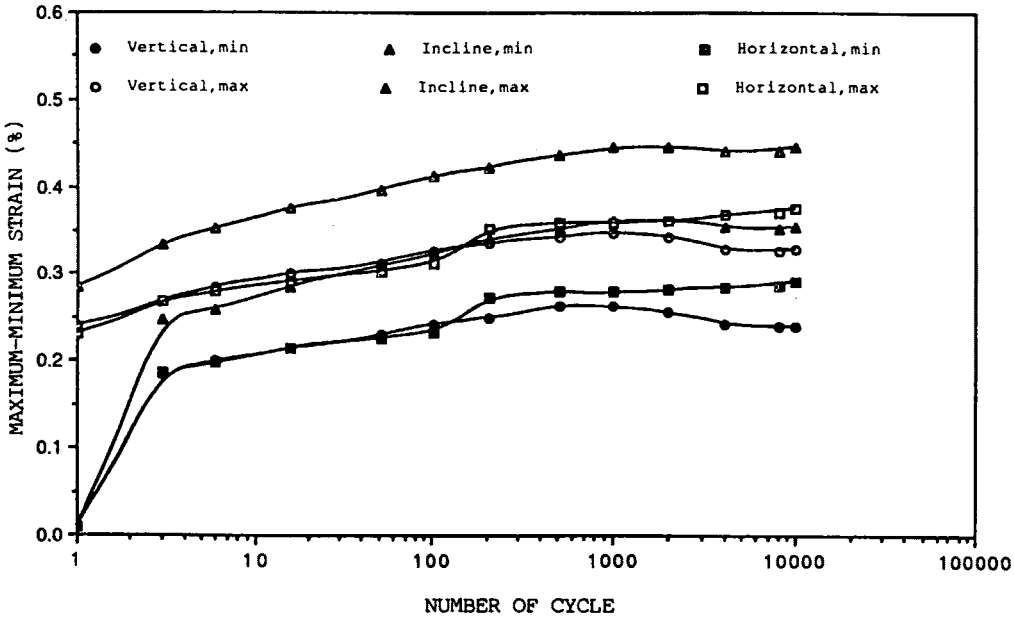

FIGURE 10 Strain versus load cycle response of specimens compacted with cylindrical protrusion base, below OMC.

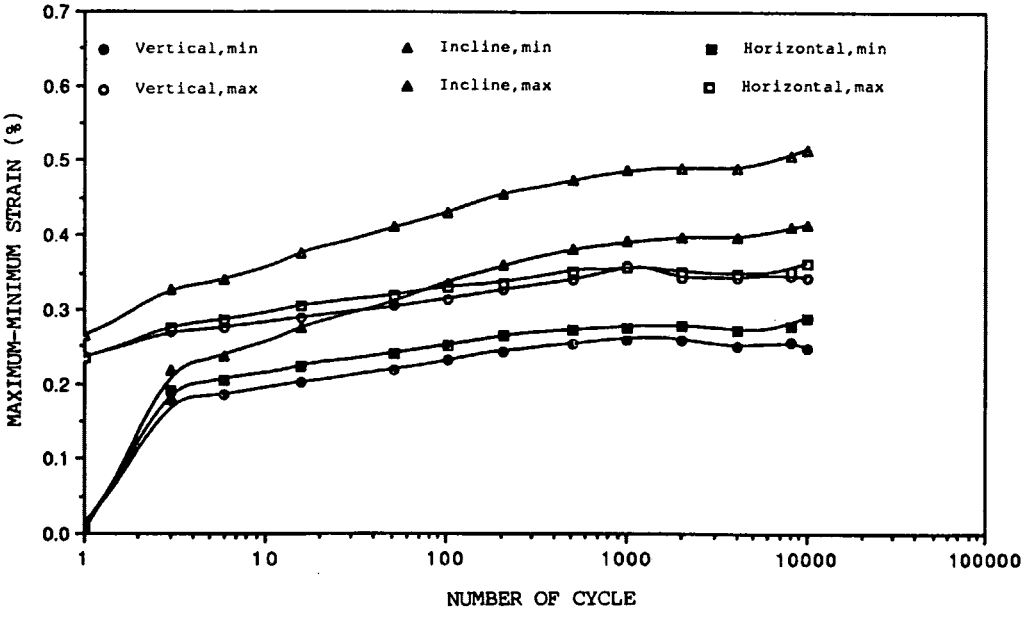

FIGURE 11 Strain versus load cycle response of specimens compacted with pyramid frustum base, below OMC.

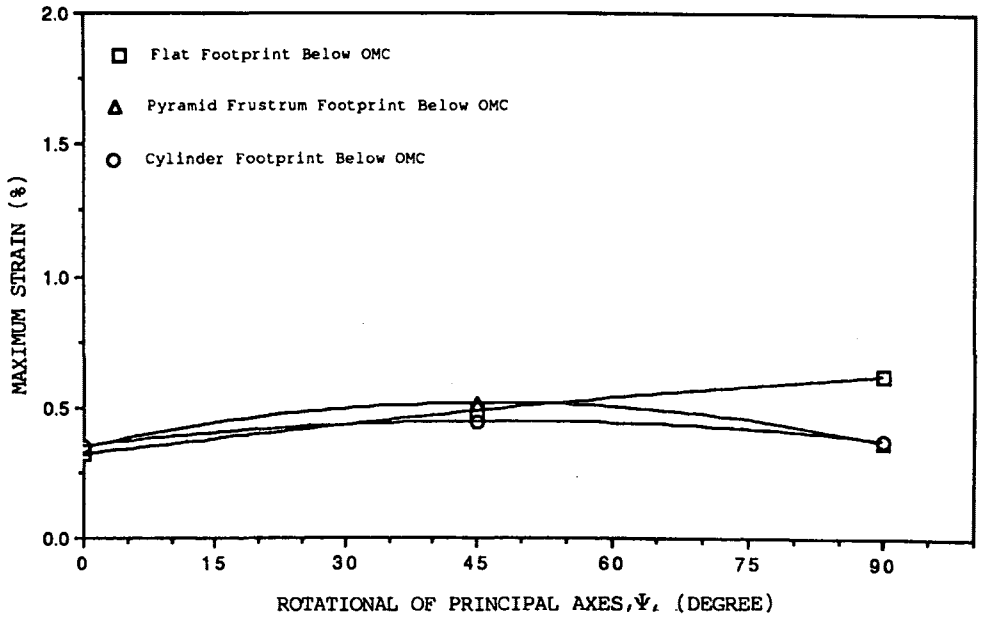

FIGURE 12 Maximum strain versus angle of principal stress direction response, below OMC.

specimens compacted below OMC than that in those compacted above OMC.

The results also show that, regardless of the type of footprint used, the specimens become anisotropic as a result of compaction. Consequently, they possess different characteristics in different directions with respect to the orientation of the compaction load (maximum pressure). In general, they are stiffer in the direction of maximum past pressure and softer or weaker in the direction perpendicular to the maximum past pressure, especially for samples compacted at a higher moisture content. The effects of the footprints on the constitutive response are also clearly depicted; the protrusion significantly increases the stiffness in the inclined and horizontal samples. The shape of the protrusion is more influential in samples that are above OMC than those below OMC.

MODEL TEST RESULTS AND DISCUSSION

Three model tests of each moisture content were performed in the laboratory to observe the influence of the types of compactor footprints on the deformation within the subgrade layer. These models represented a segment of the pavement system. Because the wheel load is symmetrical about the center of each lane of the roadway, only half of the section was necessary for modeling. Each model was compacted with the compactor having one of the three different types of footprints: the flat base, the cylindrical protrusion base, or the pyramid frustum protrusion base similar to those used for preparing triaxial specimens. The models were constructed in a Plexiglas box. The Plexiglas walls were reinforced with steel C-channels from the outside to provide rigid boundaries for plane strain conditions. The transparent walls allowed direct observation of the subgrade. The subgrade layer of 10.16 × 50.8 × 30.48 cm was compacted in 12 layers using the undercompaction method similar to that used in preparing the triaxial samples. For the asphalt layer of the model, cold ready-mixed asphalt was used and compacted to a density of 2 g/cm^3. Thin teflon sheets were placed between the walls and the soil to eliminate friction at the interface. To allow observation of the deformation within the subgrade, 12 slender steel rods of 2.5 mm in diameter were inserted into the subgrade model through holes drilled on one side of the wall. The monitoring rods were inserted in the subgrade at specified coordinates. During loading, linear voltage displacement transformers monitored and periodically recorded the horizontal and vertical displacements of the rods that were implanted in the subgrade. Deformation within the subgrade was also observed by photographing 88 pins in a grid pattern on the opposite side of the section. To implant these pins, the wall opposite to the side where the steel rods were inserted was temporarily removed, and 88 monitoring pins were inserted into the subgrade in a grid formation through the teflon sheet, exposing only the pinheads. The pinheads were periodically photographed to trace their movement.

The loading machine previously used for the dynamic triaxial tests was used in this experiment. The dynamic loads of passing vehicles were assumed as haversine loads. A square plate of 10.16 × 10.16 cm was mounted to the base of the loading ram. In turn, the dynamic contact pressure of 448 kPa was transferred to the center of the model through this plate.

The results of the three model tests with a high water content are presented in Figure 13. The deformations of five rods that were relatively far from the loaded area were too small to be analyzed. The analysis then focused on the results of the remaining seven rods: Rods 1–3, 5–7, and 9.

Rod 1 was located at the top of subgrade and below the center of the loaded area. For the model compacted with the flat base footprint, Rod 1 reached a vertical displacement of 4 mm after 500 load cycles. For models compacted with cylinder or pyramid frustum footprints, the same magnitude

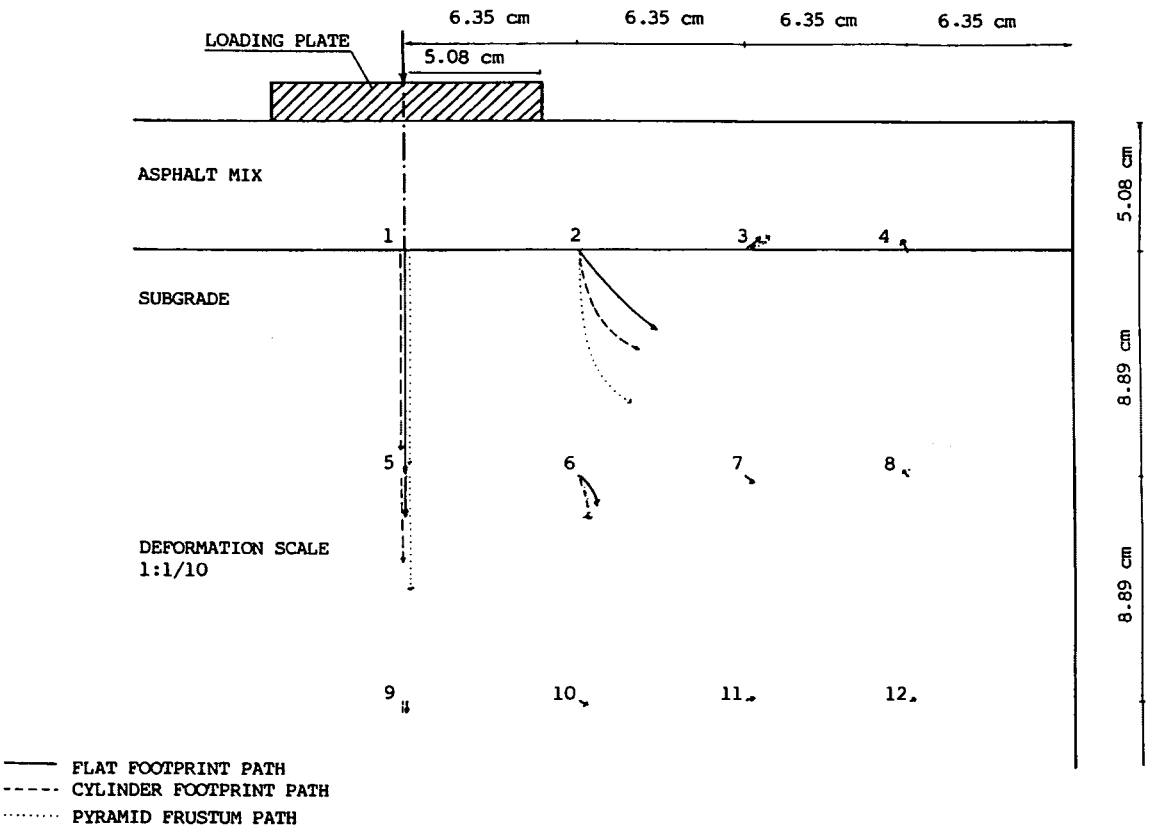

FIGURE 13 Displacement of rods within the pavement model, above OMC.

of displacement for Rod 1 was reached after only 25 load cycles. These observations show that the model compacted with the flat base compactor is stiffer in the vertical direction than the models compacted with a cylinder or pyramid frustum compactor.

After 10,000 load cycles, it was also observed that on Rods 2 and 6, the horizontal displacements were larger in the model compacted with the flat base compactor than in the models compacted with the cylinder or pyramid frustum compactor. To the contrary, the largest vertical displacement for these two rods occurred in the model compacted with the pyramid frustum compactor, followed by the displacement in the model compacted with the cylinder and flat base compactors, respectively.

Rods 3 and 4 moved upward from the loaded area; however, the magnitude was minuscule. Rods 5 and 9 on the model compacted with the flat base compactor deformed the least compared to the models compacted with cylinder or pyramid frustum base compactors. This shows that the model compacted with the flat base compactor is stiffer in the vertical direction than the other two models.

For the models compacted with a moisture content below optimum, after 10,000 load cycles, no measurable deformation of the rods was recorded. Subsequently, the load was increased to 620 kPa for each test to obtain measurable deformations. The results are presented in Figure 14. For Rods 1 and 5, the vertical displacements for the model compacted with the flat base compactor do not show significant difference in magnitude as opposed to the results from the models with a high moisture content. The response of Rod 5 showed less deformation in the sample compacted with the flat base footprint than the one with the cylindrical protrusion base. The displacement on Rods 2–4 and 6 indicates that the largest horizontal displacements occur in the model compacted with the flat base compactor. This observation is consistent with the results of the first series of tests, which show that the stiffness in the horizontal direction of the model compacted with the flat footprint is the lowest for both water contents.

Observation of the response of Rods 1–4, which were located at the interface between the asphalt layer and the subgrade soil, reveals that if a line were drawn connecting the arrow heads of the plot from each model test, the line would show that the worst rutting occurred in the model compacted with the flat footprint compactor. In the model with flat compactor, the vertical component of the displacement of Rods 3 and 4 were displaced relatively upward. In the other two models, these rods were not displaced upward. To control the density and uniformity of the specimens, the laboratory specimens were compacted using static compaction and did not simulate the conditions of field compaction.

CONCLUSIONS

The results of these model tests are consistent with the results of the dynamic triaxial tests. It is obvious that the subgrade layer is anisotropic and the stiffness modulus in the horizontal direction can be increased by using a compactor with a protrusion base. During construction, the type of compactor footprint used for compaction also significantly influences the load-deformation behavior of the soil. This was demonstrated

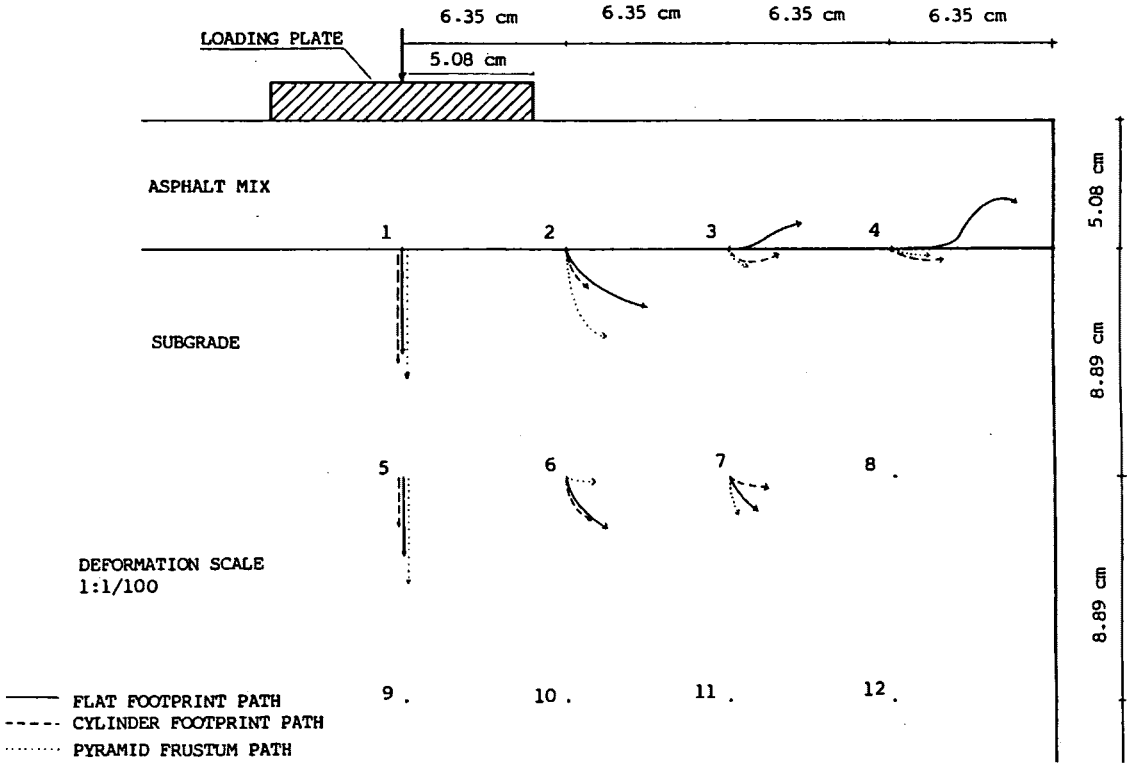

FIGURE 14 Displacement of rods within the pavement model, below OMC.

by the fact that all specimens in this study were compacted to the same dry density; however, they possessed different characteristics. This study also showed the importance of recognizing the material anisotropy because using the stiffness modulus in the vertical direction alone as a design criterion may result in a faulty prediction of the service life of the pavement. The study results suggest that compaction using a protruded wheel produces a pavement that better withstands rutting.

The goal of this study was to investigate the effects of the footprints on the material response under loading. This investigation used the static compaction method to avoid variation in the samples due to the compaction process. Because static compaction does not simulate a field compaction mechanism, further investigation on specimens compacted with rollers that have different types and sizes of footprints on various types of soils is highly recommended. Further study in this direction should reveal other critical information on how to improve the endurance of the subgrade material against permanent deformation.

ACKNOWLEDGMENTS

The authors greatly appreciate the financial support of the Engineering Foundation.

REFERENCES

1. S. Sture, J. S. Budiman, A. K. Ontuna, and H-Y. Ko. Directional Shear Cell Experiments on a Dry Cohesionless Soil. *Geotechnical Testing Journal*, ASTM, Vol. 10, No. 2, 1987.
2. M. Oda. Anisotropic Strength of Cohesionless Sands. *Journal of the Geotechnical Division*, ASCE, Vol. 107, GT9, 1981, pp. 1,219–1,231.
3. A. S. Saada and C. D. Ou. Stress-Strain Relations and Failure of Anisotropic Clays. *Journal SMF Division*, ASCE, Vol. 99, No. SM 12, 1973.
4. T. W. Lambe. The Engineering Behavior of Compacted Soil. *Journal SMFE*, Proc. Paper 1655, ASCE, Vol. 84, 1958.
5. R. D. Holtz and W. D. Kovacs. *An Introduction to Geotechnical Engineering*. Prentice-Hall, Englewood Cliffs, N.J., 1981.
6. R. S. Ladd. Preparing Test Specimen Using Undercompaction. *Geotechnical Testing Journal*, ASTM, Vol. 1, 1978, pp. 16–23.
7. J. R. F. Arthur, S. Bekenstein, J. T. Germain, and C. C. Ladd. Stress Path Tests with Controlled Principal Stress Directions. *Laboratory Shear Strength of Soil*, STP 740, ASTM, Philadelphia, Pa., 1980.
8. J. S. Budiman, S. Sture, and H-Y. Ko. Constitutive Behavior of Stress Induced Anisotropic Cohesive Soil. *Geotechnical Engineering Journal*, ASCE, Sept. 1992.
9. N. D. Pumphrey, Jr. and R. W. Lentz. Deformation Analysis of Florida Highway Subgrade Sand Subjected to Repeated Load Triaxial Tests. In *Transportation Research Record 1089*, TRB, National Research Council, Washington, D.C., 1986.
10. S. F. Brown and A. F. L. Hyde. The Significance of Cyclic Confining Stress in Repeated Load Triaxial Testing of Granular Materials. In *Transportation Research Record 537*, TRB, National Research Council, Washington, D.C., 1975.
11. H. B. Seed and C. K. Chan. Effect of Duration of Stress Application on Soil Deformation Under Repeated Loading. *Proc., Fifth International Conference on Soil Mechanics and Foundation Engineering*, Paris, 1961.

Publication of this paper sponsored by Committee on Transportation Earthworks.

Geotechnical Characteristics of Salt-Bearing Soils in Kuwait

NABIL F. ISMAEL

Salt-bearing soils exist along the shorelines of Kuwait and the Persian Gulf states. Many areas inland are also covered by these sediments, which are locally called "Sabkha." The geotechnical properties and behavior of these soils were examined by a comprehensive field and laboratory testing program. The program included penetration tests, sampling, basic properties, consolidation and triaxial tests at two locations within one site in Doha, Kuwait. In addition, plate load tests were conducted using a 0.3-m diameter plate to determine the bearing capacity. The variation of the soil properties with depth was assessed. Test results indicate that a cemented crust develops at ground surface because of the arid climate, which causes continuous evaporation and precipitation of salts in the soil matrix. Below this crust, the soil remains loose with low strength. Sabkha consists of loose gypsiferous fine sandy silt with little clay. It has lower specific gravity and higher moisture contents than other granular soils. Sulphates exceed 60 percent of the soil composition at ground surface and decrease sharply with depth. Consolidation and triaxial tests indicate increased compressibility and decreased strength with depth. The static cone penetration values ranged from 200 to 600 kPa for the point resistance and 0 to 150 kPa for the frictional resistance. The bearing capacity varied from 40 to 50 kPa at 0.3 m depth with a higher value at the ground surface. The problems associated with these soils, including volume changes, corrosive behavior, and low strength, are discussed.

Salt-bearing soils extend along the coastline of Kuwait and the Persian Gulf states as well as throughout the Middle East, Central Asia, the western coast of South America, and parts of the United States. This soil is locally called "Sabkha," which defines coastal flat areas that extend above the high-tide level and are covered by evaporate-rich clastic sediments (*1*). Due to the high salinity of the near-surface ground water and the excess of evaporation over rainfall, salts (particularly gypsum, chlorides, and carbonates) are precipitated in the surface layers, leading to salt crusts. Under dry conditions, the Sabkha provides an excellent running surface for wheeled vehicles, but under high water table conditions, or as a result of heavy rainfall, the soluble salts dissolve and the surface becomes impassable (*2*). Vehicles can break through the surface crust, but they are then up to their axles in liquid mud (*3*).

Several geological studies were conducted on these deposits to determine origin and deposition (*4,5*). The damage to bituminous-paved roads following construction on these soils has long been well recognized (*6*). The problems associated with volume changes due to dehydration of gypsum at high temperatures followed by rehydration in the presence of water are documented (*7*). Parameters for pavement design purposes were determined recently by field and laboratory tests on these soils (*3*). However, there is no detailed or comprehensive geotechnical investigation of the properties and the characteristics of these deposits that provides a clear understanding of their behavior under load. Such an understanding is essential to design and construct structures on these soils and to improve or stabilize soil if necessary.

With the presence of these deposits in areas of potential development in Kuwait, such as Al-Subbiyah, Al-Doha, and Al-Khiran (Figure 1), an extensive field and laboratory testing program was conducted at the site of the proposed Olympic village in Doha, Kuwait. The work included sampling, classifications, static and dynamic cone penetration tests, basic properties, chemical analyses, and consolidation and triaxial tests on undisturbed samples. Plate load tests were also performed using a 0.3-m diameter plate. Other tests involving laboratory and field leaching tests are included in a separate paper (*8*).

In this paper, the author presents and discusses the field and laboratory test results, emphasizing the special and unique geotechnical characteristics of salt-bearing soils. The change of the soil properties with depth is noted and discussed, as is the influence of environmental factors on the soil properties.

SITE CHARACTERIZATION

The testing site location in Doha, Kuwait, and the locations of major Sabkhas in Kuwait are shown in Figure 1. Two points within the site located along a line 2.9 km from the shoreline and spaced 400 m apart were selected for the detailed soil investigation. At each location, one hollow stem auger boring was advanced to a depth of 9 m. Standard penetration tests and linear samples were taken at 0.5 m intervals to a depth of 4 m and at 1 m intervals below this depth. Another boring was drilled nearby to obtain undisturbed thin-walled Shelby tubes at the different depths in the boreholes. The field tests included dynamic and static cone penetration tests (CPTs) at two points 3 m apart in the vicinity of the boreholes. To carry out the tests, the Dutch cone penetrometer conversion kit was used. The kit easily converts the CME 750-XL drill rig to a mechanical Dutch cone penetrometer tester. Details of the test procedure can be found elsewhere (*9*).

The soil conditions at the two test locations are summarized in Figures 2 and 3. The soil profile consists of a surface layer of loose gypsiferous fine sandy silt with a little clay (Sabkha) to a depth of 2.5 m. This is underlain by silty clayey sands, sands, and silty sands to the bottom of the boreholes. The

Civil Engineering Department, Kuwait University, P.O. Box 5969, Safat 13060, Kuwait.

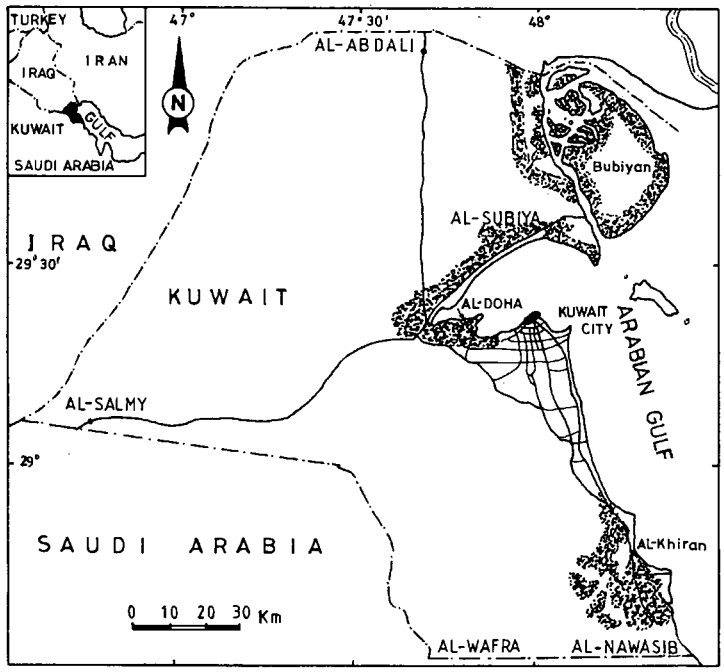

FIGURE 1 Map of test site and location of Sabkhas in Kuwait.

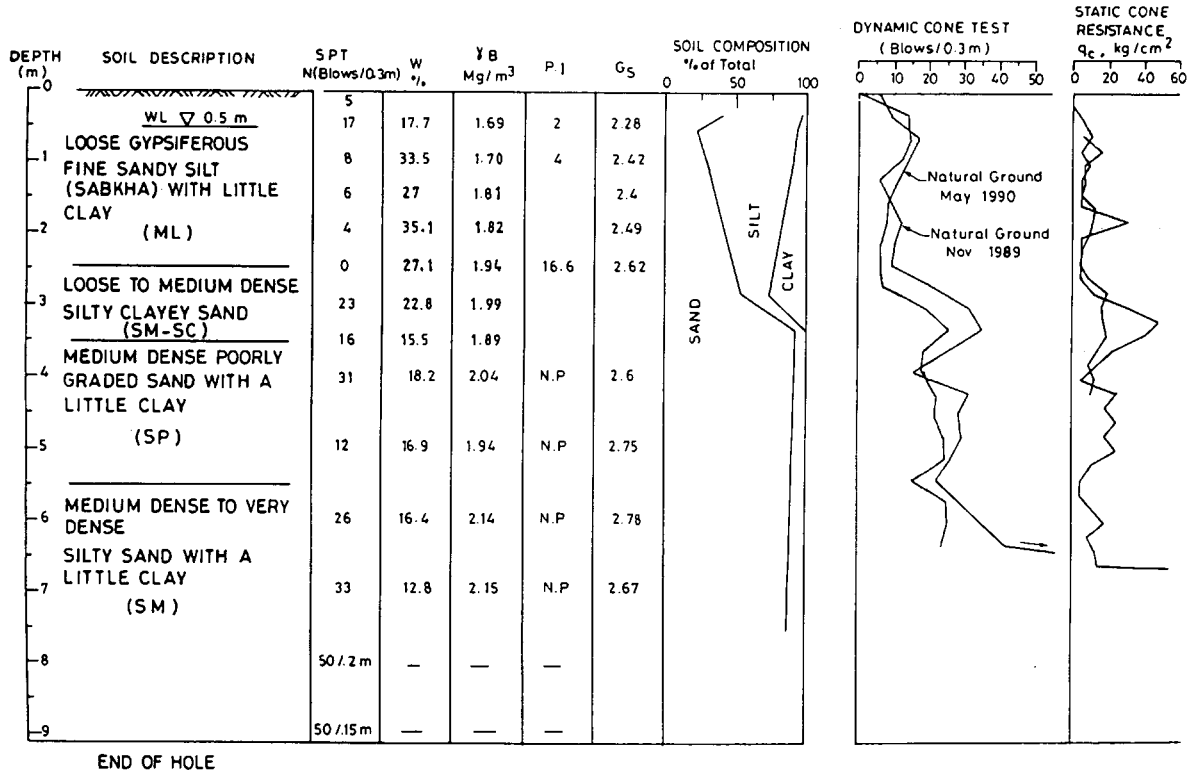

FIGURE 2 Soil conditions at test site—Borehole 1 (*8*).

upper layer contains lenses of gypsum, particularly near the ground surface. Groundwater was encountered at a depth of 0.5 m below the ground level.

A close examination of Figures 2 and 3 reveals that the upper layer has lower specific gravity and a higher moisture content than most granular soils. The specific gravity ranges from 2.3 to 2.5, and the moisture content varies up to 35 percent. The dynamic penetration resistance with depth indicates a hard salt crust up to a depth of 1.0 m, followed by low penetration resistance to the bottom of the layer. A similar tendency is visible in the static cone penetration resistance measurements, which are shown in Figure 3. These low values range from 200 to 600 kPa for the point resistance (q_c), and 0 to 150 kPa for the frictional resistance (f_s).

Figure 4 shows the main soil components as determined from the chemical analysis on the samples of Borehole 1. As

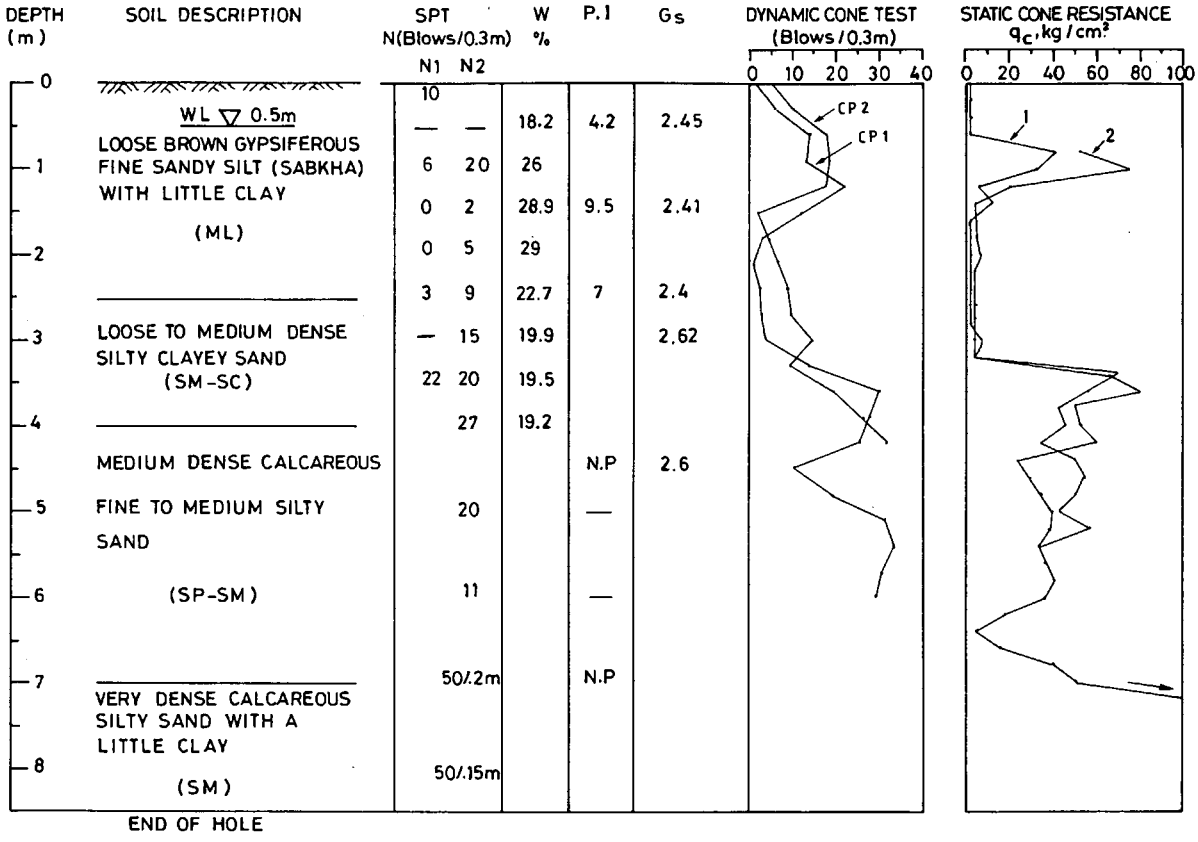

FIGURE 3 Soil conditions at test site—Borehole 2.

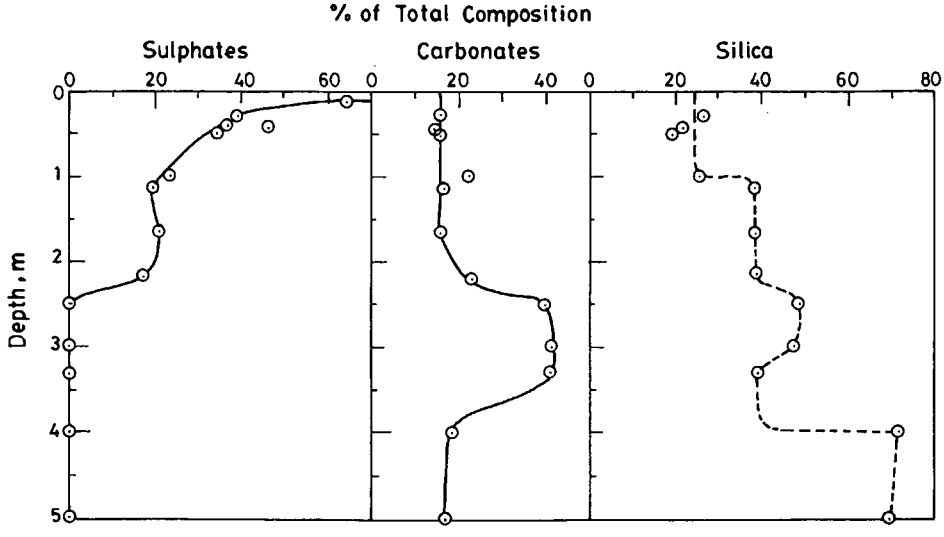

FIGURE 4 Main components of Sabkha as determined from chemical analysis (*8*).

shown, sulphates exceeded 60 percent of the soil composition at ground surface and decreased sharply with depth, reaching 20 percent at a depth of 1 m and zero at a depth of 2.5 m. Carbonates consisting mainly of calcium carbonate ranged from 15 to 20 percent in the upper layer. Silica constituted 25 percent, increasing to 40 percent below a depth of 1 m.

The presence of sulphates affects the behavior of salt-bearing soils (*8*). The sulphates consist of either gypsum or anhydrite. The main difference between the two minerals is that gypsum has two weakly bound molecules of water, whereas anhydrite has no such molecular water (*7*). The properties of gypsum and anhydrite are summarized in Table 1. The molecular water in gypsum is unstable and at high temperature dehydrates to form anhydrite. A volume decrease of 39 percent occurs with this reaction if the molecular water evaporates. The hydration of anhydrite results in a 63 percent volume increase.

One of the more interesting characteristics of salt-bearing soils is the influence of the drying temperature in the laboratory on the moisture content and other basic properties. Oven drying the gypsum soils tested at 60°C or using a vacuum desiccator and a temperature ranging from 23°C to 60°C for drying in accordance with ASTM D2216 brings identical results. However, drying at temperatures from 80°C to 110°C results in significant loss of hydrated water and large moisture contents. Drying also affects other properties, including specific gravity and Atterberg limits. The values shown in Figures 2 and 3 were obtained for samples that were oven dried at 60°C. It is interesting to note that one way to find the thickness of these deposits is by determining the moisture contents by oven drying the soil at temperatures of 60°C and 110°C. The layer ends where there is no difference in the moisture content obtained from the two methods. This is shown in Figure 5 where the variation of the moisture content and the specific gravity are plotted for samples from Borehole 1. At a depth of 2.5 m, the moisture content is the same for the drying temperatures of 60°C and 110°C, indicating the end of the gypsum deposit.

Wherever possible, the soils used for Atterberg limit tests should not be oven dried at temperatures exceeding 60°C before testing. Higher liquid and plastic limits are obtained from oven drying gypsum and tropical soils at high temperatures compared with air drying preparation. A 30-percent increase, for both liquid and plastic limits, is measured from tests on the present soils. Conversely, lower liquid and plastic limits are usually associated with oven drying organic soils.

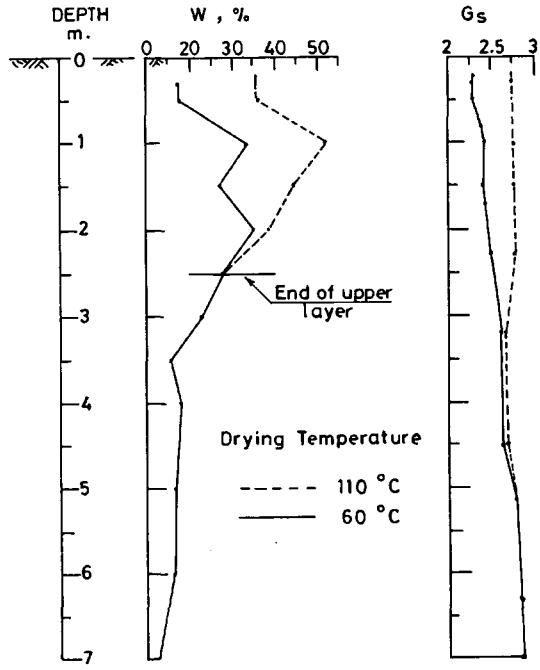

FIGURE 5 Moisture content and specific gravity with depth—Borehole 1.

The preceding results emphasize the importance of the drying temperature on the properties of salt-bearing or gypsum soils. Oven drying at a high temperature also causes the soil particles to subdivide, changing the grading characteristics of these soils. Figure 6 shows the grain-size distribution curves of two natural samples taken at a depth of 0.3 m from Borehole 1. One sample was air dried, whereas the second was oven dried at a temperature of 110°C prior to sieving. The difference in the grading curves for these samples is significant.

TABLE 1 Properties of Gypsum and Anhydrite (*7*)

	Gypsum ($CaSO_4H_2O$)	Anhydrite ($CaSO_4$)
% $CaSO_4$ (by weight)	79.1	100
Mohs Hardness	1.5 - 2	3 to 3.5
Specific gravity	2.3 to 2.4	2.92 to 2.98
Weight kg per m^3	2,250 to 2,400	2,885
Crystal system	Monoclinic	Orthorhombic
Dilute HCl	Soluble without effervescence	Slightly soluble without effervescence
At temperatures above 42°C	Converts to hemihydrate or anhydrite	No reaction
At temperatures below 42°C	No reaction	Converts to gypsum in the presence of water

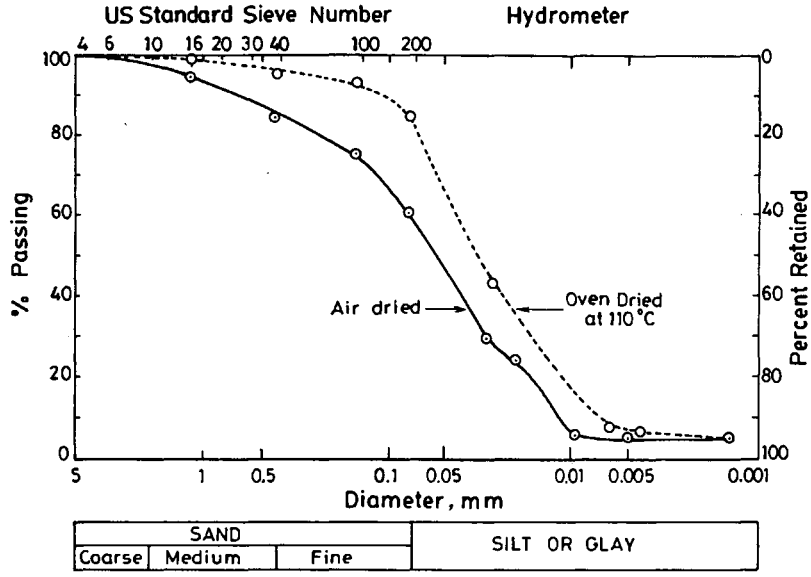

FIGURE 6 Grain-size distribution curves—Borehole 1 (depth = 0.3 m).

CONSOLIDATION TEST RESULTS

Consolidation tests were conducted on undisturbed samples from Boreholes 1 and 2 to determine the compressibility characteristics of the upper salt-bearing layer. The specimens were 71.8 mm in diameter and 20 mm in height. Initially all specimens were saturated with fresh water and seated under a pressure of 2 kPa. The e log p plots for samples from Boreholes 1 and 2 are shown in Figures 7 and 8, respectively. The consolidation and strength parameters are summarized in Table 2. An examination of Table 2 and Figures 7 and 8 reveals that both the compression index (c_c) and the swelling index (c_s) increase substantially with depth in the upper layer. The increase in c_c is nearly twofold, with a magnitude of 0.11 at the sampling depth of 0.3 m increasing to 0.2 at a depth of 1.5 m. The corresponding values of c_s are 0.01 and 0.015, respectively. If the ratio $c_c/(1+e_o)$ is considered as an index of compressibility, this ratio was 0.058 to 0.059 at a depth of 0.3 m and increased to 0.099 at a depth of 1.5 m. This is nearly a 70 percent increase in compressibility within the layer. Results on samples from Borehole 2 are similar to those from Borehole 1. However, tests in the upper layer were conducted on samples at a depth of only 1.5 m. Other samples tested from this borehole were taken from a depth of 4.5 m in the lower medium-dense calcareous silty sand layer.

These findings and the penetration resistance shown in Figures 2 and 3 indicate that a harder cemented crust usually exists in the upper half to 1 m of these deposits, which is

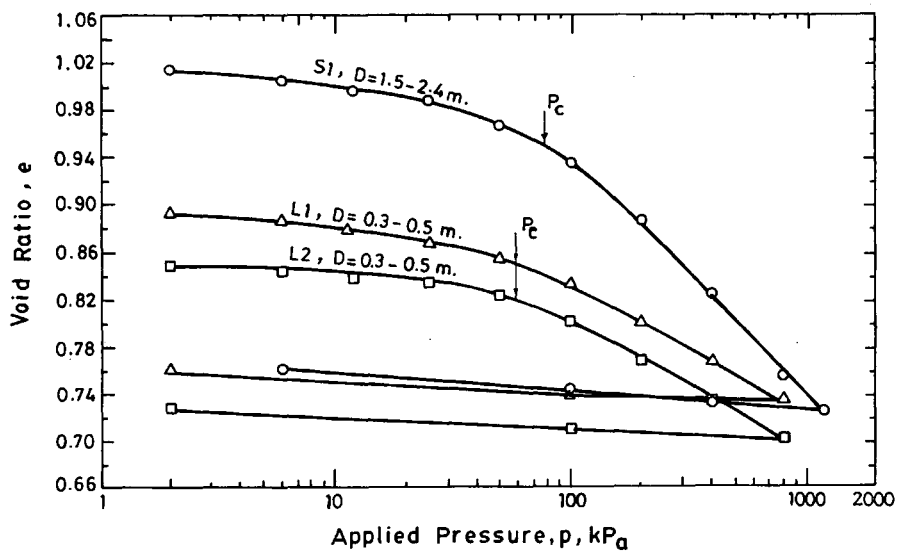

FIGURE 7 e log p curves for samples from Borehole 1.

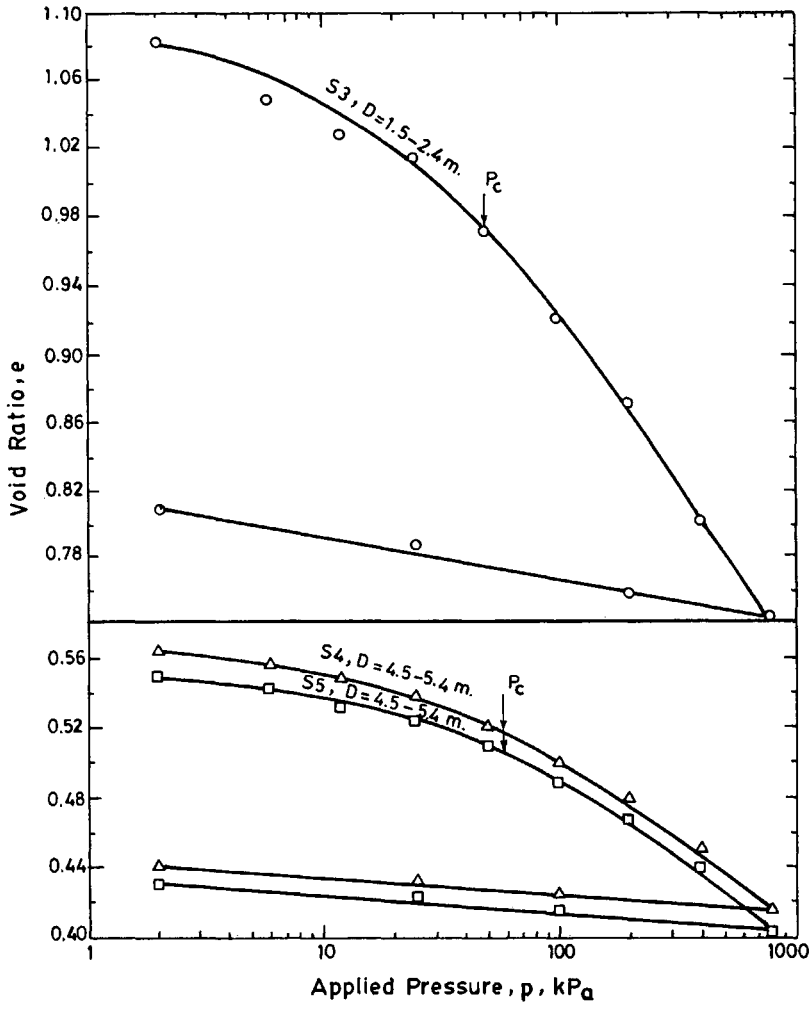

FIGURE 8 *e* log *p* curves for samples from Borehole 2.

TABLE 2 Summary of the Consolidation and Strength Parameters

Bore-hole No.	Sample Type	Depth m	γ_B Mg/m³	W (%)	γ_d Mg/m³	e_o	P_c kPa	C_c	C_s	$C_c/1+e_o$	c′ kPa	φ°′
35	L_1	0.3-0.5	1.693	19.6	1.42	0.893	60	0.11	0.01	0.058	20	37
35	L_2	0.3-0.5	1.804	24.5	1.45	0.849	60	0.11	0.01	0.059	20	37
35	S_1	1.5-2.4	1.909	43.6	1.33	1.016	80	0.2	0.015	0.099	0	28
36	S_2	0-0.8	1.76	23.0	1.43	--	--	--	--	--	20	37
36	S_3	1.5-2.4	1.84	43.2	1.28	1.086	50	0.22	0.020	1.055	0	13
36	S_4	4.5-5.3	2.09	21.5	1.72	0.564	60	0.10	0.01	0.064	0	36.9

L Pushed Liner

S Shelby Tube

-- Not Measured

usually above the groundwater level. This is due to the abundance of sulphates in the form of gypsum close to the ground surface. Below this zone, the deposit is much softer and more compressible with virtually little or no penetration resistances as evident in Figures 2 and 3. After continuous flooding by heavy rain, soluble salts dissolve and leach down, and the upper crust becomes softer and more compressible (*8*).

STRENGTH PARAMETERS

Consolidated, undrained triaxial tests with pore pressure measurements were conducted on undisturbed samples from Boreholes 1 and 2. The testing program was implemented using a fully computerized triaxial testing system supplied by Engineering Laboratory Equipment Limited, England in accordance with the procedure described by Bishop and Henkel (*10*). The specimens with nominal dimensions of 71.8 mm diameter and 150 mm length were saturated with fresh water under an incrementally applied back pressure of 200 kPa. The sequence of isotropically applied consolidation pressures was 50, 100, 200, 300, and 400 kPa. End and radial drainage was allowed by using porous stones and filter paper strips, respectively. The specimens were left for 24 hr under the full back pressure of 200 kPa and a slightly elevated cell pressure of 205 kPa. This precautionary measure was adopted to eliminate the chances of possible collapse of the specimens. It was followed by an application of isotropic consolidation pressure. Earlier, a saturation check performed on each specimen indicated that the degree of saturation was 98 to 100 percent. After full consolidation was ensured, the specimens were sheared at a strain rate of 4 percent per hour under undrained conditions. Correction was applied for the rubber membrane using the method suggested by Bishop and Henkel (*10*).

Results of the triaxial tests (Figure 9) show the stress strain curves and pore pressure versus axial strain curves for samples from Borehole 1 at a depth of 0.5 m. Figure 10 shows the effective stress path and failure envelope for the same samples on a *q-p* plot. The cohesion (c') and angle of shearing resistance (ϕ') were determined from Figure 10 as (20 kPa, 37°). The presence of a small cohesion intercept is typical of cemented sands in the area. However, the presence of a large concentration of gypsum near the surface of this deposit leads to nonhomogeneity and some variations in the measured strength characteristics for points in the vicinity of each other at the same depth. Other measurements made (*8*) indicated strength parameters of (0, 36.5°).

The strength envelope for samples from Borehole 1 at a depth of 1.5 m is superimposed in Figure 10. It indicates strength parameters of (0, 28°). The lower strength is obtained from similar samples in Borehole 2 (Table 2). Thus, softer conditions exist below the surface crust in the zone located permanently below the groundwater level. These results are compatible with the dynamic penetration resistance plotted in Figures 2 and 3, indicating a surface crust of 1 m with high penetration resistance reaching 15 to 20 blows/0.3 m underlain by softer ground with low penetration resistance.

Because the water level is located 0.5 m below ground at the time of the measurements (November) and considering tidal and seasonal fluctuations, it is evident that the portion

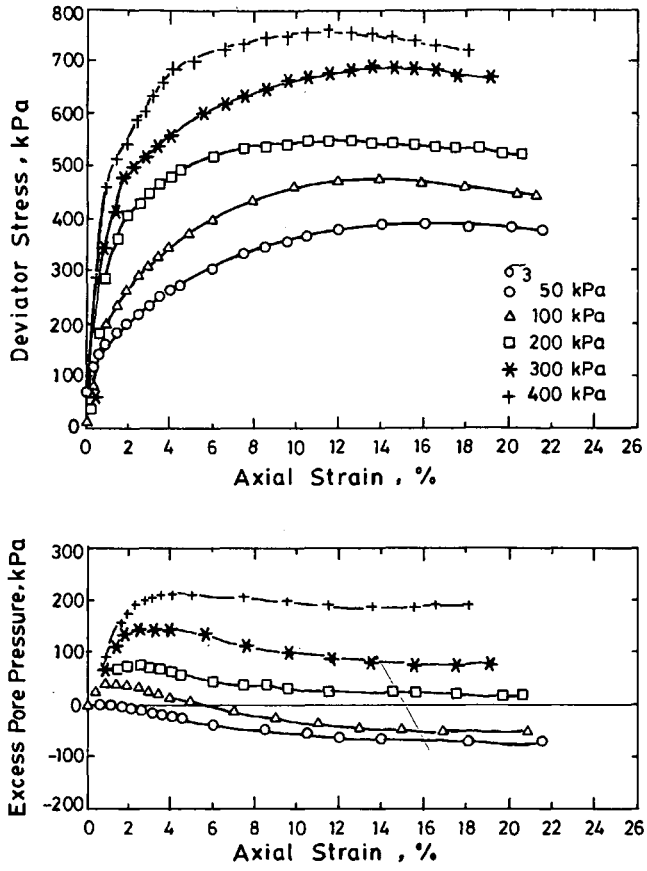

FIGURE 9 Stress and pore water pressure versus axial strain from consolidated undrained triaxial tests—Borehole 1.

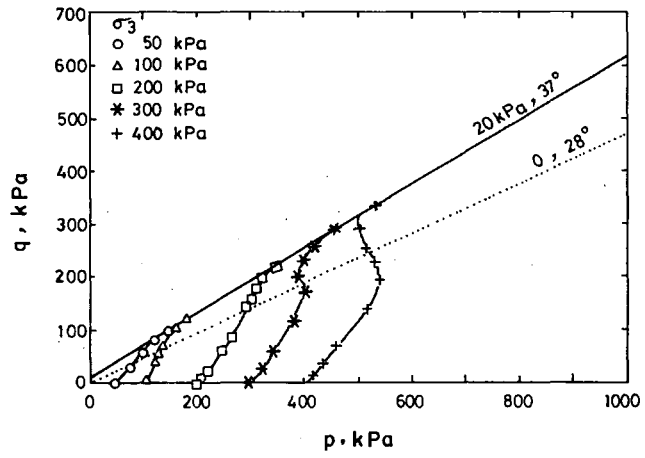

FIGURE 10 Effective stress path and failure envelopes for two samples from Borehole 1.

of this deposit located permanently below the groundwater level—approximately 1 m deep—remains soft and experiences no cementation, in contrast to the surface zone. The surface crust, displaying higher strength and lower compressibility in the dry season, becomes softer and weaker upon wetting.

BEARING CAPACITY

Plate load tests were conducted at the sites of Boreholes 1 and 2 to examine the bearing capacity of the near-surface Sabkha. A circular steel plate 0.3 m in diameter and a 10-ton hydraulic jack attached to a hand pump were used for the tests. A calibrated pressure gauge was connected to the pump, and equal load increments of 10 kPa were applied to the plate. The weight of the CME 750-XL drill rig was sufficient to provide a reaction. Each load increment was maintained for at least 15 min and until all settlements had ceased. Settlements were measured by three dial gauges attached to the plate from a reference beam. Each test was repeated at least once to ensure accuracy and consistency of the test data.

The test results are plotted in Figure 11 in the form of pressure-settlement curves. Each curve is the average of two plate load tests. Because the failure load was not well defined, the slope tangent method was used to determine this load, denoted by q_f. The failure loads were determined as 52 kPa and 40 kPa at Sites 1 and 2, respectively, at a depth of 0.3 m. The corresponding settlements were 2 mm and 2.2 mm, respectively. Tests at Site 1 (at a very shallow depth of 0.1 m) resulted in a higher bearing capacity of 125 kPa, which occurred at a settlement of 3 mm. The pressure-settlement curve at this depth (Figure 11) indicates a well-defined failure, followed by a large settlement caused by the breaking of the plate through the upper highly cemented crust. Punching failure was clearly evident below the plates in all tests.

The preceding results indicate a low bearing capacity for the salt-bearing soils at the test site. Considering the results of the unconfined compression strength tests that indicated an average undrained shear strength (c_u) of 25 kPa within a depth of 1.5 m, it is evident that failure occurs under undrained conditions. Furthermore, the measured bearing capacity is less than that calculated by the bearing capacity theory due to the high compressibility of the soil and the occurrence of punching shear failure.

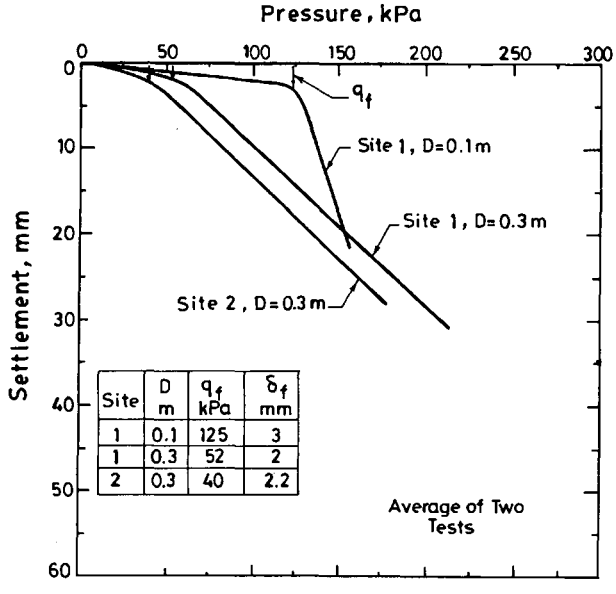

FIGURE 11 Pressure-settlement curves for 0.3-m diameter plates.

The lack of homogeneity of the deposit near the ground surface is reflected by the decreasing bearing capacity with depth in the upper crust. The bearing capacity decreased from 125 kPa at a depth of 0.1 m to 50 kPa at a depth of 0.3 m. This is due to the cementation caused by the large salt concentration at ground level (Figure 4).

SPECIAL CHARACTERISTICS

The presence of a large concentration of salts in these soils raises questions as to the influence of leaching soluble salts on their properties and behavior. A program of field and laboratory tests was carried out recently to investigate this problem (*8*). Identical undisturbed samples were taken from a depth of 0.3 m and tested before and after leaching. The results indicated that leaching led to reduced unit weight, plasticity, and specific gravity, and to increased permeability and void ratio. Leaching also resulted in increased compressibility and reduced shear strength. Field plate load tests and dynamic CPT before and after leaching by fresh water indicated a reduction in the bearing capacity of 40 to 50 percent and penetration resistance within a shallow depth of 1 to 1.5 m. However, no visible change was recorded below this depth (*8*).

Many other problems are associated with these soils and should not be underestimated. These problems include dehydration and volume decrease, which occur in the summer at high temperatures, and hydration and volume increase in the winter due to rain and the presence of water. Temperatures often exceed 50°C during July and August in Kuwait, thus initiating the process of dehydration.

The corrosive reaction of these soils should also be dealt with carefully if any concrete or steel structures are placed on it. Sabkha is not considered a suitable soil for backfilling, and foundations should not placed in direct contact with it. Moreover, foundations should be coated with a bituminous binder or other suitable inert material to prevent deterioration of concrete and corrosion of steel due to the aggressive action of salts in the soil and groundwater (*11*).

For locations that have deep deposits of Sabkha, driven piles may be necessary, particularly for multistory structures and heavy axial loads. The piles will develop their support from point resistance in the underlying competent deposits.

CONCLUSIONS

A program of field and laboratory tests were conducted to establish the basic properties and behavior of salt-bearing soils in Kuwait. On the basis of the test results, the following conclusions and recommendations were reached:

1. The soil investigated is loose, gypsiferous sandy silt of low plasticity. It extends from ground surface to a depth of 2.5 m at the test site.
2. A hard surface crust occurs to a depth of 1 m. Below this crust, the deposit remains soft and compressible.
3. Salt-bearing soils are characterized by low specific gravity and large moisture contents. They are generally loose,

having low penetration resistance, except for the upper surface crust.

4. Salt-bearing soils are sensitive to the method of drying used to perform the laboratory tests. It is recommended that salt-bearing or gypsum soils be oven dried at 60°C or with a vacuum desiccator at a temperature from 23°C to 60°C.

5. Cementation of a surface crust leads to increased shear strength and decreased compressibility above the groundwater level.

6. Salt-bearing soils (Sabkha) have low bearing capacity. The values measured were 40 to 50 kPa at a depth of 0.3 m.

7. Several environmental factors affect the properties and behavior of salt-bearing soils. Leaching of soluble salts causes loss of strength and increased compressibility. Volume changes resulting from dehydration at high temperatures followed by hydration in the presence of water are undesirable conditions for construction.

REFERENCES

1. F. I. Khalaf, I. M. Gharib, and M. Z. Al-Hashash. Types and Characteristics of the Recent Surface Deposits of Kuwait, Arabian Gulf. *Journal of Arid Environments*, Vol. 7, 1984, pp. 9–33.
2. A. S. Stipho. On the Engineering Properties of Salina Soil. *Quarterly Journal of Engineering Geology*, London, Vol. 18, 1985, pp. 129–139.
3. H. Al-Sanad. Characterisation of Salt-Bearing Soils (Sabkha) for Pavement Design Purposes in the State of Kuwait. *Journal of the University of Kuwait* (Sci), Vol. 13, No. 1, 1986, pp. 29–41.
4. G. Evans, C. G. St. C. Kendall, and P. Skipwith. Origin of the Coastal Flat, the Sabkha, of the Trucial Coast, Persian Gulf. *Nature*, Vol. 202, No. 493, 1984, pp. 759–761.
5. G. Evans and P. Bush. Some Sedimentological and Oceanographic Observations on Persian Gulf Lagoons, *Proc., Mem. Symp. Intern. Lagunas Casteras UNAM-UNESCO Mexico*, 1969, pp. 155–170.
6. P. G. Fookes and W. J. French. Soluble Salt Damage to Surfaced Roads in the Middle East. *Journal of the Institute of Highway Engineers*, Vol. 24, 1977, pp. 10–20.
7. D. R. Jones. Gypsum/Anhydrite: A Brief Review of Geotechnical Problems Related to Construction in North Kuwait. *Proc., First Symposium on Geotechnical Problems in Kuwait*, Kuwait University, 1, 1989, pp. 43–51.
8. N. F. Ismael. Laboratory and Field Leaching Test on Coastal Salt Bearing Soils. *Journal of the Geotechnical Engineering Division*, ASCE, Vol. 119, No. 3, 1993.
9. N. F. Ismael and A. M. Jeragh. Static Cone Tests and Settlement of Calcareous Desert Sands. *Canadian Geotechnical Journal*, Vol. 23, No. 3, 1986, pp. 297–303.
10. A. W. Bishop and D. J. Henkel. *The Measurements of Soil Properties in the Triaxial Test*, 2nd ed. Edward Arnold Ltd., London, 1962.
11. A. M. Jeragh and N. F. Ismael. Corrosion of Reinforced Concrete Foundations in Kuwait. *Proc., First Arabian Conference on Corrosion*, Kuwait, Pergamon Press, 1984, pp. 523–537.

Publication of this paper sponsored by Committee on Soil and Rock Properties.

Deformation Characteristics of Subgrade Soils in Kuwait

FOUAD M. BAYOMY AND HASSAN A. AL-SANAD

Comprehensive laboratory triaxial dynamic testing of subgrade soils in Kuwait was conducted to determine the engineering parameters for pavement design and construction. A literature survey and a review of ongoing road construction projects indicated that the subgrade soils were predominantly granular (A-1-b and A-2-4) according to the AASHTO classification system. A chemical and mineralogical analysis indicated that quartz is the principal component. Gypsum, calcium magnesium, and sodium sulphate are also present in varying proportions. The results of California bearing ratio (CBR) and direct shear tests indicated that these soils exhibited the characteristics of a high-performance subgrade. The angle of internal friction ranged from 20 to 40°, with an average value of about 30. The soaked CBR ranged from 10 to 47. Varying the moisture content around the optimum by ±2% resulted in significant changes in soil strength and deformation in certain cases and had an insignificant effect in some other conditions. This depends on the soil compaction curve. Soils with nearly flat curves around the optimum were less sensitive to moisture variation. A model for rut depth prediction was developed, and its material constants were evaluated. The model was implemented in a rut depth prediction system. The developed model and its guidelines were demonstrated to be of practical significance for the range of the investigated soils.

During the past decade, road construction in Kuwait has advanced, and the road network has increased considerably. The expressway network has been under construction since the mid-1970s; most of the major arterial highways have been improved to urban freeways. Because the roads department became concerned about the maintenance management of the newly developed network, it began to establish an engineering data base of inventories and construction records, which are needed for a successful pavement management system. The research for the data base, which was performed before the Gulf War, established engineering data about the subgrade soils in Kuwait, with an emphasis on locations of the freeways for pavement design and evaluation purposes. The data base was an essential element in the rebuilding of the road network after the Gulf War in 1991.

Four main objectives were set for this project:

1. Identify different types of subgrade soils existing under the major expressways;
2. Establish design values for the subgrade moduli at different conditions of moisture and stress;
3. Establish procedures to estimate the pavement rutting contributed by the subgrade soils;
4. Develop an implementation plan and guidelines for using the research results in the design system currently adopted in Kuwait.

The scope of this paper is limited to the subgrade evaluation with respect to its deformation characteristics as related to soil types and their modulus of resilience.

F. M. Bayomy, Department of Civil Engineering, University of Idaho, Moscow, Idaho 83843. H. A. Al-Sanad, Civil Engineering Department, Kuwait University, P.O. Box 5969, Safat 13060, Kuwait.

SURVEY OF RECORDS ON SUBGRADE SOILS IN KUWAIT

There are few documented records on subgrade soils in Kuwait. Some published reports addressed classification and general types. However, no research was found about the deformation characteristics, especially under dynamic traffic loads. One report summarized in a map form the types and distribution of surface soils (*1*). Another report described the general classes of soils according to AASHTO classification system (*2*). Unpublished reports at the Kuwait Institute of Scientific Research (KISR) (*3*) and Research Station of the Ministry of Public Works (*4,5*) have information on the geological and geographical distribution of the surface soils in Kuwait. Data documented in these reports indicate that the surface and near-surface soils are generally granular, ranging from gravelly sand to silty sand. They are mostly calcareous sandy soils, which are known locally as "Gatch."

Gatch soils have sufficient fines content to give a measure of cohesion when watered and rolled. Fines in the Gatch have low plasticity indices; therefore, the control of moisture content during compaction and rolling is quite critical. In the best situation, moisture varied from 7 to 12 percent, depending on the degree of compaction. However, a small variation in moisture may cause a large variation in soil strength (*3,4*).

The literature indicates that there are a lot of wind-blown uniform sands (*1*) that are difficult to compact. These sands are readily broken by traffic, and once in a loose state, they cannot be recompacted.

Another characteristic feature of Kuwait's arid region is the presence of salts in the ground close to the surface, especially in locations where the groundwater level is high, as it is near the Gulf shore. The effect of these salts in the crystalline state may render strong subgrade materials for road construction. However, under high-moisture conditions, the salts would dissolve, causing loss of cohesion and thus a considerable weakening of the subgrade materials.

Soil reports from road and building construction projects indicate that the groundwater table may be as close to the surface as 508 mm (20 in.), and it may be as deep as a few

meters under the surface for inland locations far from the sea shore. Construction reports of Riyadh and Fahaheel Expressways (Figure 1) indicated that, although the subgrade compaction was acceptable in almost all cases on the basis of measured field density and moisture content at the time of testing, it was observed that the moisture content (MC) changed rapidly, deviating from the optimum by as far as 50 percent of the optimum moisture content (OMC). For example, reported data on an OMC of 8.4 percent at the surface have shown an MC as low as 4.3 percent 2 days after the subgrade has been compacted. However, at deeper depths, MC did not vary much. A deviation of about ±2 percent from the optimum was found in most of the surveyed records. The effect of temperature on moisture variation was not evaluated because there were no temperature records available for MC filed measurements. A moisture variation of ±2 percent was considered in the laboratory program.

EXPERIMENTAL PROGRAM

The methodology adopted was to collect soil samples from several locations to cover most of the construction projects of the expressway network in Kuwait. Physical and mechanical properties of soil samples were then evaluated to determine the engineering properties as well as the chemical composition of these soils. Laboratory-made samples were then tested under triaxial dynamic testing to determine the resilient

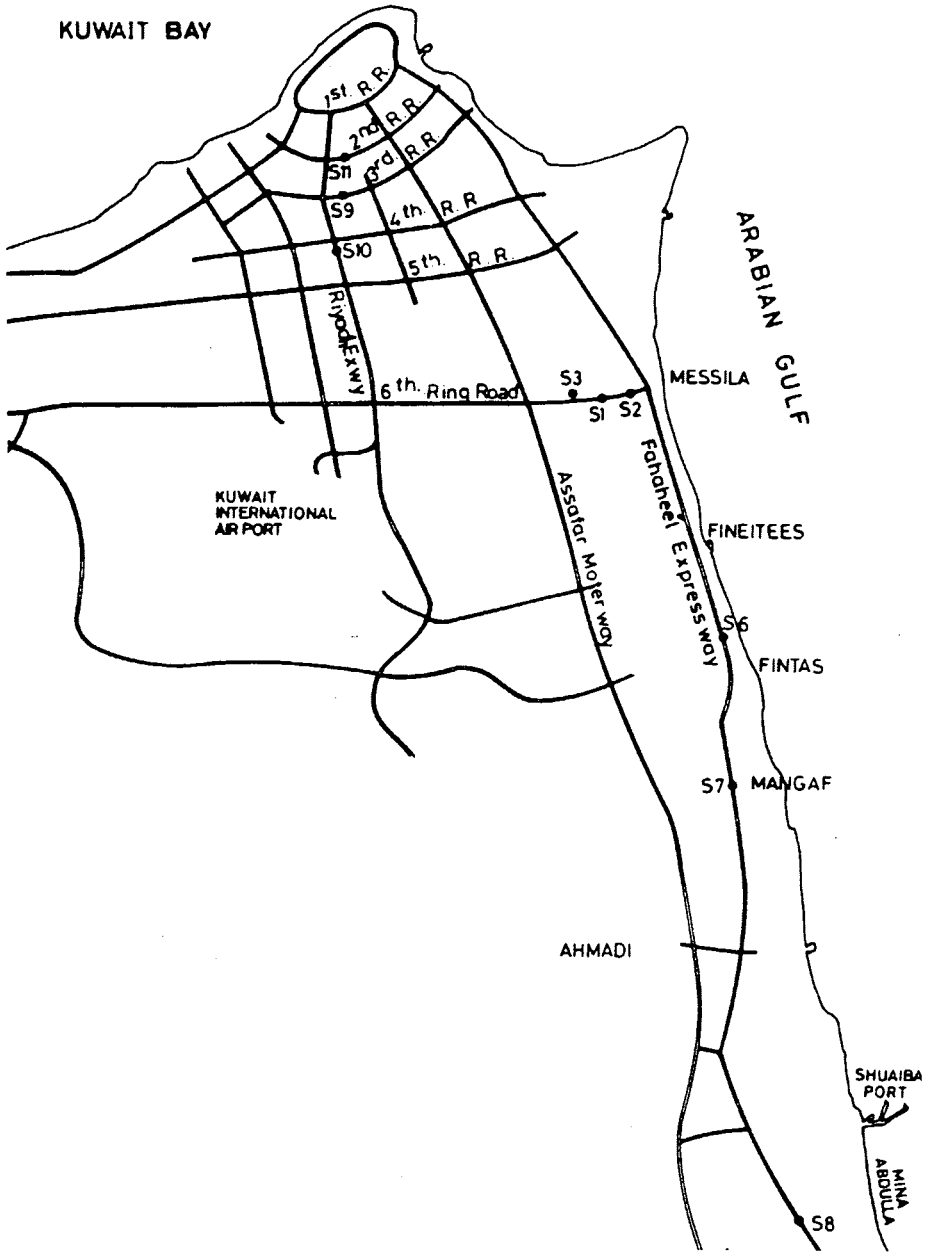

FIGURE 1 Kuwait major road network showing subgrade soil sites.

and permanent deformation (residual) characteristics of these soils at OMC as well as at an MC within ±2 percent of the optimum. The nine sites selected had varied soil conditions and covered almost all geographical locations. The site locations, shown in Figure 1, are denoted by S1, S2, and S3 on the 6th Ring Road; S6, S7, and S8 on the Fahaheel Expressway; and S9, S10, and S11 on the Riyadh Expressway. Representative soil samples were collected from each site for laboratory testing.

Basic tests required for classification (AASHTO, ASTM D 3282 and Unified, ASTM D 2487) and compaction (moisture-density relationship, ASTM D 1557) were performed on all soils. Shear strength was determined by the direct shear test (ASTM D 3080), and the bearing capacity was determined by the California bearing ratio (CBR) test (ASTM D 1883). Dynamic triaxial testing was performed on three of the nine soils to determine the resilient and residual deformation behavior under cyclic repeated loads at different moisture and stress conditions. The test adopted was similar to that of the AASHTO T 274 testing method. The test, however, was modified to develop the relationship between the permanent deformation and the number of loading cycles.

CHARACTERIZATION

Classification

Grain size distribution and Atterberg limits were performed to determine the fine content (percent passing a #200 sieve) and the soil classification. The results are provided in Table 1. The nine sites fit into four groups according to AASHTO (A-1-b, A-3, A-2-4, and A-2-6). According to the Unified system, all soils were in the range of poorly graded to well-graded sand.

Chemical and Mineral Composition

Using x-ray diffraction and chemical analysis, the chemical and mineral composition of the soil samples were determined as shown in Tables 2 and 3. Quartz constituted the main component (the SiO_2 ranged from 71 to 87 percent). Gypsum, calcium salts, magnesium, and sodium sulphate were found in varying proportions, indicating that the soils were contaminated with calcium carbonate and sulfates.

TABLE 1 Physical Characteristics and Classification of Soils at Selected Sites

Soil No.	% Pass. No. 200	Cu	Cc	Liquid Limit	Plastic Limit	Plasticity Index	Classification	
							Unified	AASHTO
S1	5.50	4.67	1.17	23.2	--	NP	SW	A-1-b
S2	4.08	4.62	1.23	17.8	--	NP	SW	A-1-b
S3	3.78	4.31	1.24	22.8	--	NP	SW	A-1-b
S6	1.08	2.75	1.11	20.6	--	NP	SP	A-1-b
S7	1.93	3.00	1.33	22.2	--	NP	SP	A-1-b
S8	1.81	2.89	0.96	23.6	22.5	1.1	SP	A-3
S9	4.29	6.83	1.47	28.1	23.9	4.2	SW	A-2-4
S10	3.50	5.92	1.32	24.0	11.1	12.9	SW	A-2-6
S11	7.50	5.75	0.69	21.3	--	NP	SP	A-3

TABLE 2 Chemical Composition (%) of Soils at Selected Sites

Soil No.	SiO2	Al2O3	Fe2O3	MgO	CaO	SO3	Cl	% Loss in Ignition
S1	81.50	3.65	0.56	1.59	2.17	0.46	0.085	10.05
S2	80.74	6.96	0.64	1.63	3.99	0.23	0.144	5.14
S3	82.60	5.06	0.56	1.62	1.75	0.46	0.089	7.93
S6	87.52	4.92	0.48	1.56	2.40	0.15	0.025	2.67
S7	79.44	4.71	0.72	2.23	5.52	0.42	0.032	6.91
S8	80.38	4.32	0.48	1.56	5.84	0.49	0.021	6.81
S9	74.86	4.71	0.81	2.58	6.14	0.66	0.032	9.13
S10	71.82	5.14	0.88	2.81	6.64	0.66	0.039	7.96
S11	71.02	6.78	1.28	2.97	8.80	1.24	0.067	8.88

TABLE 3 Presence of Minerals in Soils at Selected Sites

Soil No.	Quartz	Clay	Feldspar	Dolomite	Gypsum	Calcite	
S1	Y	Y					
S2	Y	Y	Y			Y	Note:
S3	Y	Y		Y			Y: YES it is present
S6	Y	Y	Y		Y	Y	
S7	Y					Y	
S8	Y					Y	
S9	Y	Y	Y		Y	Y	
S10	Y	Y		Y			
S11	Y	Y	Y		Y	Y	

Compaction

Moisture-density relationships were developed for all soils using the modified AASHTO procedures, AASHTO T 180 (ASTM D 1557). Fresh soil samples were used at each moisture content to eliminate degradation of weak minerals. OMC and the maximum dry density for all soils are listed in Table 4. The OMC ranged from 7.5 to 9.2 percent. The maximum dry density was in the order of about 2,083 kg/m^3 (130 pcf).

Bearing Ratio

The soaked CBR test (ASTM D 1883) conducted at 95 percent compaction indicated a CBR range of 10 to about 48 percent, whereas the maximum swell was about 0.22 mm (0.0087 in.) (Table 5). Comparing these values with the ones specified in the general specifications of road construction in Kuwait, the soils tested satisfied the minimum CBR value of 15 and the maximum swell of 2 mm (0.08 in.), except Soil S11, which had a lower CBR value.

TABLE 4 Compaction Test Results

Soil No.	Optimum Moist. Cont. (OMC), %	Max. Dry Density, kg/meters cubed
S1	8.8	2070
S2	8.0	2150
S3	8.5	2080
S6	7.5	2050
S7	9.2	2050
S8	8.9	2060
S9	7.5	2100
S10	7.5	2140
S11	7.5	2140

1 kg/meters cubed = 0.0642 pcf

TABLE 5 CBR and Swell Test Results

Soil No.	Swell, mm at 65 Blows	CBR at 95 % Compaction
S1	--	47.5
S2	--	22.5
S3	--	21.0
S6	0.005	19.5
S7	0.220	10.0
S8	0.060	27.5
S9	0.150	16.0
S10	0.090	16.5
S11	0.060	10.0

1 mm = 0.0394 in.

Shear Strength

Direct shear testing was conducted on the nine soils (12 samples each). The results show that, although the soils were classified as sands, they exhibited cohesive intercepts. Shear strength parameters, cohesion (c) and angle of internal friction (ϕ), were determined using linear regression. Results of c and ϕ values are presented in Table 6. In general, c values confirm the trend of decreasing strength with increased moisture content. However, the angle of internal friction ϕ did not change significantly. A study of the dilation of all tested samples revealed that the samples were in a very dense state.

DEFORMATION CHARACTERISTICS

Two types of deformation are generally generated under the repetition of traffic loads, elastic or resilient and nonelastic (residual) or permanent deformation. The latter is often called rutting.

To evaluate the resilient and residual characteristics, three of the nine soils were selected on the basis that they differ in their plasticity and classification. The basic tests performed revealed that Soils S1, S2, S3, S6, and S11 have similar characteristics. Soils S9 and S10 are similar, and Soil S8 was distinct among the others. Therefore, Soils S2, S8, and S10 were selected for permanent deformation evaluation. Soil S2 was a nonplastic well-graded sand, S8 was a nonplastic poorly graded sand, and S10 was a well-graded sand with a plasticity index of about 13 (Table 1).

Cylindrical samples that were 101.6 mm (4 in.) in diameter and about 177.8 mm (7 in.) were tested for rutting using a cyclic haversine stress function in a dynamic triaxial test. The stress function has a frequency of 2 pulses per second with a loading period of ⅛ sec and a rest period of ⅜ sec. Four levels of deviatoric stress were designated in the range of 10 to 40 percent of the ultimate uniaxial compressive strength. For each soil, three groups of samples (at OMC, OMC − 2 percent, and OMC + 2 percent) were tested under the aforementioned conditions.

A rutting model, as given by the following equation, was used to study the behavior of the investigated soils (*6,7*).

$$\varepsilon_p = A(N)^b \quad (1)$$

where

ε_p = permanent strain (mm/mm or in./in.),
N = number of load cycles, and
A and b = rutting parameters.

A literature review on the rutting behavior of subgrade soils indicated that three main parameters control the rutting behavior of a certain soil: the soil type and its particle structure, the applied stress, and the density-moisture condition of the compacted soil (*8–10*). It has been well documented that soil type and condition could be well represented by the modulus of resilience (M_r) of the soil at a specified applied stress (*7,10–12*). Accordingly, this study attempted to relate the variation of the rutting parameters A and b to M_r.

The parameters A and b were determined for each tested sample by fitting the experimental data to Equation 1. The

TABLE 6 Shear Strength Parameters (Direct Shear Test)

Soil No.	Cohesion "C", kPa			Angle of Internal Friction, Degrees		
	OMC-2%	OMC	OMC+2%	OMC-2%	OMC	OMC+2%
S1	346.2	270.2	116.4	33.6	31.1	36.5
S2	79.8	168.3	31.7	35.5	26.6	32.5
S3	227.0	222.1	120.2	30.9	28.6	31.8
S6	85.6	54.8	9.6	32.8	31.7	32.8
S7	250.0	192.3	98.1	29.3	28.4	32.0
S8	278.9	221.2	89.4	25.6	25.3	30.5
S9	557.8	438.5	327.9	21.0	13.4	16.2
S10	413.5	273.1	76.9	37.6	38.7	41.0
S11	253.9	269.3	4.8	40.0	36.3	41.2

1 kPa = 0.145 psi

modulus of resilience for each sample was determined by the following equation

$$M_r = \sigma_d/\varepsilon_e \quad (2)$$

where

M_r = modulus of resilience (kPa or psi),
σ_d = applied deviatoric stress ($\sigma_1 - \sigma_3$) (kPa or psi), and
ε_e = elastic (resilient) strain (mm/mm or in./in.).

Rutting parameters A and b as well as the modulus of resilience for each tested groups are presented in Table 7.

Variation of Modulus of Resilience

The results of M_r presented in Figure 2 show that variation of the M_r with applied stress is not significant in the range of stresses considered. This means that the soil resiliency has

TABLE 7 Results of Modulus of Resilience (M_r) and Rutting Parameters A and b

Soil No. and Moist. Condition	Statistical Parameter*	Modulus of resilience, MPa				Parameter "A"				Parameter "b"			
		Stress level, kPa				Stress level, kPa				Stress level, kPa			
		44.13	87.56	131.69	175.82	44.13	87.56	131.69	175.82	44.13	87.56	131.69	175.82
S2 OMC	AVG	316.4	351.0	318.7	328.0	5.57E-05	2.26E-03	3.65E-03	7.70E-03	3.01E-01	1.02E-01	5.20E-02	3.53E-02
	Std. Dev.	29.8	10.0	39.2	69.3	3.60E-05	1.30E-03	7.79E-04	1.78E-03	8.47E-02	8.32E-02	1.58E-02	8.08E-03
S2 OMC + 2%	AVG	239.5	206.8	265.9	232.6	7.63E-05	2.05E-03	6.52E-03	1.43E-02	2.29E-01	2.13E-01	1.32E-01	1.16E-01
	Std. Dev.	98.0	67.5	80.5	45.9	0.00E+00	1.17E-11	4.43E-11	9.84E-11	0.00E+00	1.33E-09	5.88E-10	0.00E+00
S2 OMC - 2%	AVG	607.5	358.3	358.6	314.8	1.28E-05	4.68E-04	1.58E-03	2.86E-03	3.33E-01	1.89E-01	9.25E-02	6.93E-02
	Std. Dev.	270.0	7.3	66.0	36.2	2.92E-06	2.18E-04	5.85E-04	1.27E-03	1.07E-01	4.00E-03	1.16E-02	7.65E-03
S8 OMC	AVG	172.7	189.9	227.0	263.7	5.95E-04	2.02E-03	3.88E-03	6.09E-03	2.18E-01	1.08E-01	7.04E-02	5.21E-02
	Std. Dev.	61.4	38.0	25.6	21.0	4.39E-04	9.42E-04	1.58E-03	1.99E-03	1.56E-01	1.86E-02	1.40E-02	9.95E-03
S8 OMC + 2%	AVG	138.9	199.3	192.0	212.5	3.08E-03	5.21E-03	9.87E-03	1.72E-02	7.43E-02	6.78E-02	7.79E-02	4.40E-02
	Std. Dev.	31.0	61.1	28.8	15.2	9.03E-04	8.30E-04	3.18E-03	3.63E-03	1.96E-02	1.75E-02	2.27E-02	1.06E-02
S8 OMC - 2%	AVG	280.9	227.3	244.5	265.2	1.51E-04	8.16E-04	1.85E-03	2.93E-03	2.87E-01	1.38E-01	7.11E-02	6.44E-02
	Std. Dev.	43.8	39.4	13.3	22.1	1.82E-04	4.74E-04	8.57E-04	1.29E-03	1.83E-01	3.69E-02	2.26E-02	2.11E-02
S10 OMC	AVG	194.0	215.1	215.9	256.6	4.08E-04	1.32E-03	3.06E-03	4.86E-03	1.49E-01	1.34E-01	7.06E-02	3.16E-02
	Std. Dev.	26.1	25.3	36.2	69.7	1.27E-04	6.49E-04	1.71E-03	2.65E-03	2.91E-02	2.40E-02	2.49E-02	1.89E-02
S10 OMC + 2%	AVG	174.0	193.0	225.4	207.8	2.27E-03	5.19E-03	9.95E-03	1.93E-02	1.20E-01	1.19E-01	7.71E-02	3.26E-02
	Std. Dev.	47.1	53.7	53.6	37.1	1.52E-03	3.09E-03	3.95E-03	5.45E-03	4.68E-02	5.77E-02	1.87E-02	1.72E-03
S10 OMC - 2%	AVG	256.0	302.8	312.9	294.6	1.21E-04	3.37E-04	9.12E-04	1.30E-03	1.36E-01	1.26E-01	8.10E-02	6.20E-02
	Std. Dev.	59.1	34.3	35.8	41.1	4.14E-05	8.41E-05	1.98E-04	4.40E-04	5.10E-02	1.39E-02	1.82E-02	1.90E-02

* Based on three samples (1 kPa = 0.145 psi, 1 MPa = 145 psi)

slight stress dependency. For granular soils, the modulus of resilience would be stress-dependent (*11,12*). A suggested formula for M_r less the stress relationship is

$$M_r = k1(\theta)^{k2} \quad (3)$$

where

M_r = modulus of resilience (kPa or psi),
θ = bulk stress = $(\sigma_1 + \sigma_2 + \sigma_3)$ (kPa or psi), and
$k1$ and $k2$ = stress sensitivity factors.

However, data obtained for the investigated soils did not verify this stress dependency formula within the considered range of stresses. The moisture content, on the other hand, has shown a more pronounced effect of the modulus of resilience for the tested soils. The effect was different from one soil to another. For instance, for Soil S2, a well-graded sand for which OMC was 8 percent, the M_r values at the optimum and at OMC − 2 percent were close, while M_r values at OMC + 2 percent dropped significantly. This is unlike Soil S10, for which M_r values at the optimum and at +2 percent from the optimum were close. This difference may be attributed to (a) the slight OMC variance within samples and (b) whether the determined OMC was closer to the dry side or the wet side of soil compaction curve. The results suggest that moisture variation of ±2 percent from the optimum may not have a significant effect on the resilient moduli of sandy subgrade soils. However, more variation may lead to considerable changes in the soil modulus. For the tested soils, S8 and S10 showed close M_r values, whereas S2 showed slightly higher values at the different stress levels.

Variation of Rutting Parameters

Variation of rutting in subgrade may be detected through the variation of the rutting parameters A and b as previously discussed. For cohesive fine grained soils, it was found that the slope of the rutting curve b is quite independent of the testing conditions and may be a characteristic of the soil type itself. Parameter "A" is dependent on the testing conditions and the soil type as well (*7–10*). Data developed in this research were analyzed to determine the variation of these parameters for the sandy subgrades in Kuwait.

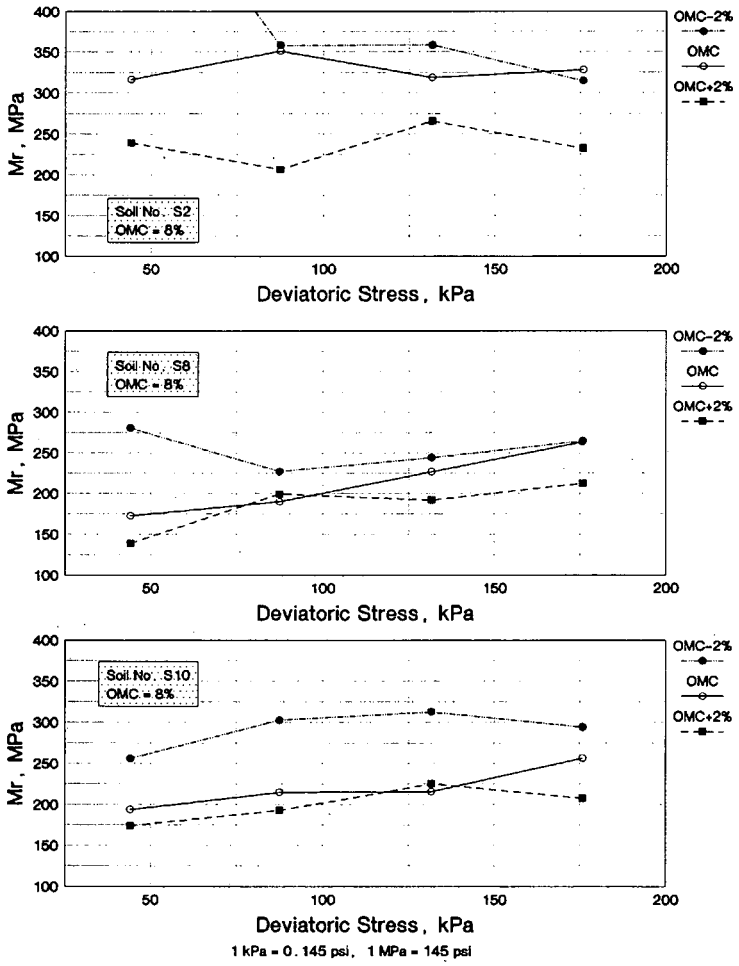

FIGURE 2 Relationship between M_r and deviatoric stress.

Parameter A

Parameter A is the intercept of the regression line $\log_e \varepsilon_p$ versus $\log_e N$ as given in Equation 1. The calculated values of A at different applied stresses are presented in Figure 3. The results show that A increases with the increase of stress and depends on the soil type and moisture. By comparing M_r results in Figure 2 and A results in Figure 3, it can be concluded that effects of moisture are similar in both cases. This suggests that parameter A could be related to the modulus of resilience at a given stress.

Based on previous research on cohesive soils (*7–10*), a relationship was suggested to relate Parameter A to the soil condition as presented by M_r and the deviatoric stress. The relationship can be presented in the form

$$A = R(M_r)^s \, x \, \exp(c\sigma_d) \quad (4)$$

where R, s, and c are material constants to be determined experimentally. These constants are independent of the stress level and the compaction conditions because the M_r value represents these conditions for a given soil.

Using regression analysis to fit the model in Equation 4, the parameters R, s, and c were determined using the Statistical Analysis System (SAS) (*13*). The results are given in Table 8. The parameter A model given in Equation 4 fits very well. The r^2 (square of the coefficient of correlation) and the F statistical test (*14*) indicate that the suggested model is statistically significant to correlate Parameter A with the modulus of resilience (M_r) and the applied deviatoric stress (σ_d). Figure 4 shows the observed A values, which are experimentally determined, versus the predicted A values using Equation 4. Figure 4 shows that A could be significantly predicted by the model in Equation 4.

Parameter b

Parameter b is the slope of the regression line $\log_e \varepsilon_p$ versus $\log_e N$ as given in Equation 1. Values of Parameter b are given in Table 7 for the tested soil groups. Unlike Parameter A, Parameter b was found to be independent of the stress applied or the moisture condition. It is a material property that would be unique for a soil type. Results of b values plotted versus M_r for each soil in Figure 5 indicate that b is unrelated to M_r. The best expected value, statistically, would be the grand mean b_{mi} of all tested samples for each soil. For instance, b_{m2} is the mean b value for Soil S2 for all various stress and

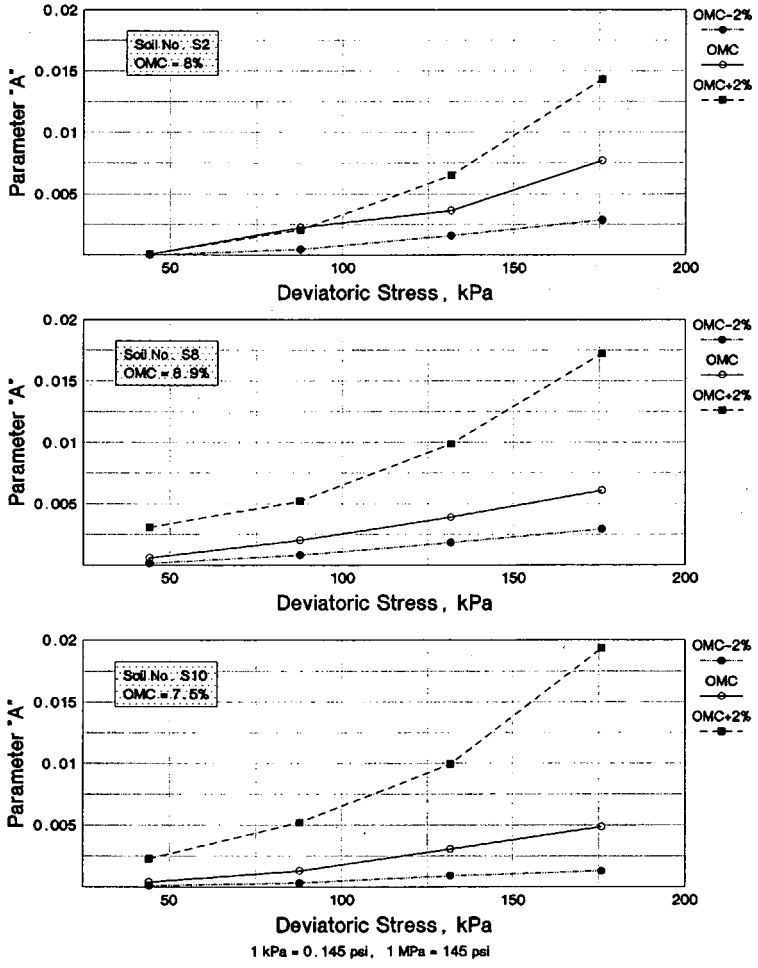

FIGURE 3 Relationship between Parameter A and deviatoric stress.

TABLE 8 Results of Regression Analysis of Parameter A Model

Soil No.	Regression Constants				R-Square, r^2	F Statistic	Prob. > F
	Log_e R	R	s	c			
S2	17.858	5.7×10^7	-2.659	0.222	0.931615	54.49	0.0001
S8	2.725	15.256	-1.021	0.201	0.950057	86.60	0.0001
S10	51.198	1.72×10^{22}	-5.797	0.183	0.863242	28.40	0.0001

Note: R, s and c constants are defined in equation {4}, Values given are for M_r and σ_d in psi units.

moisture conditions. The grand mean values and their standard deviations are listed in Table 9.

Inspecting the distribution of Parameter b in Figure 5, it was suggested that there probably was no significant difference among the grand means. To test the hypothesis that $b_{m2} = b_{m8} = b_{m10}$, an analysis of variance was performed to determine the F^* statistic for the b distribution. Results of the F-test are presented in Table 9. Because the F^* value is less than the critical F at the level of significance $\alpha = 0.05$, the null hypothesis that the b means are equal cannot be rejected. Therefore, it was concluded that the sandy soils investigated would not exhibit variation in their Parameter b. The data show an average b value of about 0.113 may be appropriate for a rutting prediction using the rutting model given in Equation 1.

ESTIMATION OF RUT DEPTH IN SUBGRADE LAYER

Methodology

The rut depth R_d contributed by a subgrade layer in a pavement system can be determined by means of Equations 1 and

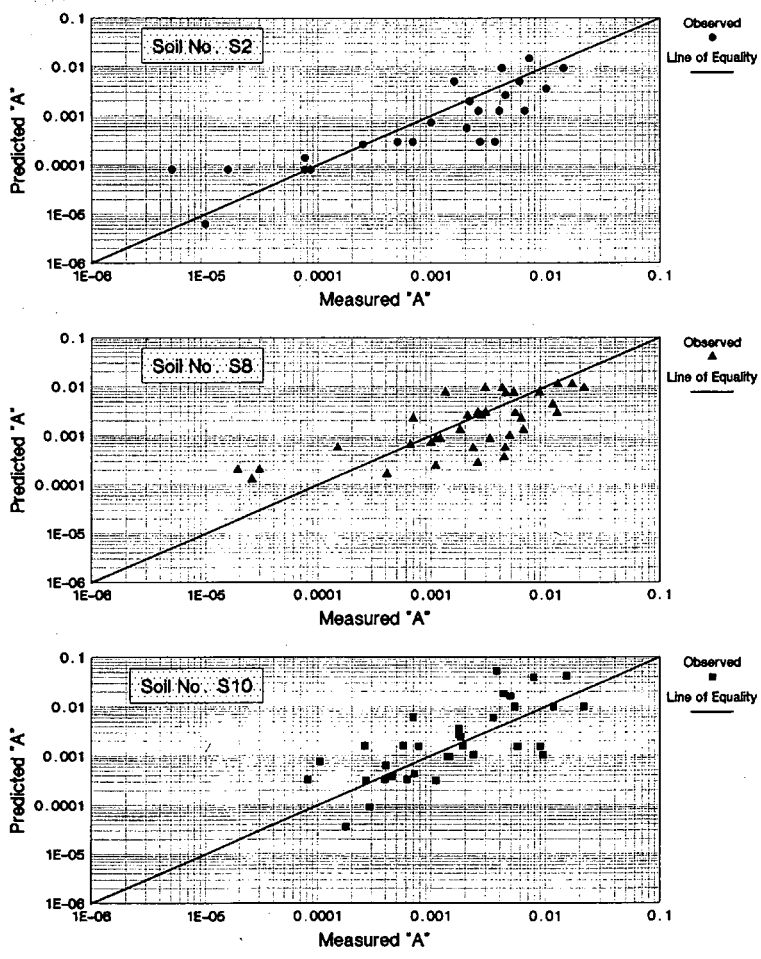

FIGURE 4 Predicted versus observed (measured) Parameter A.

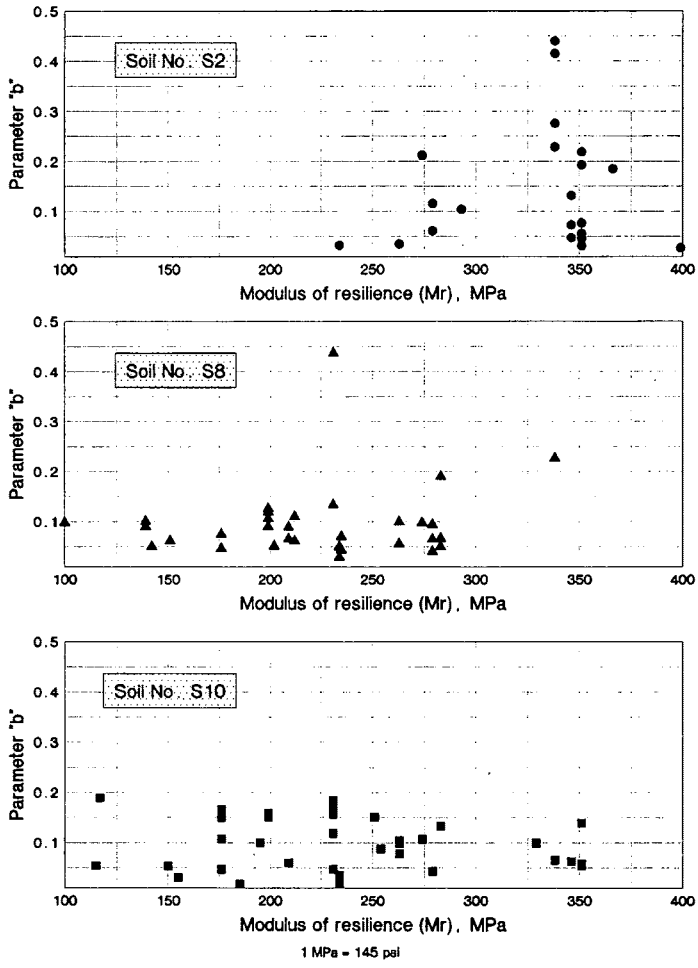

FIGURE 5 Variation of Parameter b with modulus of resilience (M_r).

TABLE 9 Mean Values of Parameter b

Statistical Parameter	Soil No.		
	S2	S8	S10
No. of samples	24	36	35
Mean Value of Parameter "b_{mi}"	0.147041	0.106094	0.095345
Standard Deviation	0.113881	0.101049	0.050721
Minimum Value	0.027100	0.029000	0.0175
Maximum Value	0.440000	0.535000	0.189000
Standard Error of Mean	0.022836	0.017075	0.008527

F^* - test for the null hypothesis,

Ho: Mean values of b_{mi} are equal

Results: Calculated $F^* = 0.212640$,
Critical $F(0.05, 2,92) = 3.11$

Decision: Do not reject the null hypothesis that b_{mi} are equal.

4, where the permanent strain in a thin subgrade Layer i with a thickness Δh_i can be determined by

$$\varepsilon_{pi} = R(M_{ri})^s \cdot \exp(c\sigma_{di}) \cdot N^b \quad (5)$$

Then the total rut depth of all subgrade layers would be equal to

$$R_d = \sum_{i=1}^{n} \varepsilon_{pi} \cdot \Delta h_i \quad (6)$$

where

R, s, c, and b = constants of the subgrade soil;
M_{ri} = modulus of resilience of Layer i;
σ_{di} = deviatoric stress at the mid-depth of Layer i;
Δh_i = thickness of Layer i; and
n = number of subgrade layers.

Using a multilayer elastic analysis computer program, such as CHEVRON or ELSYM5, the stress state in the pavement system can be determined. Hence, the rut depth (R_d) can be determined as follows:

1. Determine the soil constants—R, s, c, and b—by performing a triaxial repeated load test as performed in this research. The given values in this study may be suggested for sandy soils similar to those investigated.
2. Determine an effective value of the modulus of resilience to represent the soil conditions around the year. The AASHTO 1986 design guide (*15*) or the field estimated modulus of resilience using backcalculation techniques from falling weight deflection tests may be used to determine this value.
3. Use multilayer elastic analysis to determine the stress state of the pavement system at the midpoint of subgrade layers. Then determine the deviatoric stress using $\sigma_d = \sigma_1 - \sigma_3$.
4. Estimate the design life of the pavement in N cycles. For instance, N may be considered the design value of $ESAL_{18}$ (equivalent 18-kips single axle load).
5. The rut depth (R_d) may be determined by using Equations 5 and 6 if the deviatoric stress and thickness at each layer are known.
6. Check the value of rut depth (R_d) determined in Step 5 against a preselected critical value of rut depth that may be allowed in the subgrade.

It is important to note that the critical value of rut depth has to be field calibrated and correlated to values obtained in the lab. This investigation does not suggest certain values because no field data were available. However, on the basis of measurements made in the AASHTO road test, rut depth in the subgrade could be assumed to be between 0 to 20 percent of the total rut depth in the pavement system. If a total rut depth of 25.4 mm (1 in.) is allowed in the pavement, then a maximum value of 5.1 mm (0.2 in.) may be allowed in the subgrade. The determination of R_d as presented here is entirely laboratory based and may not be assumed to equal the field value. However, due to the confinement of the pavement system in the field and the protection of the subgrade by the pavement layers, it is expected that the values obtained by this laboratory-based method may be higher than the actual field value.

Example for Rut Depth Calculation

For a flexible pavement composed of 140 mm (5.5 in.) asphalt concrete surface course with M_r = 2,068,400 kPa (300,000 psi), constructed on a sandy subgrade soil with M_r = 310,260 kPa (45,000 psi), the rut depth contributed by the top 381 mm (15 in.) of the subgrade after 1 million 18-kips ESAL load applications was estimated. The constants R, s, c, and b were assumed to equal those of Soil S2 in this paper.

The CHEVRON program for multilayer elastic analysis was used to determine the stress state at the mid-depth of three 127-mm (5-in.) layers in the subgrade. Using Equations 5 and 6, the total rut depth in the top 381 mm (15 in.) of the subgrade was estimated to be 2.1 mm (0.083 in.). When the analysis was repeated using 103,420 kPa (15,000 psi) subgrade modulus of resilience (high moisture content) instead of 310,260 kPa (45,000 psi), the rut depth increased to 8.8 mm (0.347 in.).

CONCLUSIONS

On the basis of the results of this study, the following conclusions are drawn:

1. Subgrade soils in Kuwait are mostly granular materials composed mostly of sand with little silt and clay fines. Soils tested from various locations were classified as A-1-b, A-2-4, A-2-6, and A-3 group soils, according to the AASHTO Classification System, with A-1-b being the most predominant group type.
2. Chemical and mineralogical analysis indicated that quartz is the principal component. Gypsum, calcium, magnesium, and sodium sulfates are found in varying proportions.
3. The strength and bearing ratio indicated good quality support conditions of these soils at the optimum moisture content. Varying the moisture content around the optimum by ± 2 percent resulted in significant changes in soil strength and deformation in certain cases and insignificant effects in other conditions. This depended on the soil optimum moisture content, whether it was close to the dry side or the wet side of the compaction curve.
4. The rutting of subgrade soils could be evaluated using the models given by Equations 5 and 6. Parameters included in these equations have been evaluated. Analysis of these parameters revealed that the Rutting Parameter A depended on the soil modulus of resilience and the existing stress, whereas Parameter b was constant for the material and independent of the stress and the moisture conditions.
5. The developed rutting model was based on the laboratory findings. The predicted rut depth value may differ significantly from the actual field value. However, it is anticipated that the model predicted value may be more conservative (higher) than the actual value expected in the field.

ACKNOWLEDGMENT

This research was partially supported by the Kuwait Foundation for Advancement of Science.

REFERENCES

1. F. I. Khalaf, I. M. Gharib, and M. A. Al-Hashash. Types and Characteristics of Recent Surface Deposits of Kuwait. *Journal of Arid Environment*, Vol. 7, No. 2, 1984.
2. S. N. Doshi and H. R. Guirguis. Correlation of CBR with density and moisture content. *Indian Geotechnical Journal*, Vol. 12, No. 4, 1983.
3. J. S. Al-Sulaimi, M. I. El-Sayed, A. Salman, and A. Akbar. *The Study of the Gatch Deposits in Kuwait City and Suburbs*. Report EES-46. Kuwait Institute of Scientific Research, 1982.
4. N. Ismael, A. Jeragh, O. Al-Khalidi, and S. Abdul Hadi. *A Study of the Properties of Surface Soils in Kuwait*. Government Laboratories and Testing Station, Kuwait, 1985.
5. A. F. Bissada. Low Cost Pavement Situation in Kuwait. *Proc., Conference on Low-Cost Roads*, Arab Engineers Federation, Kuwait, Nov. 25–28, 1974.
6. C. Monismith, N. Ogawo, and C. Freeme. Permanent Deformation Characteristics of Subgrade Soils Due to Repeated Loading. In *Transportation Research Record 537*, TRB, National Research Council, Washington, D.C., 1975.
7. K. Majidzadeh, S. Khedr, and H. Guirguis. Laboratory Verification of a Mechanistic Subgrade Rutting Model. In *Transportation Research Record 616*, TRB, National Research Council, Washington, D.C., 1976, pp. 34–37.
8. K. Majidzadeh, H. Guirguis, and Josef. *Fundamentals of Soil Compaction*. Final report of Project EES 248. Ohio State University, Engineering Experiment Station, Columbus, 1971.
9. S. Khedr. Variation of Parameters of Permanent Deformation Mechanistic Model. M.S. thesis. Ohio State University, Columbus, 1975.
10. K. Majidzadeh, F. Bayomy, and S. Khedr. Rutting Evaluation of Subgrade Soils in Ohio. In *Transportation Research Record 671*, TRB, National Research Council, Washington, D.C., 1978, pp. 75–84.
11. H. B. Seed, F. G. Mitry, C. L. Monismith, and C. K. Chan. *Prediction of Pavement Deflections From Laboratory Repeated Load Tests*. Report No. TE–65–6. Institute of Transportation and Traffic Engineering, University of California, Berkeley, Oct. 1965.
12. J. Hardcastle. *Subgrade Resilience Modulus for Idaho Pavements*. Department of Civil Engineering, University of Idaho, Moscow, June 1992.
13. Statistical Analysis System. SAS Institute, Cary, N.C., 1986.
14. E. Crow, F. Davis, and M. Maxfield. *Statistical Manual*. (Released within the Department of Defense as NAVORD REPORT NOTS 948.) Dover Publications, Inc., New York, 1960.
15. *AASHTO Guide for Design of Pavement Structures*, Vol. 1. AASHTO, Washington, D.C., 1986.

Publication of this paper sponsored by Committee on Soil and Rock Properties.

Field and Laboratory Evaluation of the Mechanical Behavior of Unbound Granular Materials in Pavements

M. A. KAMAL, A. R. DAWSON, O. T. FAROUKI, D. A. B. HUGHES, AND A. A. SHA'AT

Laboratory and full-scale pavement studies were conducted as a part of an overall program to evaluate the engineering properties and performance of eight gradings of unbound granular roadbase materials. A repeated load triaxial testing program was conducted in conjunction with shear box and permeability tests on unbound mixes with grading curves ranging between the two extremes of the envelope currently used as a specification in the United Kingdom. After analyzing the laboratory results, full-scale trials were conducted using eight experimental gradings. The pavement test strip was divided into eight 22-m bays. Dynamic cone penetrometer, density, and moisture content measurements were performed on the subgrade, capping layer, and roadbase material. The performance of each bay under heavy traffic was monitored for 6 months. The rut depth profile was recorded using an automatic computerized rut profiler, and deflection measurements were recorded weekly by the deflectograph. Falling weight deflectometer testing was conducted three times. The objective of the research was to identify a material that would allow free drainage and hence reduce pumping and excess pore water pressure but maintain a high in situ stiffness with good resistance to permanent deformation.

The triaxial test is commonly used to assess the resilient modulus of unbound granular materials. The effect of aggregate grading was studied by Shaw (*1*). A comparison was made between 40-mm maximum-size broadly graded crushed rock roadbase material and a 3-mm single-sized stone from the same source. The broadly graded material was found to be much stiffer than the single-size stone, partly due to the large difference in maximum particle size. Thom (*2*) conducted a series of repeated load tests on 10-mm maximum-sized crushed dolomitic limestone and found a high stiffness for uniformly graded materials, but broadly graded material showed a higher shear strength. Thompson and Smith, however (*3*), reported that permanent deformation under repeated loading provides a more definitive evaluation of granular base materials than does resilient modulus or shear strength.

M. A. Kamal, O. T. Farouki, and D. A. B. Hughes, Civil Engineering Department, The Queen's University of Belfast, Stranmillis Road, Belfast, BT9 5AG Northern Ireland. A. R. Dawson, Civil Engineering Department, University of Nottingham, University Park, Nottingham, NG7 2RQ England. A. A. Sha'at, Civil Engineering Department, Dundee Institute of Technology, Dundee, Scotland.

SAMPLE PREPARATION, APPARATUS, AND TEST ROUTINE

A large sample of aggregates obtained from a local gritstone quarry was air dried and separated into 10 single-sized fractions from which 10 mixes and 2 gradings at the extreme ends of the current United Kingdom specification (*4*) of unbound roadbase material were prepared by mixing appropriate weights of each fraction. The following equation proposed by Cooper et al. (*5*) was used to select the new gradings:

$$P = \frac{(100 - F)(d^n - 0.075^n)}{(D^n - 0.075^n)} + F$$

where

P = percentage passing a sieve of size d mm,
D = maximum particle size (mm),
F = percentage of material passing through a 0.075 mm sieve, and
n = increment in 0.1 steps.

This formula was selected because it maintains the fines content (i.e., passing through a 0.075-mm sieve) at a predetermined level, enabling the effective fines content (i.e., percentage of material passing through a 5-mm sieve) to be varied by adjusting the value of n. Some of the selected gradings are shown in Figure 1.

A specimen that was 150 mm in diameter and 300 mm long was tested in a repeated load triaxial facility developed by Boyce (*6*) at Nottingham. Six representative gradings were chosen in such a way as to cover a full range of mixes, that is, mixes 1, 3, 4, 6, 8, and 10 [see Figure 1(*a*)] along with the extreme ends of the current specification represented by gradings A and B in Figure 1(*b*). All specimens were identically prepared to achieve a dry density in the range of 1,950 to 2,170 kg/m^3 typical of field densities (see Full-Scale Trials in this paper). Specimens were compacted in five layers in a four-section split steel mould lined with a neoprene membrane. Each layer was compacted for 60 sec using a vibrating table and small surcharge, enabling the density to be controlled. Axial and radial strain measurements were taken by attaching linear variable differential transformers (LVDTs) and strain hoops to studs embedded in the sides of each specimen as shown in Figure 2. The apparatus was controlled by and the data were collected to a personal computer and high-

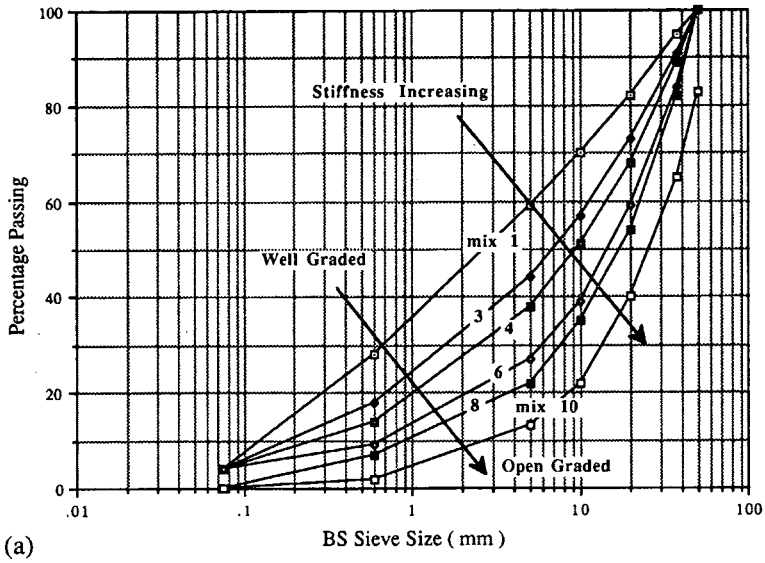

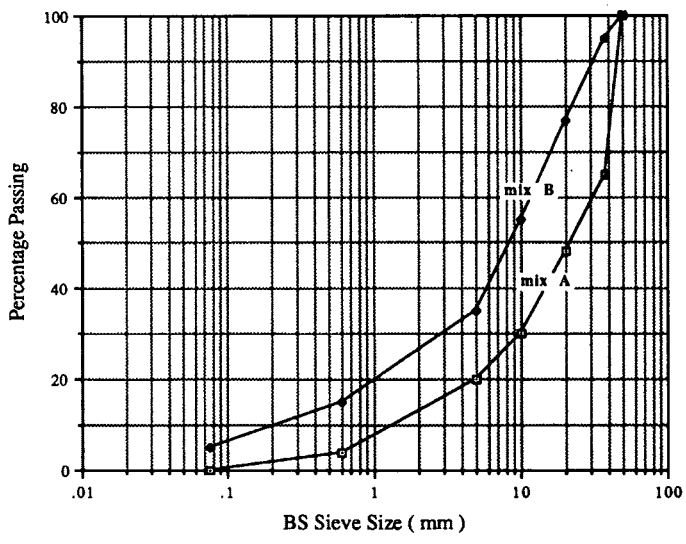

FIGURE 1 Selected gradings: (*a*) gradings used for triaxial and field testing and (*b*) extreme limits of current specifications (Mixes A and B).

speed digital/analogue control and acquisition hardware. The testing conducted on each specimen is described next.

First, to eliminate any seating problems between the load platens and the specimen, and to account for the initial traffic compaction experienced in field conditions, the load on each sample was repeatedly applied for 25,000 cycles at a deviator stress from 0 to 100 kPa, a confining pressure of 35 kPa, and a frequency of 5 Hz, allowing the plastic strain to develop before performing the repeated load elastic testing. The 25,000 cycles cause some bedding down and may represent long-term effects.

Second, repeated load elastic testing at a frequency of 1 Hz was performed along stress paths defined in terms of p and q, where p is the mean normal stress and q the deviator stress. The paths applied are presented in Table 1. All samples were tested at the dry end; therefore it is expected that changes in p accurately reflect the changes in p' (the mean normal effective stress). However, suctions were not measured, so the absolute value of p' is unknown.

Third, each sample was subjected to a repeated load plastic testing program as described in Step 1 for 10,000 cycles.

Finally, a failure test was performed at a constant confining stress of 35 kPa by increasing the deviator stress until the sample failed.

Mixes 1, 4, 6, 8, A, and B were subjected to stress paths from 1 to 28 (Table 1), whereas only stress paths 1 to 14 were used for mixes 3 and 10. For each test, the applied stress, axial strain, radial strain, and Poisson's ratio were directly recorded in the computer. Using the analysis package, the resilient modulus, stress-strain relationship, and permanent strain behavior of the dry granular material were analyzed. The results are described next.

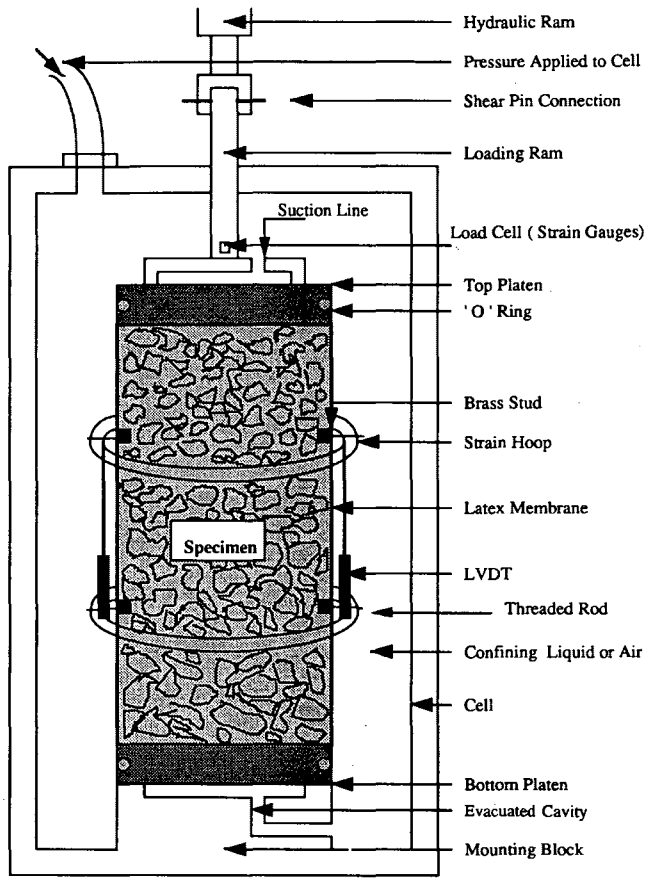

FIGURE 2 Triaxial cell arrangement.

TABLE 1 Stress Paths Used

Stress Path	qinit (kPa)	qfinal (kPa)	pinit (kPa)	pfinal (kPa)	σ 3 (kPa)	σ1init (kPa)	σ1final (kPa)
1	0	50	25	41.67	25	25	75
2	0	100	25	58.33	25	25	125
3	0	50	50	66.67	50	50	100
4	0	100	50	83.33	50	50	150
5	0	150	50	100	50	50	200
6	0	200	50	116.67	50	50	250
7	0	50	75	91.67	75	75	125
8	0	100	75	108.33	75	75	175
9	0	150	75	125	75	75	225
10	0	200	75	141.67	75	75	275
11	0	50	100	116.67	100	100	150
12	0	100	100	133.33	100	100	200
13	0	150	100	150	100	100	250
14	0	200	100	166.67	100	100	300
15	0	50	125	141.67	125	125	175
16	0	100	125	158.33	125	125	225
17	0	150	125	175	125	125	275
18	0	200	125	191.67	125	125	325
19	0	50	150	166.67	150	150	200
20	0	100	150	183.33	150	150	250
21	0	150	150	200	150	150	300
22	0	200	150	216.67	150	150	350
23	50	100	66.67	83.33	50	100	150
24	100	150	83.33	100	50	150	200
25	150	200	100	116.67	50	200	250
26	50	100	91.67	108.33	75	125	175
27	100	150	108.33	125	75	175	225
28	150	200	125	141.67	75	225	275

RESULTS

Elastic Behavior

To analyze the results from the repeated load triaxial testing, the stress was expressed in terms of the sum of principal stresses ($\theta = 3p = \sigma_1 + 2\sigma_3$) and the deviator stress ($q = \sigma_1 - \sigma_3$. Resilient strain in a triaxial test has two components: resilient volumetric strain and resilient shear strain. For each mix, the resilient modulus (M_r), shear strain (e_s), and volumetric strain (e_v) were calculated from the following relationships:

- Resilient modulus $M_r = q/e_1$,
- Shear strain $e_s = \frac{2}{3}(e_1 - e_3)$, and
- Volumetric strain $e_v = e_1 + 2e_3$.

Suffixes 1 and 3 represent axial and radial directions, respectively.

Resilient Modulus

For a direct comparison of the mixes at the same confining pressure when cycling from zero deviator stress, the resilient modulus of all the mixes was plotted against the sum of the principal stresses at 50 kPa confining pressure, as shown in Figure 3. It can be observed from Figure 3 that generally the resilient modulus increases from the finer to the coarser mix. It may also be seen that there is a slight increase in resilient modulus with increasing deviator stress. This latter effect is more noticeable at the higher values of stiffness.

An increase in resilient modulus was observed by increasing the confining pressure in the same manner for all the mixes for the stress paths 1 to 22 (shown in Table 1), that is, when cycling the deviator stress starting from zero. Stress Paths 23–25 start at nonzero values of deviator stress but end at the same stress levels as Paths 4–6, respectively; the repeated deviator stresses thus being smaller than for the earlier stress paths. For a higher confining pressure, Paths 26–28 may similarly be compared with Paths 8–10. Paths 3, 23, 24, and 25 may also be treated as a series of paths with the same repeated deviator stress, but at increasing levels of base deviator stress. The resilient moduli for Paths 23–28 are shown in Figure 4.

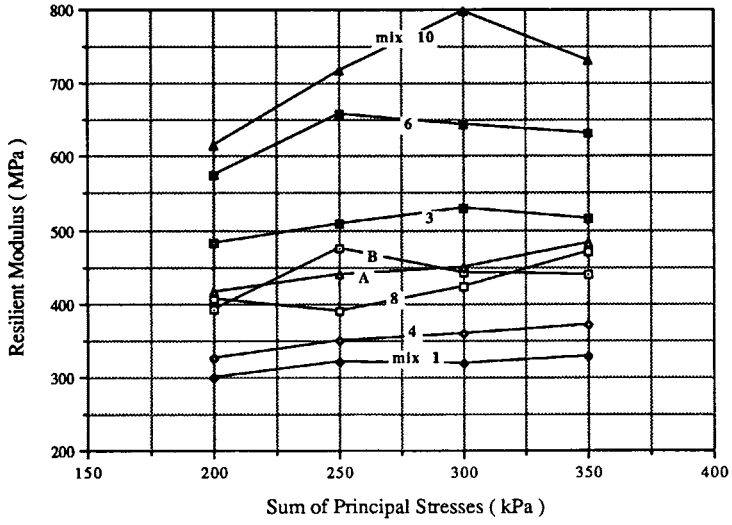

FIGURE 3 Resilient modulus of each mix at 50 kPa confining pressure (all mixes).

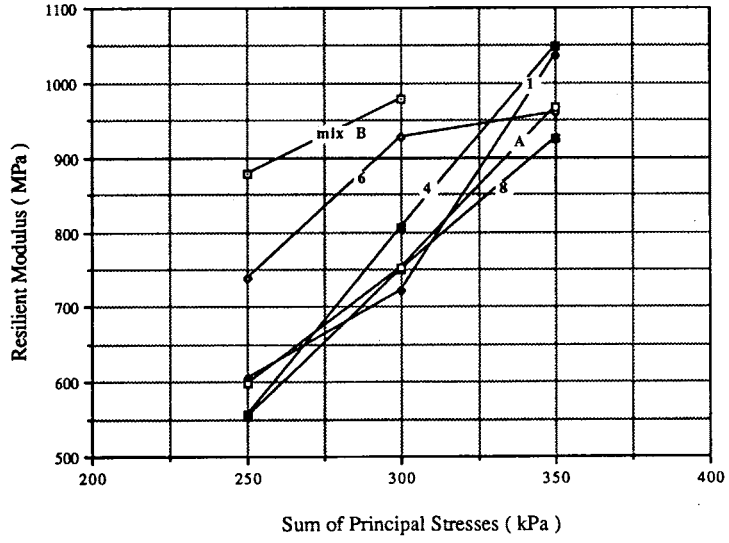

FIGURE 4 Resilient modulus of each mix at 50 kPa confining pressure (Paths 23–28).

By comparing Paths 4 and 23, 5 and 24, 6 and 25, 8 and 26, 9 and 27, and 10 and 28 (Figures 3 and 4), it can be seen that the stiffness increases as the base deviator stress rises, that is, the development of strain during a repeated load pulse varies during different parts of the pulse. This confirms the stress-dependent nature (i.e., nonlinearity) of the resilient modulus of unbound granular material. The same findings were reported by Lister and Jones (*7*) that unbound granular materials in a pavement usually have a markedly nonlinear stress-strain relationship and their effective modulus of elasticity increases with the increase of uniaxial pressure because of the increase in the contact area between adjacent grains.

Volumetric and Shear Strain

Volumetric strains are plotted against the natural logarithm of the stress ratio, that is, ln (p_{final}/p_{init}), in Figure 5 for all the mixes at a confining pressure of 50 kPa. It can be seen that generally the volumetric strain decreases from the finer to the coarser mix. A decrease in volumetric strain with increasing confining pressure was also observed. The results show that the volumetric strain is directly affected by the presence of finer particles in the mixes, that is, it increases with increasing equivalent fines content, as discussed earlier. A similar trend with an increase in deviator stress and an

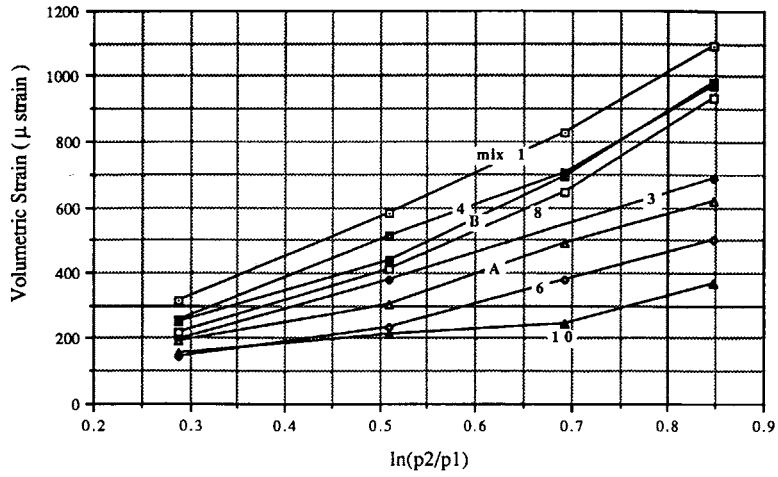

FIGURE 5 Volumetric strain versus ln(p2/p1) for different mixes.

increase in mean normal stress was observed when the volumetric strain was plotted against the deviator stress and change in mean normal stress.

The shear strains are directly affected by the shear stress ratio (q/p) (*8*) and therefore shear strains are plotted against change in shear stress ratio [δ (q/p)] for all the mixes at 50 kPa confining pressure, as shown in Figure 6. It can be seen from Figure 6 that the shear strain has the same trend as that of volumetric strain, that is, it decreases from the finer to the coarser mixes, indicating an increase in stiffness in the mix from the finer to the coarser end of the envelope. A decrease in shear strain with increasing confining pressure was also observed.

Plastic Behavior

Plastic behavior of a material in a repeated load triaxial apparatus was observed by applying a repeated deviator stress to the specimen and measuring the buildup of nonrecoverable strain against the number of cycles applied before performing the elastic testing program. The results for the log of permanent strain versus the log of the number of load repetitions are plotted in Figure 7. It can be seen that the resistance to permanent deformation generally increases for well-graded materials as compared to that of open-graded materials.

Before failure tests were performed, all samples were again subjected to repeated load testing to compare the rate of buildup of nonrecoverable strain before and after elastic testing. Each sample was confined at a pressure of 35 kPa, and the deviator stress was cycled from 0 to 100 kPa at a frequency of 5 Hz. Permanent deformation was recorded throughout the test until 10,000 stress repetitions had been applied. All materials were found to be stable, and the rate of permanent strain was negligible compared with the earlier results before the elastic testing as shown in Figure 7. The results are in good agreement with work by Morgan (*9*), who showed that even for 10^6 cycles, the material had not reached steady behavior.

Failure Tests

Failure tests were conducted on mixes A, 1, 4, 6, 10, and 5-mm single-sized aggregate to compare the shear strength of

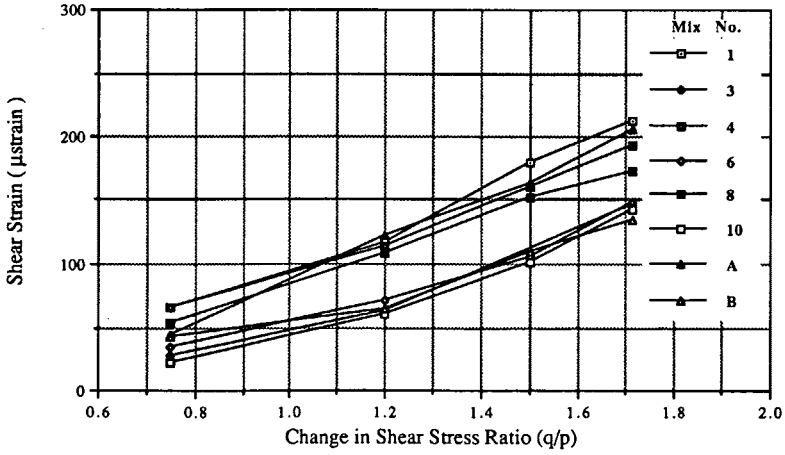

FIGURE 6 Shear strain versus change in shear stress ratio for each mix at 50 kPa confining pressure.

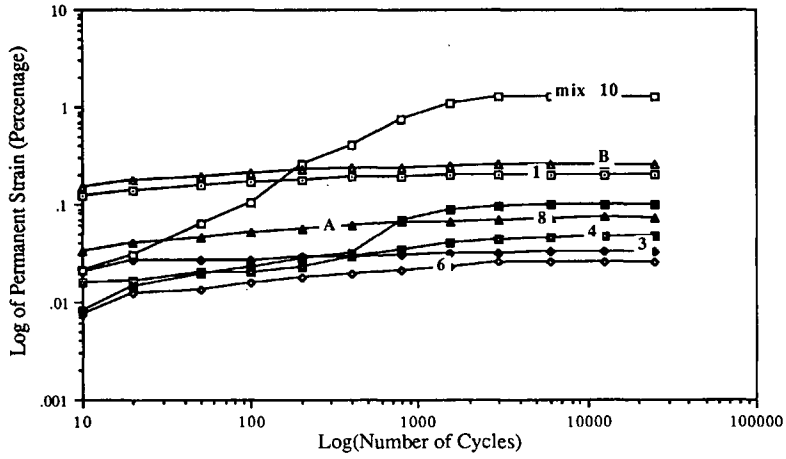

FIGURE 7 Permanent strain versus number of cycles applied before resilient tests.

the materials. All the mixes were confined at a pressure of 35 kPa, and the deviator stress was increased from an initial value of zero until the specimen failed with a strain limit of 3 percent.

The principal stress ratio (σ_1/σ_3) at failure relating to 35 kPa confining pressure was assumed as a simple strength indicator for a direct comparison of the designed mixes. The shear strength versus the principal stress ratio for the different mixes is shown in Figure 8. It can be seen that shear strength increased from the finer to the coarser side of the envelope. A similar trend was also observed when the shear stress ratio (q/p) was assumed to be a failure measure.

PERMEABILITY TEST

Permeability tests were conducted on unbound granular material (*10*) on typical gritstone and basalt, ranging from well- to open-graded mixes, using the permeameter recommended by the Department of Transport Highways and Traffic Advice Note (*11*). As a result of this investigation, the following permeability-grading relationship was proposed:

$$k = -69.2 - 22.1D_{10} + 24.7D_{20} + 228e + 6.96D_{10}^2 - 1.56D_{20}^2$$

where

k = permeability 10^{-3} m/s,
D_{10} and D_{20} = effective sizes (mm) through which 10 percent and 20 percent material passes, respectively,
e = voids ratio of compacted sample with a value ranging from 0.26 to 0.58, and
R = correlation coefficient = 0.99.

The specific gravity of the aggregates was assumed to be 2.65.

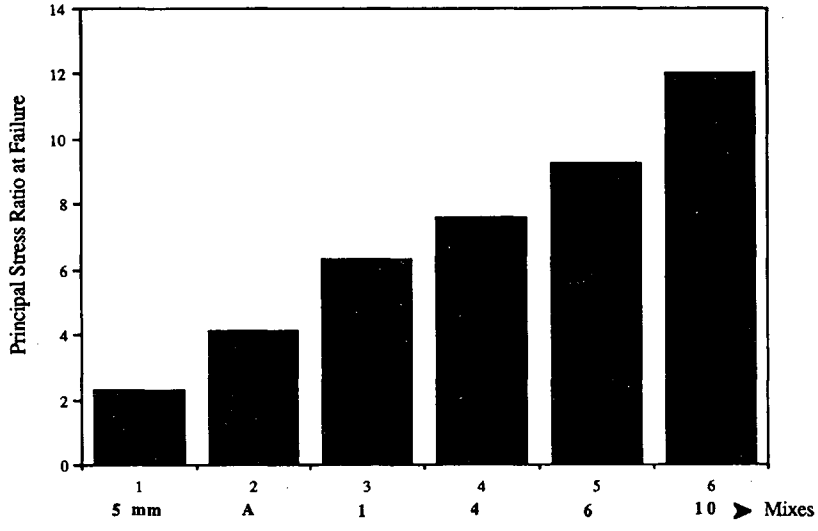

FIGURE 8 Shear strength of different mixes at failure.

FULL-SCALE TRIALS

Construction of the test strip started in July 1991, and the final surface was placed September 26, 1991. The test section at Dargan Road was located on an access point to a refuse disposal site. The test strip, 176 m long and 3.5 m wide, was excavated to a depth of about 700 mm to leave the finished surface of the test strip level with the existing pavement surface. A crusher run capping material with a maximum particle size of 75 mm was laid and compacted in two layers to provide a 350-mm thick layer and therefore a homogeneous platform for laying the proposed roadbase gradings. The test strip was divided into eight equal sections and the material was laid using a mechanical spreader and compacted using an 8-ton roller (five passes on both longitudinal ends) to achieve a 225-mm thick roadbase layer. Samples were collected during the laying process and brought to the laboratory for sieve analysis. The achieved gradings were found to be within 5 percent of the intended mixes. A 30-mm thick bituminous layer was laid on top of the roadbase to obtain a finished surface.

In Situ Dynamic Cone Penetrometer (DCP), Moisture, and Density Measurements

DCP soundings were conducted on the subgrade, capping layer, and roadbase layer to assess the strength of each layer. At least three tests were performed in each bay. The California bearing ratio (CBR) values obtained using the DCP for the subgrade were analyzed on a personal computer using Kleyn's equation (*12*). The capping layer and roadbase were analyzed using the equation developed from laboratory testing of unbound granular material (*13*). The CBR values for the subgrade and capping layer were consistent (13 percent and 16 percent, respectively), showing that the subgrade and capping layer provided a homogeneous platform and allowed a realistic comparison of the behavior of the different bays.

In situ moisture contents and densities for the subgrade, capping layer, and roadbase were measured using a nuclear density meter. The densities of the subgrade for the bays, with the exception of Bay 2, were in the range of 1,900 to 2,100 kg/m^3. Bay 2 (Mix B) was 20 percent lower compared with the other bays. It was also observed that the subgrade moisture content of Bay 2 was about 50 percent higher than that for the other bays. The density and moisture content of the capping layer and the roadbase of all the bays were consistent. After construction, the number and loading of vehicles passing over the test section were assessed using a weigh bridge, and the data were used to convert the number of vehicles to equivalent standard axles.

Falling Weight Deflectometer (FWD)

FWD and deflectograph tests were also conducted on the test strip. An average deflection and contact pressure for each bay was calculated to compare the different bays. Mix 1, which had a high effective fines content (percentage of material passing through a 5-mm sieve) with a coefficient of uniformity C_u (i.e., D_{60}/D_{10}) of 26, gave the maximum deflection. It was also observed that as C_u increased to a certain value, deflection reached a minimum, after which it started to increase. Therefore, the material with a greater percentage of effective fines content gave a higher deflection, and as the percentage of effective fines content decreased, the deflection also decreased to reached a minimum after which a further reduction in percentage of effective fines resulted in a higher deflection. This explains the minimum deflection achieved for both Mixes 4 and 6 with a C_u of 39 and 25, respectively. The mixes with lower effective fines content resulted in a more porous material, and the deflections were greater. There was an optimum percentage of effective fines, which gave a high density and good binding effect.

The values of the elastic modulus of the roadbase material for the different bays were analyzed using EVERCALC (*14*) and are shown in Figure 9. This figure shows that Mixes 4 and 6, with a C_u of 39 and 25, respectively, exhibited the greatest elastic moduli. The mixes on the finer side of the

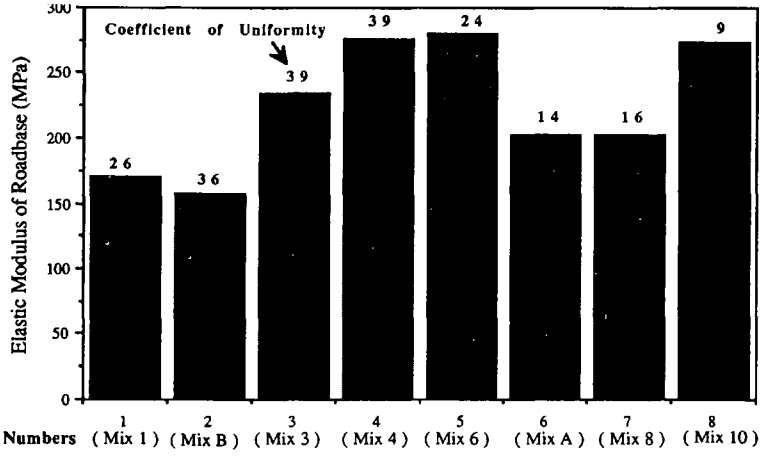

FIGURE 9 Elastic modulus for each roadbase material backcalculated from FWD measurements at Dargan Road.

envelope gave an increased number of possible contact points for movement within the mix to take place. This leads to a low value of elastic modulus as exhibited by Mix 1, which has a large percentage of effective fines. On the other hand, mixes on the coarser side of the other envelope with a smaller number of particles in a given volume showed higher elastic moduli.

Deflectograph Testing

Deflection measurements were taken at the Dargan test strip fortnightly for 6 months with the British version of the deflectograph. For each bay, the representative value of the deflection bowl was computed and plotted against the number of standard axles passed in Figure 10. It was found that the deflection of all the bays was large before opening the test section to traffic. Densification occurred during the application of the first 2,500 standard axles. The observed deflections after this time were quite consistent in the respective bays. Mixes 4 and 6 showed the least deflection.

It was also observed that the materials having more than 40-percent effective fines showed a higher deflection. As the percentage of effective fines decreases and the coefficient of uniformity increases, the deflection decreases. A further reduction in effective fines produces a decrease in C_u and a more porous mix, resulting in an ultimate increase in deflection. This shows that the finer side of the proposed envelope (Figure 1) gives the higher deflection. The deflection decreases from the finer to the coarser side of the envelope up to a certain value, after which a further reduction in effective fines results in an increase in the deflection. This again shows that there is an optimum effective fines content. The anomalous behavior of Mix B could be due to the low density and higher moisture content for the subgrade in that bay as well as due to its low shear strength found in the laboratory. (For more details, refer to the section on DCP, moisture, and density measurements in this paper.)

Automatic Rut Profiler

A realistic method for comparing the relative performance of the different proposed mixes is to measure the rut depth under actual vehicular loads and then compare the different designed mixes directly. As discussed previously, the subgrade, capping layer, and surfacing were the same for all the bays in the test strip. The only variable was the roadbase material. Therefore, the comparison of rut depth in the different bays provides a direct indication of the performance of the designed roadbase mixes. Rut depth was measured fortnightly using an automatic rut profiler.

The portable rut profiler consists of a 51-mm^2 steel beam with a recording box (175 mm × 120 mm) at one end. The three beams are fitted together for testing. The total length of the profiler is approximately 2.75 m. The beam sits on three large adjustable screws, and a steel trolley fitted with a flexible sensor (which sits on the surface of the pavement during the testing and records the rut) can slide on the beam. This instrument is used to plot the rut profile of the pavement; these data may be stored directly on a personal computer.

During this testing program, the rut profile of all the bays was measured in the transverse direction before opening the test section to traffic and was considered to be the baseline. Subsequently the rut measurements were conducted fortnightly. The transverse rut profiles for Mixes 6 and A are plotted against the standard axles passed in Figures 11 and 12 to show a comparison between the proposed (Mix 6) and current specifications (Mix A). The results showed that the base course in all the cases increased in thickness between the wheel paths, which is in good agreement with the findings of the AASHO Road Test (*15*). It was also observed in trials at Dargan Road that the depth of rut was more than twice as great for the open-graded material as for the well-graded ones. This shows that the resistance to permanent deformation decreases for the coarsely graded material as compared with the more well-graded materials. The same trend was observed from the repeated load plastic tests conducted in

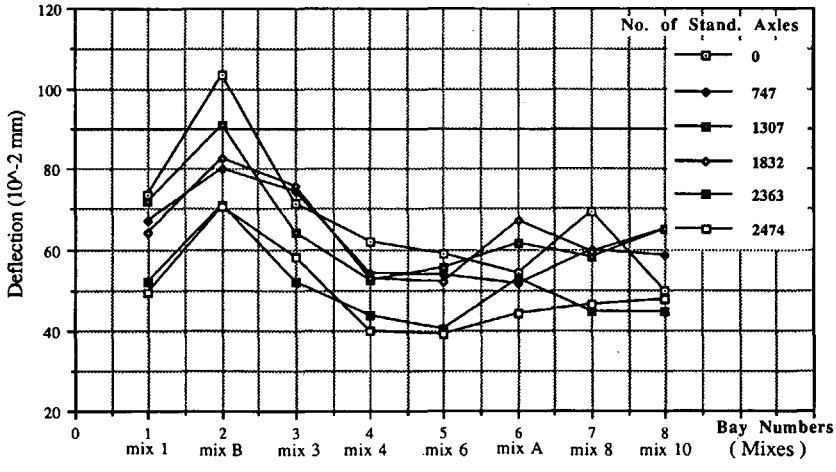

FIGURE 10 Deflection versus standard axle passed at Dargan Road in first month.

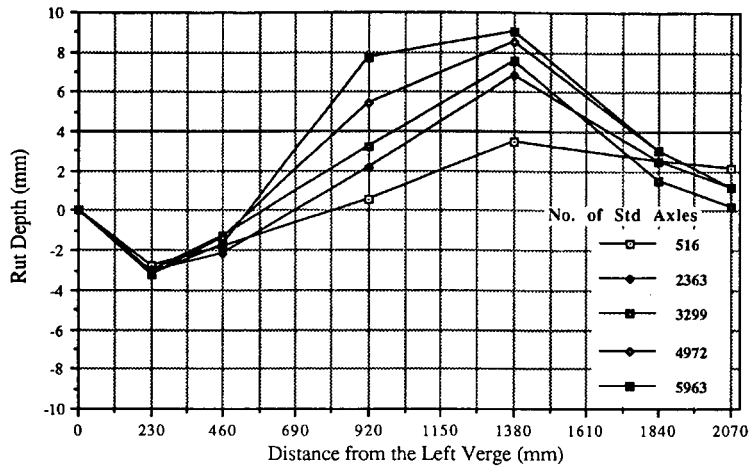

FIGURE 11 Rut depth versus standard axles passed for Bay 5 (Mix 6).

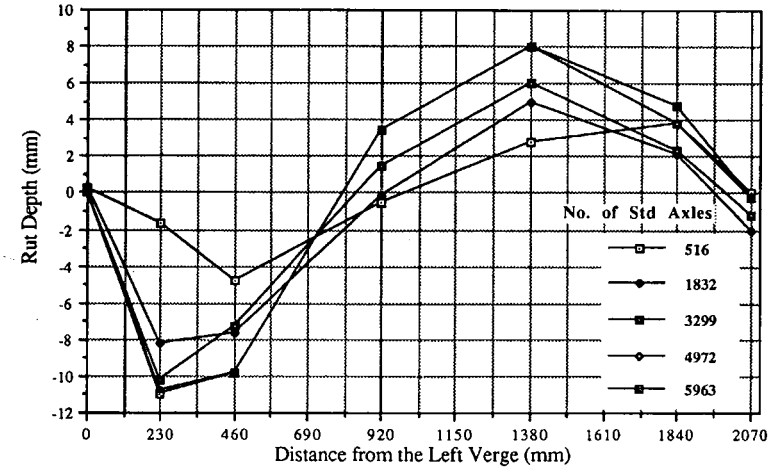

FIGURE 12 Rut depth versus standard axles passed for Bay 6 (Mix A).

the laboratory (Mixes 8 and 10 showed higher plastic strain than the other mixes).

DISCUSSION OF RESULTS

The above findings showed that the greater the percentage of material retained on a 5-mm sieve, the higher the stiffness. Whereas the open-graded mixes showed less resistance to permanent deformation, the well-graded mixes with a percentage of effective fines more than 50 percent showed less resistance to permanent deformation. It can be seen in Figure 3 that Mixes 3, 6, and 10 showed a greater stiffness than the other mixes tested, and mixes 3 and 6 also showed greater resistance to permanent deformation (Figure 7).

Similar trends were observed on the full-scale testing strip. Mixes 3, 4, 6, and 10 showed lesser deflection, confirming that they had a higher elastic stiffness. The rut depths for mixes on the finer side of the envelope (Mixes 1, 3, 4, and 6, with high C_u) were less than about half of those for the mixes on the coarser side of the envelope (Mixes 8 and 10, with low C_u). This was also confirmed by the trends obtained for the plastic strain for Mixes 8 and 10 in the repeated load triaxial laboratory tests; that is, they showed a higher permanent deformation as compared with Mixes 1, 3, 4, and 6. It can also be concluded that permanent deformation under repeated loading provides a more definitive evaluation of unbound granular materials than do resilient modulus and shear strength.

CONCLUSIONS

The following may be concluded from the laboratory tests:

1. The elastic stiffness increases from the finer to the coarser end of the envelope.
2. The resilient volumetric and shear strains also implied a similar trend, that is, the resistance to shear and volumetric

strains increases from the finer to the coarser end of the proposed grading envelope.

3. The resistance to permanent deformation was less for more open-graded mixes compared with well-graded ones.

4. Shear strength increases from the finer to the coarser end of the envelope.

5. The permeability for the base, subbase, and capping layers for material used for road construction may be assessed with the help of the equation proposed in the section on permeability testing.

The following may be concluded from the test strip:

1. The material that had more effective fines showed a higher deflection, and as the effective fines content decreased, the deflection also decreased up to a certain value, after which a further reduction in effective fines resulted in a higher deflection. Thus, there was an optimum effective fines content for minimum deflection and rut.

2. Materials with a C_u from 25 to 40 and having an effective fines content from 27 to 44 percent showed low values for deflection and rut.

3. The elastic modulus was generally found to increase from the finer to the coarser end of the envelope.

4. The rut depth was found to be more than twice as great for the open-graded material as for the well-graded materials.

ACKNOWLEDGMENTS

This research was sponsored by the Roads Service of the Department of the Environment. The authors wish to acknowledge the help of the staff of the Department of Civil Engineering, University of Nottingham; the laboratory equipment provided by that department; and the sponsorship provided by the government of Pakistan.

REFERENCES

1. P. Shaw. *Stress-Strain Relationships for Granular Materials Under Repeated Loading*. Ph.D. thesis. University of Nottingham, 1980.
2. N. H. Thom. *Design of Road Foundations*. Ph.D. thesis. University of Nottingham, 1988.
3. M. R. Thompson and K. L. Smith. Repeated Load Triaxial Characterisation of Granular Bases. Presented at 69th Annual Meeting of the Transportation Research Board, Washington, D.C., 1990.
4. Roads Circular No. 19/87. Department of the Environment for NI Roads Service Headquarters, 1987.
5. K. E. Cooper, S. F. Brown, and G. R. Pooley. The Design of Aggregate Gradings for Asphalt Base Courses. *Proc., Association of Asphalt Paving Technologists, Technical Session*, San Antonio, Tex., 1985.
6. J. R. Boyce. *The Behaviour of Granular Material Under Repeated Loading*. Ph.D. thesis. University of Nottingham, 1976.
7. N. W. Lister and R. Jones. The Behaviour of Flexible Pavements Under Moving Wheel Loads. *Proc., 2nd International Conference on the Structural Design of Asphalt Pavements*, Ann Arbor, Mich., 1967.
8. J. W. Pappin. *Characteristics of a Granular Material for Pavement Analysis*. Ph.D. thesis. University of Nottingham, 1979.
9. J. R. Morgan. The Response of Granular Materials to Repeated Loading. *Proc., 3rd ARRB Conference*, 1966.
10. M. A. Kamal, O. T. Farouki, D. A. B. Hughes, and A. A. Sha'at. Influence of Grading on the Permeability and Performance of Subbase Materials. *The International Journal of Construction Maintenance and Repair*, Vol. 5, No. 6, Nov./Dec., 1991.
11. A Permeameter for Road Drainage Layers. Department of Transport Highways and Traffic, Departmental advice note HA 41/90, 1990.
12. E. G. Kleyn. *The Use of Dynamic Cone Penetrometer*. Report 12/74. Transvaal Roads Dept. Pretoria, South Africa, 1975.
13. M. A. Kamal. Behaviour of Granular Materials used in Flexible Pavements. 2nd Progress Report. Department of Environment, Northern Ireland, 1991.
14. Pavement Evaluation Program EVERCALC, Version 2.0., Washington State Transportation Center, 1988.
15. *Special Report 73: The AASHO Road Test*. HRB, National Research Council, Washington, D.C., 1962.

Publication of this paper sponsored by Committee on Soil and Rock Properties.

Applicability of Resilient Constitutive Models of Granular Material for Unbound Base Layers

M. KARASAHIN, A. R. DAWSON, AND J. T. HOLDEN

Analytical design methods for pavements require the determination of the resilient behavior of each layer. Granular material behavior under traffic loading is nonlinear and stress path dependent. Because the deformation characteristics of the material are significantly affected by stress magnitude and path, stress-strain behavior must be modeled accurately. A wide range of graded granular material types was selected to assess the applicability of stress-strain models. A repeated load triaxial test apparatus, which can cycle deviatoric and cell pressure, was used to test a variety of stress paths for furnace bottom ash, graded washed river sand, sand and gravel, Fontainebleu sand, limestone, and gritstone. Linear and nonlinear regression programs were used to obtain the parameters for five different models. The results indicated that there is no unique model to represent the granular material behavior under all circumstances. Elhannani's model can be used for predicting the response to cyclic deviatoric stress with cyclic cell pressure test data. Using K–Θ and Pappin and Brown models, approximate predictions can be made of axial stiffness under the cycling of both stresses using parameters obtained from more-simple only-cyclic deviatoric stress test data.

Analytical design methods for pavements require the determination of the resilient behavior of each layer. It is well known that granular material behavior under traffic loading is nonlinear and stress path dependent. Although density, degree of saturation, stress history, and grading have some effect on the behavior of granular material, the deformation characteristics of the material are significantly affected by stress magnitude and path. Therefore, it is important to model accurately the stress-strain behavior.

Granular material in the road is generally used in a moist but unsaturated condition. However, this makes it difficult to measure the effective stress in the laboratory. To eliminate this problem, four triaxial tests were conducted on different materials in the dry condition so that the stress-strain characteristics of the material could be obtained in terms of effective stress. Two other triaxial tests were conducted on partially saturated materials and analyzed in terms of total stress.

A range of graded granular material types was selected to assess the applicability of different stress-strain models. A repeated load triaxial test apparatus with a wide range of stress paths was used to test furnace bottom ash, graded washed river sand, sand and gravel, Fontainebleu sand, limestone, and gritstone. From the results, parameters were obtained for several different models developed in the last two decades. The strain behavior of the models under the individual stress paths were predicted, and the predictions were compared with the measured data to assess the performance of those models under different stress paths.

M. Karasahin and A. R. Dawson, Department of Civil Engineering, University of Nottingham, University Park, Nottingham, NG7 2RD England. J. T. Holden, Department of Theoretical Mathematics, University of Nottingham, University Park, Nottingham, NG7 2RD England.

MATERIALS

To see the general behavior of granular material under traffic loading and to test resilient constitutive models on a variety of aggregate types, materials from different origins were tested. The materials selected for the repeated load triaxial test were crushed limestone, sand and gravel, gritstone, graded washed river sand, Fontainebleu sand, and furnace bottom ash. All are more or less commonly used in Europe for base layers, subbase layers, or capping. Materials were tested without changing the grading. The grading curves are shown in Figure 1.

REPEATED LOAD TRIAXIAL TEST APPARATUS

Although it is unable to produce stress conditions representative of the real pavement structure, the triaxial test apparatus has been used for many years to investigate the stress-strain behavior of granular materials. In connection with the repeated loading of granular materials, a triaxial apparatus was developed by Boyce (*1*) at Nottingham University able to cycle both the deviator and confining (chamber) stress. Pappin (*2*) slightly modified some parts of the apparatus to apply tensile stress to the granular material. In 1991 the electronic control system of the apparatus was replaced by a digital control system (*3*). More details about the development of the apparatus can be obtained from work by Boyce (*1*), Pappin (*2*), Boyce et al. (*4*), and Brown et al. (*5*).

The apparatus (Figure 2) is capable of applying an axial load of 3 kN by a 50.8-mm diameter hydraulic actuator at a frequency range of 0–16 Hz. Confining stress is also applied by a hydraulic actuator at a frequency range of 0–2 Hz. This actuator operates a cylinder pump that pressurizes the cell fluid. Silicone oil is used as the cell fluid because of its low density and excellent electrical insulation, which allows on-sample instrumentation to be used without difficulty.

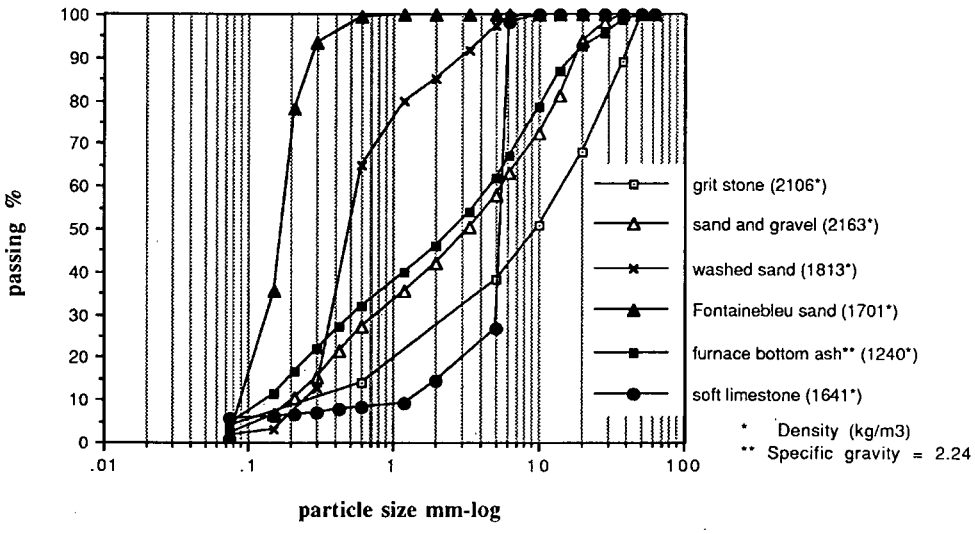

FIGURE 1 Grading curves and densities.

Axial deformations are measured using two linear variable differential transformers (LVDTs) mounted between two pairs of threaded rods. Radial deformations are measured by two hoops incorporating strain gauges fixed to the same rods. The rods are screwed into studs, which are clamped to the membrane and extend a short way into the sample.

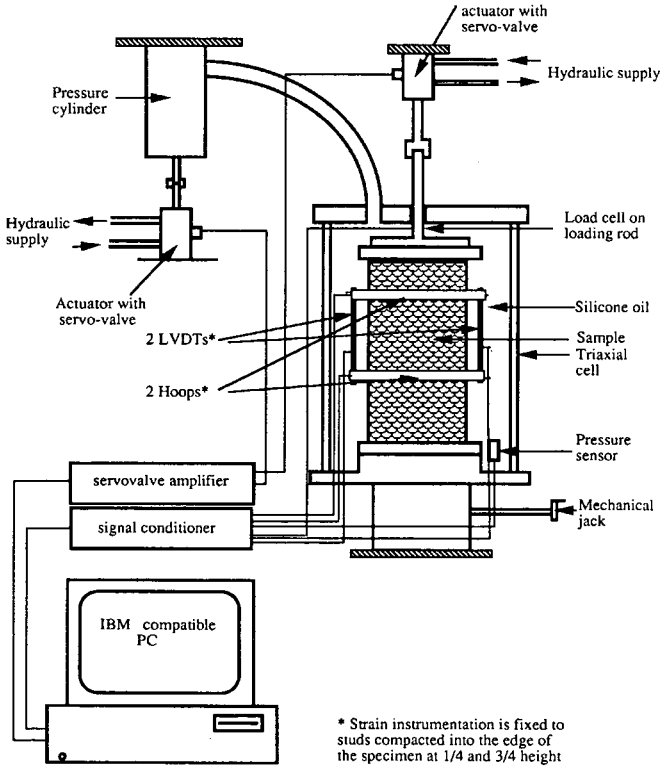

FIGURE 2 Diagram of repeated load triaxial apparatus.

SAMPLE PREPARATION

To form a sample, six layers of material were compacted from bottom to top. A vibrating table was used as a compaction tool, and each layer was subjected to vibration for 15 sec under a surcharge of 30 N (*1,2,6*). A leveling disc was used during the compaction process to apply the compaction evenly across the top of the sample. It was seen from previous experience that fine grains tended to migrate down during the compaction, whereas coarse particles moved up. To prevent this migration, coarse grains were placed in the mold by hand at the bottom before the vibration commenced. Each sample was enclosed in two latex membranes. During the sample preparation, the inner one was held against the porous inner surface of the mold by applying a vacuum. The outer one was added after compaction to cover any possible punctures produced in the inner membrane during the compaction process. An internal partial vacuum was applied to the sample while it was instrumented and before external cell pressure was applied. Before instrumenting the sample, it was visually checked for uniformity. Suspect samples were rejected. The densities of the samples are included in parentheses in the legend of Figure 1.

TEST PROGRAM

Six resilient strain tests were conducted by applying a range of stress paths (Table 1). To determine independently the resilient strain behavior of the plastic strain developed (*6*), 50 cycles of loading were applied for each stress path, and the mean response during the last 5 cycles was recorded. For materials a long way from saturation, the resilient behavior is affected little by loading frequency, so a frequency of 1 Hz was chosen (*7*).

Stress paths of different amplitudes were applied in several stress directions. The applied stress paths can be divided into two groups (Table 1). Type 1 is composed of cyclic deviatoric

TABLE 1 Stress Paths

Cyclic deviatoric stress (Type 1)		Cyclic Both stresses (Type 2)	
Cell pressure (kPa)	Deviatoric stress (kPa)	Cell pressure (kPa)	Deviatoric stress (kPa)
250	0-50	183-167	50-100
250	0-100	150-133	0-50
250	0-150	150-117	0-100
250	0-200	150-100	0-150
200	0-50	100-83	0-100
200	0-100	100-67	0-100
200	0-150	100-33	0-150
200	0-200	100-150	0-50
150	0-50	100-150	0-100
150	0-100	100-150	0-150
150	0-150	100-150	0-200
150	0-200	50-100	0-50
100	0-50	50-100	0-100
100	0-50	50-100	0-150
100	0-50	50-100	0-200
100	0-50		
50	0-50		

(axial) stress paths under a constant cell (confining) pressure. Type 2 is composed of paths in which both cell pressure and deviatoric stress are cycled in phase. This group can better represent real pavement loading.

Many laboratories still use constant confining pressure testing (Type 1) to determine the resilient behavior of the material because this type of equipment is more cost effective when compared with the apparatus, which can cycle both pressures at the same time. The testing procedure here aimed to determine to what extent models could predict the behavior under general stress cycling from data collected under the simplified regime of a constant confining stress (Type 1).

MODELS OF RESILIENT STRAIN BEHAVIOR

Because granular material behavior is markedly nonlinear and stress dependent, nonlinear stress-strain relationships should be used to model the real behavior of pavement structures.

For this particular work, five different granular material models were investigated to fit the data obtained from the repeated load triaxial tests. These models will be introduced briefly. All models are expressed in terms of p (mean normal stress, which is one-third of the bulk stress, Θ) and q (deviatoric or additional axial stress). Material (model) constants are shown by capital letters (A, B, C, etc.).

K–Θ Model

The most commonly used nonlinear elastic model is the so-called K–Θ model (*6*) in which the resilient modulus (M_r in units of stress) is expressed in the form of

$$M_r = A(3p_{max})^B \tag{1}$$

which strictly applies to triaxial testing involving the application of relatively small axial repeated loading starting from the $q = 0$ condition.

The model is widely used by pavement engineers to introduce a stress-dependent resilient modulus because it is easy to implement in finite element and backcalculation programs. However, Poisson's ratio in the model is assumed to be constant, and the effect of the deviatoric stress on the resilient properties is not considered. This latter effect is certainly not negligible in pavement engineering (*8*), and therefore, may be used only for low deviatoric stress levels. Clearly, such a limitation is unsatisfactory for pavement applications where, in general, shear stresses are relatively large. The model has been developed from simple laboratory triaxial tests in which the initial deviatoric stress is always zero. This limitation does not apply to tests described in this paper, and the implications of this are discussed later in the paper. Note that constant A must have dimensions controlled by constant B for the equation to be dimensionally correct.

Uzan Model

Uzan (*9*) modified Equation 1 to introduce the effect of deviatoric stress. The modified model is

$$M_r = A(3p_{max})^B q^C \qquad q > 0.1\sigma_r \tag{2}$$

where σ_r is radial stress. The problems of constants' dimensions, zero initial deviator stress, and a fixed Poisson's ratio remain.

Pappin and Brown Model

It has been considered useful to separate behavior into shear and volumetric components. For nonlinear behavior, no assumption would then be made regarding a constant Poisson's ratio (*10*). Pappin and Brown (*11*) developed a model framed in this manner—the contour model for granular material behavior. It was designed to model general stress path excursions regardless of the p,q stress state. Mayhew (*12*) concluded that stress path length (which was included in the Pappin and Brown model) had no significant effect on the shear strain behavior. The model could then be rewritten (*7*) in the form

$$\varepsilon_v = \left(\frac{p}{A}\right)^B \left(1 - C\frac{q^2}{p^2}\right) \tag{3}$$

$$\varepsilon_s = \left(\frac{p}{D}\right)^E \frac{q}{p} \tag{4}$$

where ε_v, ε_s are volumetric and shear strain, respectively, and material constants A and D have units of stress.

The stress paths in this and the following models are assumed to be from zero to the conditions indicated by p and q. For actual stress paths, the strain is computed by comparing the predicted values for each end of the path. Bulk and shear moduli are usually defined, respectively, on the basis of the

strains as

$$K = \frac{p}{\varepsilon_v} \tag{5}$$

$$G = \frac{q}{3\varepsilon_s} \tag{6}$$

Boyce Model

While Pappin and Brown's (*11*) approach sought to describe observed data, Boyce (*13*) developed a similar $G-K$ model from first principles, using the theorem of reciprocity (*14*), also expressing it in volumetric and shear parts. The model is nonlinear elastic and isotropic. The model is expressed in the form

$$\varepsilon_v = p^B\left[\frac{1}{A} - \frac{(1-B)}{6C}\frac{q^2}{p^2}\right] \tag{7}$$

$$\varepsilon_s = \frac{p^B}{3C}\frac{q}{p} \tag{8}$$

In this formulation, constants A and C have dimensions controlled by constant B.

It is worth noting that Mayhew (*12*) found that the influence of the mean normal stress (p) on the bulk modulus differs from that on the shear modulus (G), even when the ratio q/p is constant. On this basis, it is evident that B in Boyce's model should be different for the volumetric and shear strain formulations. This approach was taken by Sweere et al. (*15*), Sweere (*16*), and Jouve et al. (*17*) to fit their data into the model. A nonlinear regression analysis revealed that constants B and C should be different for the volumetric and shear strain formulae. The resulting model is the same as the Pappin and Brown model as rewritten by Brown and Selig (*7*) and given in Equations 3 and 4. It has five parameters instead of the three parameters in the original Boyce model.

Elhannani Model

Elhannani (*18*) introduced anisotropy into the original Boyce model, taking the form

$$\varepsilon_v = p_a^{1-B}p^B\left[\frac{1}{A} - \frac{(1-B)}{6C}\left(\frac{q}{p}\right)^2 - \frac{B}{D}\left(\frac{q}{p}\right)\right] \tag{9}$$

$$\varepsilon_s = p_a^{1-B}p^B\left[\frac{1}{3C}\frac{q}{p} - \frac{1}{D}\right] \tag{10}$$

where p_a is atmospheric pressure (100 kPa) and A, C, and D have units of stress.

All of the models could use the device Elhannani (*18*) introduced that uses atmospheric pressure as a normalizing factor to make stress terms nondimensional. Elhannani used his approach to model behavior on a variety of stress paths that radiated from a single initial stress state at low p,q.

MODEL PARAMETERS

For each model, parameters must be determined from experimental results. Ideally, this determination should be simple, which is possible if the model can be rewritten in a linear form. K–Θ and Uzan (*9*) models may be converted to a linear form by taking the logarithm of both sides of the equations. Hence, any linear regression program for the former and a multivariable regression program for the latter model may be used to find the constants. Considering the Type 1 stress paths, the Uzan (*9*) and K–Θ models result in the same form of Equation 1 because $q = 3p$. Therefore, for the Type 1 paths, the results are presented as K–Θ results.

For the more complex models reviewed here, the BMDP (*19*) statistical package was used. This provides a derivative-free nonlinear regression program with a pseudo-Gauss-Newton iterative algorithm (*19*). For each model, a short program was written in the BMDP code defining the initial values of parameters, boundaries, number of iterations, accuracy limit, and model. The imposed stresses and measured strains for each stress path were then supplied to provide the data set that must be predicted by the program with minimum error. The initial values are important when performing a nonlinear regression analysis. If they are not close to the solution, it is almost impossible to find a feasible solution. Initial values must be adjusted until a reasonable solution is found. Sometimes it is possible to find a local solution that does not satisfy all the data. For this situation, initial values and boundary conditions need to be checked. Sometimes, although the boundary conditions and initial values are changed, no improvement in the results can be seen, raising the possibility that the test data supplied do not fit the model well.

PREDICTIONS WITH THE MODELS

Parameters were obtained for each model using the repeated load triaxial test data. For each model, two different sets of parameters were obtained—one from Type 1 stress paths and one from Type 2 paths—to fit both volumetric and shear strain models where appropriate. Predictions of axial and radial strain have been made using the different stress path data sets, the different materials, and the different models. (For comparison purposes, only axial strain predictions are presented because the resilient modulus, perhaps the most important parameter in pavement design, is a direct function of this strain.) The derived model parameters are given by Karasahin (*20*).

The parameters were then used to predict the data sets from which they had been derived to assess the applicability of the models. Axial strain was also predicted for the Type 2 paths using the parameters obtained from the Type 1 stress path test data. Satisfactory results would indicate that relatively simple cyclic deviatoric stress tests could be used to predict behavior when both stresses are cycled (as in real pavements).

DISCUSSION OF RESULTS

The results are discussed in relation to the following three categories:

1. Predicted axial strain for cyclic deviatoric stress (Type 1 path data to predict the behavior under Type 1 loading);
2. Predicted axial strain for both stresses cycled (Type 2 data to predict Type 2 behavior); and
3. Predicted axial strain under both stresses cycling using the parameters derived from the cyclic deviatoric stress testing (Type 1 data to predict Type 2 behavior).

Predictions of Cyclic Deviatoric Stress Behavior (Type 1)

The results for furnace bottom ash were least successfully predicted. The results shown in Figure 3 show some of the difficulties involved.

The predictions of the K–Θ model (*6*) had a similar pattern for all materials, as shown in Figures 3–5. Values of strain were underpredicted at high levels. Predicted values are almost equal to each other for the same cell pressure, although the deviatoric stress level and hence the measured axial strain were different (sets of points on subhorizontal lines in Figure 3).

The Boyce model predicted a somewhat better match to the measured results, although there was still a small tendency for the effect of increasing deviatoric stress to be underestimated. For the furnace bottom ash, a particularly poor fit was recorded (Figure 3). This lack of fit reflects, in part, the need for both volumetric and shear (and thus axial and radial) strains to be modeled using the same three parameters (see Equations 7 and 8), although only the matching of one strain set is illustrated.

The Pappin and Brown (*11*) model often provides a good fit at low strain levels where granular material has a high resilient modulus. However, for high strain levels, the model greatly underestimated the strain. Nevertheless, the predictions of the model are without significant scatter.

The Elhannani (*18*) model predicts higher axial strains at low strain levels, although at high strain levels, it gave an excellent fit to and prediction of the recorded data.

Prediction of Behavior When Both Stresses Are Cycled (Type 2)

The K–Θ and Uzan models showed a similar pattern for the prediction of axial strain (Figures 6 and 7). Both models gave a reasonable fit to data. The results for the gritstone (Figure 7) were fairly typical of the six materials tested as far as the K–Θ and Uzan models were concerned. The prediction of axial strain by the Uzan model was generally greater than the K–Θ approach, and its average was more nearly on the line of equality. However, both models showed considerable scatter. Nevertheless, the prediction of strain using the K–Θ model was better for the Type 2 loading than for the Type 1 loading. The result for the Fontainebleu sand was exceptional (Figure 6). Neither model gave acceptable predictions.

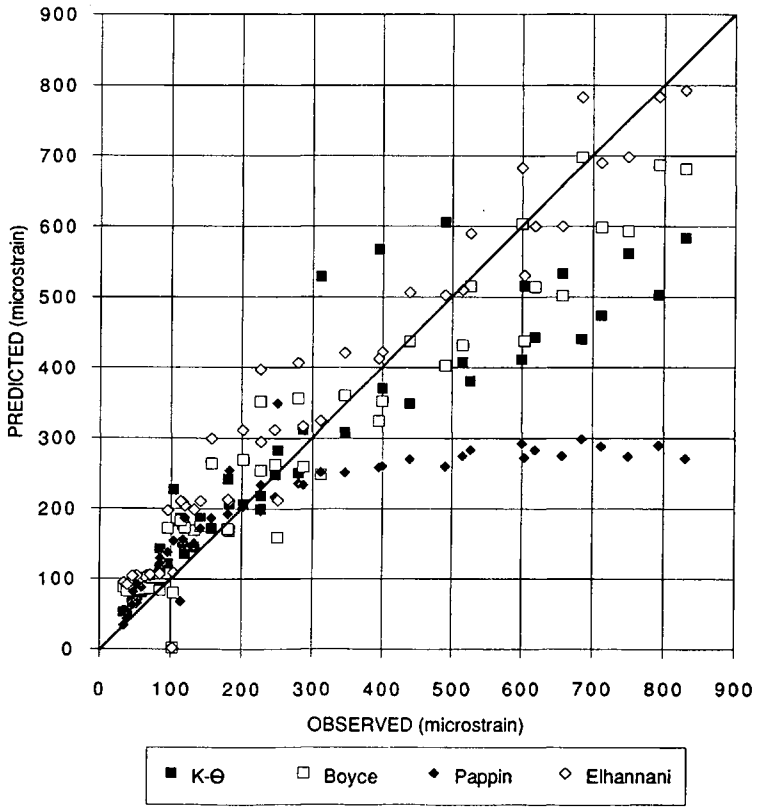

FIGURE 3 Furnace bottom ash—axial strain due to cyclic deviatoric stress.

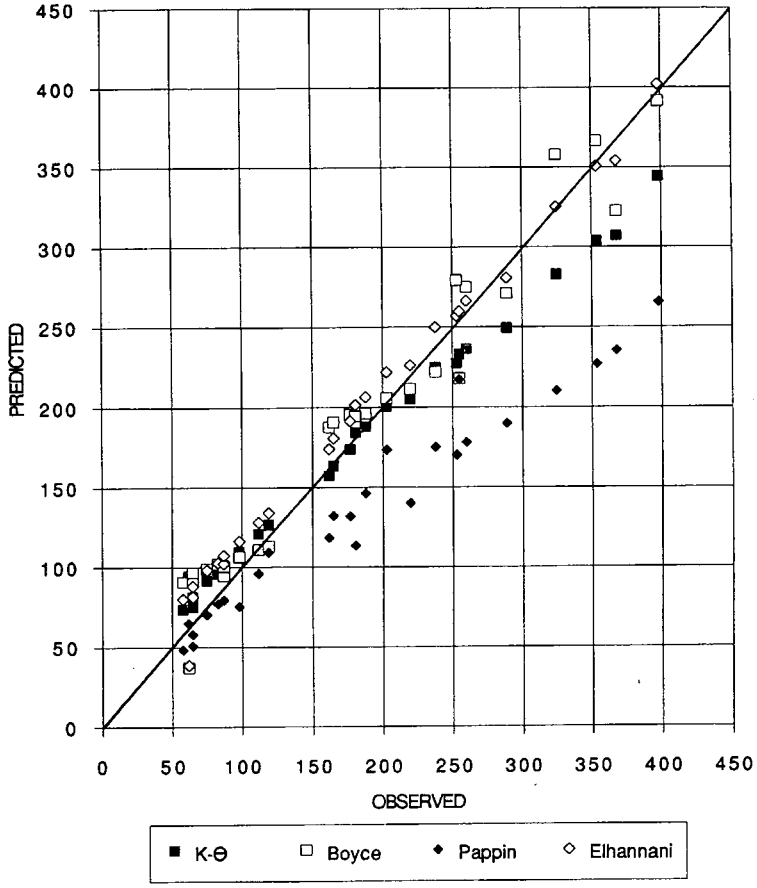

FIGURE 4 Fontainebleu sand—axial strain due to cyclic deviatoric stress.

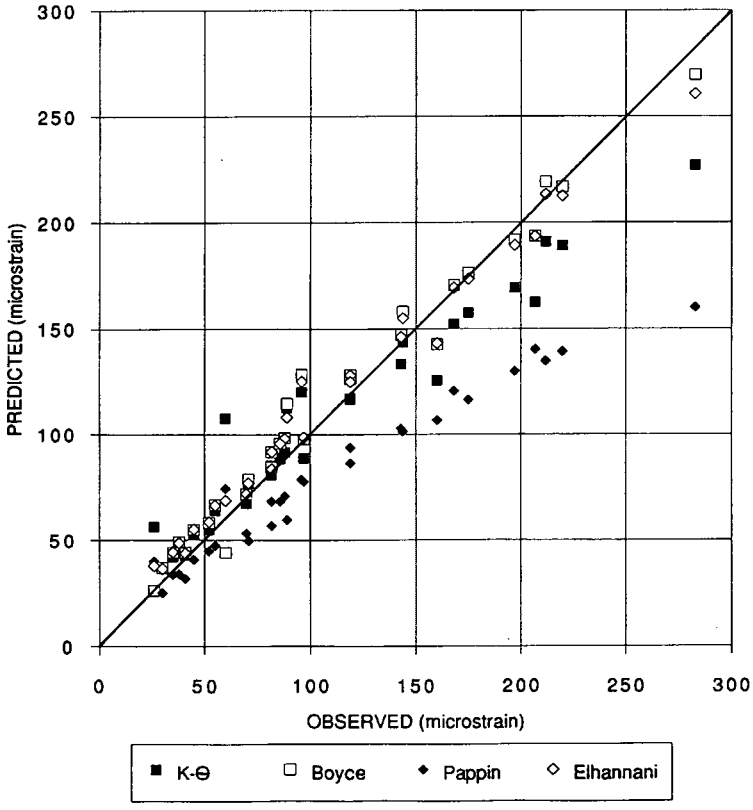

FIGURE 5 Gritstone—axial strain due to cyclic deviatoric stress.

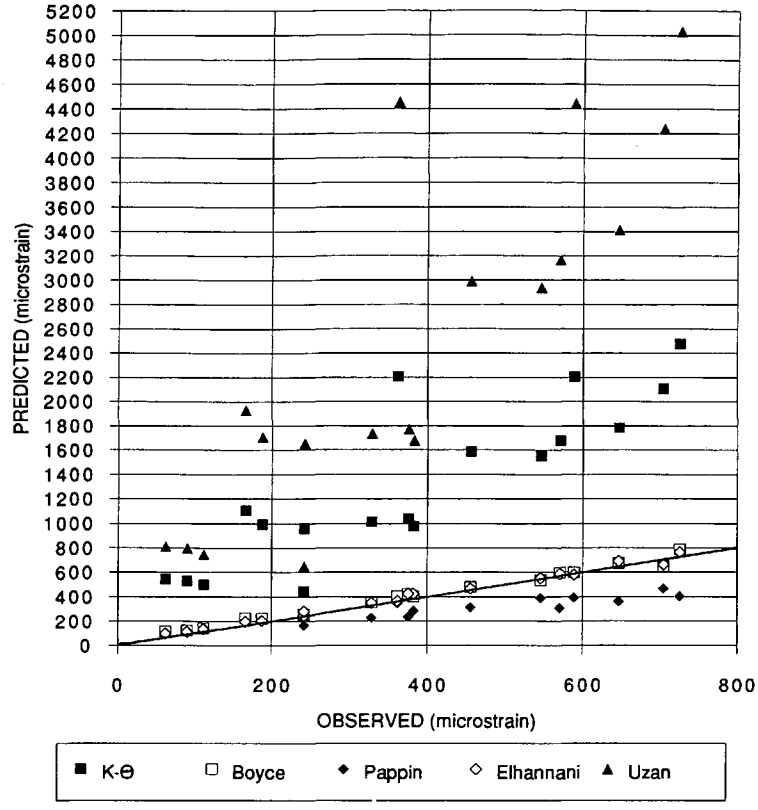

FIGURE 6 Fontainebleu sand—axial strain due to both stresses cycling.

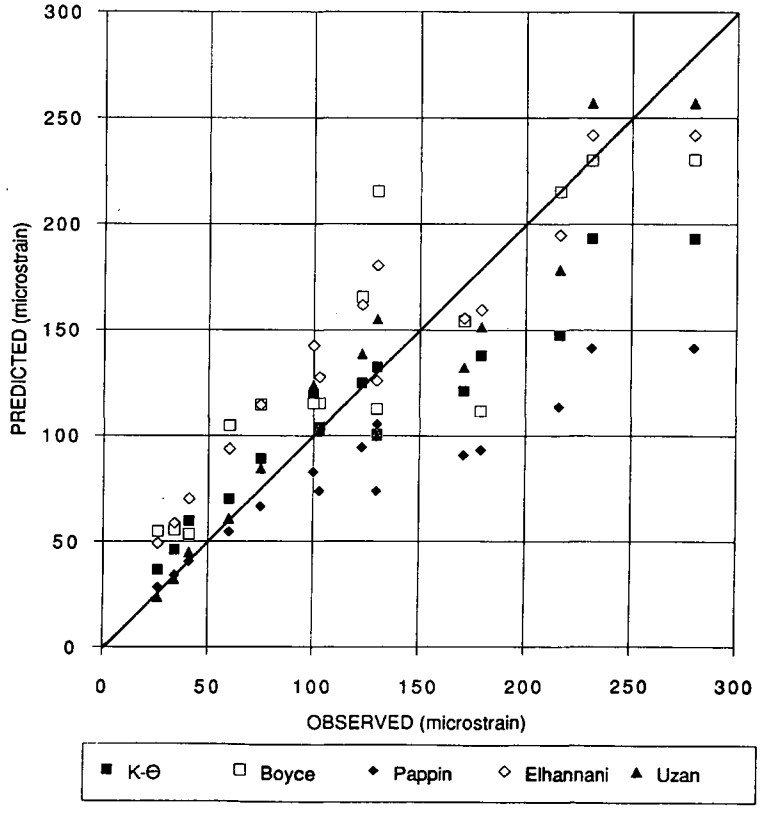

FIGURE 7 Gritstone—axial strain due to both stresses cycling.

The Pappin and Brown model exhibited the same drawback as mentioned in the previous section. In addition, it had greater scatter.

The Boyce and Elhannani models showed almost the same patterns as before, except for the soft limestone for which the Boyce model was unable to predict axial strain accurately. The Elhannani model again provided a good prediction and a relatively nonscattered fit for most aggregates, but it overestimated strain at low levels. In the case of the furnace bottom ash, all the models performed quite well, showing less scatter than that in Figure 3.

Predictions of Behavior under Cycling of Both Stresses Using Parameters Obtained from Cyclic Deviatoric Stress Tests Data (Type 2 Behavior Predicted on Basis of Type 1 Loading)

An aim of the study was to show whether cyclic deviatoric stress test results (which are relatively simple to perform) may be used to predict the stress-strain relationships when both stresses are cycled. This stress-strain is more relevant to the situation found in the pavement.

The Pappin and Brown model generally gave an underestimated prediction of axial strain for sand and gravel, soft limestone, and Fontainebleu sand, which is consistent with its underestimation of strain discussed in the last two sections (compare Figure 8 with Figure 6). For the other three materials, the initial prediction using the Pappin and Brown approach is generally good or a little high at low strains, but it underestimates strain at high levels.

The Boyce and Elhannani models also underestimated strain at low levels for all the materials (see Figure 9). However, the Boyce and the Elhannani models overestimated sand and gravel, furnace bottom ash, soft limestone, and Fontainebleu sand at high strain levels. Hence it appears that the Boyce and Elhannani models are unable to model accurately, on the basis of simple tests, the stiffening of these materials under stress paths closest to those experienced in the pavement.

The Boyce and K–Θ models were the least successful in modeling the behavior of gritstone. For this material the Elhannani model performed best (Figure 9). Predictions that used the K–Θ model were slightly superior to other models when all test results were considered; however, this is because they usually lie about the 1:1 observed:predicted line. In addition, the scatter in predictions of strain under individual stress paths is inconsistent in over-, under-, or on-prediction from material to material. Therefore, the K–Θ model with the parameters derived from the cyclic deviatoric stress tests (Type 1 paths) can be used to predict only approximate behavior of the material under the cycling of both stresses (Type 2 paths).

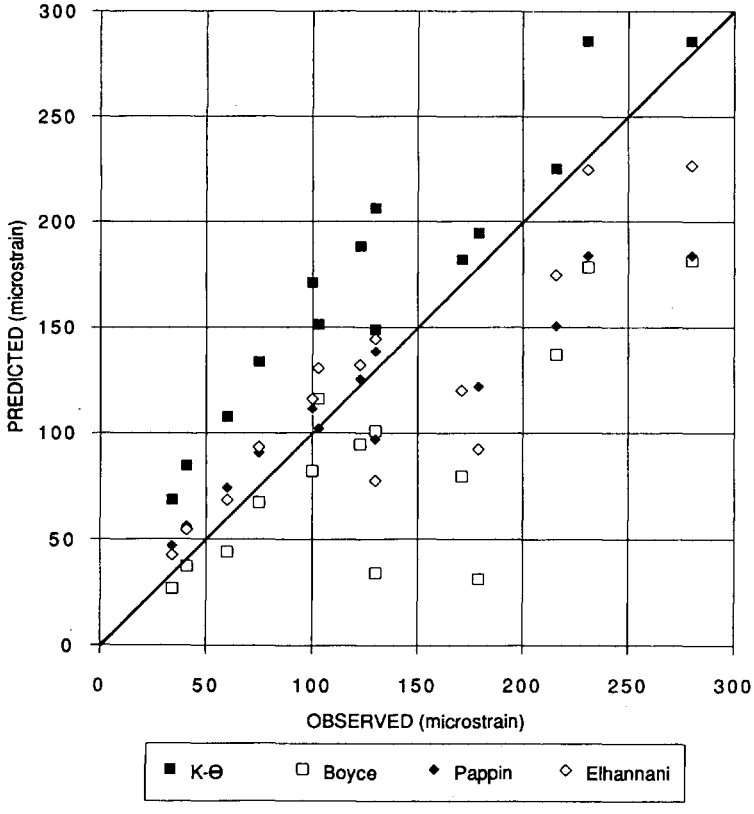

FIGURE 8 Gritstone—axial strain due to both pressures cycling, predicted from simple tests.

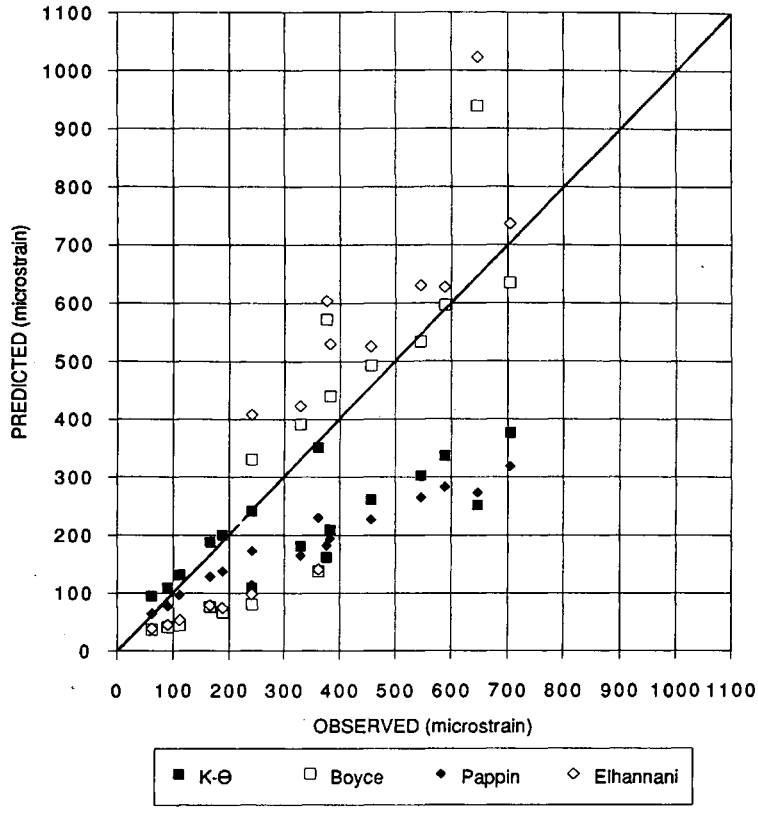

FIGURE 9 Fontainebleu sand—axial strain due to both pressures cycling, predicted from simple tests.

CONCLUSIONS

The testing and modeling program conducted on a range of different aggregate types has demonstrated the following:

1. It is difficult to predict strains (as measured in triaxial testing) by using available resilient constitutive models for aggregates under pavement-type loading.
2. The use of multivariate nonlinear regression programs can be operator-sensitive and may not be an acceptable method for routinely determining model parameters.
3. Of the models available, the Elhannani model (*18*) proved best when applied to cycling deviatoric stress testing.
4. The Elhannani approach is also best for modeling behavior when deviatoric and confining pressures are cycled.
5. There remain considerable uncertainties in using any model, with parameters derived from simple repeated deviator stress testing, for predicting behavior when both stresses are cycled. Of those studied, the K–Θ model (*6*) had the fewest errors.
6. Modeling a range of different types of stress path appears to be the most demanding aspect. In this situation, the Pappin and Brown approach (*11*) has the most value.

These findings can be partially explained by referring to the inherent limitations of the models. The Boyce model (*13*) satisfied the reciprocity theorem (no gain or loss of energy during cycling), and this is certainly invalid for hysteretic materials. By dropping this limitation, Pappin and Brown's model is somewhat better. The limitations of the K–Θ model (in ignoring deviatoric stress effects) have already been described. The improvements of Uzan (*9*) do not appear to be significant. Elhannani's approach, by incorporating an allowance for anisotropy, appears to overcome many of the deficiencies of other models.

ACKNOWLEDGMENTS

The authors acknowledge gratefully the Turkish Government for providing funds for the principal author to perform the study. The facilities of the Department of Civil Engineering, University of Nottingham, were readily made available. The service of the Cripps Computing Centre, University of Nottingham, is also acknowledged.

REFERENCES

1. J. R. Boyce. *The Behaviour of a Granular Material under Repeated Loading*. Ph.D. thesis. University of Nottingham, England, 1976.
2. J. W. Pappin. *Characteristics of a Granular Material for Pavement Analysis*. Ph.D. thesis. University of Nottingham, England, 1979.

3. C. K. Chan and J. B. Sousa. State-of-the-Art on Geotechnical Laboratory Testing. *Proc., Geotechnical Congress*, Geotechnical Engineering Division, ASCE, Boulder, Colo., 1991.
4. J. R. Boyce, S. F. Brown, and P. S. Pell. The Resilient Behaviour of a Granular Material under Repeated Loading. *Proc., Australian Road Research Board*, Vol. 8, Session 9, 1976, pp. 8–19.
5. S. F. Brown, M. P. O'Reilly, and J. W. Pappin. A Repeated Load Triaxial Apparatus for Granular Materials. In *Unbound Aggregates in Roads* (Jones and Dawson, eds.). Butterworths, London, England, 1989, pp. 143–159.
6. G. R. Hicks and C. L. Monismith. Factors Influencing the Resilient Response of Granular Materials. In *Highway Research Record 345*, TRB, National Research Council, Washington, D.C., 1971, pp. 15–31.
7. S. F. Brown and E. T. Selig. The Design of Pavement and Rail Track Foundations. In *Cyclic Loading of Soils: From Theory to Design* (O'Reilly and Brown, eds.). Blackie, Glasgow, England, 1991, pp. 249–306.
8. R. W. May and W. W. Witczak. Effective Granular Modulus to Model Pavement Responses. In *Transportation Research Record 810*, TRB, National Research Council, Washington, D.C., 1981, pp. 1–9.
9. J. Uzan. Characterization of Granular Material. In *Transportation Research Record 1022*, TRB, National Research Council, Washington, D.C., 1985, pp. 52–59.
10. L. Domaschuk and N. H. Wade. A Study of Bulk and Shear Moduli of a Sand. *Journal of Soil Mechanics and Foundations Division*, ASCE, 1969, pp. 561–581.
11. J. W. Pappin and S. F. Brown. Resilient Stress-Strain Behaviour of a Crushed Rock. *Proc., International Symposium on Soils Under Cyclic and Transient Loading*, Swansea, England, 1980, pp. 169–177.
12. H. C. Mayhew. *Resilient Properties of Unbound Road Base Under Repeated Triaxial Loading*. TRRL Laboratory Report 1088. TRRL, Crowthorne, Berkshire, England, 1983.
13. J. R. Boyce. A Non-Linear Model for the Elastic Behaviour of Granular Materials Under Repeated Loading. *Proc., International Symposium on Soils Under Cyclic and Transient Loading*, Swansea, England, 1980, pp. 521–542.
14. S. P. Timoshenko and J. N. Goodier. *Theory of Elasticity*, 3rd ed. McGraw-Hill International Editions, Engineering Mechanics Series, 1970.
15. G. T. H. Sweere, A. Renning, and E. Vos. Development of a Structural Design Procedure for Asphalt Pavements with Crushed Rubble Base Courses. *Proc., Sixth International Conference—Structural Design of Asphalt Pavements*, Vol. 1, 1987, pp. 34–49.
16. G. T. H. Sweere. *Unbound Granular Bases for Roads*. Ph.D. thesis. University of Delft, Netherlands, 1990.
17. P. Jouve, J. Martinez, L. L. Paute, and E. Regneau. Rational Model for the Flexible Pavement Deformations. *Proc., Sixth International Conference—Structural Design of Asphalt Pavements*, Vol. 1, 1987, pp. 50–64.
18. M. Elhannani. *Modelisation et Simulation Numerique des Chaussees Souples*. Ph.D. thesis. University of Nantes, France, 1991.
19. W. J. Dixon, M. B. Brown, L. Engelman, M. A. Hill, and R. I. Jennrich. *BMDP Statistical Software Manual*. University of California Press, Berkeley, Calif., 1988, pp. 357–419.
20. M. Karasahin. *Resilient Behaviour of Granular Materials for Analysis of Highway Pavements*. Ph.D. thesis. University of Nottingham, 1993.

Publication of this paper sponsored by Committee on Soil and Rock Properties.

Methodology for Resilient Modulus Testing of Cohesionless Subgrades

SOHEIL NAZARIAN AND MANUEL FELIBERTI

Because more emphasis is being placed on incorporating resilient modulus testing in mechanistic pavement design, a reliable method for conducting the tests should be developed. The strengths and limitations of the resilient modulus testing procedure as applied to cohesionless subgrade soils are detailed in this paper. The overall objectives of this paper are to evaluate the accuracy of the resilient modulus test procedures, to modify the existing resilient modulus testing procedures as applied to granular materials, and to develop a more rigorous constitutive model for describing the results from resilient modulus tests. With a careful literature search in the areas of dynamic testing of soils as applied to transportation engineering, geotechnical engineering, and earthquake engineering, one can obtain a list of parameters that influence the results of cyclic tests (such as the resilient modulus tests). The compliance of the testing device, specimen preparation, level of deviatoric stress, and the sequence and number of loading schemes are the major parameters. Through extensive testing of synthetic specimens using state-of-the-art equipment, the accuracy, precision, and limitations of the procedure have been established. It was found that (a) a rigid system was required to minimize the compliance effects; (b) below a deviatoric stress of 2 psi, the results were questionable, and (c) the sequence of loading proposed by the AASHTO T-274 should be extensively modified. It was also found that the Strategic Highway Research Program protocol suggested for granular materials may result in excessive specimen disturbance. A newly developed procedure has been recommended herein. Given the level of emphasis in improving the resilient modulus testing procedure, it is reasonable to expect more advanced constitutive models representing the collected data. A new constitutive model was evaluated. The proposed model appears to be theoretically more accurate and describes the data more clearly.

In recent years, resilient modulus testing has gained tremendous popularity. This increased interest has been attributed to the new AASHTO design procedure adopted in 1986. In the new design procedure, the resilient modulus of subgrade soil is considered as one of the most important input parameters.

Since 1986, numerous research projects have focused on improving the laboratory procedure involved in conducting resilient modulus tests. A workshop was held at Oregon State University in 1989 to summarize the state of practice in resilient modulus testing. The major conclusions of the workshop were straightforward:

1. Using the resilient modulus as a design parameter would significantly improve the design procedures.
2. Available testing procedures were inadequate.
3. Resilient modulus testing devices needed modifications.
4. The constitutive models proposed were incomplete.

The Strategic Highway Research Program (SHRP) and many state agencies (such as those in Texas and Kentucky) have studied and suggested improved testing procedures and more advanced constitutive models.

Some of the inadequacies related to laboratory testing and modeling of resilient modulus tests conducted on cohesionless subgrades are addressed in this paper. Extensive laboratory tests were conducted to study the limitations of the existing methods proposed by SHRP and AASHTO using three synthetic specimens of known properties. An improved testing procedure was proposed that appears to induce the least amount of degradation and disturbance to the specimen. In addition, an improved constitutive model was proposed for cohesionless soils.

BACKGROUND

Many factors affect the resilient modulus of cohesionless subgrades. Resilient modulus is equivalent to dynamic modulus measured for geotechnical earthquake engineering projects. Cyclic triaxial tests (*1*) and resonant column tests (*2*) are two examples of tests typically used for this purpose. Dynamic modulus is the most important parameter used in this field. Naturally, a wealth of information is available, which cannot and should not be ignored.

Based on numerous laboratory tests, Hardin and Drnevich (*3*) proposed many parameters that affect the moduli of soils. They suggested that state of stress, void ratio, and strain amplitude are the main parameters affecting moduli measured in the laboratory.

Basically, as void ratio decreases, the dynamic modulus of soil increases. One of the most important factors that affects the dynamic modulus of soils is the applied confining pressure. Hardin and Drnevich (*3*) concluded that a linear logarithmic relationship exists between the modulus and the applied confining pressure.

The strain level has a significant effect on the dynamic modulus. Stokoe et al. (*4*) identified four ranges of strain amplitude. The thresholds are shown in Figure 1. The strain can be divided into four categories:

1. Small strains—also called elastic or low-amplitude strains, where linear behavior occurs;

S. Nazarian, Center for Geotechnical and Highway Materials Research, University of Texas at El Paso, El Paso, Tex. 79968. M. Feliberti, California Department of Transportation, Eureka, Calif. 95501.

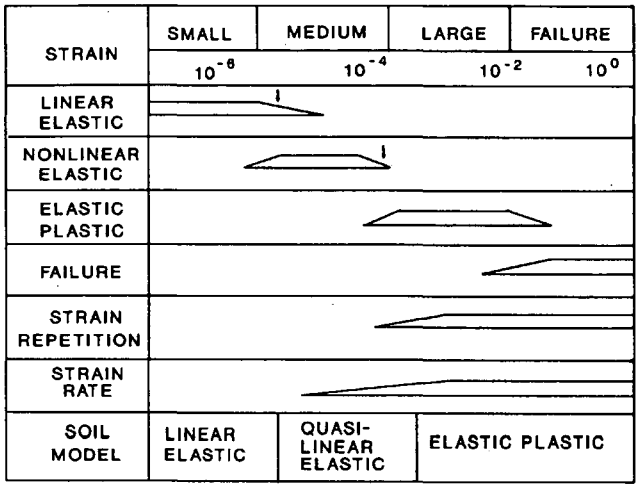

FIGURE 1 Soil behavior and associated strain ranges (*4*).

2. Medium strains—where nonlinear elastic behavior dominates this strain range;
3. Large strains—where significant plastic deformation occurs, but failure is not reached; and
4. Failure strains—all greater-than-large strains.

Two other threshold strains shown in the figure are the boundaries where the number of cycles of loads (denoted as strain repetition threshold) and strain rate of the load applied (denoted as strain rate threshold) become important in soils. The strain rate threshold roughly coincides with the limit of the small strains, and the strain repetition is located within medium strain level. As soon as the strain repetition threshold has passed, progressive failure will be imminent.

In pavement design, the strain levels are typically within ranges of small strains and medium strains. Higher strains will cause almost instantaneous rutting or fatigue cracking of the pavement.

Several constitutive models have been proposed for describing the results of resilient modulus tests. For cohesionless soils, the following relationship may be used:

$$M_R = k_1\theta^{k_2} \quad (1)$$

where

k_1 and k_2 = constants,
θ = bulk stress = $3\sigma_c + \sigma_d$,
σ_c = confining pressure, and
σ_d = deviatoric stress.

This relationship is extensively used for granular materials as recommended by AASHTO.

TESTING PROCEDURES

Recently much attention has been focused on conducting and implementing resilient modulus tests. As such, several new testing procedures and methodologies have been developed. Second to AASHTO, SHRP is the leading organization pursuing the implementation of resilient modulus tests. SHRP has suggested some improvement to the AASHTO T-274 procedure. Based on the type of material to be tested, both AASHTO and SHRP have proposed two separate procedures. Granular materials are tested differently than cohesive materials. The following sections present the AASHTO and SHRP procedures for testing cohesionless materials. An alternative procedure is also proposed.

The resilient modulus tests were performed with a closed-loop servo-valve system manufactured by MTS, Inc. The details of the equipment can be found in work by Feliberti et al. (*5*). An extremely rigid triaxial cell was used.

AASHTO Procedure

The AASHTO testing procedure is lengthy because it requires testing of the specimen under numerous stress states and loading conditions. There are 33 steps in this procedure. At each loading step, 200 cycles of load are applied. The resilient modulus is calculated from the results of the 200th cycle. The initial six steps, which are called conditioning steps, would presumably help the specimen to become more homogeneous. In other words, during the conditioning steps, any voids in the specimen are supposedly removed and it is hoped that a good contact between the specimen and load platens is achieved. Data are not collected during these steps. During this study, the six pretesting steps resulted in unrecoverable deterioration of many specimens before the actual testing. After the conditioning steps, the specimen is tested at five confining pressures, and at each confining pressure, increasing deviatoric stress is applied. The deviatoric stress ranges from 1 to 20 psi. During this study, a complete test on one specimen (including preparation of the specimen) required about 4.5 hr.

SHRP Procedure

Contrary to AASHTO's recommendation, SHRP requires only one conditioning step. The substantial decrease in the number of pretesting steps would certainly decrease the chances for specimen degradation or disturbance.

The actual test consists of 15 loading steps. The load is applied for 100 cycles with the 100th cycle being the cycle where the resilient modulus is calculated. The authors found this procedure easy to follow and perform. The test period for one specimen was approximately 2.5 hr because of fewer loading steps and fewer cycles of load. This procedure requires five confining pressures with deviatoric stresses from 3 to 40 psi.

The authors experienced one major problem with the SHRP procedure: the specimens were disturbed due to large deviatoric stresses applied at low confining pressures. These steps result in excessive deformation of specimens, especially if the specimen has a low modulus. During the authors' testing program, several specimens failed before completion of all the loading steps.

One advantage of the resilient modulus test is that it is a stage test. The specimen should not fail during testing, nor should its properties significantly alter between consecutive loading sequences. As such, the test had to be modified so that the specimen would not be subjected to high stress levels. A new loading sequence for cohesionless soils was developed to minimize the disturbance to a specimen during testing.

Proposed Procedure

In the AASHTO and SHRP methods, the confining pressure is kept constant and the deviatoric stress is varied. In this proposed method, the deviatoric stress is held constant while the confining pressure is increased.

The loading steps for the proposed procedure are shown in Table 1. The first row, where the loading sequence is 0, is the conditioning step. It is the same as for the SHRP method except that 50 cycles of load are applied. The rest of the 15 loading steps are run for 100 cycles. A complete test, including specimen preparation, takes approximately 2 hr. Three deviatoric stresses are used in this procedure. Five confining pressures are tested at each deviatoric stress. The confining pressures range from 3 to 20 psi. The fourth column specifies the number of load repetitions to apply at each loading step, and the fifth column indicates whether data are collected.

The proposed method was developed to minimize the disturbance to specimens during staged testing as observed with the SHRP procedure. The stress levels are much lower than both the AASHTO and SHRP procedures. The advantages of this testing procedure over others are demonstrated later.

EXPERIMENTAL RESULTS

Synthetic Specimens

Three synthetic specimens were tested before testing actual soil specimens. The synthetic specimens were composed of a two-component urethane elastomer resin (*6*). The three were named TU-700 (soft specimen), TU-900 (medium specimen), and TU-960 (hard specimen).

Stokoe et al. (*6*) extensively tested similar specimens using the static compression test and torsional resonant column test. Young's moduli obtained from the static compression tests for soft (TU-700), medium (TU-900), and hard (TU-960) specimens were 1,670, 6,550, and 32,300 psi, respectively. The Poisson's ratios were 0.48, 0.50, and 0.47 for the soft, medium, and hard specimens, respectively.

Moduli obtained from the resonant column tests were also reported. Young's moduli for the soft, medium, and hard samples were 2,430, 10,070, and 52,000 psi, respectively. They attributed the difference in the numbers to the loading frequency. In other words, the elastomer specimens exhibited viscoelastic behavior.

In summary, through a rigorous series of laboratory testing, Stokoe et al. (*6*) demonstrated that the elastomer specimens were excellent tools for evaluating a resilient modulus device. Three correction factors had to be applied to each specimen before the accurate resilient modulus could be found. These three corrections compensated for (a) loading frequency, (b) testing temperature, and (c) mode of testing (torsional versus axial). The shear modulus of the elastomer specimens can be measured with an accuracy of 3 percent (*6*). All three specimens were approximately 2.8 in. in diameter and 6.5 in. in height.

An extensive amount of data was collected. Basically, each specimen was tested following the SHRP and AASHTO procedures. In addition, the proposed procedure was also evaluated. Tests were carried out securing the specimen to the platens with and without the hydrostone grouting mix.

There are several reasons for conducting such an extensive testing program. First, any incompatibility associated with the loading sequences could be found. Second, the specimen is subjected to numerous combinations of confining pressures and deviatoric stresses. Most tests were repeated at least three times. Although not shown here, in all cases the results were repeatable and demonstrated small deviations.

Typical results from resilient modulus tests on the medium specimen (TU-900) are discussed here. The results from the other two are included in Feliberti et al. (*5*).

The AASHTO and SHRP results for the granular (Type 1) testing procedures are summarized in Figures 2(*a*) and 2(*b*), respectively. The results from the two sets are similar. Much scatter in data is evident from the AASHTO procedure due to the numerous steps involving deviatoric stress levels of less than 2 psi. If the modulus corresponding to these stress levels is ignored, the results from the SHRP and AASHTO procedures are compatible. For both cases, the modulus is unaffected by the bulk stresses and is more or less constant.

The results from the proposed procedure are shown in Figure 2(*c*). The results and trends are similar to those obtained from the AASHTO and SHRP procedures. There is some scatter in the data because the tests were accidentally performed at deviatoric stresses of slightly less than 2 psi (instead of 3 psi).

The average modulus obtained from each testing procedure is summarized in Tables 2–4 for the soft material (TU-700), medium material (TU-900), and the hard material (TU-960), respectively. Also included in the tables are the standard deviation and coefficient of variation associated with each procedure.

The resilient modulus values for three elastomer specimens corrected for loading frequency, temperature, and mode of vibration were determined to be 2,318 psi, 9,794 psi, and 42,083 psi, respectively. (The synthetic specimens and their moduli were graciously provided by the University of Texas at Austin.) These specimens were subjected to similar tests,

TABLE 1 Loading Sequence Proposed for Type 1 Soils

Loading Sequence	Deviatoric Stress, psi	Confining Pressure, psi	Number of Repetitions	Deformation Record(Y or N)
0	5	15	50	N
1	3	3	100	Y
2	3	6	100	Y
3	3	10	100	Y
4	3	15	100	Y
5	3	20	100	Y
6	6	3	100	Y
7	6	6	100	Y
8	6	10	100	Y
9	6	15	100	Y
10	6	20	100	Y
11	9	3	100	Y
12	9	6	100	Y
13	9	10	100	Y
14	9	15	100	Y
15	9	20	100	Y

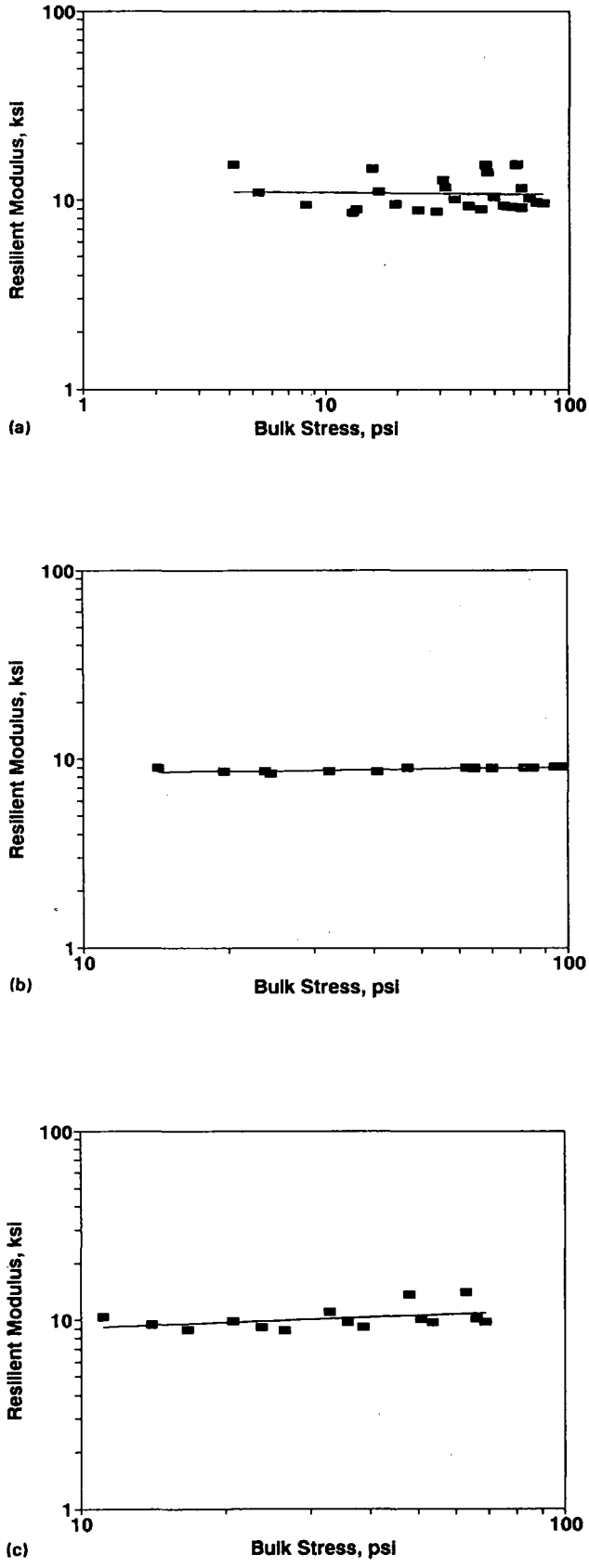

FIGURE 2 Variation in resilient modulus with bulk stress for TU-900 specimen: (*a*) AASHTO procedure; (*b*) SHRP procedure; (*c*) proposed procedure.

TABLE 2 Summary of Results from Tests on Soft Specimen (TU-700)

Testing Method	Hydrostone	Modulus (psi)	Standard Deviation (psi)	Coefficient of Variation (percent)	Percent Difference (percent)
SHRP	Y	2420	160	6.6	4.4
	N	2360	83	3.5	1.8
AASHTO with σ_d of 1 and 2 psi	Y	2800	380	13.6	20.8
	N	2460	370	15.0	6.1
AASHTO without σ_d of 1 and 2 psi	Y	2570	160	6.2	10.9
	N	2340	60	2.6	1.0
Proposed	Y	2390	190	8.0	3.1

Note: $\textit{Percent Difference} = \frac{\textit{Modulus from this Study - Modulus from Torsional Tests}}{\textit{Modulus from Torsional Tests}}$

TABLE 3 Summary of Results from Tests on Medium Specimen (TU-900)

Testing Method	Hydrostone	Modulus (psi)	Standard Deviation (psi)	Coefficient of Variation (percent)	Percent Difference (percent)
SHRP	Y	8850	256	2.9	-9.6
	N	10140	610	6.0	3.5
AASHTO with σ_d of 1 and 2 psi	Y	11060	2400	21.7	12.9
	N	10100	830	8.2	3.1
AASHTO without σ_d of 1 and 2 psi	Y	9320	480	5.2	-4.8
	N	10150	410	4.0	3.6
Proposed	Y	9950	911	9.2	4.5

Note: $\textit{Percent Difference} = \frac{\textit{Modulus from this Study - Modulus from Torsional Tests}}{\textit{Modulus from Torsional Tests}}$

TABLE 4 Summary of Results from Tests on Hard Specimen (TU-960)

Testing Method	Hydrostone	Modulus (psi)	Standard Deviation (psi)	Coefficient of Variation (percent)	Percent Difference (percent)
SHRP	Y	45700	1440	3.2	4.4
	N	N/A	N/A	N/A	N/A
AASHTO with σ_d of 1 and 2 psi	Y	46270	3700	8.0	5.7
	N	38660	4780	12.4	-11.7
AASHTO without σ_d of 1 and 2 psi	Y	46270	1050	2.3	5.7
	N	41260	3000	7.3	-5.7
Proposed	Y	44580	1260	2.8	1.9

Note: $\textit{Percent Difference} = \frac{\textit{Modulus from this Study - Modulus from Torsional Tests}}{\textit{Modulus from Torsional Tests}}$

that is, torsional resonant column tests, reported by Stokoe et al. (*6*).

Average moduli from different testing procedures generally compare reasonably well with those measured using the torsional devices. For the soft specimen, the modulus varies from a minimum of 2,104 psi to a maximum of 2,800 psi. The device used in this study is unable to yield consistent results at deviatoric stresses of 1 and 2 psi. If the two AASHTO cases where the deviatoric stresses of 1 and 2 psi were considered were ignored, the lower and upper bounds would change to

2,104 psi and 2,606 psi, respectively. Similarly, for the medium specimens, the modulus varied between 8,850 psi and 10,150 psi, and for the hard specimens, between 39,860 psi and 46,270 psi. In almost all cases, the deviations in modulus from those determined from the torsional tests were within a 10 percent range.

The effects of the grouting of the specimens to the top and bottom platens were also studied. Tests were conducted on each specimen with and without applying the hydrostone mix. The addition of the grouting agent would ensure a good contact between the specimen and the platen. Precision machining was required to obtain flat surfaces necessary for performing the tests without the grouting agent. In general, the variation in results among the specimens grouted and those not grouted was about 10 percent. The variation was random. That is, in some cases, the grouted specimens yielded a higher modulus; and in other cases, the ungrouted specimens yielded a higher modulus. It seems that with the grout in place, moduli should be equal to or greater than those of ungrouted specimens. Although extremely unlikely, it is possible that the grout had not set completely before the tests were performed. This would account for some variations in the results. No reason other than random scatter in data can be found for this matter.

One advantage of grouting is that in some instances, the scatter in data decreases as judged by the coefficient of variation. Once again, favorable results shown here for ungrouted materials were possible after the ends of the specimens were precisely machined. It is important that the two ends be flat and parallel. Without this precision machining, practically any modulus value could be obtained depending on the setup.

The authors' conclusion is that as suggested by Pezo et al. (*7*), grouting the specimens is a good practice. However, for cohesionless materials, this may be infeasible because the grouting agent may flow inside the specimen. In that case, careful preparation of the specimen would result in satisfactory results.

Sand Specimens

The second phase of the testing program consisted of characterizing and testing a sand commonly found in El Paso, Texas. The properties of the sand and the development of the proposed method are described in this section.

The sand was first sieved with only the fraction passing through a #40 sieve and retained on a #60 sieve used for testing. This sand was extensively used by De Lara Rico (*8*). The maximum and minimum unit weight for the sand were 106.9 pcf and 93.2 pcf, respectively. Based on the gradation, the sand was classified as A-3 by AASHTO soil classification and as SP in the Unified Soil Classification System.

Of the 13 specimens, 3 were tested at a relative density (r_d) of 100 percent following the SHRP testing protocol, 7 were tested at a r_d of 100 percent, and 3 were tested at a r_d of 70 percent. The proposed procedure, not the AASHTO procedure, was followed for testing in this study.

The first three specimens, with a r_d of 100 percent, were tested to evaluate the proposed procedure. Each specimen was tested at different deviatoric stresses to analyze the effects of deviatoric stress on specimen degradation. A more detailed testing program was conducted and can be found in work by Feliberti et al. (*5*). Those results, which are not discussed here for the sake of brevity, support the conclusions drawn here.

A typical variation in modulus with bulk stress for a sand specimen using the SHRP protocol is illustrated in Figure 3. The scatter in the data is relatively small. Generally, the modulus increases with the bulk stress. The data are clustered into five groups corresponding to the five different confining pressures.

Repeatability was checked by testing three specimens. The results were the same for the first confining pressure. However, when the specimen was subsequently tested at a different confining pressure, the results obtained were erratic. This indicated possible degradation of the specimen at high deviatoric stresses, suggesting that the SHRP procedure might require some modifications.

Under the proposed procedure, the variation in resilient modulus with bulk stress for a sand specimen at 100 percent r_d (similar to the specimen tested with the SHRP procedure) at deviatoric stresses 3, 6, and 9 psi is shown in Figure 4(*a*). The scatter in data is relatively smaller than that obtained from the SHRP method. The modulus increases linearly with bulk stress. To demonstrate that the specimen degradation is minimal, two other specimens were tested. The first specimen was tested at deviatoric stresses of 6 and 9 psi [Figure 4(*b*)], and the final specimen was tested at only the deviatoric stress of 9 psi (Figure 5). The modulus values at the deviatoric of 9 psi for the three specimens compare closely, as shown in Figure 5. In the authors' experience, this degree of repeatability cannot be achieved with the SHRP procedure. For the first level of confining pressures, similar results could be achieved. However, for the subsequent confining pressures, the moduli would be lower, and the results would not be repeatable.

After repeatability of results with the proposed procedure was established, two other specimens were tested at 100 percent r_d. These results were similar to those presented in Figure 4(*a*). Three tests yielded almost identical results, with moduli

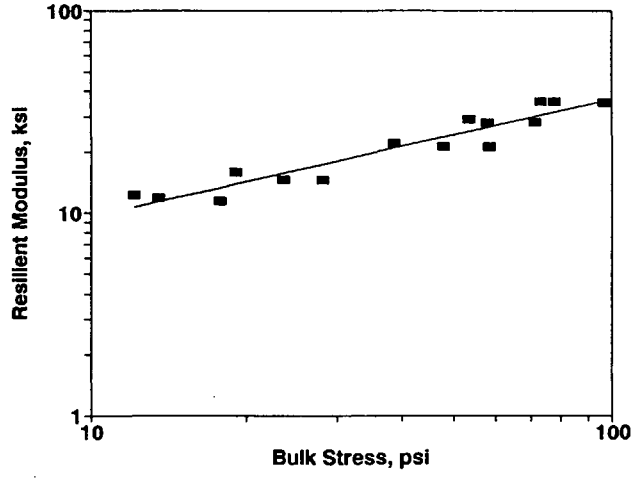

FIGURE 3 Variation in resilient modulus with bulk stress for a sand specimen at a relative density of 100 percent following SHRP procedure.

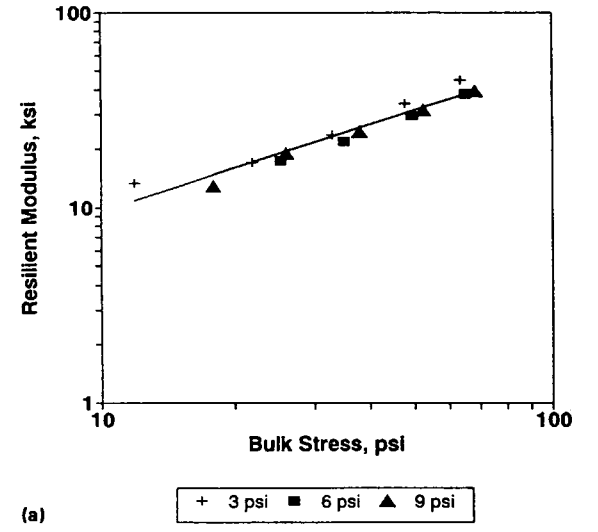

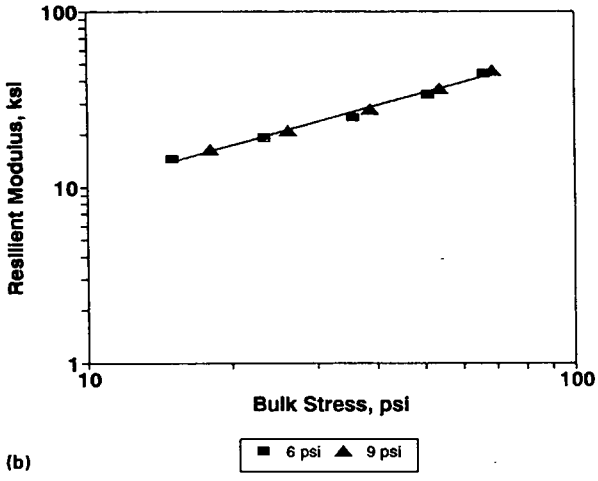

FIGURE 4 Variation in resilient modulus with bulk stress for a sand specimen at a relative density of 100 percent following the proposed procedure: (*a*) tested at three confining pressures; (*b*) tested at two confining pressures.

from the last being slightly lower. In any case, the variation in modulus was quite small among the four specimens.

Finally, three specimens were tested at a relative density of 70 percent. Variation in modulus with bulk stress for one representative specimen at this relative density is shown in Figure 6. The resilient modulus increases with an increase in bulk stress. However, some scatter in the data is evident. The moduli from the three tests were within 10 percent of each other.

CONSTITUTIVE MODELS

The constitutive model proposed by SHRP or AASHTO is presented in Equation 1. For granular materials, both SHRP and AASHTO recommend a relationship between resilient modulus (M_R) and bulk stress (θ).

For the sandy material tested, using a least-squares best fit method, Equation 1 yields R-squared values from 0.78 to 0.98

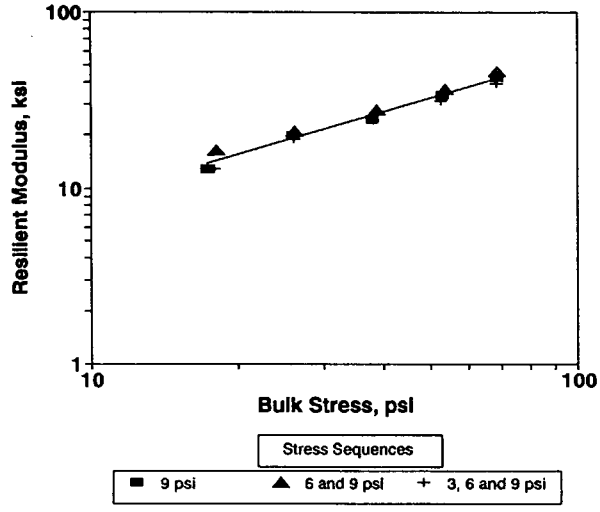

FIGURE 5 Comparison of variation in resilient modulus with bulk stress for three sand specimens tested at different deviatoric stresses following proposed procedure.

with an average of about 0.85. The average values for k_1 and k_2 were 0.399 and 0.581, respectively. Given the recent emphasis on improving the experimental aspects of resilient modulus tests, such a level of correlation may not be adequate.

As mentioned before, for a given soil, Hardin and Drnevich (*3*) found that two parameters significantly contribute to the stiffness (modulus) of soils. These two parameters (besides void ratio) are the state of stress and the strain level. As such, the models proposed by AASHTO and SHRP directly consider the effects of the state of stress (bulk stress) but ignore the effects of strain amplitude. One model studied that considers both of these factors is in the form

$$M_R = 10^{k_1} \theta^{k_2} \varepsilon^{k_3} \quad (2)$$

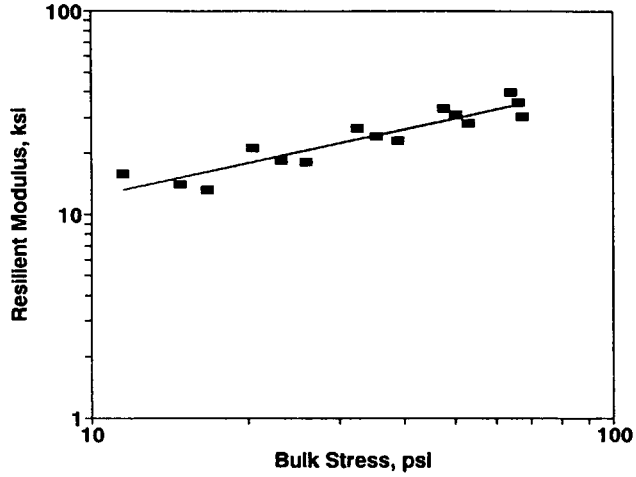

FIGURE 6 Variation in resilient modulus with bulk stress for a sand specimen at a relative density of 70 percent following proposed procedure.

where k_1, k_2, and k_3 are the material constants to be obtained from tests performed on a given soil. When the model was applied to the resilient moduli from different tests, the R-squared values were generally above 0.95, except for some isolated cases, with an average of 0.98. The average values for k_1, k_2, and k_3 were -0.131, 0.668, and -0.128, respectively. The difference between the measured modulus and calculated modulus from the AASHTO/SHRP equation for the granular material (Figure 3) is shown in Figure 7(*a*). The figure corresponds to the modulus values obtained from three similar specimens tested at a relative density of 100 percent. There is a significant difference between the actual data and the modeled data. The deviation between the two is as high as 45 percent, but it is typically within 30 percent. The similar plot for the same data, but for the model presented in Equation 2, is shown in Figure 7(*b*). The measured and calculated moduli compare better, and the scatter is usually less than 15 percent.

It should be mentioned that the tests in this study yielded strain amplitudes in the range of 10^{-3} to 10^{-1} percent. Therefore, the above discussion is pertinent only in this range of strains.

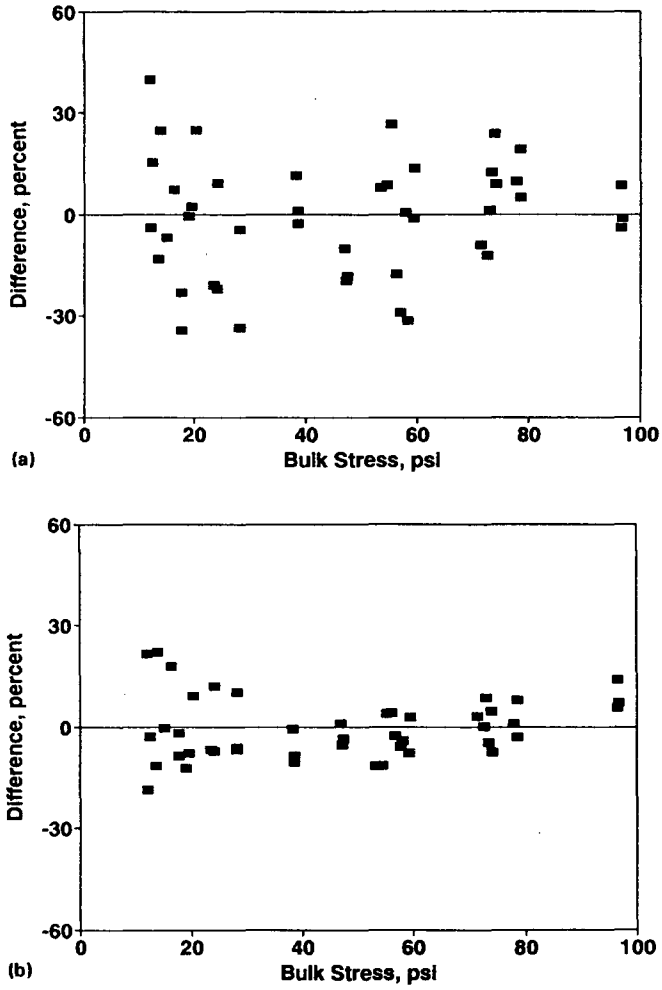

FIGURE 7 Typical variation in percent difference between measured and modeled moduli: (*a*) AASHTO/SHRP model; (*b*) proposed constitutive model.

SUMMARY AND CONCLUSIONS

This paper evaluates the resilient modulus testing procedure for cohesionless materials and reviews the state-of-the-art for obtaining and interpreting resilient modulus data. The initial testing procedure was proposed by AASHTO and then improved by SHRP. These two approaches are evaluated. In addition, a new testing procedure for granular materials is proposed and evaluated.

On the basis of this study, the following conclusions can be drawn:

1. The AASHTO procedure for resilient modulus testing is inadequate.
2. The SHRP protocol for testing granular (Type 1) soils induces specimen disturbance during the first level of confining pressure.
3. The new procedure proposed here for testing granular materials appears to minimize specimen degradation and disturbance.
4. The models proposed by AASHTO may be incomplete for sands.
5. A general constitutive model based on considering both state of stress and strain amplitude, which seems more appropriate for describing the behavior of the material tested, is introduced.

ACKNOWLEDGMENT

This work was supported by the Texas Department of Transportation. The authors greatly appreciate the support of that organization.

REFERENCES

1. M. L. Silver. *Laboratory Triaxial Testing Procedure to Determine the Cyclic Strength of Soils.* Report NUREG-31. U.S. Nuclear Regulatory Commission, 1976.
2. V. P. Drnevich. Recent Developments in Resonant Column Testing. Presented at Annual Meeting of the American Society of Civil Engineering, Detroit, Mich., 1985, p. 29.
3. B. O. Hardin and V. P. Drnevich. Shear Modulus and Damping in Soils: Measurement and Parameters Effects. *Journal of the Soil Mechanics and Foundation Division*, ASCE, Vol. 98, No. SM7, 1972, pp. 603–624.
4. K. H. Stokoe II, S. Nazarian, G. J. Rix, J. S. Salinero, J. C. Shue, and Y. J. Mok. In-Situ Testing of Hard-To-Sample Soils. *Proc., Earthquake Engineering and Soil Dynamics II—Recent Advances in Ground Motion Evaluation*, ASCE, Park City, Utah, 1988, pp. 264–278.
5. M. Feliberti, S. Nazarian, and T. Srinivasan. *Critical Evaluation of Parameters Affecting Resilient Modulus Tests on Subgrades.* Research Report 1177-2. Center for Geotechnical and Highway Materials Research, University of Texas at El Paso, El Paso, Tex., 1992.
6. K. H. Stokoe II, D. S. Kim, and R. Andres. Development of Synthetics Specimens for Calibration and Evaluation of MR

Equipment. Presented at 69th Annual Meeting of the Transportation Research Board, Washington, D.C., 1990.
7. R. F. Pezo, G. Claros, and W. R. Hudson. An Efficient Resilient Modulus Test for Subgrades and Nongranular Subbase Materials. Presented at 71st Annual Meeting of the Transportation Research Board, Washington, D.C., 1992.
8. A. De Lara Rico. *Evaluation of Friction Effects on the Pull-Out Capacity of Horizontal Strip Anchor Plates*. M.S. thesis. Department of Civil Engineering, University of Texas at El Paso, 1990.

Publication of this paper sponsored by Committee on Soil and Rock Properties.

Verifying Kneading Resilient Modulus of Soils with Backcalculated Values

K. P. GEORGE AND WAHEED UDDIN

The characterization of soils in terms of resilient behavior is gaining support because of its immediate application in the mechanistic analysis of pavements. This report investigates an alternative procedure of resilient testing using the U.S. Army Corps of Engineers gyratory testing machine (GTM). The development of the GTM test procedure, focusing on the simulating conditions of a moving load, is summarized. With consideration to specimen confinement in the mold, a revised equation for kneading resilient modulus (M_{rk}) is presented. The primary objective is to validate the GTM test procedure. For that purpose, six subgrade soils and three subbase materials are investigated using the GTM and the repeated load triaxial test, AASHTO T274-82. For in situ determination of resilient modulus of some of those soils (five samples only), Dynaflect and falling weight deflectometer deflections are obtained on finished pavements as well. Two computer programs—MODULUS and FPEDD1—were used to backcalculate the moduli of all of the layers.

The GTM moduli compare poorly with the triaxial moduli in this nine-soil comparative study, nor was there any correlation between M_{rk} and the backcalculated moduli when the latter was not corrected for nonlinear effects. However, the in situ modulus values (only five sites tested) agree with the GTM moduli with appropriate nonlinear correction, as programmed in FPEDD1. On the basis of the successful comparison with the in situ backcalculated moduli, it is concluded that GTM has the potential for resilient modulus characterization of subgrade soils.

The physical properties of subgrade soils are important parameters for designing, maintaining, and rehabilitating pavements. Traditional test procedures for characterizing subgrade soils are now replaced by resilient testing. For example, in the revised AASHTO guide (*1*), the resilient modulus (M_r) replaced the soil support value used in the previous editions of the guide.

The repeated load triaxial (RLT) test proposed for determining M_r (AASHTO T274-82) is relatively complex. Accordingly, highway agencies have sought alternative test methods. The diametral testing procedure, an alternative used in experiments by the Oregon Department of Transportation (*2*), was found adequate for cohesive soils, but it is not recommended for noncohesive soils. After a careful study of the literature review, this study was initiated to assess whether the U.S. Army Corps of Engineers gyratory testing machine (GTM), developed originally for the design of bituminous mixtures and later used successfully for density control of base and subgrade soils, would be a viable alternative for resilient modulus testing. The GTM is described in a U.S. Army Corps of Engineers report (*3*).

Department of Civil Engineering, University of Mississippi, University, Miss. 38677.

OBJECTIVE AND SCOPE

The overall objective of this study was to verify the application of GTM in resilient testing of soils. To accomplish this, several subgrade soils (four fine-grained and five coarse-grained) were tested in the laboratory using both the conventional repeated load mode (AASHTO T274-82) and the GTM. First, the M_r from RLT is compared with the kneading resilient modulus (M_{rk}) for all the soils. To further substantiate the laboratory moduli, nondestructive testing (NDT) deflections [both Dynaflect and falling weight deflectometer (FWD)] of five pavements (soil samples from those five tested in the laboratory) were obtained for backcalculation. The subgrade moduli were backcalculated using two PC-based computer programs: MODULUS and FPEDD1. The backcalculated moduli were compared with the laboratory values to establish the reasonableness of the M_{rk} values, and, in turn, the feasibility of using GTM to estimate the resilient modulus of subgrade soils.

WHY GYRATORY TESTING MACHINE?

The GTM—a combination kneading compaction, "dynamic consolidation," and shear testing machine—simulates abrasion effects caused by repetitive stress and intergranular movement within the mass of material (subgrade, subbase, or base) in a flexible pavement structure. Figure 1 is a schematic side view section of the gyrating mechanism: Mold A, containing a test specimen, is clamped in position in the flanged mold chuck B. Vertical pressure on the test specimen is maintained by upper ram E and lower ram F, acting against head G and base H, respectively. Note that head G acts against roller bearing and is free to slip, while base H remains horizontal. A "gyratory motion" is imparted to mold chuck B by rollers C and D as they travel around the flanged portion of the chuck. Roller C is adjustable in elevation to permit setting any desired gyratory angle (degree of shear strain). The recording mechanism I in Figure 1 shows gyratory motion or shear strain. The recording, referred to as a gyrograph, is a direct indicator of plasticity of the material being investigated.

By producing a uniform shearing action in the test specimen by a gyratory motion of the test mold, the apparatus is believed to simulate field compaction more closely than impact tamping, which is used in AASHTO and ASTM procedures. In an earlier Waterways Experiment Station study (*4*), good correlation was obtained between the gyratory-compacted densities and the densities of samples obtained from the test sections after traffic had been applied.

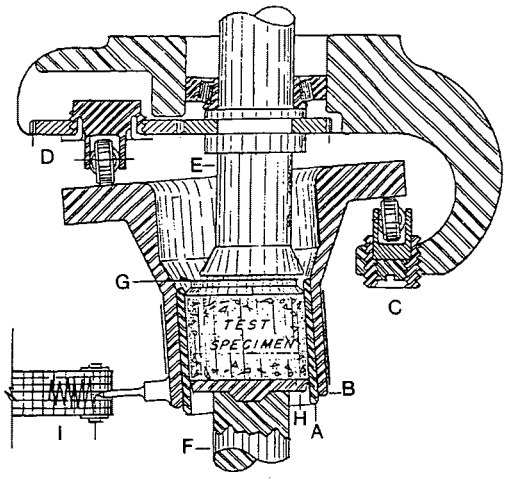

FIGURE 1 Schematic illustration of gyratory testing machine.

The GTM, originally a bituminous-mixture laboratory compactor, is modified in this research program to accommodate repeated load application. The soil specimen, confined in mold A, is subjected to a repeated load stress through the lower ram F and shear stress reversal through gyratory motion. Whereas the axial repeated stress is applied at a frequency of 1 Hz with a 4-sec rest period, the frequency of the roller carriage is 0.2 Hz, as is the gyratory displacement. Figure 2 shows the position of the top face of the specimen as the roller rotates through one full cycle (360 degrees). Employing finite element computations, the senior author has shown that the shear stress in the sample undergoes nearly sinusoidal variation (*5*,*6*).

In a recent study, George (*6*) analyzed the stress state, especially the stress reversal in the underlying pavement material, and concluded that repeated load GTM has the potential to simulate the moving load traversing a road. Not only are the vertical stresses cycled, but the shear stresses undergo sinusoidal variation as the GTM specimen is gyrated during resilient testing. Further evidence of similarity was presented by comparing the stress paths of three different loadings: (a) a GTM sample gyrated at 0.1 degree and subjected to a cyclic load, (b) a stress state resulting from a 9-kip single tire load, and (c) a repeated load triaxial sample subjected to a cyclic load as per AASHTO T274. The resemblance of the GTM stress path to the field stress path is construed as further evidence of GTM resilient testing's ability to better simulate the field conditions than the RLT counterpart.

Based on the foregoing discussion, three features favoring the use of GTM for resilient modulus can be cited as follows:

1. The GTM is capable of performing the compaction and resilient testing in one pass without having to extrude the specimen from the mold and subsequently mount the specimen for resilient testing.
2. The GTM avoids specimen extrusion and remounting for further testing averting any possible sample disturbance.
3. The GTM has the added capability of inducing stress reversal in the specimen during resilient testing.

Resilient Modulus Testing Using GTM

Previously the primary use of GTM has been to determine compaction characteristics of road materials and compaction, plasticity, and shear characteristics of bituminous mixtures. Consequently, the repeated load gyratory test procedure envisioned in this study had to be developed and standardized. Because sample compaction is performed in the GTM, a compaction procedure is conveniently combined with the repeated load test. The compaction pressure and the gyration angle are chosen to simulate the stress state of the soil material during field densification and to attain a unit weight representative of the ultimate in-place condition after extensive traffic load application. Based on the results of numerous trials, it is recommended that granular soils be compacted at 345 kPa (50 psi) compaction pressure and 0.5 degree gyration angle, whereas fine-grained soils should be compacted with the same gyration angle but at an elevated pressure of 482 kPa (70 psi).

Because resilient behavior of a soil is controlled by stress state, among other factors, the stress levels during modulus testing should correspond to those anticipated under traffic loading. Because of the need to compact the sample at pressures greater than those called for in resilient modulus testing, a 2 hr waiting period (allowing for specimen rebound) is also programmed into the testing procedure. George (*5*) lists a

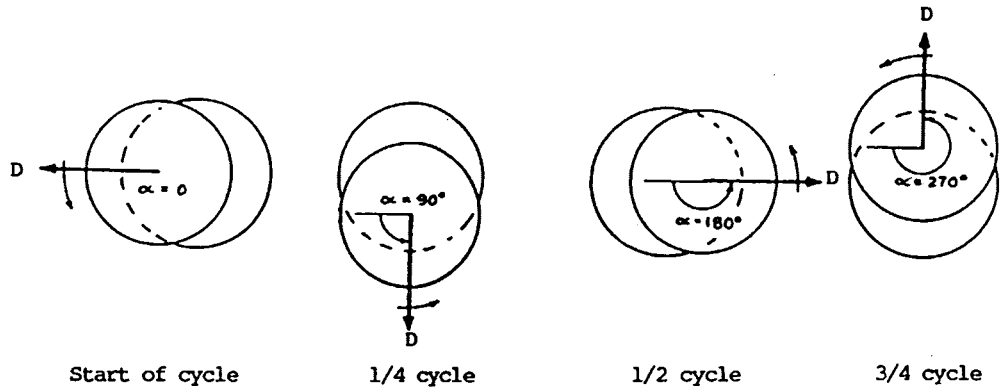

FIGURE 2 A constant rotating displacement (D) applied to top of specimen produces a gyratory motion (for 5 sec) during gyratory shear test.

step-by-step procedure of the test along with the test parameters adopted in this study.

Equation for Kneading Resilient Modulus

After being compacted to the specified density, the specimen in the GTM is subjected to a stress pulse, with the peak value smaller than the compaction pressure. With the tacit assumption of nearly zero wall friction, due to a light greasing of the mold, an equation for the resilient modulus (M_{rk}) is derived as follows (*5*):

$$M_{rk} = \frac{\sigma_r}{\varepsilon_r} \frac{(1 + \nu)(1 - 2\nu)}{(1 - \nu)} \quad (1)$$

where

σ_r = rebound stress in axial direction;
ε_r = recoverable strain; and
ν = Poisson's ratio.

EXPERIMENT DESIGN

Six subgrade soils covering a range of soils in the state of Mississippi were selected for resilient modulus determination. Three "class C" subbase materials were also included in the testing program. All of the nine soil materials have been used recently in pavement construction. Dynaflect and FWD deflections were obtained on five of these pavements at various stages of construction, making it possible to backcalculate the in situ modulus of each layer. Table 1 presents the index properties and classification symbols of nine soil materials. A range of gradations is represented, as indicated in Table 1.

The experiment design called for three series of testing. The first series comprised three or more specimens from each soil, at optimum moisture and AASHTO T99 (standard Proctor) density, tested in accordance with the AASHTO T274. The second series included specimens from the same soils at optimum moisture and density tested in a repeated gyratory machine. All of the latter specimens were compacted at 0.5 degree gyration angle and tested at gyration angles of 0.1 degree and 0.0 degrees. Five field sites, where the soil samples 2–5 and 10 have been obtained, were subjected to NDT deflection testing using both the Dynaflect and the FWD. The NDT was the third phase (series) of tests programmed in this investigation.

DISCUSSION OF RESULTS

For both the RLT and GTM devices, the deformations measured during repeated loading were corrected to account for machine compliance and seating errors. Failure to do so would result in apparent low resilient moduli. In the RLT tests, the deformation was sensed outside the triaxial cell, and, therefore, the measured deformations included seating errors, which can be significant at times. To correct the measurements for the seating error, the linear variable differential transformer rebound deflection registered at 14 kPa (2 psi) deviatoric stress is subtracted from the respective deformation at higher stress levels. A sample calculation illustrating this correction procedure is provided by George (*5*). However, in GTM a compliance curve was prepared, which is simply a plot of pressure versus deformation ascertained while loading a steel cylinder (relatively stiff compared with that of the soil) between the upper and lower load plungers. A correction was applied to the soil specimen deformation, commensurate with the pressure in the specimen.

Both RLT and GTM resilient tests were conducted on three replicated specimens with three or more observations on each specimen. Outliers for each soils were scrutinized using Chauvenet's criterion (*7*) before combining the results of each soil specimen to arrive at the representative resilient modulus.

TABLE 1 Soil Characteristics

Soil No.	Location Hwy/County	Passing #200 Sieve, %	Atterberg Limits LL	Atterberg Limits PI	Proctor Test Data Maxm. Density kN/m³	Proctor Test Data Optimum Moisture %	Soil Classification AASHTO/Unified	Poisson's Ratio	Lateral Stress Ratio, K_o[a]
2	US98/Forrest & Perry	19	0	NP	19.2	10.4	SP-SM/A-3	0.25	0.33
3	MS7/Yalobusha	26	22	4	18.9	11.9	SM-SC/A-2-4	0.30	0.43
4	US49/Sunflower	70	32	13	18.4	15.1	CL/A-6(7)	0.35	0.54
5	US49/Sunflower	89	40	18	17.3	15.7	CL/A-6(16)	0.35	0.54
6	US61/Coahoma	97	70	39	15.3	23.0	CH/A-7-5(45)	0.40	0.67
7	US78/Benton & Union	51	26	7	19.4	11.5	ML-CL/A-4(1)	0.30	0.43
8[b]	US98/Forrest & Perry	23	0	NP	19.3	10.7	SM/A-2	0.25	0.33
9[b]	MS7/Yalobusha	12	0	NP	17.5	10.8	SP-SM/A-2	0.25	0.33
10[b]	US98/Forrest	10	0	NP	18.8	9.5	SP-SM/A-3	0.25	0.33

a $K_o = \frac{\nu}{1 - \nu}$

b subbase material
1 kN/m³ = 6.37 lbf/ft³

TABLE 2 RLT Resilient Modulus of Nine Soils Compared with Those of Other Researchers

Soil Group	Soil Number/ Classification	Percent Passing #200 (PF)	Atterberg Limits		RLT Resilient Modulus, kPa			
					Repeated Load Triaxial	Carmichael & Stuart (8)	Drumm et al. (9)	Elliot et al. (10) σ_c = 45 kPa
(1)	(2)	(3)	LL (4)	PI	(5)	(6)	(7)	(8)
Coarse-Grained	10/A-3	10	0	NP	140,220[a]	155,670		
	9/A-2	12	0	NP	146,570[a]	150,080		
	2/A-3	19	0	NP	120,650[a]	148,570		
	8/A-2	23	0	NP	164,280[a]	146,290		
	3/A-2-4	26	22	4	123,200[a]	142,570		
Fine-Grained	7/A-4(1)	51	26	7	122,020[a]	111,890	27,580	49,360
	4/A-6(7)	70	32	13	92,860[b]	65,420	79,940	41,020
	5/A-6(16)	89	40	18	78,590[b]	28,400	74,800	47,640
	6/A-7-5(45)	97	70	39	114,510[b]	174,490	123,540	66,600

[a]Resilient modulus at bulk stress 275 kPa
[b]Resilient modulus at deviatoric stress 70 kPa and confining pressure 21 kPa
1 kPa = 0.145 psi

The resilient moduli of nine soil samples, which were determined using RLT, are listed in column 5 of Table 2. Because the resilient behavior of a soil sample is influenced by the applied confining pressure and the deviatoric stress, relations were sought between M_r and each of these stress variables. To remain consistent with the AASHTO recommendation, resilient modulus values are plotted with bulk stress ($\theta = \sigma_d + 3\sigma_3$) and cyclic deviatoric stress for the coarse- and fine-grained soils, respectively. As expected, the resilient moduli of coarse-grained soils increase with the bulk stress (see Figure 3). The effect of confining pressure on the resilient modulus showed a substantial modulus increase of as much as 40 percent when the confining pressure was increased from 35 to 70 kPa (5 to 10 psi). In fine-grained soils, resilient modulus is graphed against the cyclic deviatoric stress and the results show that M_r is decreased only slightly with the latter (Figure 4).

For comparison purposes, the moduli of soils tested in this research are predicted using empirical equations of other researchers. Columns 6–8 of Table 2 list resilient moduli calculated using the empirical equations of Carmichael and Stuart (*8*), Drumm et al. (*9*), and Elliot et al. (*10*), respectively. Recognizing that the experimental precision is ±16,536 kPa (±2,400 psi), the equations of Carmichael and Stuart predict the moduli of coarse-grained soils rather well. Of the four fine-grained soils, only the modulus of Soil 7 agrees with that predicted by Carmichael's equation. The Drumm et al. equation is meant to predict only the modulus of fine-grained soils. With the exception of Soil 7, the agreement is satisfactory. The Elliot et al. equation, which again is recommended for fine-grained soils, underpredicts the test values determined in this study.

Gyratory Resilient Modulus

The gyratory modulus results are discussed in detail by George (*5,6*), with some specific results in Table 3. Columns 3 and

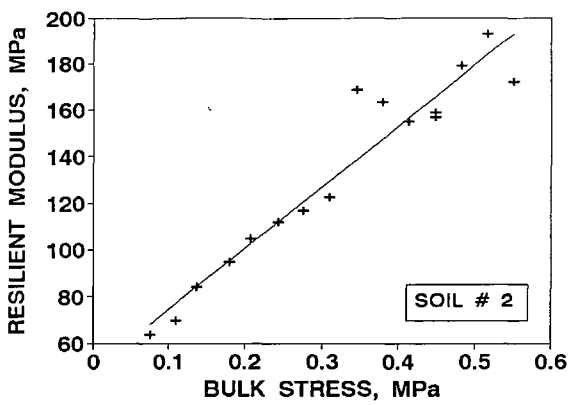

FIGURE 3 Resilient modulus related to bulk stress ($\theta = \sigma_1 + \sigma_2 + \sigma_3$).

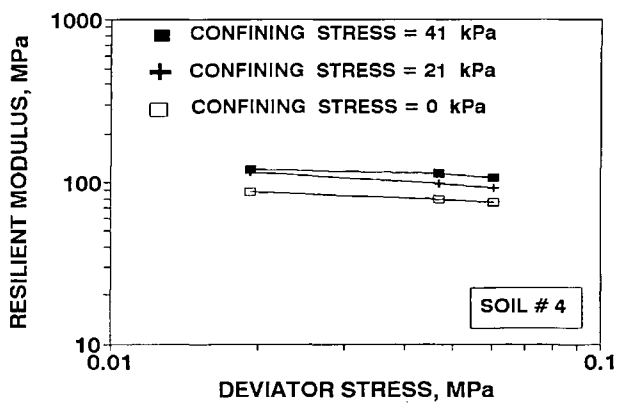

FIGURE 4 Resilient modulus related to deviatoric stress at different levels of confining stress (1 MPa = 145 psi).

TABLE 3 RLT and GTM Resilient Modulus Compared with Backcalculated Modulus

Soil Number	RLT Modulus, M_r, kPa	Kneading Modulus, kPa		Dynaflect Backcalculated Modulus, kPa		FWD Backcalculated Modulus, kPa	
		0.0 degree, $M_{r_{k0}}$	0.1 degree, M_{r_k}	FPEDD1 (w/o correction)	FPEDD1 (w/correction)	FPEDD1	MODULUS 4.0
(1)	(2)	(3)	(4)	(5)	(6)	(7)	(8)
10[a]	140,220	211,650	108,790	198,750	121,270	235,020	229,570
2[a]	120,650	202,890	111,340	177,310	108,170	222,680	220,610
3[a]	123,200	161,460	88,520	178,000	78,390	221,300	199,240
4[b]	92,860	95,760	62,800	101,760	69,150	145,600	146,840
5[b]	78,590	86,380	43,640	114,230	76,870	148,840	149,600
6[b]	114,510	92,040	52,600				
7[b]	122,020	99,340	76,590				
8[a]	164,280	205,860	111,750				
9[a]	146,570	194,480	114,510				

[a]coarse-grained soil
[b]fine-grained soil
1 kPa = 0.145 psi

4, list the gyratory resilient moduli at 0.0 and 0.1 degree gyration angles, respectively. The variation of M_{rk} with soil composition (texture), and dry density and stress state agreed with the reported results of the repeated load triaxial device. M_{rk}, however, is influenced little by fluctuations in compaction moisture. Comparing Columns 3 and 4, the authors concluded that the modulus increases under no-kneading condition (designated as M_{rk0}). The fact that the resilient modulus is significantly affected by the angle of gyration (which induces shear strain) suggests that for realistic modulus determination, the test must simulate shear stress reversal, a condition inherent in the field under moving loads. Values for M_{rk}, which are determined at various cyclic stress levels, are normalized with respect to M_{rk} at 70 kPa/140 kPa (10 psi/20 psi) stress level and plotted against the corresponding volumetric stress in Figure 5. The intermediate and minor principal stresses, which are equal in the GTM sample, are estimated using the lateral stress ratio, K_0 ($K_0 = \nu/1 - \nu$). K_0, estimated from Poisson's ratio, is listed in Table 1. The gyratory modulus results for two coarse-grained and two fine-grained are shown in Figures 5(*a*) and 5(*b*), respectively. No significant change with volumetric stress was observed in either soil group. This result was somewhat different from what has been observed with the RLT data, as shown in Figure 3.

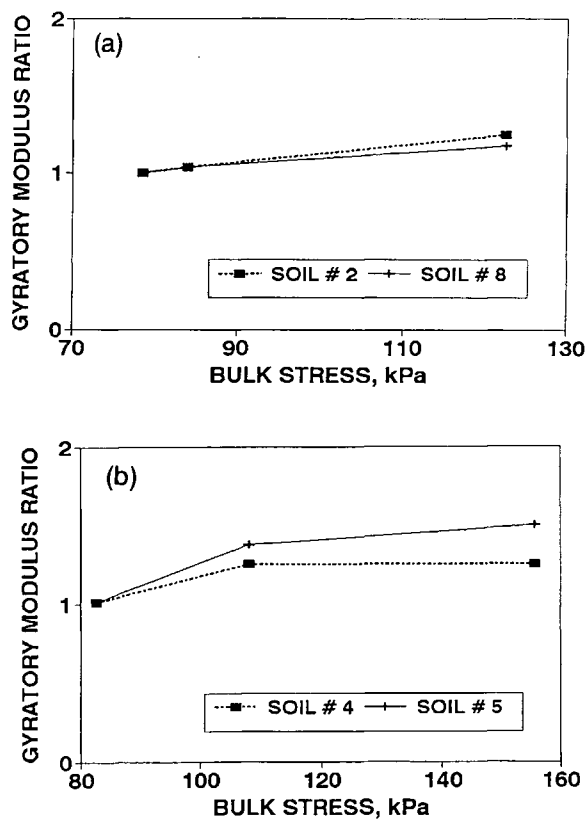

FIGURE 5 Gyratory shear modulus, normalized with respect to M_{rk} at 138/69 kPa plotted against volumetric stress: (*a*) coarse-grained soils and (*b*) fine-grained soils (1 kPa = 0.145 psi).

Backcalculated Moduli from In Situ Tests

To validate the laboratory moduli values, in situ moduli of five subgrade soils were determined from NDT deflection in conjunction with backcalculation procedure. Thirteen deflection tests were conducted in November 1991 on each of the

five pavements using the Dynaflect. FWD tests at the same sites were more elaborate because deflection data were ascertained using four different loads: 26,688 kN, 40,032 kN, 53,376 kN, and 71,168 kN (6,000 lbf, 9,000 lbf, 12,000 lbf, and 16,000 lbf). FWD data were obtained in May, June, and October 1992, 6 to 11 months later than the Dynaflect tests. Asphalt surface temperatures were measured during both Dynaflect and FWD tests, but no temperature correction was applied to the results reported in Table 4. The mid-depth temperature of the asphalt surface during the FWD test is reported in Column 1 of Table 4. Moduli of the various layers were backcalculated for each FWD basin using MODULUS 4.0 and FPEDD1 programs, with the results presented in Table 4. The FPEDD1 program readings showed consistent values within the 13 adjacent sites. Note that in Soil (site) 3, the MODULUS program failed to give reasonable values at 6 of the 13 locations. Therefore, only seven results are included in Row 5 of Table 4. Although there is good agreement in the subgrade moduli calculated from both programs, the surface moduli (Column 4, Table 4) and base moduli (Column 5, Table 4) from FPEDD1 are more realistic than those calculated using MODULUS 4.0. Similar results have been reported by George (*5*) where Dynaflect data are used in conjunction with FPEDD1. The relatively small coefficient of variation of the layer moduli, especially with FPEDD1, reflects the robustness of the backcalculation procedure.

Because the force applied by Dynaflect is 4,448 kN (1,000 lbf), substantially smaller than the wheel load of 40,032 kN (9,000 lbf), a correction for the nonlinear constitutive relationship is recommended. FPEDD1 includes the required algorithm to account for the nonlinear behavior. An empirical relationship developed in earthquake engineering studies has been adopted for this purpose (*11*). The strain versus modulus relationship in FPEDD1 for nonlinear correction is described by Uddin et al. (*12*). Corrected and uncorrected backcalculated moduli from Dynaflect deflection basins are reported in Columns 6 and 5 of Table 3, respectively. Nonlinear correction is not required when using FWD. Accordingly, backcalculated modulus values in Columns 7 and 8 of Table 3 are not corrected.

A comparison of the uncorrected Dynaflect backcalculated moduli with those from FWD basins, (Table 3, Columns 5 and 7) reveals that the FWD values are consistently larger than their Dynaflect counterparts. From the point of view of nonlinear considerations, an opposite trend would have been more appropriate, that is, moduli from the heavier FWD (40,030 kN load) would be smaller than the Dynaflect moduli, where the load is only 4,448 kN (1000 lbf). Side-by-side FWD and Dynaflect tests were conducted on one site (Soil 3) in October 1992, and the backcalculated moduli showed the same trend, that FWD moduli (Row 5, Column 6, Table 4) were larger than their Dynaflect counterparts, 221 MPa versus 169 MPa. Similar results have been reported by Zhou et al. (*13*). The effect of the loading mode (impact versus steady-state vibratory) may have had a significant role in the measured deflection. This will be further investigated by dynamic analysis.

FEASIBILITY OF GTM FOR RESILIENT MODULUS TESTING

Now that resilient modulus values of nine soils have been determined by (a) employing repeated load triaxial test,

TABLE 4 Sample Results of Backcalculated Moduli Using FWD Data in Conjunction with Modulus 4.0 and FPEDD1

Soil/Test Temp./ Test Date (1)	Program Used (2)	Statistical Measure (3)	Hot Mix Surface Binder Modulus, MPa (4)	Base Modulus, MPa (5)	Subgrade Modulus, MPa (6)
2/27°C[a]/05-20-92	MODULUS 4.0	Mean/CV[d]	3790/(21%)	827[b]/(18%)	221/(4%)
	FPEDD1 (w/o correction)	Mean/CV[c]	1994/(16%)	1172[b]/(17%)	223/(4%)
10/27°C[a]/05-20-92	MODULUS 4.0	Mean/CV[d]	5854/(27%)	717[b]/(8%)	230/(2%)
	FPEDD1 (w/o correction)	Mean/CV[d]	2581/(26%)	1132[b]/(26%)	235/(3%)
5/24°C[a]/06-24-92	MODULUS 4.0	Mean/CV[d]	3399/(11%)	174[c]/(40%)	147/(8%)
	FPEDD1 (w/o correction)	Mean/CV[d]	2412/(16%)	260[c]/(26%)	146/(9%)
5/24°C[a]/06-24-92	MODULUS 4.0	Mean/CV[d]	3373/(11%)	128[c]/(32%)	150/(8%)
	FPEDD1 (w/o correction)	Mean/CV[d]	2221/(15%)	240[c]/(28%)	149/(8%)
3/20°C[a]/10-7-92	MODULUS 4.0[e]	Mean/CV[d]	3916/48%	2009[b]/72%	216/23%
	FPEDD1 (w/o correction)	Mean/CV[d]	2928/31%	1997[b]/31%	221/33%

[a]Mid-depth temperature of hot mix surface
[b]Lime-fly ash base course
[c]Granular material
[d]Coefficient of Variation
[e]Only seven out of 13 deflection bowls gave reasonable solution
1 MPa = 145 psi

(b) using GTM test at 0.1 and 0.0 degree gyration angles, and (c) using NDT in conjunction with the backcalculation procedure, the kneading resilient moduli, M_{rk} and M_{rk0}, may be compared with other values. The objective is to validate the gyratory modulus and, in turn, the applicability of the gyratory testing procedure for resilient modulus determination. At the outset, it should be remarked that a one-to-one comparison between GTM–M_{rk}/M_{rk0} and RLT–M_r should not be expected, for the reason that the states of stress in the respective specimens are far from similar. Because of its stress-dependency, the resilient modulus should be determined under a stress state, as close to the field loading conditions as possible. To evaluate GTM for resilient modulus testing, emphasis should be placed on comparing the GTM modulus with the in situ modulus, although a comparison with RLT–M_r is certainly desired. Four different comparative discussions will be presented as follows:

1. M_{rk} with M_r values,
2. M_{rk0} with M_r values,
3. M_r with in situ backcalculated modulus values (both Dynaflect and FWD), and
4. M_{rk}/M_{rk0} with backcalculated modulus values.

First, by comparing M_{rk} and M_r values in Columns 4 and 2, respectively, of Table 3, it can be seen that M_{rk} values are consistently lower than the M_r values. Between the two groups, fine-grained soils show pronounced reduction in modulus values in GTM at 0.1 degree gyration. The lower moduli in GTM may be attributed to the nonlinear constitutive relationship. As shown by George (*5,6*), fine-grained soils, being highly nonlinear, show a relatively large reduction in M_{rk}, which may be attributed to increased deviatoric stress (resulting from GTM-induced shear), a valid explanation for the pronounced decrease in moduli of fine grained soils.

Second, the 0.0 degree kneading modulus, M_{rk0}, does not show any one trend when compared with the corresponding M_r-values. As noted in Columns 3 and 2 of Table 3, the M_{rk0} of coarse-grained soils is higher than M_r, whereas in the fine-grained soils, they are equal or the M_{rk0} is slightly lower. An explanation of this result is that when coarse soils are tested under confinement (zero lateral strain), they exhibit a tendency to be stiff, whereas confinement plays only a minor role in cohesive soils. The question now arises why M_{rk0} values of fine-grained soils are slightly lower than the corresponding M_r values. It may be that because the clayey soils are plastic, they have "memory" to reflect the large (0.5 degree gyratory angle) shear strains imposed in the specimen during compaction. Note that the 0.0 degree gyratory test invariably followed the 0.1 degree test in the same specimen. The presence of residual deformation was corroborated by observing a nonzero angle in the test gyrograph when the chuck was set to read zero angle.

The third comparison is between the triaxial M_r values with the backcalculated values. In all of the five soils, the M_r values lie somewhere between the uncorrected and corrected in situ values in Columns 5 and 6 of Table 3, respectively. Note that in situ backcalculated values (both Dynaflect and FWD) are larger than the corresponding triaxial moduli. Similar results have been reported by other researchers (*14*) in that the backcalculated moduli are consistently larger than the triaxial counterpart by roughly 50 to 75 percent.

Fourth, the validity of M_{rk} or M_{rk0} was examined with the basic tenet that the backcalculated moduli form the basis for comparison. As indicated earlier, the moduli corrected for strain sensitivity are a better measure than the uncorrected values. As can be verified in Table 3 (Columns 6 and 4), those corrected in situ values of four soils are in good agreement with the GTM kneading modulus (M_{rk}), with deviations of +10, −3, −13, and +9 percentage points in soils 10, 2, 3, and 4, respectively. In Soil 5, a heavy clay, the corrected backcalculated value lies between the 0.0 degree and 0.1 degree kneading moduli. An angle of gyration smaller than 0.1 degree could have resulted in a value comparable to the corrected NDT value. Very limited tests with a 0.05 degree gyration have confirmed this contention. Evidenced by this result is the basic premise of this research: that resilient modulus testing conducted under stress reversal indeed has some merit. Coincidentally, the 0.0 degree kneading moduli of the five soils reasonably agree with the uncorrected in situ moduli from Dynaflect, but far exceed the corrected moduli, which are considered more realistic than the uncorrected values. Therefore, the researcher concludes that gyratory tests at 0.1 degree or smaller have the potential for resilient modulus characterization of subgrade soils.

The gyratory resilient modulus test, with some modifications in the test apparatus, promises to be a viable test for resilient modulus determination. The gyratory angle setting provision needs to be modified, and the cyclic load duration should be adjusted to a fraction of a second. With these modifications, the GTM could be fine-tuned to suit the testing needs in pavement design.

SUMMARY AND CONCLUSIONS

The resilient modulus is a significant parameter in the design and rehabilitation of pavements. This parameter can be highly nonlinear and influenced by stress state, moisture content, soil type, and density. The resilient modulus most be determined under simulated traffic loading conditions. In this investigation, the resilient modulus was formulated from repeated load tests conducted in the laboratory using the triaxial device and the U.S. Army Corps of Engineers GTM and from using backcalculation techniques using Dynaflect and FWD deflection.

With the objective of investigating the feasibility of the GTM for resilient testing of subgrade soils, nine soils—five coarse grained and four fine grained—were tested in the laboratory. Dynaflect and FWD deflections from five of the nine pavement sites were also ascertained after the pavement structure was in place. The adequacy of the GTM procedure is judged by comparing the GTM resilient modulus values with those of the repeated load triaxial test AASHTO T274 and backcalculated moduli from NDT deflection.

The GTM modulus of coarse-grained soils is compared with the triaxial resilient modulus to note that the former values are 8 to 47 percent lower than the latter. The decrease is more pronounced in fine-grained soils. The same general trend (a lower GTM modulus) is observed with the backcalculated modulus with no correction applied for nonlinearity. Because

the two independent backcalculation programs (MODULUS 4.0 and FPEDD1) identify nearly equal subgrade moduli, they support the credibility of the back-calculation techniques. FPEDD1, however, results in more realistic surface and base moduli. A comparison of Dynaflect and FWD backcalculated values reveals that the Dynaflect deflection basin can well characterize conventional flexible pavement structures. The in situ moduli adjusted for low stresses (Dynaflect load only 4,448 kN), as derived by FPEDD1 with a correction for nonlinear behavior, agree with the 0.1 degree kneading resilient modulus. Encouraged by this comparison, the authors recommend that the 0.1 degree GTM test be further explored and modified for possible use in the resilient characterization of subgrade soils.

ACKNOWLEDGMENTS

This report includes results of a study entitled Resilient Modulus of Subgrade Soil Using Gyratory Testing Machine, which was sponsored by the Mississippi State Highway Department and FHWA. Joe Sheffield and Alfred Crawley of the Mississippi State Highway Department were instrumental in developing the project scope. The tests were performed by graduate research assistants in the Civil Engineering Department, University of Mississippi.

The opinions, findings, and conclusions expressed in this report are those of the authors and not necessarily those of the Mississippi State Highway Department or FHWA. This paper does not constitute a standard, specification, or regulation.

REFERENCES

1. *AASHTO Guide for Design of Pavement Structure*, AASHTO, Washington, D.C., 1986.
2. J. R. Montalvo, C. A. Bell, J. E. Wilson, and J. T. Scofield. *Application of Resilient Modulus Test Equipment for Subgrade Soils*. Report FHWA-OR-84-3, Oregon State University, Corvallis, Oreg., 1984.
3. *Development of the Gyratory Testing Machine and Procedures for Testing Bituminous Paving Mixtures*. Technical Report 3-595. U.S. Army Engineer Waterways Experiment Station, Corps of Engineers, Vicksburg, Miss., 1962.
4. *Gyratory Compaction Method for Determining Density Requirements for Subgrade and Base of Flexible Pavements*. Miscellaneous Paper 4-494. U.S. Army Engineer Waterways Experiment Station, Corps of Engineers, Vicksburg, Miss., 1962.
5. K. P. George. *Resilient Modulus of Subgrade Soil Using Gyratory Testing Machine*. Mississippi State Highway Department, Jackson, Miss., 1991.
6. K. P. George. Resilient Testing of Soils Using Gyratory Testing Machine. In *Transportation Research Record 1369*, TRB, National Research Council, Washington, D.C., 1992.
7. H. W. Coleman and W. G. Steele. *Experimentation and Uncertainty Analysis for Engineers*. John Wiley and Sons, Inc., New York, N.Y., 1989.
8. R. F. Carmichael and E. Stuart. Predicting Resilient Modulus: A Study to Determine the Mechanical Properties of Subgrade Soils, In *Transportation Research Record 1043*, TRB, National Research Council, Washington, D.C., 1985.
9. E. C. Drumm, Y. Boateng-Poku, and T. J. Pierce. Estimation of Subgrade Resilient Modulus from Standard Tests. *Journal of Geotechnical Engineering*, ASCE, Vol. 116, No. 5, 1990.
10. R. P. Elliot, S. I. Thornton, K. Y. Foo, K. W. Siew, and R. Woodbridge. *Resilient Properties of Arkansas Subgrades*. TRC-94. Arkansas Highway and Transportation Research Center, 1988.
11. H. B. Seed and I. M. Idriss. *Soil Moduli and Damping Factors for Dynamic Response Analysis*. Report EERC 70-10. Earthquake Engineering Research Center, University of California, Berkeley, Sept. 1970.
12. W. Uddin, A. H. Meyer, W. R. Hudson, and K. H. Stokoe II. Project Level Structural Evaluation Based on Dynamic Deflections. In *Transportation Research Record 1007*, TRB, National Research Council, Washington, D.C., 1985.
13. H. Zhou, R. G. Hicks, and I. J. Huddleston. Evaluation of the 1986 AASHTO Overlay Design Method. In *Transportation Research Record 1215*, TRB, National Research Council, Washington, D.C., 1989.
14. M. S. Mamlouk, W. N. Houston, S. L. Houston, and J. P. Zaniewski. *Rational Characterization of Pavement Structures Using Deflection Analysis*. Report FHWA-AZ88-254, I, CART. Arizona State University, Tempe, 1988.

Publication of this paper sponsored by Committee on Soil and Rock Properties.

Stress State Considerations for Resilient Modulus Testing of Pavement Subgrade

WILLIAM N. HOUSTON, SANDRA L. HOUSTON, AND TIMOTHY W. ANDERSON

The stress state imposed on subgrade materials during laboratory resilient modulus testing is compared with the anticipated stress state for in situ conditions during traffic loading. Revisions to AASHTO and the Strategic Highway Research Program resilient modulus testing procedures are under way; however, previously most resilient modulus tests have been performed according to the former AASHTO T274-82 specification. In this study, the stress state called for in AASHTO T274 was found to overstress subgrade specimens compared to traffic loading. The issue of stress state needs to be evaluated carefully in making revisions to the testing procedure. The probable effect of overstressing is discussed. Overstressing from shear and normal loading, which have opposite effects on the laboratory-measured resilient modulus, are both considered. Recommendations for resilient modulus testing of subgrade materials are made. The recommended procedure is designed to eliminate overstressing the test specimen. It is also designed to improve the degree to which preconditioning of the specimen removes plastic strains prior to obtaining measurements required for determining the resilient modulus. Laboratory tests on several subgrade materials are conducted using the modified procedure.

The resilient modulus has become a common parameter for characterization of pavement materials. Numerous state and federal agencies, as well as many engineering consulting companies, are developing the capability to perform the laboratory tests required for obtaining the resilient modulus. The resilient modulus is obtained by subjecting a specimen to repeated loading at a particular stress level and measuring the recoverable strain. Ideally, the specimen is exhibiting only elastic strains at the time the resilient modulus is measured. The resilient modulus can therefore be thought of as the secant Young's modulus of the material, which is typically different than the initial tangent value of Young's modulus, as can be seen in Figure 1.

The laboratory procedure being followed by most laboratories is AASHTO T274-82 (which is currently being revised as T292-91I). This laboratory procedure (*1*) includes specifications for preconditioning the soil specimen during testing. One of the intents of the preconditioning loading phase of the resilient modulus test is to induce any plastic strains that are prone to occur, so that mostly elastic strains remain during resilient modulus loading. It is best if the preconditioning loading phase of the test would use stress levels anticipated for in situ conditions, that is, stress levels comparable to those imposed by traffic loads and overburden. Overstressing a soil subgrade specimen in the laboratory can cause permanent changes in the material, thus decreasing the chance of obtaining a resilient modulus measurement that is indicative of in situ conditions. Investigation of the laboratory-imposed stress state on subgrade specimens compared to the in situ stress state is the subject of this paper.

W. N. Houston and S. L. Houston, Center for Advanced Research in Transportation, Arizona State University, Tempe, Ariz. 85287. T. W. Anderson, Foree and Vann, Inc., Phoenix, Ariz. 85021.

EFFECT OF STRESS OVERLOAD

It is a known fact that when stresses on a soil specimen are increased to a level higher than ever applied previously, plastic strains will occur (*2,3*). Therefore, the resilient modulus cannot be measured for such a cycle of loading. Stresses may be described broadly as either normal (spherical) stresses or shear (deviatoric) stresses. When discussing stress level, it is important to distinguish between normal stress level and shear stress level because normal and shear stresses produce somewhat differing effects on soil specimens (*4–6*). When a specimen is overstressed by normal stress, plastic strains occur and bonds between particles are broken. However, bonds are reformed at a higher normal stress, and the net effect of having been loaded to a higher normal stress is that the specimen is now denser, stiffer, and stronger than it was previously (*7*). By contrast, when shear stress is raised to a level higher than ever before, plastic strains result in bonds breaking; either these bonds do not reform, or new bonds are formed that are typically weaker than previous bonds (*7*). Therefore, the net effect of increasing the shear stress to a new higher value is to produce a specimen that is softer and weaker than before. Overloading by shear is generally more damaging than overloading by normal stress.

Thus the effect of shear stress elevation on the modulus is opposite to the effect of normal stress elevation (*4*). In the laboratory, separation of and distinction between shear and normal stresses are relatively easy. In the field, wheel loads produce both shear and normal stresses, and the predominant type of loading varies with the point of consideration within the pavement structure.

The measured modulus is sensitive to an increase in either normal or shear stress to levels higher than ever applied before because plastic strains are induced. However, when significant plastic strains occur, the resilient modulus cannot be measured in a straightforward manner because elastic and plastic strains must first be separated. Thus, the resilient modulus is most readily quantified when the following conditions are met:

1. The stresses applied (both shear and normal) are less than or equal to the maximum level of stress previously applied.

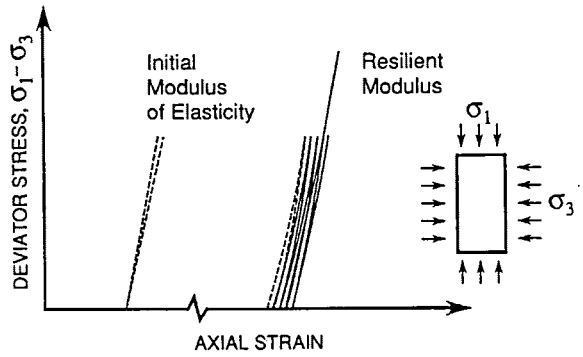

FIGURE 1 Definition of resilient modulus.

2. The stress has been applied for a sufficient number of times that the strains become essentially completely recoverable.

If the conditions of the laboratory test are such that the normal or shear stress imposed on the specimen is greater than that the specimen has ever been exposed to in situ, or if the stresses are greater than the stresses that the specimen will be exposed to in situ in the life of the pavement, then the laboratory modulus would be expected to differ from the field modulus, even if sampling were perfect and sample disturbance were absent. If the specimen is overstressed by normal stress loading, the effect on the modulus would be opposite to that for shear stress overloading.

As a part of the preconditioning, the former AASHTO T274 procedure calls for levels of both shear and normal stress that in most cases are well beyond those estimated to have been applied by in situ traffic stresses. For example, T274 calls for application of shear stresses to triaxial specimens of clayey soils when the confining pressure is zero, a condition that never exists for a subgrade in situ.

As noted above, it is also important for all plastic strains to have been removed by preconditioning before the resilient modulus is measured. The former AASHTO T274 procedure calls for preconditioning to only 200 cycles at each stress state. This number of cycles of loading is often insufficient to remove all significant plastic strains. Revisions to the AASHTO procedure and the Strategic Highway Research Program (SHRP) procedure (both under development at the time of this writing) call for additional conditioning of 1,000 repetitions. In the laboratory testing program conducted as part of this study, it was found that several thousand cycles of loading were often needed to remove the plastic strains, as noted by other researchers (*2,3,8,9*).

STRESS LEVEL

Because the subgrade material properties are generally stress dependent, the resilient modulus varies at different stress states. The moduli of subgrade materials change with changes in confining pressure and deviator stress (*6,10*). Changes in confinement correspond to changes in normal stress level, and changes in deviator stress correspond to changes in shear stress level. To determine the specific modulus in the laboratory that corresponds to the in situ condition, the state of stress of the sample in the laboratory has to match that anticipated for the field condition.

It is most convenient to represent the stress state of a soil specimen by stress invariants. Stress invariants are functions of the stress tensor that are independent of coordinate transformation. Functions of the principal stresses are probably the most-used stress invariants for describing the stress state for soil (*5,7,11*). It is common to use the octahedral normal and shear stresses, or other representations of the first and second stress tensor invariants, for describing the stress state of a material when it is important to consider normal and shear stress changes (*6,10,11*). For this purpose, the octahedral normal stress (σ_{oct}) and the octahedral shear stress (τ_{oct}) in the laboratory should be compared with the octahedral normal and shear stresses in the field. The octahedral normal and shear stresses are defined, respectively, as follows:

$$\sigma_{oct} = (\sigma_1 + \sigma_2 + \sigma_3)/3 \quad (1)$$

$$\tau_{oct} = \tfrac{1}{3}[(\sigma_1 - \sigma_2)^2 + (\sigma_1 - \sigma_3)^2 + (\sigma_2 - \sigma_3)^2]^{1/2} \quad (2)$$

Figure 2 shows the three-dimensional stress space. Figure 2(*a*) shows the view looking down the hydrostatic axis. The hydrostatic axis is the line along which the three principal stresses are all equal. Figure 2(*b*) shows a different perspective of the stress space, showing the octahedral shear stress is zero along the hydrostatic axis. As the octahedral normal stress increases, the point corresponding to the state of stress of the soil moves outward along the hydrostatic axis. Increasing octahedral shear stress is also indicated in Figure 2(*b*). Compressive stresses are positive for Figure 2.

A typical soil failure surface is shown in Figure 3. A projection of this failure surface in the more customary shear stress versus normal stress space would look like the Mohr Coulomb failure surface. Two perspectives of this failure surface are given in Figures 3(*a*) and 3(*b*), corresponding to the perspectives shown in Figures 2(*a*) and 2(*b*), respectively.

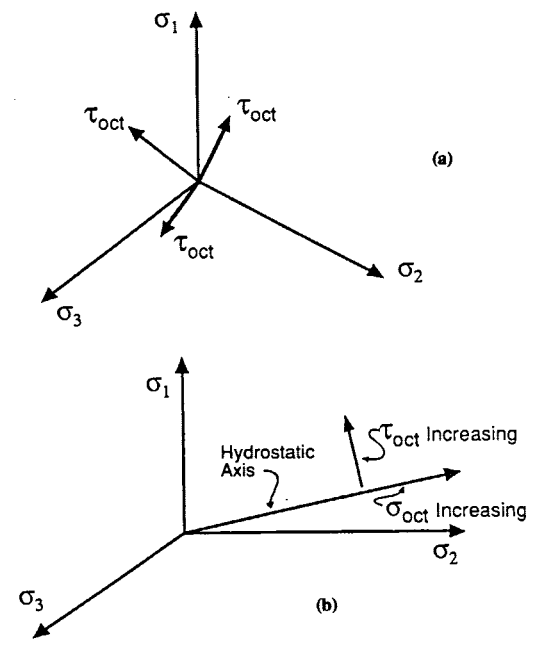

FIGURE 2 Three-dimensional stress space.

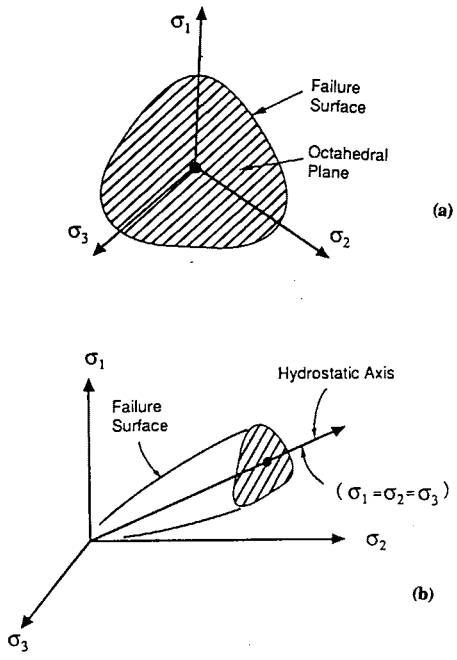

FIGURE 3 Typical soil failure surface.

It is possible to sketch a surface in stress space corresponding to the maximum stresses resulting from the maximum traffic loads plus the overburden stresses. A hypothetical surface representing the maximum in situ stress is shown in Figure 4, together with the soil failure surface. The surface of maximum in situ stresses due to traffic and overburden stress marks the desired limits for the laboratory testing program for subgrade materials.

The ELSYM5 multilayer elastic material computer program was used to compute the octahedral normal and shear stresses in the field under the pavement (*12*). An axle load of 100 kN (22,000 lb), to simulate an overloaded truck, was applied at the surface of each pavement section, and the stresses at the top of the subgrade were computed. Figure 5 shows results of the example computation of stress states for increasing wheel loads for three different depths. The dotted curve in Figure 5 represents the envelope of the maximum stresses, or the stress state associated with the 100 kN axle load. The

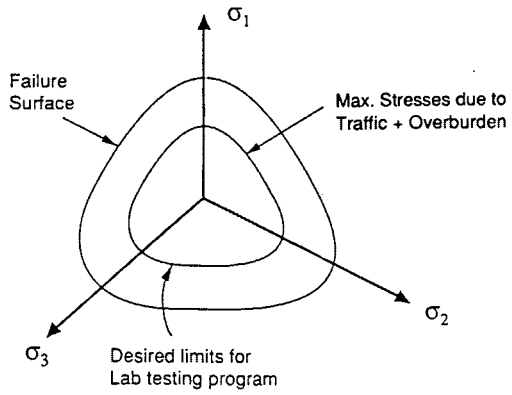

FIGURE 4 Failure surface and stress level.

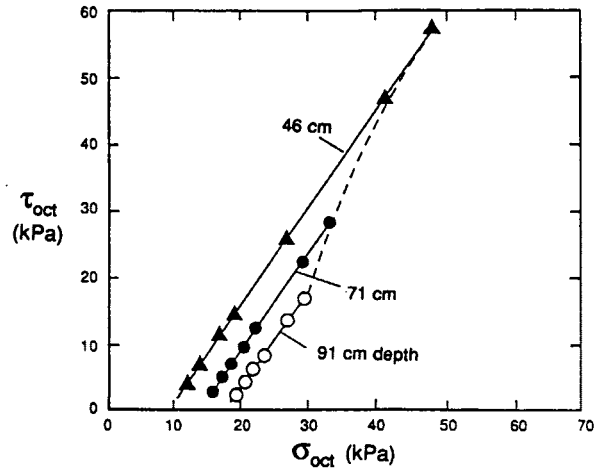

FIGURE 5 Stresses showing loading path for various depths of subgrade (1 kPa = 0.145 psi, 2.54 cm = 1 in.).

results of the computer analyses are given in terms of octahedral shear stress and octahedral normal stress for maximum generality.

Computation of in situ stresses requires the use of a layered elastic analysis computer program. The stress components from the analysis are required to compute the octahedral normal and octahedral shear stresses. Additional discussion on computation of in situ stresses is provided by Bush and Baladi (*13*). For laboratory triaxial conditions, σ_2 is equal to σ_3 and the deviator stress σ_d is $\sigma_1 - \sigma_3$. The octahedral shear and normal stresses for triaxial conditions become:

$$\sigma_{oct} = (\sigma_d/3) + \sigma_3 \quad (3)$$

$$\tau_{oct} = (\sqrt{2}/3)\sigma_d \quad (4)$$

Using these relationships, the deviator stress and confining pressure desirable for the laboratory testing program can be computed if the octahedral normal stress and the octahedral shear stress in the field are known.

Figure 6(*a*) shows the plane in which the triaxial stress conditions plot in principal stress space. Figure 6(*b*), which is given in terms of major and minor principal stresses, depicts a surface that envelopes all the stress states ever imposed by traffic plus overburden loading. This surface applies to only one point (depth) in the sublayer. Each point below the surface would have a different maximum stress surface.

To compare the stress state imposed by following the AASHTO T274 procedure for resilient modulus testing of subgrade materials to the maximum stress state that is likely to occur in situ, an example calculation was performed for a subgrade depth of 63.5 cm (25 in.) and a maximum axle load of 100 kN (22,000 lb). The resulting stress triangle, the set of octahedral shear and normal stresses enveloped by the loading path of Figure 5, is shown in Figure 7. The square data points show the prescribed stress states for the AASHTO T274 resilient modulus test procedure. Although this is only an example, it is typical, showing that the prescribed stress state for laboratory testing performed according to AASHTO T274 significantly exceeds the stress state due to traffic loading plus overburden stresses.

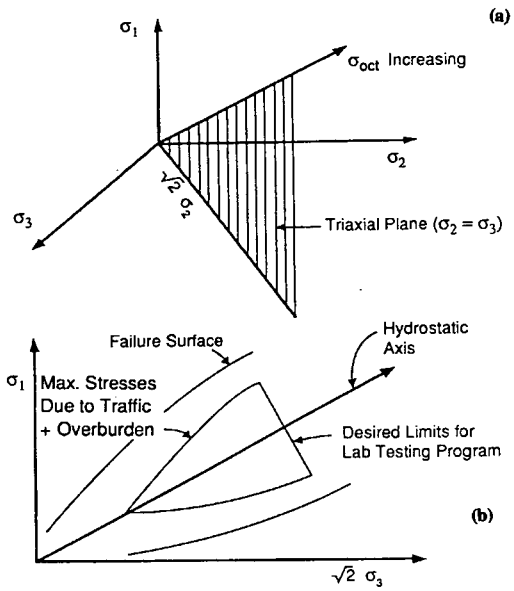

FIGURE 6 Stress states for failure, traffic loading, and laboratory testing.

SUGGESTIONS FOR RESILIENT MODULUS TESTING OF SUBGRADES

The following deviations from the AASHTO T274 procedure for resilient modulus testing appear to be justified on the basis of the preceding arguments and existing literature on the topic of resilient modulus testing of subgrade materials of varying types. It is the authors' understanding that some, though not all, of these suggestions are being considered in the new SHRP procedure and for AASHTO T292-91I.

Stress State

As part of preconditioning the specimen, the AASHTO T274 procedure called for levels of both shear and normal stresses that are in most cases greater than those estimated to have been applied by in situ traffic loading. For example, AASHTO T274 procedure called for application of shear stresses to triaxial specimens of clayey soils when the confining pressure is zero, a condition that never exists for subgrade in situ. Accordingly, a preconditioning program for each site could be selected in the following way, avoiding overloading the specimen in both shear and normal loading.

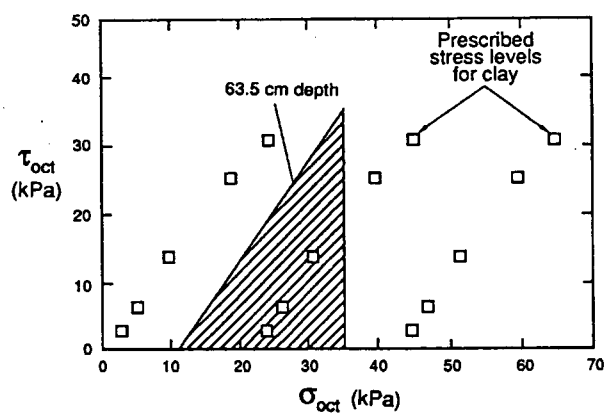

FIGURE 7 Stress triangle for element of subgrade at 63.5-cm depth (1 kPa = 0.145 psi, 2.54 cm = 1 in.).

1. Establish the pavement structure geometry for each site from boring logs and the existing data base.
2. Estimate the elastic moduli for the various layers using backcalculated values from data obtained from nondestructive testing (NDT) (*14*), or estimate a reasonable range in moduli from experience.
3. Estimate the maximum past stress state using an elastic multilayer pavement analysis program, such as ELSYM5 (*12*). An axle overload to 100 kN (22 kips) is likely to be a reasonable maximum loading for most cases.
4. Construct the "loading triangle" (see Figure 7), indicating the maximum past stress state for the subgrade.
5. Establish a preconditioning program and a testing procedure for each test specimen using the loading triangle. In general, each specimen should be loaded for 1,000 cycles at a low stress state, 1,000 cycles at a medium stress state, and 2,000 cycles at the maximum stress state (the apex of the triangle).
6. Load the specimen, after preconditioning, for 200 cycles at various lower stress states to measure the resilient modulus.

It may be possible to adopt an envelope of stress state, which would be conservative for all conceivable cases. If so, Steps 1 through 4 could be eliminated.

Preconditioning

If the sampling process were perfect and free of disturbance, then reapplication of traffic loads would produce no new plastic strains because plastic strains would have already occurred in situ. However, the sampling process is imperfect, and some plastic strains do occur during the preconditioning. Preconditioning is, in part, an attempt to erase the effects of sample disturbance.

The AASHTO T274 procedure called for preconditioning by cyclic loading to only 200 cycles at each stress state. The SHRP protocol P46 procedure (1991, unpublished) calls for 1,000 cycles of loading. In the laboratory testing conducted as a part of this study, it was consistently found that cyclic loading to several thousand cycles was needed to remove plastic strains. Other researchers have found that several thousand cycles of loading are needed to remove plastic strains (*2,9*). (This issue was addressed in Step 5 in the preceding section on stress state.)

Preparation of Specimen Ends

To ensure an intimate contact between the specimen ends and the end platens, a layer of a quick hardening cement, such as Burkstone, should be placed on the platens and allowed to set with the platens and the loading piston aligned and screwed into the top cap. If a bonding agent like this is not used, the

interface between the specimen and the end platens might be compressible and produce a significant error in the measured modulus. An alternative to Burkstone is an epoxy, such as Bondo, which is used widely for automobile body repair. The advantage of the epoxy over the cement is that it produces no change whatsoever in water content of the specimen near the end platens.

LABORATORY TESTING PROGRAM

As part of a research project conducted for the Arizona Department of Transportation (*15,16*), a series of resilient modulus tests were conducted on subgrades from 20 locations throughout Arizona. The recommended procedure described in the preceding section of this paper was used in the laboratory testing program of subgrade materials.

Sampling

At each location, cores of asphalt concrete were obtained using a portable, electric-powered coring device. A 114-cm (4.5-in.) O.D. continuous flight auger was used to advance the hole after the asphalt core had been removed. Undisturbed samples of subgrade were obtained by pushing 76-mm (3-in.) O.D., 71-mm (2.8 in.) I.D. thin-walled stainless steel sample tubes hydraulically with the drill rig. In a few instances, the tube required driving with a 0.6-kN (140-lb) drop hammer.

Resilient Modulus Testing of Subgrade Materials

A microcomputer-controlled closed-loop testing system was used to conduct the resilient modulus testing of the subgrade materials (*15,16*). An outline of the sample preparation and triaxial test sequence used is given next.

A high-strength, fast-setting cement was used to ensure intimate contact between the specimen and the top and base platens. The cement was placed on a greased sample cap and then placed on the trimmed sample base. The cement was allowed to harden, and then the cap was removed. The location of the porous stone was marked in the cement, and a small hole was drilled for air communication. This air hole was for the purpose of allowing any pore air pressure caused by consolidation to dissipate.

Being careful of the air hole alignment, researchers then extruded the sample from the tube. After the specimen was extruded, weighed, and measured, the specimen base was placed onto the base of the triaxial cell. The top of the specimen was then mated to the top cap with cement. The top cap was first attached to the piston rod. Then a thin layer of cement was applied to the top cap. The top cap was brought into contact with the top of the specimen by easing the piston down into place by hand. The piston was then vibrated until the entire surface of the specimen top was covered with cement and there were no voids between the cap and the specimen. Then the cement was allowed to harden, which required less than 5 min.

The loading piston was unscrewed from the top cap, and the specimen was placed in a membrane and sealed with O-rings to isolate it from the confining fluid of the triaxial cell, in accordance with conventional triaxial procedure. O-rings were used to seal the membrane against the top and base caps. The triaxial cell apparatus was then assembled, and the loading pistons screwed back into the top cap.

Resilient Modulus Test Results

The average values of the subgrade resilient moduli from the laboratory testing program described previously are shown in Table 1. The last column indicates the soil type. The laboratory test specimens were subjected to a range of confining stress and deviator stress to assess sensitivity to both types of stress. The values reported in Table 1 are the average of two or more tests for the various levels of stress indicated. The laboratory specimens were undisturbed specimens obtained from existing subgrades, as previously mentioned. The data in Table 1 show that the average laboratory resilient moduli vary from about 44.2 to 110.4 MPa (4.8 to 16 ksi). These values are reasonable for moduli of the subgrade materials encountered in this study. A more detailed account of the resilient modulus test results is presented in Table 2. For each combination of confining stress and deviator stress, a best estimate value of modulus was determined. The best estimate moduli correspond to the average for the range of reasonable interpretations that could be applied in computing the resilient moduli from the hysteresis loops obtained.

DISCUSSION OF LABORATORY TEST RESULTS

An inspection of Tables 1 and 2 shows that the resilient modulus for the clayey soils decreased with increasing deviator stress level, but only slightly. Other researchers have reported decreased resilient modulus with increasing deviator stress, typically to a greater extent than those observed in this study (*4,5,17*). Likewise, the effect of confining pressure was only slight for the clayey soils. The results of the data given in Tables 1 and 2 for the clayey subgrades are attributed to the following three factors:

1. The preconditioning and loading procedures recommended herein were used for this test series. Therefore, overstressing with respect to previous traffic loading was not committed. That is, the stresses applied in the laboratory were no higher than those estimated to have been applied by traffic. In addition, preconditioning with several thousand cycles of stress was effective in removing most of the plastic strains and stabilizing the modulus (*15,16*).
2. Preconditioning to the highest stress level was done first. Then moduli were measured at lower values of deviator stress. This procedure also minimized plastic strains, contributing to constancy.
3. The stress level applied was in most cases only a small fraction of the shear strength. The high shear strength is attributed to the dry climate, high pore water suction, and high degree of cementation in the subgrade.

TABLE 1 Summary of Average Resilient Moduli of Soil Samples

Site/ Station	Sample Depth (cm)	Dry Unit Weight (kN/m^3)	Water Content (%)	Confining Stress (kPa)	Deviator Stress (kPa)	Resilient Modulus (ksi)	Unified Soil Classification
1/1	63-81	19.2	5.28	14-31	18-93	10.19	SM-SC
1/4	63-81	18.9	4.51	25-35	18-76	11.96	SM
2/1	48-63	18.6	7.09	12-30	18-69	13.10	SM
2/7	96-114	17.5	7.83	20-27	18-38	15.20	SM
3/7	68-86	17.7	12.4	14-31	18-86	6.44	SM
4/1	63-81	17.6	10.4	17-41	20-86	9.76	SM
5/4	51-68	18.8	12.4	20-33	19-62	12.29	SM
7/1	68-86	18.6	10.6	15-35	19-75	12.10	SM
7/4	68-86	18.9	9.23	15-35	19-77	11.36	SM
8/1	79-96	17.7	11.1	21-29	19-47	7.99	SM
9/1	127-145	16.4	22.8	26-31	19-71	16.14	CL-CH
10/4	112-130	15.2	25.9	25-33	21-49	12.48	CH
11/1	30-48	19.3	2.21	16-48	19-80	13.33	SM
12/1	81-99	18.9	8.56	15-25	18-58	7.41	SC-SM
13/4	33-51	17.4	8.81	12-25	20-65	14.35	SC
14/4	30-48	16.0	15.4	9-22	19-58	10.42	SC-CH
16/1	43-61	18.5	7.90	12-25	20-61	9.83	SM
17/1	51-66	16.5	17.8	12-25	20-57	4.82	ML
19/1	58-76	16.4	22.7	15-27	20-55	12.01	SC
19/4	79-97	15.1	28.9	15-27	19-53	15.64	CL

Note: 1 MPa = 0.145 ksi
1 kPa = 0.145 psi
62.4 pcf = 9.807 kN/m^3
1 in. = 2.54 cm

The more granular subgrade materials showed a rather consistent trend of increasing resilient modulus with increasing confining pressure. This trend is as anticipated because, in general, cohesionless (granular) materials are more sensitive to confining stress changes than clayey materials. Increasing the resilient modulus of granular soils with increasing confinement has also been reported by numerous researchers (*8–10,17,18*). Although the three factors listed for the clayey soils were also largely present for the granular soils, the tendency of the modulus to increase with confining pressure for granular soils is too strong to be masked by the high strength of the specimens.

SUMMARY AND RECOMMENDATIONS

It is well known that subgrade materials have a nonlinear response to a load. However, if the load is repeated thousands of times, the effect of nonlinearity is reduced. A typical stress-strain relationship for a soil specimen subjected to a triaxial state of stress, where the axial stress is varied in a pulsating form while the confining pressure remains constant, will show that nonlinearity is large when the load is applied for the first time. After many applications of load, however, the response is essentially elastic and linear.

Based on the observation of many resilient modulus tests (*15,16*), it has been found that the preconditioning specified by the former AASHTO T274 procedure for resilient modulus testing was generally inadequate to remove the plastic strains from subgrade materials. The specified number of preconditioning loading cycles in the AASHTO T274 procedure was 200. As part of the laboratory testing conducted in this study, it was found that 1,000 to 2,000 cycles of a preconditioning load were required to eliminate most of the plastic deformations. The SHRP protocol P46 procedure calls for 1,000 cycles of preconditioning.

Because it is desirable to have essentially a linear elastic response of the material when the measurements are made for resilient modulus computation, a modification to most current resilient modulus testing procedures is recommended. The recommended modification is to use 1,000 cycles of loading for preconditioning samples at low to moderate stress levels, and 2,000 cycles for higher stress levels.

The modulus can be affected by the state of stress of the material. Differences in both confining pressure and deviator stress must be considered. The octahedral shear stress and normal stress have been proposed in this study as the parameters for comparing the stress state between laboratory tests and the in situ condition. It has been found that the normal and shear stresses prescribed in the AASHTO T274 procedure

TABLE 2 Laboratory Resilient Modulus Data of Subgrade Materials

Site/ Station	Sample Depth (cm)	Dry Unit Weight (kN/m^3)	Water Content (%)	Confining Pressure (kPa)	Deviator Stress (kPa)	Resilient Modulus (MPa)	Resilient Modulus (ksi)
1/1	63-81	19.2	5.28	14	93	72.4	10.5
				22	56	68.7	9.95
				31	28	91.8	13.3
				14	50	59.0	8.55
				22	26	72.1	10.45
				14	18	57.95	8.4
1/4	63-81	18.9	4.51	25	18	72.1	10.45
				25	25	77.3	11.2
				25	42	75.2	10.9
				35	25	90.4	13.1
				35	43	90.7	13.15
				35	76	89.4	12.95
2/1	48-63	18.6	7.09	17	69	80.7	11.7
				23	48	83.1	12.05
				30	22	104.9	15.2
				17	45	81.4	11.8
				20	31	83.8	12.15
				23	18	105.9	15.35
				12	21	92.5	13.4
2/7	96-114	17.5	7.83	23	27	92.1	13.35
				21	20	116.6	16.9
				20	38	86.6	12.55
				27	18	124.2	18.0
3/7	68-86	17.7	12.4	14	86	39.0	5.65
				22	53	40.0	5.8
				31	26	64.2	9.3
				14	46	36.9	5.35
				22	24	47.6	6.9
				14	18	39.0	5.65
4/1	63-81	17.6	10.4	24	84	63.1	9.15
				32	55	65.9	9.55
				41	23	86.25	12.5
				21	50	57.6	8.35
				31	24	69.35	10.05
				17	31	54.5	7.9
				17	21	64.2	9.3
				22	20	68.3	9.9
				40	86	76.9	11.15
5/4	51-68	18.8	12.4	20	62	58.0	8.4
				27	39	85.9	12.45
				33	21	93.8	13.6
				20	38	70.4	10.2
				25	21	96.3	13.95
				20	19	104.5	15.15
7/1	68-86	18.6	10.6	20	75	64.8	9.4
				15	45	53.1	7.7
				27	45	69.7	10.1
				35	19	122.9	17.8
				25	19	111.1	16.1
				15	19	79.4	11.5
7/4	68-86	18.9	9.23	21	77	71.7	10.4
				27	48	76.5	11.1
				35	21	112.4	16.3
				15	48	56.9	8.25
				26	21	87.9	12.75
				16	19	64.5	13.5
8/1	79-96	17.7	11.1	21	47	48.3	7.0
				25	35	58.3	8.45
				29	19	61.4	8.9
				21	19	48.3	7.0
				21	29	53.1	7.7
				26	19	61.4	8.9

(continued on next page)

TABLE 2 (*continued*)

Site/ Station	Sample Depth (cm)	Dry Unit Weight (kN/m^3)	Water Content (%)	Confining Pressure (kPa)	Deviator Stress (kPa)	Resilient Modulus (MPa)	Resilient Modulus (ksi)
9/1	127-145	16.4	22.8	26	71	103.5	15.0
				31	42	109.7	15.9
				31	19	124.5	18.05
				26	30	112.5	16.3
				26	19	109.4	15.85
10/4	112-130	15.2	25.9	25	49	73.5	10.65
				29	33	81.8	11.85
				33	21	88.0	12.75
				25	31	84.2	12.2
				29	21	94.5	13.7
				25	22	92.1	13.35
11/1	30-48	19.3	2.21	31	80	94.5	13.7
				37	55	97.3	14.1
				48	23	123.9	17.95
				26	57	90.0	13.05
				34	25	92.5	13.4
				20	30	77.6	11.25
				24	19	90.0	13.05
				16	19	70.0	10.15
12/1	81-99	18.9	8.56	15	58	46.6	6.75
				16	49	50.0	7.25
				21	31	50.7	7.35
				21	18	48.6	7.05
				25	19	59.7	8.65
13/4	33-51	17.4	8.81	15	65	97.3	14.1
				20	46	100.4	14.55
				25	31	123.9	17.95
				18	33	91.4	13.25
				13	55	90.0	13.05
				22	20	108.7	15.75
				12	31	81.4	11.8
14/4	30-48	16.0	15.4	12	58	82.5	11.95
				17	42	88.7	12.85
				22	22	82.1	11.9
				11	40	65.6	9.5
				16	21	64.9	9.4
				9	19	47.6	6.9
16/1	43-61	18.5	7.90	15	61	61.6	8.9
				20	40	64.35	9.35
				25	26	77.3	11.2
				13	52	56.65	8.2
				18	31	68.3	9.9
				22	20	92.5	13.4
				12	29	54.1	7.85
17/1	51-66	16.5	17.8	15	57	28.85	4.2
				25	21	43.65	6.35
				17	43	28.35	4.1
				20	31	33.05	4.8
				20	20	37.4	5.4
				12	26	27.9	4.05
19/1	58-76	16.4	22.7	15	55	66.15	9.6
				27	20	98.7	14.3
				17	41	73.1	10.6
				20	29	81.6	11.8
				20	20	94.8	13.75
19/4	79-97	15.1	28.9	15	53	111.4	16.15
				27	19	113.8	16.5
				17	39	90.05	13.05
				20	28	106.0	15.2
				15	28	119.2	17.3

Note: 1 MPa = 0.145 ksi 62.4 pcf = 9.807 kN/m^3
1 kPa = 0.145 psi 1 in. = 2.54 cm

for resilient modulus testing typically exceed those expected for in situ conditions, even considering loading by a heavily overloaded truck.

It is proposed that the stress state imposed in the laboratory during resilient modulus testing should not exceed the greatest loading expected in situ because of possible modification of subsequently measured modulus. It is important to avoid overloading the laboratory specimen in both normal and shear stresses. Therefore, it is recommended that the octahedral shear stress and octahedral normal stress be less than or equal to the maximum values anticipated for the field loading. The maximum octahedral normal stress and maximum octahedral shear stress can be estimated by using a linear elastic, multilayer pavement system analysis program. This study used falling weight deflectometer test results for estimating the moduli of the layers and the ELSYM5 program for the analysis. In the absence of NDT results, experience can usually be used to estimate layer moduli with an accuracy sufficient for calculating reasonably expectable maximum stress states in the prototype.

ACKNOWLEDGMENT

The work presented in this paper was sponsored by the Arizona Department of Transportation through the Arizona Transportation Research Center. This support is gratefully acknowledged.

REFERENCES

1. *AASHTO Guide for Design of Pavement Structures*. AASHTO, Washington, D.C., 1986.
2. H. Seed, C. Chan, and C. Lee. Resilience Characteristics of Subgrade Soils and Their Relation to Fatigue Failures in Asphalt Pavements. *Proc., International Conference on the Structural Design of Asphalt Pavements*, University of Michigan, 1962, pp. 611–636.
3. G. Raymond, P. Gaskin, and F. Addo-Abedi. Repeated Compressive Loading of Leda Clay. *Canadian Geotechnical Journal*, Vol. 16, No. 1, 1979, pp. 1–10.
4. D. Fredlund, A. Bergan, and P. Wong. Relationship Between the Resilient Modulus and Stress Conditions for Cohesive Subgrade Soils. In *Transportation Research Record 642*, TRB, National Research Council, Washington, D.C., 1977, pp. 73–81.
5. E. Drumm, Y. Boateng-Poku, and T. Pierce. Estimation of Subgrade Resilient Modulus From Standard Tests. *Journal of Geotechnical Engineering*, ASCE, Vol. 116, No. 5, May 1990, pp. 774–789.
6. A. Nataatmadja and A. Parkin. Characterization of Granular Materials for Pavements. *Canadian Geotechnical Journal*, No. 26, 1989, pp. 725–730.
7. J. Mitchell. *Fundamentals of Soil Behavior*. John Wiley and Sons, Inc., New York, N.Y., 1976.
8. S. Brown. Repeated Load Testing of Granular Material. *Journal of Geotechnical Division*, ASCE, Vol. 100, GT7, July 1974, pp. 825–841.
9. K. Tanimoto and M. Nishi. On Resilient Characteristics of Some Soils Under Repeated Loading. *Soils and Foundations*, Vol. X, No. 1, 1970, pp. 75–92.
10. R. Elliot and D. Lourdesnathan. Improved Characterization Model for Granular Bases. In *Transportation Research Record 1227*, TRB, National Research Council, Washington, D.C., 1989, pp. 128–133.
11. C. Desai and J. Christian. *Numerical Method in Geotechnical Engineering*. McGraw Hill Co., New York, N.Y., 1977.
12. G. Ahlborn. *Elastic Layered System with Normal Loads*. ITTE, University of California, Berkeley, 1972.
13. A. J. Bush and G. Y. Baladi. *Nondestructive Testing of Pavements and Backcalculation of Moduli*. STP 1026. ASTM, Philadelphia, Pa., 1989.
14. W. Houston, M. Mamlouk, and R. Perera. Laboratory versus Non-destructive Testing for Pavement Design. *Journal of Transportation Engineering*, ASCE, Vol. 118, No. 2, March/April 1992, pp. 207–222.
15. M. Mamlouk, W. Houston, S. Houston, and J. Zaniewski. *Rational Characterization of Pavement Structures Using Deflection Analysis*. Report FHWA-AZ87-254, Vol. 1. Arizona Department of Transportation, Phoenix; FHWA, U.S. Department of Transportation, 1989.
16. M. Mamlouk, J. Zaniewski, W. Houston, and S. Houston. Overlay Design Method for Flexible Pavements in Arizona. In *Transportation Research Record 1286*, TRB, National Research Council, Washington, D.C., 1990, pp. 112–122.
17. R. Elliot and S. Thornton. Resilient Modulus and AASHTO Pavement Design. In *Transportation Research Record 1196*, TRB, National Research Council, Washington, D.C., 1988, pp. 116–124.
18. R. Hicks and C. Monismith. Factors Influencing the Resilient Response of Granular Materials. *Highway Research Record 345*, HRB, National Research Council, Washington, D.C., 1971, pp. 14–31.

Publication of this paper sponsored by Committee on Soil and Rock Properties.

Simplified Direct Calculation of Subgrade Modulus from Nondestructive Pavement Deflection Testing

ANDREW M. JOHNSON AND RONALD L. BAUS

The 1986 *AASHTO Guide for Design of Pavement Structures* proposed that subgrade moduli underlying existing pavement can be determined in a direct, closed form by using peak deflections measured at a distance from the applied load during nondestructive deflection testing. The presence of the pavement layers above the subgrade could lead to significant error in the calculated subgrade modulus when this technique is applied. Subgrade correction factors are developed by calculation of error on the basis of analysis of linear elastic simulations. Least-squares regression analysis is then used to develop an equation for predicting the error. Pavement properties calculated from field data using corrected subgrade modulus are shown to vary less with time when compared with the same properties calculated using uncorrected subgrade moduli. Using field data, the corrected, directly calculated subgrade moduli are shown to compare well to the results obtained from multilayer iterative backcalculation procedures.

The 1986 *AASHTO Guide for Design of Pavement Structures* proposed that subgrade moduli underlying existing pavement can be determined in a direct, closed form by using peak deflections measured at a distance from the applied load during nondestructive deflection testing. If the subgrade modulus is known before backcalculation of pavement modulus, calculating the pavement properties through equivalent modulus, closed-form solutions, or iterative basin-matching techniques is simplified. The modulus calculation technique, which is shown in the 1986 *AASHTO Guide for Design of Pavement Structures* (*1*), is based on the Boussinesq solution of a point load acting on the surface of a linear elastic half-space.

Using a two-layer linear elastic half-space (combined pavement layer over infinite subgrade) with a circular distributed load to simulate deflection testing, theoretical linear elastic deflections may be calculated using a computer program, such as ELSYM5 (*2*). When the calculated theoretical deflections are then used to solve for subgrade modulus using the direct method, significant errors will occur because of the presence of stiffer pavement layers above the subgrade. If the subgrade modulus is in error, then the corresponding backcalculated pavement properties will also be in error. Therefore, a modified direct procedure for calculation of subgrade modulus is proposed.

A. M. Johnson, Research and Materials Laboratory, South Carolina Department of Highways and Public Transportation, P.O. Box 191, Columbia, S.C. 29202. R. L. Baus, Department of Civil Engineering, University of South Carolina, Columbia, S.C. 29208.

CALCULATION OF SUBGRADE MODULUS ON THE BASIS OF POINT LOADING

The Boussinesq equation for off-axis vertical surface deflection resulting from a point load acting on a linear elastic half-space is as follows (*3*):

$$d_z = \frac{P(1 - \mu^2)}{\pi E r} \quad (1)$$

where

d_z = vertical surface deflection at distance r from the applied load,
P = load,
E = half-space modulus of elasticity,
r = distance from load to point of deflection measurement, and
μ = Poisson's ratio.

To solve for E, Equation 1 may be rewritten as follows:

$$E = \frac{P(1 - \mu^2)}{\pi d_z r} \quad (2)$$

A modified form of Equation 2 is given on page III-86 and in Figure III-5.5 of the AASHTO Guide (*1*).

Ullidtz (*4*) refers to the results of Equation 2 as the "surface modulus." The surface modulus is purported to represent the approximate weighted mean modulus of the layered half-space at a given distance away from the test load. For a pavement overlying a linear elastic subgrade, the surface modulus should theoretically reach an asymptotic value representative of the subgrade modulus at the distance from the load at which vertical surface deflections are due entirely to strain in the subgrade layer. In the AASHTO Guide (*1*), the distance at which the surface modulus becomes asymptotic is referred to as the effective radius of subgrade stress (a_e). This relationship is shown in Figure 1(*a*) (*5*). Most nonlinear subgrades have increasing moduli with decreasing levels of vertical stress. Therefore the surface modulus is expected to increase with increasing distance from the load (*4*). This relationship is shown in Figure 1(*b*).

Estimating a_e requires making a number of assumptions about the pavement properties. Because the subgrade modulus should theoretically be represented by the minimum calculated surface modulus, it is proposed to calculate subgrade

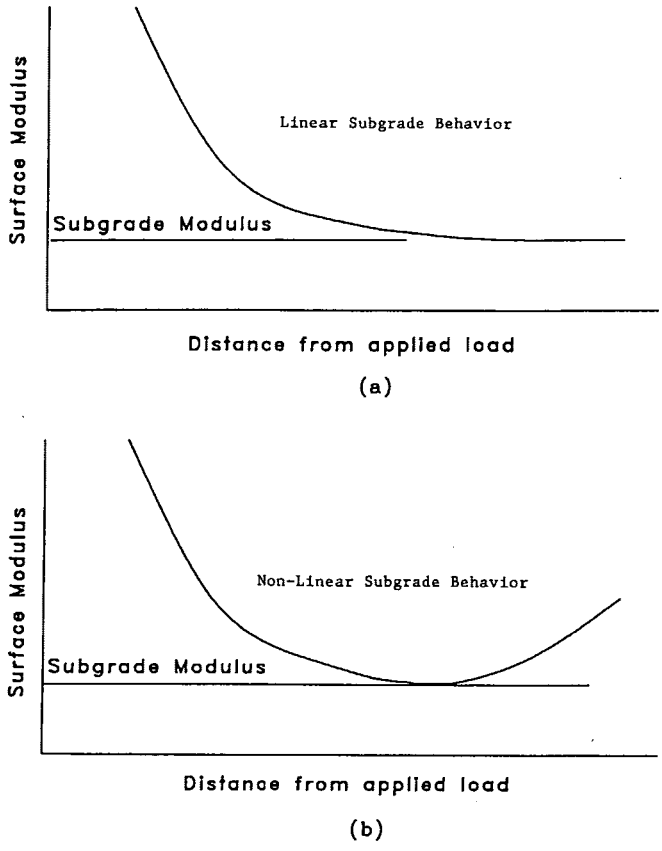

FIGURE 1 Typical expected variation in surface modulus with distance from applied load for pavements with (*a*) linear elastic subgrade and (*b*) nonlinear elastic subgrade.

moduli by calculating surface moduli at all deflection measurement locations. The subgrade modulus is then assumed equal to the minimum measured surface modulus, thus eliminating the need to make assumptions about the pavement and subgrade moduli in order to estimate a_e. However, as will be shown, the subgrade modulus (E_{sg}) may not be represented by the minimum surface modulus, and further correction is necessary.

POINT LOAD APPROXIMATION EFFECTS

The load applied by a falling weight deflectometer (FWD) or another pavement deflection measuring device is typically applied through a circular plate that is in contact with the pavement surface. However, at some distance from the applied load, the difference between the point and the distributed load cases becomes negligible for a homogeneous elastic halfspace (*4*). Because it is proposed to choose the subgrade modulus based on the minimum surface modulus, in some cases the point of calculation for the surface modulus may be too close to the applied circular load to use the point load approximation.

No closed-form solution for the analysis of off-axis deflections from a circular distributed load on a linear elastic halfspace is available. Ahlvin and Ulery (*6*) present a tabular solution for the calculation of off-axis ($r \neq 0$) vertical deflections for circular loading (*3*). The solution for surface vertical deflection from a circular loaded area is

$$d_z = \frac{pRH(1 - \mu^2)}{E} \tag{3}$$

where

p = pressure,
R = radius of loaded area, and
H = $f(r/R)$ (see Table 1).

To correct for the error induced by the point load approximation, the value of r used in Equation 2 may be transformed to an adjusted radius (r_{adj}). To find r_{adj} for a given load radius (R) and true deflection measurement distance (r), Equation 1 is set equal to Equation 3. The equation for r_{adj} then becomes

$$r_{adj} = \frac{R}{H} \tag{4}$$

where R and H are as defined in Equation 3. Using a load radius of 5.9 in., the actual and adjusted radii used for this study are presented in Table 2. Deflection measurement locations were adjusted to a distance of 4 load radii (23.6 in.) from the center of loading.

Figure 2 is a typical plot of surface modulus versus distance obtained using South Carolina FWD field data. The plot shows the changes in backcalculated moduli when adjusted radii are used and typical nonlinear soil behavior.

THEORETICAL ERROR IN SUBGRADE MODULUS CALCULATION

To test the accuracy of the direct subgrade modulus calculation method using adjusted radii, the pavement/subgrade

TABLE 1 Off-Axis Surface Deflection Factors (*3*)

Load Radius/Distance (r/R)	Deflection Factor (H)
1.0	1.27319
1.2	0.93676
1.5	0.71185
2.0	0.51671
3.0	0.33815
4.0	0.25200
5.0	0.20045
6.0	0.16626
7.0	0.14315
8.0	0.12576
10.0	0.09918
12.0	0.08346
14.0	0.07023

TABLE 2 Actual and Adjusted Geophone Radii Used for Testing Program

Geophone Number	Actual Distance from Load Center (inches)	Adjusted Distance from Load Center for Analysis (inches)
2	7.9	7.095
3	11.8	11.414
4	23.6	23.410
5	35.4	Not Adjusted
6	53.1	Not Adjusted
7	70.9	Not Adjusted

1 inch = 25.4 mm

system was modeled as a two-layer linear elastic half-space. The pavement was assumed to have an average structural layer coefficient from 0.10 to 0.40 structural number (SN)/in. and a structural number from 2 to 9. The subgrade modulus was assumed to range from 5 to 60 ksi. The thickness of the theoretical pavement layer was calculated using the relation

$$h_t = \frac{SN}{a_{avg}} \tag{5}$$

where

h_t = total pavement thickness (inches),
SN = pavement structural number, and
a_{avg} = average structural coefficient (SN/in.).

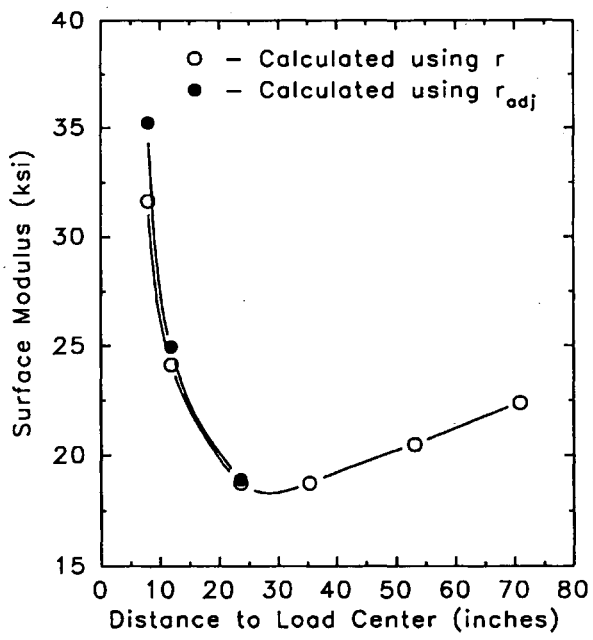

FIGURE 2 Example of variation in measured surface modulus with distance from load center (1 in. = 25.4 mm, 1 ksi = 6.89 MPa).

The value of a_{avg} was then converted to equivalent elastic modulus using the equation

$$E_e = \left(\frac{a_{avg}}{0.0043}\right)^3 (1 - \mu_e^2) \tag{6}$$

where E_e is composite pavement modulus (psi) and μ_e is pavement Poisson's ratio (*1*, Appendix PP).

Both subgrade and pavement Poisson's ratio are assumed to be 0.35. Cases for which h_t was greater than 30 in. were discarded as unrealistically thick.

Using ELSYM5, deflection basins were predicted for the theoretical pavements under a 9,000-lb loading applied to a loading plate with a 5.91-in. radius. The direct method (using minimum surface modulus computed for Equation 2 with the adjusted geophone radii given in Table 2) was then used with the theoretical deflection basins to predict subgrade modulus E_{sg}. The error in calculated E_{sg} is defined as the assumed E_{sg} minus the backcalculated E_{sg}.

Examples of the errors in predicted subgrade modulus for the ELSYM5 deflection basins are shown in Figure 3(*a*). For the E_{sg} = 20 ksi case shown in Figure 3(*b*), the backcalculated subgrade modulus was always lower than the correct value.

The effect of the errors in subgrade modulus on calculated SN are shown in Figure 4(*a*). Values of composite pavement modulus (E_e) were determined by using erroneous calculated values of E_{sg} to match correct values of under plate deflections. These values of E_e were converted to SN using the following equation given in the AASHTO Guide (*1*):

$$SN = 0.0043\left[\frac{E_e}{(1 - \mu^2)}\right]^{1/3} \cdot h_t \tag{7}$$

The error in the calculated structural number is defined as the true (assumed) SN minus the backcalculated SN.

Figures 5(*a*) and 6(*a*) show the error in calculated E_{sg} and SN for all pavement thickness and subgrade modulus combinations. Based on a two-layer elastic analysis, using the direct method of subgrade modulus calculation can result in errors in the predicted structural number of up to ±0.5.

EMPIRICAL CORRECTION OF CALCULATED SUBGRADE MODULI

A careful examination of the error data presented in Figure 5(*a*) indicated that a second-order linear regression provided an excellent fit for error versus pavement thickness, pavement stiffness, and subgrade modulus computed using minimum surface modulus and adjusted radii. Therefore, a quadratic least-squares regression was performed using h_t, the initially calculated structural number, and the initially calculated subgrade modulus to predict the error in the initially calculated subgrade modulus. The following correction equation was developed:

$$\begin{aligned} E_{sgerr} = {} & 313.964 - 482.307SN_1 + 62.40h_t - 0.06219E_{sg1} \\ & + 64.812SN_1^2 - 1.841(h_t \cdot SN_1) - 1.544h_t^2 \\ & - 0.01823(E_{sg1} \cdot SN_1) + 0.003959(E_{sg1} \cdot h_t) \\ & + 0.000000671E_{sg1}^2 \end{aligned} \tag{8}$$

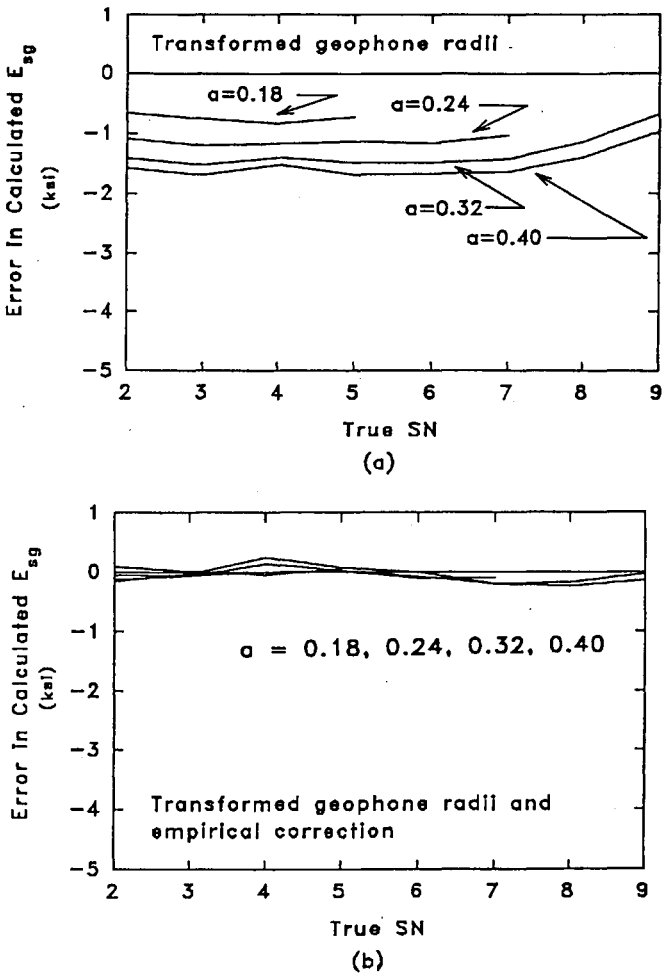

FIGURE 3 Variation of error in calculated subgrade modulus with SN for various average structural layer coefficients, (*a*) without and (*b*) with empirical correction, E_{sg} = 20 ksi (1 ksi = 6.89 MPa).

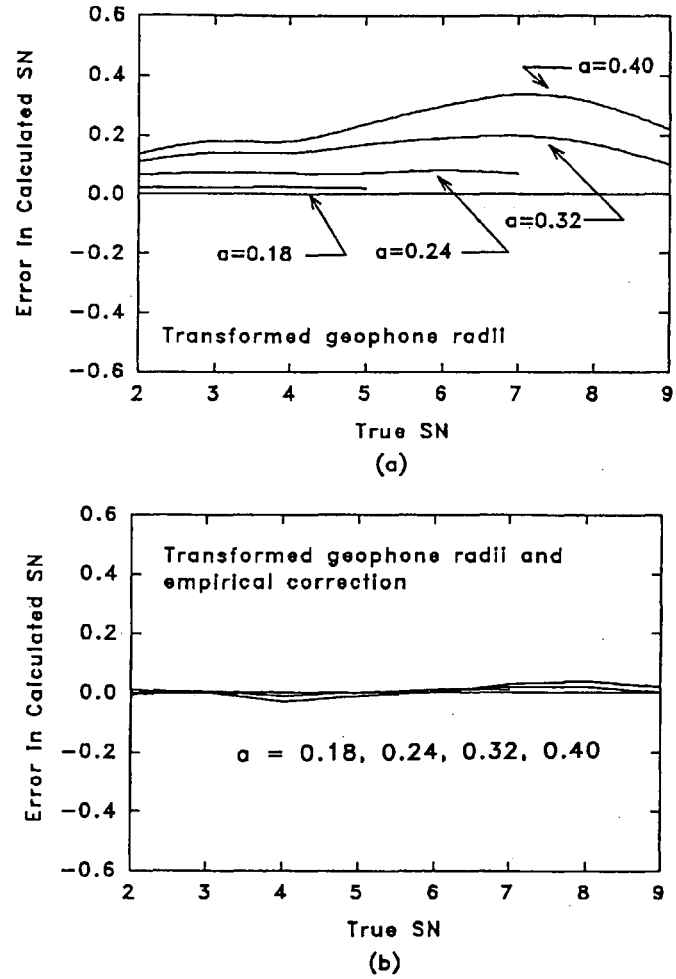

FIGURE 4 Variation in error of calculated structural number with correct structural number for various average structural layer coefficients, (*a*) without and (*b*) with empirical subgrade modulus correction, E_{sg} = 20 ksi (1 ksi = 6.89 MPa).

where

E_{sg1} = initially calculated subgrade modulus (based on minimum surface modulus and adjusted radii) (psi),
SN_1 = structural number calculated using E_{sg1},
h_t = total pavement thickness (inches), and
E_{sgerr} = error in initially calculated subgrade modulus, which is equal to E_{sg1} − correct E_{sg}.

This equation was incorporated into the University of South Carolina's backcalculation program SCSN (*7*), which was then used to recalculate E_{sg} and SN for the theoretical, ELSYM5-derived deflection basins. SCSN uses the minimum surface modulus based on adjusted geophone radii and Equation 8 for subgrade modulus error correction. The recalculated results are shown in Figures 3(*b*), 4(*b*), 5(*b*), and 6(*b*). Within the range of reasonable E_e, E_{sg}, and h_t, the corrected direct calculation technique provides an excellent estimate of lower layer modulus for a two-layer linear elastic system. Transformed geophone radii do not appear to make a large contribution to improving estimates of lower layer modulus because minimum surface modulus is usually computed using deflection measured at a distance greater than 23.6 in. (Geophone 4 location) from the center of the load plate.

COMPARISON OF CORRECTED AND UNCORRECTED DIRECT METHOD SUBGRADE MODULUS ON FIELD TEST DATA

Field deflection measurements were taken bimonthly from January 1989 to June 1990 at 14,500-ft-long test sites throughout South Carolina using a Dynatest 8000 FWD. Two additional sites were tested bimonthly from October 1989 to May 1990. The FWD deflection sensors were positioned as shown in Table 2. The FWD drop height was adjusted to provide nominal loads of 6,000, 9,000, 12,000, and 16,000 lb. Test locations were located at 50-ft stations within the test sections. Details of the pavement structure at each site are shown in Table 3. Interstate 26 in Orangeburg County was rehabilitated throughout 1989, resulting in the eventual relocation of Site 1. Site 12 was overlaid in May 1990. Further details on the deflection testing and FWD test sites are given in work by Baus and Johnson (*7*).

To investigate the improvement gained by performing the suggested subgrade correction method, the temperature corrected SNs were computed based on the nominal 9,000-lb applied load for all stations and dates at each site both with and without subgrade correction. Temperature corrections to

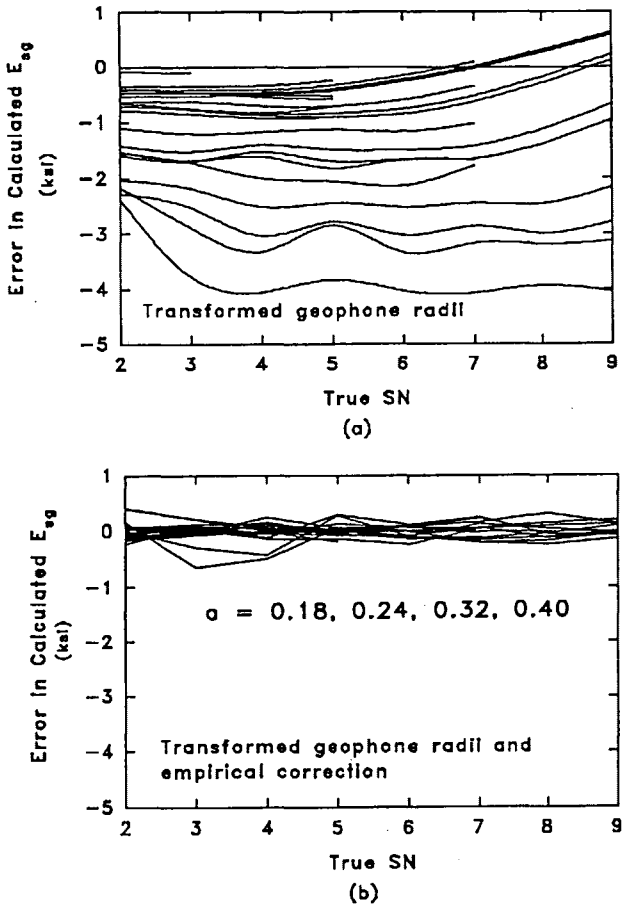

FIGURE 5 Variation of error in calculated subgrade modulus with correct structural number for E_{sg} from 5 to 60 ksi and all a_i, (*a*) without and (*b*) with empirical subgrade modulus correction (1 ksi = 6.89 MPa).

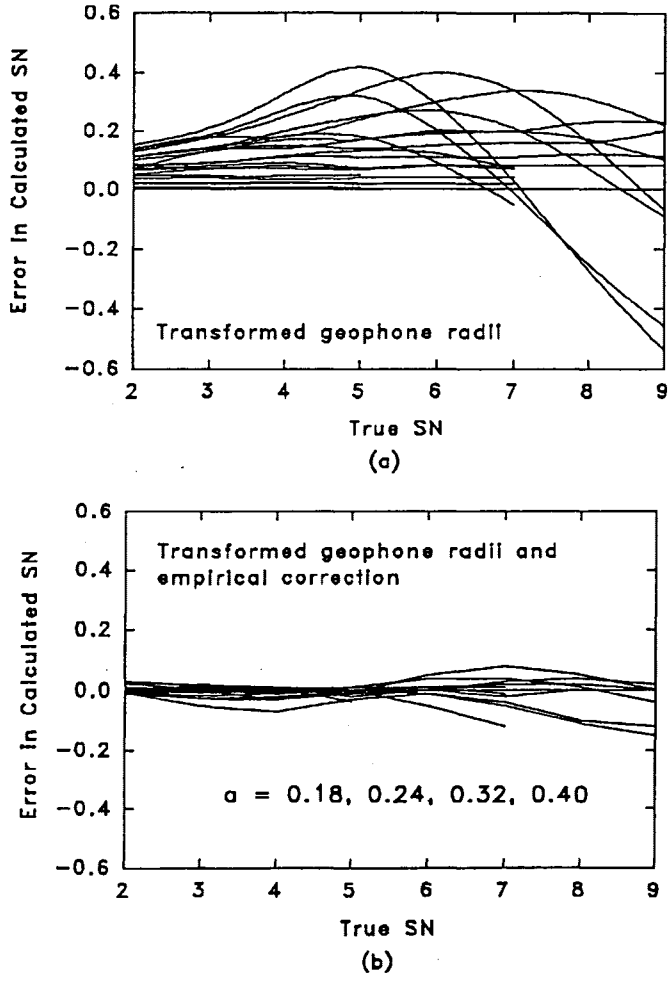

FIGURE 6 Error in calculated structural number versus correct structural number for E_{sg} from 5 to 60 ksi and all a_i, (*a*) without and (*b*) with empirical subgrade modulus correction (1 ksi = 6.89 MPa).

SN were made using the procedure described in work by Johnson and Baus (*8*). On the basis of the results at all stations, the site average temperature corrected SN was calculated for each date and site both with and without subgrade modulus correction. The standard deviations of the site average SN values with and without subgrade modulus correction are plotted against each other in Figure 7. Site 1 was omitted from Figure 7 because of its relocation during testing. Results for Sites 15 and 16 were omitted because of the relatively short time period testing was performed at these sites.

Figure 7 clearly shows that using the proposed subgrade modulus correction technique results in more uniform pavement properties over time. Because the tests represented in Figure 7 were performed over a wide range of temperatures, it is probable that the backcalculated subgrade moduli obtained without correction were affected by the variation of the overlying pavement stiffness with temperature.

COMPARISON OF DIRECTLY CALCULATED SUBGRADE MODULUS WITH BASIN-MATCHED ITERATIVE SUBGRADE MODULUS

To provide comparisons with iterative, basin-matching procedures, the EVERCALC (*9*), MODULUS (*10*), and BOUSDEF (*11*) programs were used to analyze the collected field data to determine the subgrade modulus. EVERCALC analyzed several load levels in its calculations, then normalized the subgrade modulus to a 9,000-lb applied load. For MODULUS and BOUSDEF, as well as SCSN, a single drop at a nominal 9,000-lb load level was used. The results of the comparisons are shown in Figures 8–10. Because of the time involved in performing the iterative, basin-matching procedures, only the deflections from the first station at each site were used for each date.

Generally good agreement between basin-matching and directly calculated subgrade moduli is shown, except for Sites 8–10. Data for these sites are highlighted in Figures 8–10. Pavement structures at Sites 8 and 9 are thick. The pavement structure at Site 10 is thin. In these boundary cases of thickness, the multilayer, basin-matching programs tend to assign a low value of modulus to the unbound base course and high values of modulus to both the asphalt concrete–bound toplayer and subgrade. When Site 8–10 results are taken out of consideration, the corrected subgrade moduli have a correlation coefficient (r^2) of 0.80 to 0.82 with the other backcalculation programs. When compared to each other, the basin-matching programs have r^2 values from 0.90 to 0.95. Where

TABLE 3 FWD Test Site Locations

Site No.	Road and County	Pavement Structures
1	I-26 Calhoun County	9.0 inches AC Bound* 16.0 inches Earth Type Base *Resurfaced during testing period giving 10.1 inches AC Bound
2	I-26 Orangeburg County	11.3 inches AC Bound 14.0 inches Earth Type Base
3	SC-31 Charleston County	3.2 inches AC Bound 11.5 inches Fossiliferous Limestone Base
4	US-17 Charleston County	3.5 inches AC Bound 6.2 inches Fossiliferous Limestone Base
5	US-17 Charleston County	4.9 inches AC Bound 7.4 inches Fossiliferous Limestone Base
6	US-321 Fairfield County	6.2 inches AC Bound 3.5 inches Unbound Granular Base 12.0 inches Cement Stabilized Earth Base
7	SC-9 Chester County	10.8 inches AC Bound 6.0 inches Earth Type Base
8	I-26 Newberry County	9.0 inches AC Bound 16.0 inches Macadam Base
9	I-77 Richland County	18.1 inches AC Bound 6.0 inches Cement Modified Earth Subbase
10	S-1623 Lexington County	1.3 inches AC bound 6.0 inches Macadam Base
11	I-20 Lexington County	12.4 inches AC Bound
12	US-76/378 Sumter County	6.6 inches AC Bound* 12.0 inches Earth Type Base *Resurfaced during testing period giving 8.1 inches AC Bound
13	US-76 Marion County	10.2 inches AC Bound
14	US-76/301 Florence County	7.0 inches AC Bound 4.5 inches Stabilized Earth Base 8.0 inches Earth Type Subbase
15	I-385 Greenville County	6.3 inches AC Bound 8.0 inches Macadam 4.0 inches Cement Modified Subgrade
16	US-176 Union County	4.6 inches AC Bound 8.0 inches Macadam 6.0 inches Cement Modified Subbase

1 inch = 25.4 mm

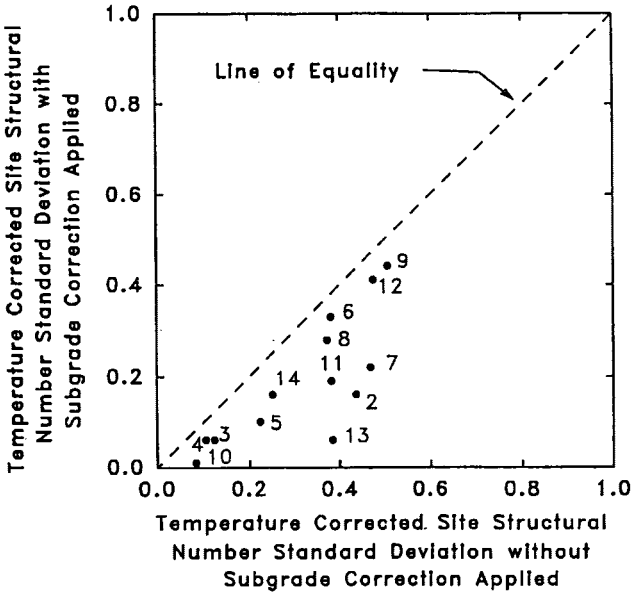

FIGURE 7 Comparison of test site average structural numbers calculated with and without empirical subgrade correction.

disagreement is substantial between SCSN and the basin-matching programs, SCSN almost always predicts a lower subgrade modulus. Extensive comparisons of SCSN and basin-matching program results are presented by Baus and Johnson (*7*).

CONCLUSIONS

Consistent analysis of subgrade stiffness is important in the backcalculation of pavement properties. A small variation in calculated subgrade modulus may lead to substantial variation in backcalculated pavement stiffness. Based on two-layer, elastic layer theory, an empirical correction is described that significantly improves direct (noniterative) computation of subgrade modulus from FWD surface deflections. The direct calculation method with empirical correction can accurately calculate the lower layer modulus of a two-layer linear elastic system. When field data are used to compare subgrade moduli calculated with iterative, multilayer backcalculation programs to corrected directly calculated subgrade moduli, good agreement is shown in the majority of cases. When substantial disagreement is found between the results of field data anal-

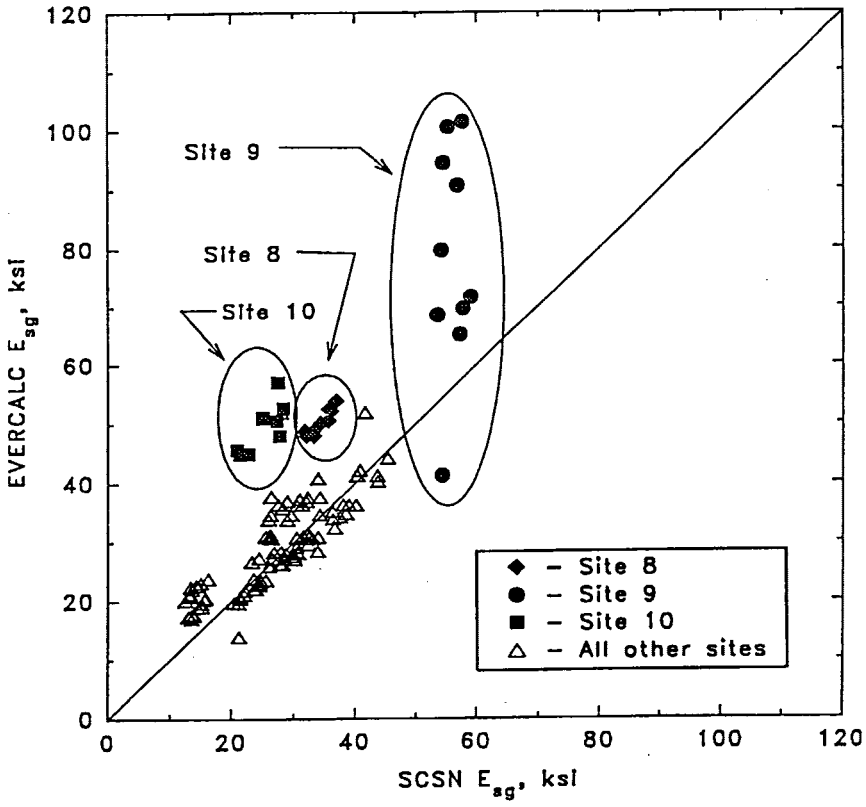

FIGURE 8 Comparison of subgrade moduli calculated directly with empirical correction and using program EVERCALC (1 ksi = 6.89 MPa).

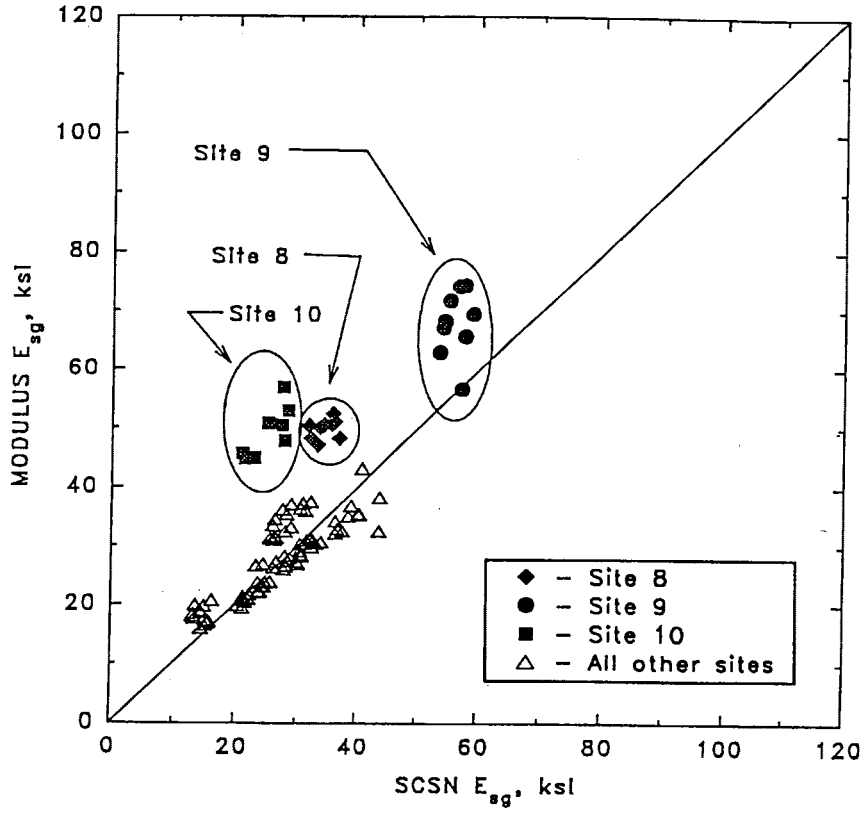

FIGURE 9 Comparison of subgrade moduli calculated directly with empirical correction and using program MODULUS (1 ksi = 6.89 MPa).

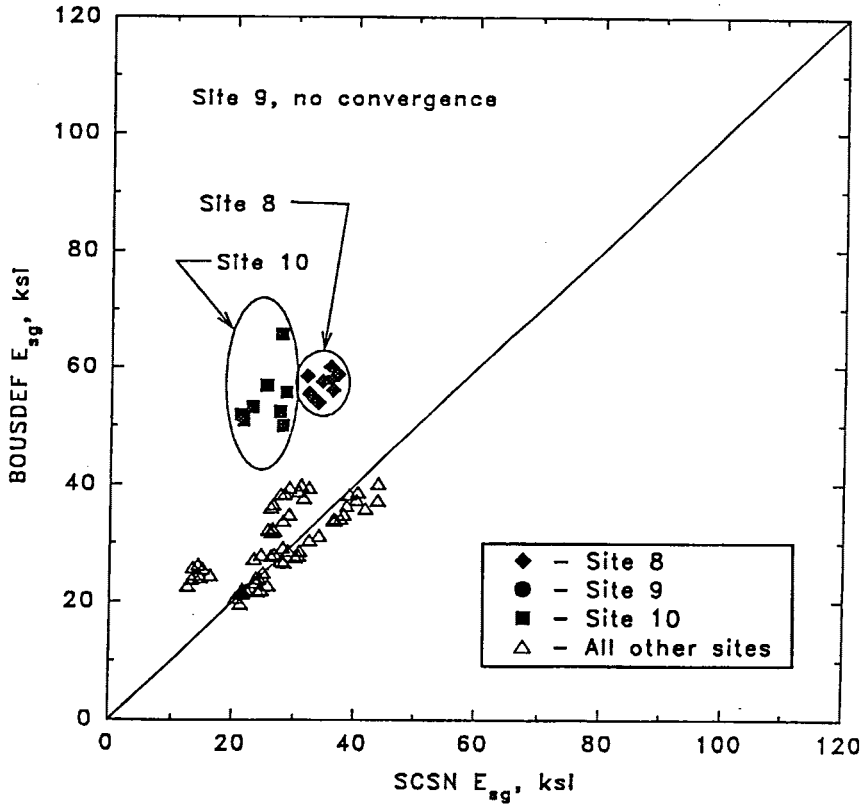

FIGURE 10 Comparison of subgrade moduli calculated directly with empirical correction and using program BOUSDEF (1 ksi = 6.89 MPa).

ysis using iterative and direct methods, the direct method almost always provides a lower value of subgrade modulus, which in some cases appears to be more reasonable. When the proposed subgrade correction technique is applied to field data, the stability of pavement properties over time improves compared with analyses without subgrade correction.

ACKNOWLEDGMENTS

This research was funded by the South Carolina Department of Highways and Public Transportation and FHWA.

REFERENCES

1. *AASHTO Guide for Design of Pavement Structures*. AASHTO, Washington, D.C., 1986.
2. S. Kopperman, G. Tiller, and M. Tseng. *ELSYM5: Microcomputer Version, User's Guide for IBM-PC's and Compatibles*. Report FHWA-TS-87-206. FHWA, U.S. Department of Transportation, 1986.
3. H. G. Poulos and E. H. Davis. *Elastic Solutions for Soil and Rock Mechanics*. John Wiley and Sons, Inc., New York, 1974.
4. P. Ullidtz. *Pavement Analysis*. Elsevier, New York, 1987.
5. G. R. Rada, M. W. Witczak, and S. D. Rabinow. Comparison of AASHTO Structural Evaluation Techniques Using Nondestructive Testing. In *Transportation Research Record 1207*, TRB, National Research Council, Washington, D.C., 1988.
6. R. G. Ahlvin and H. H. Ulery. Tabulated Values for Determining the Complete Pattern of Stresses, Strains and Deflections Beneath a Uniform Circular Load on a Homogeneous Half Space. *Bulletin 342*, HRB, National Research Council, Washington, D.C., 1962.
7. R. L. Baus and A. M. Johnson. *Flexible Pavement Overlays by Dynamic Deflections—Phase II*. Report No. F92-143. Department of Civil Engineering, University of South Carolina, 1992.
8. A. M. Johnson and R. L. Baus. Alternate Method for Temperature Correction of Backcalculated Equivalent Pavement Modulus. In *Transportation Research Record 1355*, TRB, National Research Council, Washington, D.C., 1988.
9. EVERCALC Version 3.0. University of Washington and Washington State Department of Transportation, 1990.
10. T. Scullion, J. Uzan, and M. Paredes. MODULUS: A Microcomputer-based Backcalculation System. Presented at the 69th Annual Meeting of the Transportation Research Board, Washington, D.C., 1990.
11. H. Zhou, R. G. Hicks, and C. A. Bell. BOUSDEF: A Backcalculation Program for Determining Moduli of a Pavement Structure. Presented at the 69th Annual Meeting of the Transportation Research Board, Washington, D.C., 1990.

Publication of this paper sponsored by Committee on Soil and Rock Properties.